DESIGN AND OPTIMIZATION OF EFFICIENT MAGNETIC COILS FOR BIOMEDICAL APPLICATIONS

by

Anil Kumar Ram Rakhyani

A dissertation submitted to the faculty of
The University of Utah
in partial fulfillment of the requirements for the degree of

Doctor of Philosophy

Department of Electrical and Computer Engineering

The University of Utah

August 2014

The University of Utah Graduate School

STATEMENT OF DISSERTATION APPROVAL

The dissertation of **Anil Kumar Ram Rakhyani**

has been approved by the following supervisory committee members:

Gianluca Lazzi	, Chair	**06/09/2014** Date Approved
Darrin J. Young	, Member	**04/24/2014** Date Approved
Douglas A. Christensen	, Member	**04/24/2014** Date Approved
Om P. Gandhi	, Member	**04/24/2014** Date Approved
Richard A. Normann	, Member	**04/24/2014** Date Approved

and by **Gianluca Lazzi** , Chair/Dean of

the Department/College/School of **Electrical and Computer Engineering**

and by David B. Kieda, Dean of The Graduate School.

ABSTRACT

Magnetic fields are permeable to the biological tissues and can induce electric field in the conductive structures. Some medical devices take advantage of this ability to transfer energy from the source to the receiving site without direct contact. Prosthetic devices such as retinal implants use time-varying magnetic field to achieve wireless power transfer to the implanted magnetic coil. However, devices such as magnetic stimulators use the induction principle to create an electric field at the stimulation site. Efficiency of these devices is primarily dependent on the design of the magnetic coils. Therefore, in this work, we designed and validated efficient magnetic coils for wireless power transfer to implanted devices and magnetic stimulation of the peripheral nerves.

Typical wireless power transfer (WPT) systems uses two-coil based design to achieve contactless power transfer to the implanted electronics. These systems achieve low power transfer efficiency ($< 30\%$) and frequency bandwidth. Moreover, efficient wireless system requires high coupling and load variation tolerance during device operation. To design an electromagnetic safe WPT system, the power absorbed by the tissue and radiated field due to the proximal magnetic coils needs to be minimized. In this work, we proposed a multi-coil power transfer system which solves some of the current challenges. The proposed multi-coil WPT system achieves more than twice the power transfer efficiency, controllable voltage gain, wider frequency bandwidth, higher tolerance to coupling and load variations, lower absorbed power in the tissue and lower radiated field from the magnetic coil than a comparable two-coil system. In this work, we have developed analytic models of the multi-coil WPT system and validated the accuracy of the solutions using experiments.

Magnetic coils play an important role in controlling the distribution of induced electric field inside the nerve during magnetic stimulation. In the past, homogeneous models were used to estimate the field profile inside conductive tissue due to the time varying current in the magnetic coil. Moreover, the effect of the surrounding media and stimulation mechanisms was understudied, which limits the optimization accuracy of the magnetic coils. In this work, we developed anatomically correct tissue models to study the effect of tissue heterogeneity and the surrounding media on the induced electric field. We also developed an optimization algorithm for designing energy efficient cm-size magnetic coils, that were then used for ex-vivo magnetic stimulation of the frog's sciatic nerve.

CONTENTS

CHAPTERS

APPENDICES

LIST OF FIGURES

LIST OF TABLES

ACKNOWLEDGMENTS

First of all, I would like to express my sincere gratitude to my supervisor, Prof. Gianluca Lazzi, for his whole-hearted support during the past two years. He has not only greatly helped me with the technical contributions of this dissertation, but has also constantly encouraged and guided me in the right direction in my research. His friendly and understanding attitude provided the perfect environment for me to achieve my research goals.

Secondly, I greatly thank my research committee Prof. Richard A. Normann, Prof. Om Gandhi, Prof. Darrin Young and Prof. Douglas A. Christensen for their invaluable comments. My deep appreciation goes to Dr. David J. Warren and Prof. Faisal Khan as well for their technical assistance. I would like to thank the students in Dr. Lazzi' lab: Dr. Carlos J. Cela, Dr. Ajit Rajagopalan, Kyle Loizos, Erik Gamez, Zack Kagan, Amit Qusba, and other friends. A special thanks to Shashank Pandey who accompanied and encouraged me during my PhD program.

Finally, I would like to thank my family from the bottom of my heart for their love, inspiration, and understanding for my decision to pursue higher studies. So I dedicate my dissertation to my parents, Mr. Girdhari Lal and Mrs. Kavita Devi. I would also like to thank my sisters, Ms. Kanta and Ms. Geetanjali, my fiance, Rachel Jenks, and my cats, Choji & Katie. It was their support that encouraged me to overcome many challenges.

This work is supported in part by research funding from the National Science Foundation (NSF).

CHAPTER 1

INTRODUCTION

1.1 Abstract

Applications of time-varying magnetic field for biomedical systems, such as wireless power transfer and magnetic neural stimulation, are studied in the work. This work is motivated by the need of efficient magnetic coils to achieve high efficiency and efficacy for two leading biomedical applications. The first design includes the design and applications of multi-coil telemetry system to improve the power transfer efficiency and reduce electromagnetic energy. The second design focuses on the design and usage of magnetic coils for the magnetic neural stimulation.

1.2 Introduction

Over the last three decades, magnetic field-based actuators/sensors have been used extensively in the domain of biomedical instrumentation [1–4]. Depending on the underlying applications, the operating conditions of these devices may require static (e.g., magnetic sensor) or time-varying magnetic field (e.g., transcranial magnetic stimulators or wireless power transfer). Two key features have increased interest in studying the use of magnetic field for biomedical applications. First, biological tissue has nearly unitary relative magnetic permeability. Second, it has the capability to induce electric field from time-varying magnetic field. Wireless power transfer for medical implants and magnetic neural stimulation utilizes the induced electric field in the implanted coil and tissue to cause energy transfer and neural activity, respectively. They both work on Faraday‘s principle of induction, which states that a time-varying magnetic field can induce electric field $\vec{E}$ in a conductive medium. Based on electromagnetic theory, the magnetic field density $\vec{B}$ can be written in terms of the magnetic vector potential $\vec{A}$ as Equation 1.1 and 1.2

$$\vec{\nabla}\times\vec{E} = -\frac{\partial\vec{B}}{\partial t} = -\frac{\vec{\nabla}\times\vec{A}}{\partial t} \tag{1.1}$$

$$\vec{E}(r,t) = -\frac{\partial\vec{A}(r,t)}{\partial t} - \vec{\nabla}V(r,t) \tag{1.2}$$

where $\vec{\nabla}V(r,t)$ is the electric field contribution by the surface charge.

A popular technique for wireless power transfer, particularly in biomedical implants, is inductive coupling, which was used to power an artificial heart in 1961 [3, 4]. Since then it has been commonly used in implantable devices [3, 4, 12–19]. For short range wireless power transfer systems, power transfer efficiency, voltage gain, and data bandwidth are the key performance parameters that need to be optimized to design an efficient system [5, 6]. These parameters are strong functions of the quality factor (Q) of the magnetic coils and the coupling between the external and implant coils [5]. Traditionally, a two-coil based inductive link is used for wireless power/data transfer systems. However, due to the moderate Q-factor of the coils and low coupling between the coils, these inductive coupled power/data transfer systems have limited power transfer efficiency ($< 30\%$) and limited data bandwidth ($< 10\%$ of carrier frequency) [17, 18, 25]. Moreover, to design a reliable and efficient telemetry system, additional design goals need to be included. Performance variation during the operation of the device is one of the main challenges for a two-coil based system. An implanted coil may undergo relative motion with respect to the external coil during the operation of the device [24] and cause variation in mutual coupling between the coils. Based on the operation mode of the implanted device, the effective load resistance varies and causes changes in the Q-factor of the load coil [25]. Thus, all the typical two-coil based wireless power transfer (WPT) systems suffer from unstable link performance due to variation caused by the change in operating distance, coil misalignment, device operation mode, and change in driver resistance. Moreover, current implanted coils are designed with metallic wire (gold) and are difficult to deform during implantation [24-25]. Therefore, to ensure reliable operation of the telemetry system, the implant coil should be flexible and conformal. In situations requiring relatively large power transfer, such as those encountered in high data rate neurostimulators with high electrode counts, induced Specific Absorption Rates (SARs) or radiated fields need to be considered among the design parameters and minimized.

In this work, we proposed a multi-coil based wireless telemetry system to improve the wireless power transfer efficiency between external and implant electronics, which is the key focus of Chapter 2. We published this work in IEEE Transaction of Biomedical Circuits and System, vol. 7, Feb. 2013 [6]. A novel multi-coil technique (using more than two coils) for wireless power and data transfer was considered, which overcame the moderate Q-factor limitation for the two-coil WPT system. The proposed multi-coil system was formulated using both network theory and a two-port model. Using three or four coils for the wireless link allows for the source and load resistances to be decoupled from the Q-factor of the coils, resulting in a higher Q-factor and a corresponding improved power transfer efficiency (PTE). The proposed multi-coil telemetry system includes a novel three-coil topology for improving the efficiency and data bandwidth of currently implanted systems compared to [5]. Moreover, in this work, the multi-coil WPT system is extensively studied for use in data communication. It is also commonly believed that high Q-factor external and implant coils reduce the frequency bandwidth of the inductive link [5]. It is shown here that due to the strong coupling between the driver and the transmitter coil (and/or between the receiver and the load coil), the multi-coil system achieves higher tunable frequency bandwidth as compared to its same-sized two-coil equivalent. Because of the wider range of reflected impedance in the multi-coil system case, it is easier to tune the output power to the load and achieve the maximum power transfer condition for a given source voltage than in a configuration with two coils. Chapter 2 includes the experimental results showing a three-coil system achieving twice the efficiency and a higher gain-bandwidth product compared to its two-coil counterpart. In addition, a figure of merit for telemetry systems was defined to quantify the overall telemetry system performance. We also discuss the selection of operating frequency in Appendix A. Appendix B discusses the impact of component (e.g., resonating capacitor) tolerance on the multi-coil WPT system performance and compares with the two-coil WPT system.

The proposed multi-coil WPT system is beneficial due to the multiple control parameters, which includes the coupling between individual coils and their inductances. Current work extensively demonstrates the use of a multi-coil approach to reduce the absorbed electromagnetic energy in tissue and achieve high tolerance wireless power transfer systems. Chapter 3 discusses the need for high tolerance WPT systems for implants for which implanted coils can undergo relative motion during device operation. This causes variation in the magnetic coupling observed while in a stationary position. Therefore, to ensure stable power transfer efficiency and frequency bandwidth, a multi-coil based WPT system was utilized to achieve high tolerance for system power transfer efficiency and data bandwidth. It was demonstrated that for the coupling variation, a multi-coil WPT system can reduce variation by half in power transfer efficiency (PTE) and by one third in frequency bandwidth compared to a two-coil WPT system with the same dimensions and operating conditions. Moreover, the multi-coil WPT system shows lower variation in PTE with the variation of driver (source) and load (implant) impedance. The work is published in part in IEEE Antenna and Wireless Propagation Letters, Vol. 11, 2012 [31], and IEEE ICWITS Conference, Nov, 2012, Hawaii, USA [32].

Chapter 4 focuses on the lowering specific absorption rate (SAR), which is a measure of absorbed electromagnetic energy in the tissue. Due to the close proximity of the implant coil(s) with the tissue ($\sim$ 1 mm) and high current ($\sim$ 100-300 mA) in the magnetic coil(s), a significant induced electric field can be generated for the operating frequency (1-20 MHz). Therefore, a multi-coil based WPT technique was proposed to selectively control the currents in the external and implant coils to reduce the Specific Absorption Rate. A three-coil WPT system that can achieve 26% reduction in peak 1-gram SAR and 15% reduction in peak 10-gram SAR, as compared to a two-coil WPT system with the same dimensions, was implemented and used to demonstrate the effectiveness of the proposed approach. The multi-coil system achieves the same voltage gain and bandwidth as the two-coil design equivalent with 46% improvement in the power transfer efficiency (PTE). The work was accepted for publication in IET Healthcare Technology Letters [33].

Even though inductive coupling based WPT systems are nonradiating systems, the external and the implant coils can cause sufficient radiated electric field to exceed the federal standards for communication. Thus, a multi-coil based wireless power transfer (WPT) technique was developed as discussed in Chapter 5, to selectively control the currents in the external and implant coils to reduce radiated electric field. A four-coil WPT system that can achieve more than 37% reduction in radiated electric field as compared to a two-coil WPT system with the same dimensions and design constraints was implemented and used to demonstrate the effectiveness of the proposed approach. We have submitted this work to IET Electronics Letters [35].

Chapter 6 describes the realization of a soft, flexible coil fabricated by means of a liquid metal alloy encased in a biocompatible elastomeric substrate for operation in a telemetry system, primarily for application to biomedical implantable devices. Fluidic conductors are, in fact, well suited for applications that require significant flexibility as well as conformable and stretchable devices, such as implantable coils for wireless telemetry. Therefore, the goal of the present work is to demonstrate that, despite the lower conductivity of liquid metal alloys such as EGaIn compared to materials such as copper or gold, it is still possible to realize an efficient biomedical telemetry system employing liquid metal coils on the implant side. A wireless telemetry system for an artificial retina to restore partial vision to the blind is used as a testbed for the proposed liquid metal coils. Simulated and measured results show that power transfer efficiencies of 43% and 21% are obtained at operating distances between coils of 5 mm and 12 mm, respectively. Further, liquid metal-based coil retains more than 72% of its performance (voltage gain, frequency bandwidth, and power transfer efficiency) when physically deformed over a curved surface such as the surface of the human eye. This study demonstrates that liquid metal-based coils for biomedical implant provide an alternative to stiff and uncomfortable traditional coils used in biomedical implants. The work is published in IEEE Sensors Journal, vol.14, April 2014 [30].

Magnetic stimulation, on the other hand, is a relatively new technique. The first demonstration of transcranial magnetic stimulation was conducted in 1984 by Barker et al. [1]. As compared to other noninvasive techniques, such as Electroconvulsive Therapy (ECT), magnetic stimulation is a painless method for stimulation of central and peripheral nervous systems [26]. Due to its noninvasive nature, magnetic stimulation has been used in a variety of clinical applications, which include brain mapping, treatment of mood disorders, treatment of epilepsy, and treatment of chronic pain. Deep penetration of magnetic field generally requires high current. Therefore, current applications are limited to transcranial magnetic stimulation, requiring a magnetic coil with a diameter of about 8 cm [8]. Since 1994, there have been several attempts to miniaturize the magnetic stimulator [9-11]. Studies on coil design have reported improvement in the localization and efficiency when using the magnetic stimulation [27-28]. The effectiveness of a magnetic stimulator primarily depends on the design of the magnetic coil. Therefore, the key focus of our work was to design an efficient magnetic coil. For the current-carrying air-core coil, spatial and temporal variation of the vector potential (and therefore induced electric field) can be calculated by integrating the effect of individual current segments $\vec{dl}$ at location r_0 (Equation 1.3).

$$\vec{A}(r,t) = \frac{\mu_0 I(t)}{4\pi} \int \frac{\vec{dl}}{\mid \vec{r} - \vec{r_0} \mid} \tag{1.3}$$

where μ_0 is the permeability of free space, $I(t)$ is the time-dependent current, $\vec{dl}$ is a vector oriented according to the direction of each current element, and $\mid \vec{r} - \vec{r_0} \mid$ is the distance from each point ($\vec{r}$) to the current element ($\vec{r_0}$). The tissue heterogeneity affects the surface charge distribution.

Neural stimulation using an external stimulator (electrical or magnetic) requires electric field (applied or induced) at the stimulation site. To simulate the nerve response due to an applied electric field, a passive cable model of nerve is commonly used. Neuronal structures are modeled in the form of transmission line and the membrane response can be computed by solving the equations describing the transmembrane potential of the cable in the presence of induced electric fields [11]. For infinitely long nerve fibers, the stimulation equation is,

$$-\lambda_m^2 \frac{\partial E_r(r,t)}{\partial r} = -\lambda_m^2 \frac{\partial^2 V_m(r,t)}{\partial r^2} + \tau_m \frac{\partial V_m(r,t)}{\partial t} + V_m(r,t) \tag{1.4}$$

where the length and time constants of the neural membrane (λ_m and τ_m, respectively) are defined as

$$\lambda_m = \sqrt{\frac{r_m}{r_i}}, \tau_m = c_m r_m \tag{1.5}$$

V_m is the transmembrane voltage, defined as the voltage difference between the intracellular and extracellular fluid ($V_m = V_{intracellular} - V_{extracellular}$), r_m is membrane resistance times unit length ($k\Omega$ axon length), r_i is intracellular resistance ($\Omega.cm^{-1}$) and c_m is membrane capacitance per unit length ($F.cm^{-1}$). The " activating function " $\lambda_m^2 \frac{\partial E_r(r,t)}{\partial x}$ is the gradient of the applied electric field in the direction of nerve ($\vec{r}$), which is useful for determining the initial change in V_m. We developed a low-resistance magnetic stimulator based on a pulse discharge circuit to induce high electric field at the nerve site. For an accurate prediction of magnetic coils' electric properties (inductance and resistance) and their generated induced field, we developed an analytical formulation and finite-difference models of the different magnetic coils.

Equation 1.4 shows that the efficacy of the magnetic stimulation of central or peripheral nervous systems depends on the spatial and temporal distribution of the induced electric field generated by the magnetic coil. Therefore, field estimation is a key step in designing and optimizing an efficient small magnetic coil. Magnetic materials serve an important role in the design of small dimension (diameter 4-12 mm) magnetic coils. Thus, to design an optimal implantable magnetic stimulator, material properties, such as the nonlinearity in the core's permeability, need to be incorporated. Chapter 7 presents a generalized finite-difference (FD) field solver for the solenoid coils with nonlinear magnetic core. To study the temporal distribution of the induced electric field, a pulse discharge circuit was simulated in the time domain for the implemented nonlinear magnetic coil (inductor). Five coils were fabricated with different dimensions and stimulated with the magnetic stimulation circuit. Induced electric field was measured and compared with the simulation result. Results show that the presented algorithm and numerical model can accurately predict the key performance parameters of the designed magnetic coils with less than 10% error between simulation and experiment. The work was submitted to IET Healthcare Technology Letters [34]. We also studied the different core structures (e.g., toroid, E-shape, U-shape). Appendix C discuss the experimental analysis of the effect of core shape on the induced electric field.

Due to the fast saturation of the magnetic core, air-core based magnetic coils are a commonly used topology for magnetic neural stimulation. As compared to magnetic-core-based coils, which are prone to saturation, air-core-based coils provide constant inductance over time. In Chapter 8, design and optimization for a solenoid coil is presented. Some of these coils (solenoid and figure-8) are used for the ex-vivo magnetic stimulation of frogs' sciatic nerve. It is demonstrated that solenoid coils with outer diameter as small as 23.5 mm can elicit muscle activity for a threshold charging voltage of $\sim$ 115 V in a charging capacitor of 2.2 mF [39]. A detailed analysis of the individual experiment is presented to establish the understanding of magnetic stimulation.

Generation of action potentials depends on the spatial and temporal distribution of the induced electric field. To establish the threshold value for stimulation, an animal model is required. However, to reduce the number of experiments for coil miniaturization, an accurate nerve model needs to be developed. Therefore, in Chapter 9, we propose a computational model of frog‘s sciatic nerve using the impedance method [29]. The effect of supporting media and location of stimulation is discussed for the ex-vivo experiment [38]. Using a numerical model, it was shown that the axon density and location of the myelination and node of Ranvier play an important role in the distribution of induced electric field and resultant membrane current. To simulate the transmembrane current due to cm-sized magnetic coils, a multi-resolution impedance method was developed and the effect of axon distribution inside the nerve was studied. It was shown that due to the axon distribution, proximal axons with $\sim 20 \mu m$ separation can differ more than 8% in induced electric field [37].

To design the magnetic neural stimulator for mammals (human, cat), we study the heterogeneous animal model. As discussed in Chapter 10, we developed a numerical model of a multifascicular sciatic nerve to study the effect of tissue heterogeneity on the induced electric field. Using a multi-resolution electric field solver, we can resolve feature sizes as small as $1 \mu m$, allowing inclusion of the nerve membrane and the myelination layer. Preliminary results indicate that fascicle distribution and axons' proximity to each other significantly affect the magnitude and distribution of the induced electric field as compared to traditional homogeneous tissue models for field simulation. We submitted this study in IEEE conference on Medicine and Biology (EMBC), August, 2014 [36].

The efficacy of magnetic stimulation of the central or peripheral nervous system depends on the spatial and temporal distribution of the induced electric field generated by the magnetic coil. Therefore, accurate estimation of the induced electric field is crucial to the design and optimization of magnetic coils, particularly as the coil dimensions are reduced.

1.3 Significance of Work

Biomedical implants are popular in health and medical applications due to their ability to locally stimulate internal tissues and/or monitor and communicate the internal vital signs to the outer world. Implanted sensors, drug delivery devices, neural stimulation devices, and endoscopes are some of the devices currently in use for medical applications. Some implants use (rechargeable) batteries; however, wireless power transfer schemes are often used in implantable devices to avoid transcutaneous wiring and the need to recharge or replace device batteries. Work focused on improving the power transfer efficiency and supported data rate is found in literature [6, 16]. However, current designs do not mitigate the effect of coil misalignments, and can generate significant electromagnetic energy. Thus, using our proposed telemetry system, which can achieve a high tolerance with magnetic coupling variation, low electromagnetic energy, and a flexible implant, a reliable and safe wireless power and data system can be achieved for biomedical implants. Due to its generalized design approach, our proposed multi-coil technique is easily adaptable to other practical applications that include wireless power transfer to electric cars and consumer electronics (e.g., television, mobile phone).

Most current neural stimulation requires direct contact of electrodes with the stimulated tissue. In electrical stimulation, a biphasic pulse of electric charges is transferred to the surrounding tissue to generate neural activity. Despite the tremendous success of electrical stimulation, accurate charge balance during a biphasic pulse and tissue encapsulation over electrodes can limit the longevity of the stimulating electrode. The contactless feature of magnetic stimulation seems to make it an ideal choice for long term applications. Current magnetic stimulator requires 10^9 higher energy than the equivalent electrical stimulator. Therefore, our proposed research investigates the theoretical and practical aspects of magnetic coils and stimulation mechanisms to design a miniaturized and energy efficient magnetic stimulator. With the successful design of an optimum magnetic stimulator, a tissue-independent neurostimulator can be implemented that can surpass the current limitations of electrical electrodes.

1.4 References

[1] AT Barker, R. Jalinous, and IL Freeston, "Noninvasive magnetic stimulation of human motor cortex," The Lancet, vol. 325, no. 8437, pp. 1106-1107, 1985.

[2] Sijbers J et al., "Quantification and improvement of the signal-to-noise ratio in a magnetic resonance image acquisition procedure," Magnetic Resonance Imaging, vol. 14, no. 10, pp. 1157-1163, 1996.

[3] J. C. Schuder, H. E. J. Stephenson, and J. F. Townsend, "Energy transfer into a closed chest by means of stationary coupling coils and a portable high-power oscillator," ASAIO J., vol. 7, pp. 327-331, Apr. 1961.

[4] J. C. Schuder, "Powering an artificial heart: Birth of the inductively coupled-radio frequency system in 1960," in Proc. Int. Center Artificial Organs, vol. 26, pp. 909-915, Nov. 2002.

[5] A. K. RamRakhyani, S. Mirabbasi, and M. Chiao, "Design and optimization of resonance-based efficient wireless power delivery systems for biomedical implants," IEEE Trans. Biomed. Circuits Syst., vol. 5, no. 1, pp. 48-63, Feb. 2011.

[6] A. K. RamRakhyani and G. Lazzi, "On the design of efficient multicoil telemetry system for biomedical implants," IEEE Trans. Biomed. Circuits Syst., vol. 7, no. 1, pp. 11-23, Feb. 2013.

[7] M. Yamaguchi, S. Yamada, N. Daimon, I. Yamamoto, T. Kawakami, and T. Takenaka, "Electromagnetic mechanism of magnetic nerve stimulation," Journal of Applied Physics, vol. 66, no. 3, pp. 1459-1465, Aug. 1989.

[8] H. M. Roth Y, Zangen A, "A coil design for transcranial magnetic stimulation of deep brain regions," J Clin Neurophysiol., vol. 19, pp. 36170, Aug. 2002.

[9] K. Davey, L. Luo, and D. Ross, "Toward functional magnetic stimulation (fms) theory and experiment," IEEE Transactions on Biomedical Engineering, vol. 41, no. 11, pp. 1024 1030, Nov. 1994.

[10] D. Cai, Y. Fang, X. Cao, X. Zhang, and J. Tang, "Transcranial magnetic stimulation: modeling, calculating and system design," in Proc. of 2nd International Conference on Biomedical Engineering and Informatics, 2009, pp. 1-5, 17-19 Oct. 2009.

[11] E. Basham, Zhi Yang, Wentai Liu, "Circuit and coil design for in-vitro magnetic neural stimulation systems," IEEE Transactions on Biomedical Circuits and Systems, vol. 3, no. 5, pp. 321-331, Oct. 2009.

[12] M. W. Baker and R. Sarpeshkar, "Feedback analysis and design of RF power links for low-power bionic systems," IEEE Trans. Biomed. Circuits Syst., vol. 1, no. 1, pp. 28-38, Mar. 2007.

[13] N. Neihart and R. Harrison, "Micropower circuits for bidirectional wireless telemetry in neural recording applications," IEEE Trans. Biomed. Eng., vol. 52, no. 11, pp. 1950-1959, Nov. 2005.

[14] H. Chen, M. Liu, C. Jia, C. Zhang, and Z.Wang, "Low power IC design of the wireless monitoring system of the orthopedic implants," in Proc. IEEE EMBS Conf., pp. 5766-5769, Aug. 2226, 2007.

[15] S. Smith, T. Tang, and J. Terry, "Development of a miniaturised drug delivery system with wireless power transfer and communication," Inst. Eng. Technol. Nanobiotechnol., vol. 1, pp. 80-86, Oct. 2007.

[16] G.Wang, W. Liu, M. Sivaprakasam, M. Zhou, J. D.Weiland, and M. S. Humayun, "A dual band wireless power and data telemetry for retinal prosthesi," in Proc. IEEE EMBS Conf., pp. 28-38, Aug. 30-Sep. 3, 2006.

[17] M. Catrysse, B. Hermans, and R. Puers, "An inductive power system with integrated bidirectional data transmission," in Proc. XVII Eurosensors, pp. 843-846, Sep. 21-24, 2003.

[18] M. Ghovanloo and K. Najafi, "A wireless implantable multichannel microstimulating system-on-a-chip with modular architecture," IEEE Trans. Neural Syst. Rehab. Eng., vol. 15, no. 3, pp. 449-457, Sep. 2007.

[19] L. Wu, Z. Yang, E. Basham, and W. Liu, "An efficient wireless power link for high voltage retinal implant," in Proc. BioCAS, pp. 101-104, 2008.

[20] G. Simard, M. Sawan, and D. Massicotte, "High-speed oqpsk and efficient power transfer through inductive link for biomedical implants," IEEE Trans. Biomed. Circuits Syst., vol. 4, no. 3, pp. 192-200, 2010.

[21] M. Haider, S. Islam, S. Mostafa, M. Zhang, and T. Oh, "Low-power low-voltage current readout circuit for inductively powered implant system," IEEE Trans. Biomed. Circuits Syst., vol. 4, no. 4, pp. 205-213, 2010.

[22] A. Bonfanti, M. Ceravolo, G. Zambra, R. Gusmeroli, A. Spinelli, A. Lacaita, G. Angotzi, G. Baranauskas, and L. Fadiga, "A multi-channel low-power system-on-chip for single-unit recording and narrowband wireless transmission of neural signal," in Proc. IEEE Annu. Int. Conf. Engineering in Medicine and Biology Society, Aug. 31-Sep. 4, 2010.

[23] G. B. Hmida, H. Ghariani, and M. Samet, "Design of wireless powerand data transmission circuits for implantable biomicrosystem," Biotechnol., vol. 6, no. 2, pp. 153-164, 2007.

[24] D. Yanai, J. D. Weiland, M. Mahadevappa, R. J. Greenberg, I. Fine, and M. S. Humayun, "Visual performance using a retinal prosthesis in three subjects with retinitis pigmentosa," Amer. J. Ophthalmol., vol. 143, no. 5, pp. 820-827, 2007.

[25] G.Wang, W. Liu, M. Sivaprakasam,M. Zhou, J. D.Weiland, and M. S. Humayun, "A dual band wireless power and data telemetry for retinal prosthesis," in Proc. IEEE EMBS, pp. 28-38, Aug. 30-Sep. 3 2006.

[26] M. Sekino and S. Ueno, "Comparison of current distributions in electroconvulsive therapy and transcranial magnetic stimulation," Journal of Applied Physics, vol. 91, no. 10, pp. 8730-8732, May 2002.

[27] C. Ren, P. Tarjan, and D. Popovic, "A novel electric design for electromagnetic stimulation-the slinky coil," IEEE Transactions on Biomedical Engineering, vol. 42, no. 9, pp. 918-925, 1995.

[28] J. Ruohonen and R. Ilmoniemi, "Focusing and targeting of magnetic brain stimulation using multiple coils," Medical and Biological Engineering and Computing, vol. 36, pp. 297-301, 1998.

[29] N. Orcutt and O. P. Gandhi, "A 3-D impedance method to calculate power deposition in biological bodies subjected to time varying magnetic fields," IEEE Transactions on Biomedical Engineering, vol. 35, no. 8, pp. 577-583, Aug. 1988.

[30] A. Qusba, A. K. RamRakhyani, J.-H. So, G.J. Hayes, M. D. Dickey, G. Lazzi, "On the design of microfluidic implant coil for flexible telemetry system," IEEE Sensors Journal, vol. 14, no. 4, pp.1074-1080, April 2014.

[31] A. K. RamRakhyani and Gianluca Lazzi, "Multi-coil telemetry system for compensation of coil misalignment effects in implantable systems," IEEE Antenna and Wireless Propagation Letters, vol. 11, no. 1, pp. 1675 - 1678, 2012.

[32] A. K. RamRakhyani, Gianluca Lazzi, "Use of multi-coil telemetry system for high tolerance efficient wireless power system," IEEE International Conference on Wireless Information Technology and Systems, 11-16 Nov, 2012, Hawaii, USA.

[33] Anil Kumar RamRakhyani and Gianluca Lazzi, "Multi-coil approach to reduce electromagnetic energy absorption for wireless powered implants," IET Healthcare Technology Letters, vol. 1, no. 1, pp. 21-25, March 2014.

[34] Anil Kumar RamRakhyani, Gianluca Lazzi, "Numerical modeling of cores nonlinearity for magnetic neural stimulation," submitted in IET Healthcare Technology Letters.

[35] Anil Kumar RamRakhyani, Gianluca Lazzi, "Interference free wireless power transfer system for biomedical implants using multi-coil approach," IET Electronics Letters, vol. 50, no. 12, pp. 853-855, June 2014.

[36] Anil Kumar RamRakhyani, Zack Kagan, Faisal Khan, David J. Warren, Richard Normann, and Gianluca Lazzi, "Numerical modeling of tissue heterogeneity for the magnetic stimulation of felines sciatic nerve," accepted for publication in IEEE EMBC Conf. 2014, Chicago, USA.

[37] Anil Kumar RamRakhyani, Faisal Khan, David J. Warren, Zack Kagan, Richard Normann, and Gianluca Lazzi, "Multi-resolution network modeling of inhomogeneous nerve bundle for magnetic stimulation," in BMES Conf. 2013, Seattle, USA.

[38] Anil Kumar RamRakhyani, Zack Kagan, Faisal Khan, David J. Warren, Richard Normann, and Gianluca Lazzi, "Effect of surrounding conditions on in-vitro magnetic neural stimulation," in IEEE EMBS NER Conf. 2013, San Diego, USA.

[39] Anil Kumar RamRakhyani, Faisal Khan, David J. Warren, Richard Normann, and Gianluca Lazzi, "On the design of efficient magnetic coil for the stimulation of peripheral nerve," in IEEE AP-S/URSI conf. 2013, Orlando, USA.

CHAPTER 2

EFFICIENT MULTI-COIL TELEMETRY SYSTEM FOR BIOMEDICAL IMPLANTS

© 2014 IEEE. Reprinted, with permission, from: A. K. RamRakhyani, Gianluca Lazzi, "On the Design of Efficient Multi-coil Telemetry System for Biomedical Implants", IEEE Transactions on Biomedical Circuits and Systems, vol. 7, no. 1, pp. 11-23, 2013.

2.1 Abstract

Two-coil based inductive coupling is a commonly used technique for wireless power and data transfer for biomedical implants. Because the source and load resistances are finite, two-coil systems generally achieve a relatively low power transfer efficiency. A novel multi-coil technique (using more than two coils) for wireless power and data transfer is considered to help overcome this limitation. The proposed multi-coil system is formulated using both network theory and a two-port model. Using three or four coils for the wireless link allows for the source and load resistances to be decoupled from the Q-factor of the coils, resulting in a higher Q-factor and a corresponding improved power transfer efficiency (PTE). Moreover, due to the strong coupling between the driver and the transmitter coil (and/or between the receiver and the load coil), the multi-coil system achieves higher tunable frequency bandwidth as compared to its same sized two-coil equivalent. Because of the wider range of reflected impedance in the multi-coil system case, it is easier to tune the output power to the load and achieve the maximum power transfer condition for given source voltage than in a configuration with two coils. Experimental results showing a three-coil system achieving twice the efficiency and higher gain-bandwidth product compared to its two-coil counterpart are presented. In addition, a figure of merit for telemetry systems is defined to quantify the overall telemetry system performance.

2.2 Introduction

The use of biomedical implants for stimulation and monitoring of internal vital signs has grown dramatically over the last decade. Implanted sensors, drug delivery devices [1], neural stimulation devices [2], and endoscopes [3] are just some of the devices currently in use for medical applications. For telemetry applications, performance is usually assessed in terms of power transfer efficiency (PTE) and frequency bandwidth over the wireless link [4–9]. Using inductive coupling between the external power source and the implanted device is a sensible choice when considering wireless power and data transfer [1, 10, 11]. Due to limited frequency bandwidth over the inductive link, some telemetry systems use separate transmitters (and receivers) for data and power transfer [4, 7], which increases the complexity of the design. Traditional inductive coupled power/data transfer systems use two paired coils and achieve a PTE upto 40% and a frequency bandwidth of about 10% of the carrier frequency [5].

Recently, a multi-coil based power transfer system using four resonating coils was proposed, and a high PTE of 82 % was achieved [12]. In comparison to two-coil based systems, four-coil systems consist of a driver coil (connected to the power source), a high Q-factor transmitter coil (in close proximity to the driver coil), a load coil (connected to the implant electronics) and a high Q-factor receiver coil (in close proximity to the load coil). A three-coil system to achieve high power delivered to the load [13] employing only a driver, a receiver and a load coil has also been proposed. In both configurations [12, 13], the implant coil must be modified, which is not feasible for powering implanted devices that are in clinical use [14]. Moreover, the multi-coil approach has been used for wireless power transfer only. To the best of the authors' knowledge, the multi-coil approach has never been used before to improve the frequency bandwidth of the inductive link.

In this work, a multi-coil system (which we define as a system with more than two coils) for power and data transfer using an inductive link is proposed for telemetry applications. Power and data transfer models for a multi-coil system with three coils (for systems that cannot accommodate more than a single implanted coil for compatibility with previously developed electronics) and four coils are formulated. A new three-coil configuration to improve the PTE of existing implants and improve the frequency bandwidth of the inductive link are the main contributions of this work. Moreover, a detail analysis of the proposed multi-coil system highlights a distinct trade-off between PTE, voltage gain and bandwidth, thus providing design guidelines for the new power transfer system. The use of a multi-coil system is proposed to achieve higher PTE, tunable voltage gain, higher bandwidth and maximum power transfer condition than a similarly sized two-coil system. The design focuses on the PTE and frequency bandwidth of the inductive link; thus, the design of input power source (power amplifier) and the data modulator/demodulator is not considered in the present work. However, the effect of the power amplifier impedance on the link efficiency is emulated and downlink Frequency-Shift Keying (FSK) data transmission is simulated to demonstrate the increase in the inductive link frequency bandwidth.

For biomedical applications, wireless telemetry system must generally be compact in size. The two-coil and multi-coil systems are considered equivalent if they share the same physical dimensions. For example, the sum of turns of the driver and transmitter in the three-coil system is the same as the number of turns of the driver in the two-coil system. This results in the same physical dimension of the system (Figure 2.1) and provides a fair comparison between two-coil and multi-coil system. Two experiments are conducted to compare a three-coil and its two-coil equivalent design. In all experiments and simulations, both the multi-coil and the two-coil system share the same physical dimensions. Section 2.3 presents two different methods to model the multi-coil based system. Section 2.4 presents the PTE analysis for both the two-coil and the multi-coil case. The voltage gain for power links is calculated in Section 2.5. Section 2.6 studies the improvement in frequency bandwidth achieved by using a multi-coil system. Section 2.7 formulates the conditions for maximum power transfer to the load. Experimental results are shown in Section 2.8. Finally, Section 2.9 discusses the experimental results and proposes a figure of merit for comparing different designs.

2.3 Multi-coil Model: Theory

The multi-coil structure for wireless power transfer consists of three (or four) coils. Figure 2.1 shows the block diagram of the two-coil and the multi-coil systems. A three-coil based system is considered to upgrade the currently used two-coil system by modifying only the external coil and its components. The coils connected to the power source and implant circuit are named driver coil and load coil, respectively. For the two-coil system, coupling between the driver and the load coil is defined as k. In the three-coil system, the driver and transmitter coils are coupled with coupling k_1, while the transmitter coil is coupled with the load coil with coupling k_2. In the case of a four-coil system, coupling coefficients k_1, k_2 and k_3 are used to define the coupling between driver and transmitter, between transmitter and receiver, and between receiver and load coils respectively. In a multi-coil system, k_4, k_5, and k_6 are the coupling between driver and load coil, driver and receiver coil, and transmitter and load coil, respectively. At resonant frequency f_{res}, the Q-factor of the coil ($Q = 2\pi f_{res} L/R$) is denoted using Q_d, Q_t, Q_r, and Q_l for driver, transmitter, receiver and load coils, respectively. In the rest of the paper, the above convention will be used.

The PTE of an inductive link strongly depends on the magnetic coupling between the coils and their electrical properties (e.g., inductance and resistance). In an inductive link, the power is dissipated in source and coil resistances. In a traditional two-coil inductive telemetry link, the maximum achievable coupling is limited by the size, geometrical structure, physical spacing, and relative location of both coils. The Q-factor can be increased using low-resistance Litz wires, thus

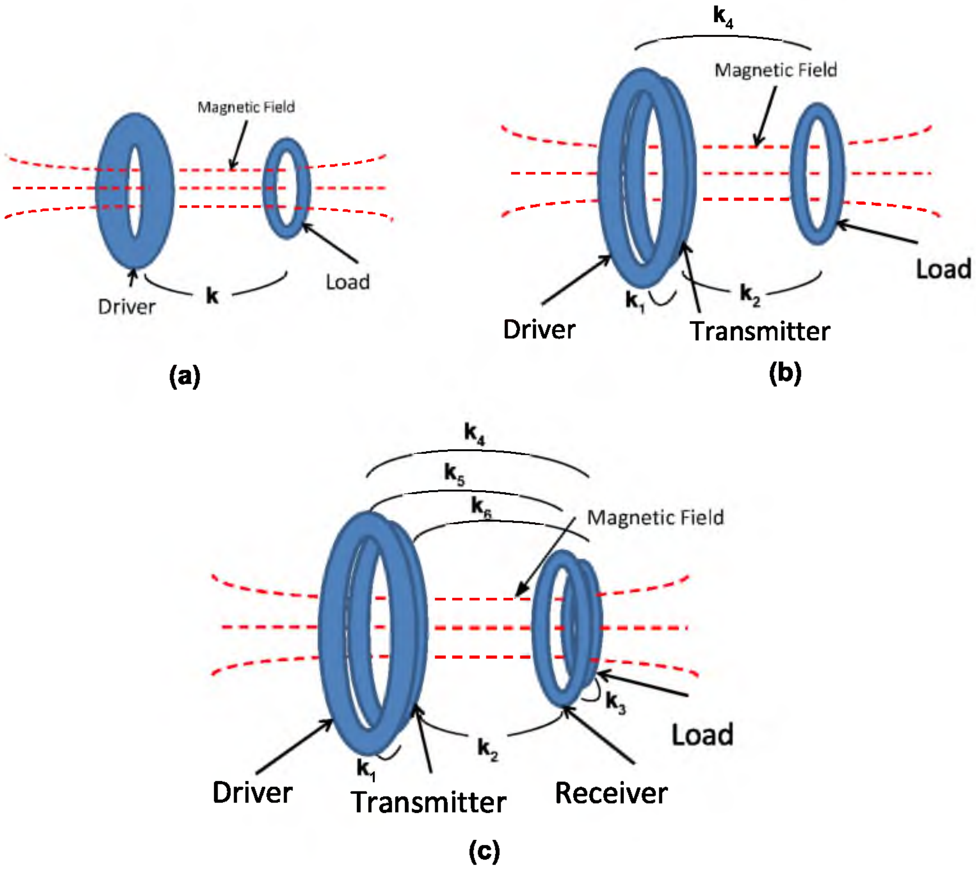

Figure 2.1. Block diagram for (a) two-coil, (b) three-coil, and (c) four-coil based telemetry system. Load and receiver coil (if present) are implanted. Driver and transmitter coil (if present) are part of the external device.

reducing the resistance of the coils; however, in the loaded condition, this increase is countered by the finite source resistance of the driver and high impedance of the load [15, 16], thus limiting the PTE. In a multi-coil system, thanks mainly to the strong coupling between driver and high-Q factor transmitter coils, less current needs to be fed from the driver to generate higher current in the transmitter coil. Thus, a multi-coil approach is characterized by low resistive losses in the driver. Similarly, resistive losses can be reduced in the implanted coil by using high Q-factor receiver coil and strongly coupled load coil.

To model the performance of the multi-coil system, two approaches are considered, based on network theory and circuit theory, respectively.

2.3.1 Network Model

The network model is formulated using Kirchoffs voltage law for each coil and using a voltage source V_1 as the forcing function. The current ($I_n, n \in \{1,2,3,4\}$) in each coil is calculated as a function of self ($Z_{mn}, m = n$) and mutual impedances ($Z_{mn}, m \neq n$). Based on the network model, Equations 2.1, 2.2, and 2.3 can be used to calculate the current flow in each coil for the two-coil, the three-coil, and the four-coil system, respectively.

2.3.1.1 Two-coil

$$\begin{bmatrix} I_1 \\ I_2 \end{bmatrix} = \begin{bmatrix} Z_{11} & Z_{12} \\ Z_{21} & Z_{22} \end{bmatrix}^{-1} \begin{bmatrix} V_1 \\ 0 \end{bmatrix} \tag{2.1}$$

2.3.1.2 Three-coil

$$\begin{bmatrix} I_1 \\ I_2 \\ I_3 \end{bmatrix} = \begin{bmatrix} Z_{11} & Z_{12} & Z_{13} \\ Z_{21} & Z_{22} & Z_{23} \\ Z_{31} & Z_{32} & Z_{33} \end{bmatrix}^{-1} \begin{bmatrix} V_1 \\ 0 \\ 0 \end{bmatrix} \tag{2.2}$$

2.3.1.3 Four-coil

$$\begin{bmatrix} I_1 \\ I_2 \\ I_3 \\ I_4 \end{bmatrix} = \begin{bmatrix} Z_{11} & Z_{12} & Z_{13} & Z_{14} \\ Z_{21} & Z_{22} & Z_{23} & Z_{24} \\ Z_{31} & Z_{32} & Z_{33} & Z_{34} \\ Z_{41} & Z_{42} & Z_{43} & Z_{44} \end{bmatrix}^{-1} \begin{bmatrix} V_1 \\ 0 \\ 0 \\ 0 \end{bmatrix} \tag{2.3}$$

For coil's inductance L_n, series resistance R_n and resonant capacitance C_n, the self-impedance $(Z_{mn}, m = n)$ and mutual-impedance $(Z_{mn}, m \neq n)$ of the coils are expressed by Equation 2.4:

$$\begin{aligned} Z_{mn} = Z_{nm} &= R_n + j\omega L_n + \frac{1}{j\omega C_n} \quad for \;\; m = n \\ &= j\omega M_{mn} = j\omega k_{mn}\sqrt{L_m L_n} \;\; for \;\; m \neq n \end{aligned} \tag{2.4}$$

where k_{mn} is the magnetic coupling between the coil 'm' and the coil 'n'.

After solving the network model for n-coil system (where n is 2, 3 or 4) using Equations 2.1, 2.2, and 2.3, the RMS (root mean square) input power P_{in}, the RMS output power $P_{out}|_n$ and the output voltage $V_{out}|_n$ can be calculated.

$$P_{in} = (1/2)|V_1||I_1| \tag{2.5}$$

$$P_{out}|_n = (1/2)|I_n|^2 R_n; \quad n \in \{2,3,4\} \tag{2.6}$$

$$V_{out}|_n = I_n R_n \tag{2.7}$$

PTE η and the voltage gain can be expressed as in Equation 2.8 and Equation 2.9, respectively.

$$\eta = P_{out}|_n / P_{in} \tag{2.8}$$

$$|Gain| = V_{out}|_n / |V_1| = (|I_n| R_n) / |V_1| \tag{2.9}$$

2.3.2 Two-port Model

To measure the system performance, the two-port equivalent model can be defined as in Figure 2.2(a). Using a two-port model, voltages at port 1 and 2 (V_1 and V_2) can be calculated from the port currents I_1 and I_2 and the two-port impedance matrix Z_{eff} (Equation 2.10).

$$\begin{aligned} V_1 &= Z_{11(eff)}I_1 + Z_{12(eff)}I_2 \\ V_2 &= Z_{21(eff)}I_1 + Z_{22(eff)}I_2 \end{aligned} \tag{2.10}$$

In Equation 2.10, $Z_{ij(eff)}$ is the entry of i^{th} row and j^{th} column of the two-port model of the system impedance matrix.

To simulate the transient response of the system, the internal components of the two-port model for the two-coil, the three-coil and the four-coil configurations can be represented as in Figure 2.2 (b), (c) and (d), respectively. In general, the driver coil has smaller inductance than the transmitter coil of the three-coil system, which causes smaller mutual inductance between driver and load coil as compared to mutual inductance between the transmitter and load coil. Thus the effect of coupling k_4 can be neglected during the representation of the lumped element equivalent in Figure 2.2 (c). Similarly, in the four-coil case, using small value of driver and load coils' inductance, the effect of k_4, k_5, and k_6 can be neglected.

For an n-coil system (where n is 2, 3 or 4), the output voltage V_2 is measured across the load resistance R_n and no current flows through the port 2 ($I_2 = 0$). For an applied input voltage V_1, Equation 2.10 can be simplified to calculate the input current I_1 and the output voltage V_2. The RMS input power P_{in} and the RMS output power $P_{out}|_n$ of the system can be expressed as a function of V_1 and Z_{eff} (Equations 2.12 and 2.13).

$$V_{out}|_n = V_2 = Z_{21(eff)}I_1 \tag{2.11}$$

$$P_{in} = (1/2)|V_1||I_1| = (1/2)V_1^2/|Z_{11(eff)}| \tag{2.12}$$

$$P_{out}|_n = \frac{|V_2|^2}{2R_n} = \frac{|Z_{21(eff)}|^2 V_1^2}{2R_n|Z_{11(eff)}|^2}; \quad n \in \{2,3,4\} \tag{2.13}$$

The PTE η and the voltage gain of the n-coil system are expressed as in Equations 2.14 and 2.15.

$$\eta = \frac{P_{out}|_n}{P_{in}} = \frac{|Z_{21(eff)}|^2}{R_n|(Z_{11(eff)}|} \tag{2.14}$$

$$|Gain| = \frac{|V_2|}{|V_1|} = \frac{|Z_{21(eff)}|}{|(Z_{11(eff)}|} \tag{2.15}$$

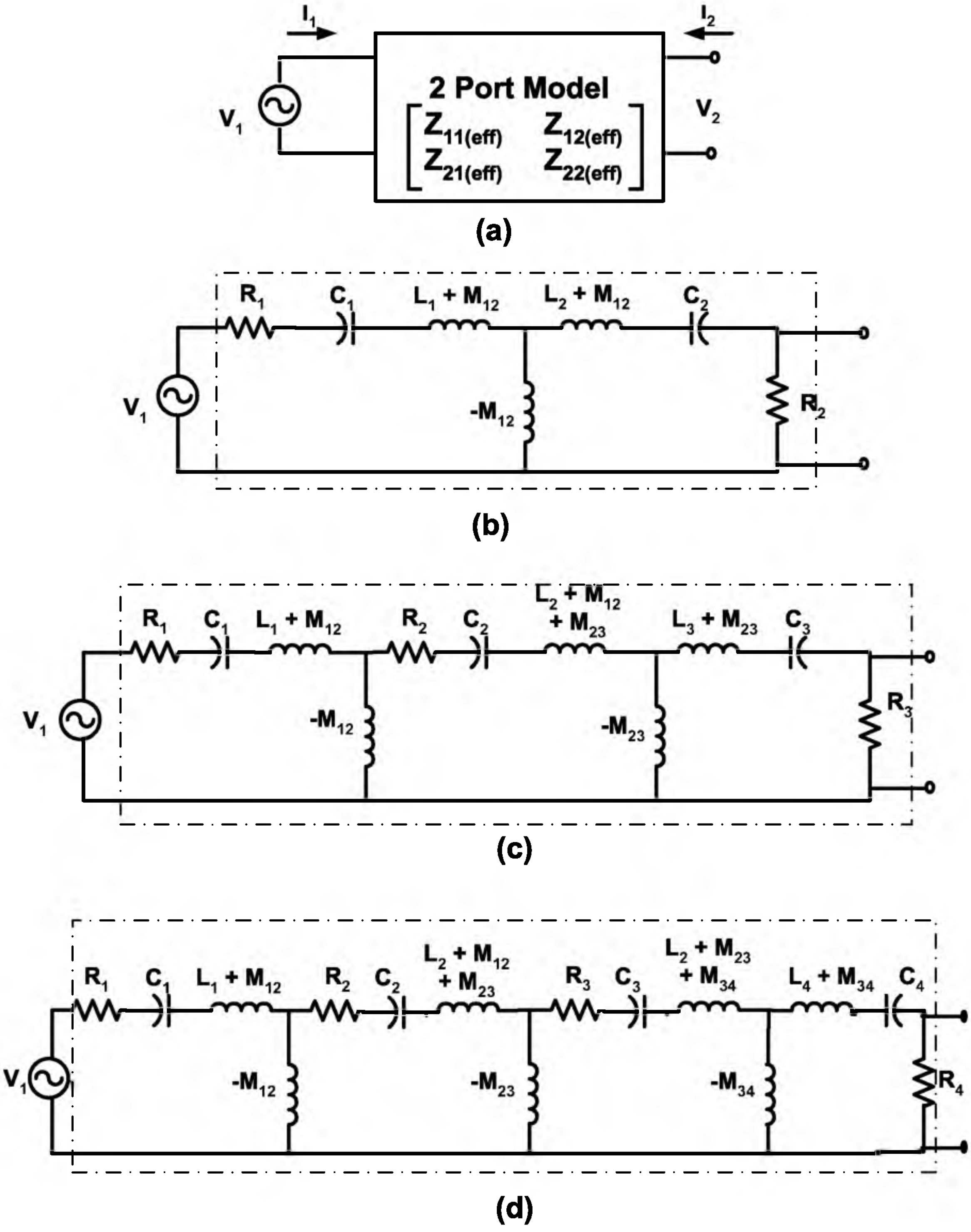

Figure 2.2. Lumped element model. (a) Two-port circuit model of a wireless power transfer system. Lumped circuit model of (b) two-coil, (c) three-coil, and (d) four-coil systems, based on self and mutual impedance of the coil and external components (Equation 2.4). For the n-coil system, the output voltage (V_2) is measured across the load resistance R_n.

While both the network model and the two-port model can be used to calculate the basic performance of the system (efficiency, voltage gain, and bandwidth), the network model makes it simpler to include the coupling effects between each of the coils and calculates the currents through them. Experimental measurements of the system are straightforward using the two-port model. Using a network analyzer, the S-parameters of the two-port equivalent model can be directly measured and later converted to the Z-parameters in order to calculate the system efficiency and gain.

Using T- or pi- matching networks at the source side of the two-coil system, a schematic equivalent to the multi-coil architecture can be obtained (Figures 2.2(c) and 2.2(d)). However, such matching network implementation requires an ideal inductor and capacitors to keep the resistive losses small in the matching network. Conversely, the multi-coil method creates a nonphysical mutual inductance due to the interaction of the resonating coils. Such mutual inductance does not have any resistive losses and is not constrained over the current carrying capability.

2.4 Power Transfer Efficiency

In our previous work [12, 17], a four-coil system was used for the purpose of wireless power transfer application only. Using a similar approach, at the resonant frequency the PTE is formulated for the three-coil system for the existing implanted system. In similar work [13], a three-coil based system, consisting of driver, receiver and load coil, and requiring a modification of the implant coil, was proposed.

In the following section, the PTE of a multi-coil system is formulated by solving the network model equations at the resonant frequency.

2.4.1 Two-coil System

In general, for two-coil systems with a given load condition and source resistance, the loaded Q-factors of the driver and the load coil are smaller than 30 and 10, respectively [4, 16]. For a nominal distance $k \sim 0.05$, this limits the PTE to values lower than 40%. Using Equations 2.1 and 2.8, at the resonant frequency, the PTE of a two-coil system is derived and expressed in Equation 2.16 [15].

$$\eta = \frac{k^2 Q_d Q_l}{1 + k^2 Q_d Q_l} = \eta_{dl} \tag{2.16}$$

2.4.2 Three-coil System

To build an equivalent three-coil system, the driver coil is divided in two coils, namely the driver coil and the transmitter coil. This effectively decouples the source resistance from the Q-factor of the transmitter coil. The transmitter coil has higher inductance than the driver coil, and at the resonant frequency, it can achieve a high Q-factor. The driver coil has a low Q-factor because of its low inductance and moderate source resistance ($\sim 5\Omega$). The driver and the transmitter coils are strongly coupled (k_1 ~0.5), and this increases the efficiency of the power transfer between them. Overall, for a given operating distance, the PTE between the transmitter coil and the load coil is improved because of the high Q-factor of the transmitter coil. By solving Equations 2.2 and 2.8 at the resonant frequency, the PTE of the three-coil system can be expressed as in Equation 2.17. In general, using a low-inductance driver coil, the effect of the mutual inductance between the driver and the load coil can be made much smaller than the mutual inductance between the transmitter and the load coil. Because of this, the effect of coupling k_4 is neglected in the derivation of Equation 2.17.

$$\eta = \frac{k_1^2 Q_d Q_t}{1 + k_1^2 Q_d Q_t + k_2^2 Q_t Q_l} \frac{k_2^2 Q_t Q_l}{1 + k_2^2 Q_t Q_l} \tag{2.17}$$

For high k_1 and Q_t, $(1 + k_1^2 Q_d Q_t) >> k_2^2 Q_t Q_l$, Equation 2.17 can be approximated as in Equation 2.18.

$$\begin{aligned} \eta &\simeq \frac{k_1^2 Q_d Q_t}{1 + k_1^2 Q_d Q_t} \frac{k_2^2 Q_t Q_l}{1 + k_2^2 Q_t Q_l} \\ &= \eta_{dt} \eta_{tl} \end{aligned} \tag{2.18}$$

Equation 2.18 shows a two-step power transfer from the driver coil to the transmitter coil and from the transmitter coil to the load coil with the PTE of η_{dt} and η_{tl}, respectively. Due to the high coupling k_1, η_{dt} can easily be made higher than 0.9, while η_{tl} is improved by 2 times or more compared to the two-coil PTE (η_{dl}, Equation 2.16) because of the high value of Q_t.

2.4.3 Four-coil System

The four-coil power transfer system is an extension of the three-coil system in which the load coil is split into two coils, namely the receiver coil and the load coil. This decouples the Q-factor of the receiver coil from the high load resistance. Due to the strong coupling k_3, energy can be efficiently transferred between the receiver and the load coil. A four-coil system can achieve higher PTE compared to its two-coil and three-coil equivalent due to high Q-factor of both the transmitter and the receiver coil. Due to the small size of the driver and the load coils, the mutual inductances between driver and load coils, between driver and receiver coils, and between transmitter and load coils, are small and can be neglected. Using a network model of the four-coil system (Equations 2.3 and 2.8), at the resonant frequency, PTE can be expressed as Equation 2.19 [12].

$$\eta = \frac{(k_1^2 Q_d Q_t)(k_3^2 Q_r Q_l)}{(1+k_1^2 Q_d Q_t)(1+k_3^2 Q_r Q_l)+k_2^2 Q_t Q_r} \frac{k_2^2 Q_t Q_r}{1+k_2^2 Q_t Q_r+k_3^2 Q_r Q_l} \tag{2.19}$$

With high coupling k_1 and k_3, and high Q-factor for transmitter and receiver coils, $(1+k_1^2 Q_d Q_t)(1+k_3^2 Q_r Q_l) \gg k_2^2 Q_t Q_r$ and $(1+k_2^2 Q_t Q_r) \gg k_3^2 Q_r Q_l$, Equation 2.19 can be approximated as Equation 2.20.

$$\begin{aligned} \eta &\simeq \frac{k_1^2 Q_d Q_t}{1+k_1^2 Q_d Q_t} \frac{k_2^2 Q_t Q_r}{1+k_2^2 Q_t Q_r} \frac{k_3^2 Q_r Q_l}{1+k_3^2 Q_r Q_l} \\ &= \eta_{dt} \eta_{tr} \eta_{rl} \end{aligned} \tag{2.20}$$

The approximated efficiency model of the four-coil system (Equation 2.18) shows a three-step power transfer from the driver coil to the transmitter coil, from the transmitter coil to the receiver coil, and from the receiver coil to the load coil with the PTE of η_{dt}, η_{tr} and η_{rl}, respectively. Using high Q_t and Q_r, η_{tr} can be 3 to 4 times higher than the two-coil PTE (η_{dl}, Equation 2.16).

The approximated power transfer equations (Equations 2.18 and 2.20) provide insight in the PTE improvement due to multi-coil system and are useful while defining the coil specifications under design constraints.

2.5 Voltage Gain

For the telemetry system, voltage gain is an important design parameter to consider when calculating the required voltage level for the operation of the implanted device. This section provides the voltage gain ($Gain = V_{out}/V_{in}$) of the two-coil and the multi-coil system at the resonant frequency.

2.5.1 Two-coil System

Using the network model of a two-coil system (Equations 2.1 and 2.9), the voltage gain can be formulated as shown in Equation 2.21.

$$Gain|_2 = -j\sqrt{\frac{R_2}{R_1}} \frac{k\sqrt{Q_d Q_l}}{1+k^2 Q_d Q_l} \tag{2.21}$$

For nominal coupling $k \sim 0.05$ for implanted devices and moderate Q-factor of driver and load coils [4, 5, 15, 16], $k^2 Q_d Q_l \ll 1$. Therefore the gain of a two-coil system can be approximated as Equation 2.22.

$$Gain|_2 \sim -j\sqrt{\frac{R_2}{R_1}} k\sqrt{Q_d Q_l} \tag{2.22}$$

2.5.2 Three-coil System

Similarly, voltage gain of a three-coil system is formulated in Equation 2.23 by solving Equation 2.2 and 2.9 at the resonant frequency (for a small inductance value driver coil).

$$Gain|_3 = -\sqrt{\frac{R_3}{R_1}}\frac{(k_1\sqrt{Q_dQ_t})(k_2\sqrt{Q_tQ_l})}{1+k_1^2Q_dQ_t+k_2^2Q_tQ_l} \tag{2.23}$$

For high coupling k_1 and Q_t, $k_1^2Q_dQ_t \gg 1+k_2^2Q_tQ_l$, the gain can be approximated as Equation 2.24.

$$Gain|_3 \sim -\sqrt{\frac{R_3}{R_1}}k_2\sqrt{Q_tQ_l}\frac{1}{k_1\sqrt{Q_dQ_t}} \tag{2.24}$$

2.5.3 Four-coil System

From Equations 2.3 and 2.9, the expression for the voltage gain for a four-coil system can be expressed as Equation 2.25 (for small size driver and load coils).

$$Gain|_4 = j\sqrt{\frac{R_4}{R_1}}\frac{(k_1\sqrt{Q_dQ_t})(k_2\sqrt{Q_tQ_r})(k_3\sqrt{Q_rQ_l})}{(1+k_1^2Q_dQ_t)(1+k_3^2Q_rQ_l)+k_2^2Q_tQ_r} \tag{2.25}$$

Considering high couplings k_1 and k_3, and high Q-factor for transmitter (Q_t) and receiver coils (Q_r), $(1+k_1^2Q_dQ_t)(1+k_3^2Q_rQ_l)+k_2^2Q_tQ_r \simeq (k_1^2Q_dQ_t)(k_3^2Q_rQ_l)$, the voltage gain can be approximated as in Equation 2.26.

$$Gain|_4 \sim j\sqrt{\frac{R_4}{R_1}}k_2\sqrt{Q_tQ_r}\frac{1}{k_1\sqrt{Q_dQ_t}}\frac{1}{k_3\sqrt{Q_rQ_l}} \tag{2.26}$$

An approximated model (Equations 2.22, 2.24 and 2.26) of the voltage gain is useful to characterize the effect of dominant parameters, as well as to compare the voltage gain of two-coil, three-coil, and four-coil systems. Figure 2.3 shows the tuning of the voltage gain of a three-coil system with respect to the coupling k_1 for *Design 2* (Table 2.1).

In general, as coupling k_1 increases, the PTE of the three-coil system increases and voltage gain decreases. However, it can be seen from Figure 2.3 that there exists a region ($0.125 < k_1 < 0.2$) in which both PTE and voltage gain of the multi-coil system are higher than its two-coil equivalent. By varying the coupling between the driver and transmitter coils, the inductive link voltage gain can be tuned to the desired value. The supply voltage of the implanted electronics changes with different integrated circuit (IC) technology. With the freedom of tunable voltage gain, a desired output voltage can be generated without using a specific source voltage value. Selection of required

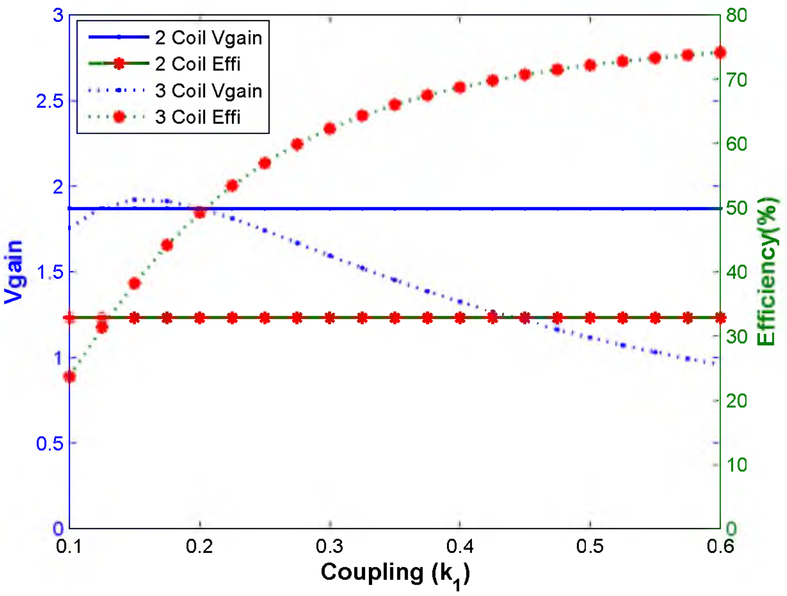

Figure 2.3. Voltage gain and efficiency (PTE) variation of the two-coil and its equivalent three-coil system with change in coupling k_1 for *Design 2* (Table 2.1). Both systems use the same operating distance between the external and the implanted coils (k = 0.074 , k_2 = 0.065 for *Design 2* (Table 2.1)

voltage gain primarily depends on the implant input voltage and the external device supply voltage. For example, with the use of 12 V external source, a voltage gain of approximately 0.5 will be sufficient to generate 5 V DC supply after diode full wave rectification (assuming 0.5 V diode forward voltage drop). While using a battery voltage of 3 V, voltage gain of 2 will be required to generate the same output voltage of 5 V. Thus, by tuning the voltage gain of multi-coil system, adequate voltage can be generated at the implant terminals.

2.6 Frequency Bandwidth

In telemetry applications, most designs focus on a high data rate communication link to reduce the system response time and allow real-time data transfer. However, the available data rate strongly depends on the carrier frequency, inductive link frequency bandwidth and data modulation scheme. Due to simplicity of the design, ASK (amplitude shift keying) and OOK (ON-OFF keying) based modulation schemes are popular for low data rate communication. To achieve relatively higher data rate, FSK or BPSK (Binary Phase Shift Keying) based modulation is used [18]. Other than these standard schemes, for uplink communication over inductive link, an attractive modulation method known as LSK (Load Shift Keying) can be used [18]. In this scheme, the effective load of the data is modulated with the data signal and its effects are monitored at the driver side to retrieve the data.

Table 2.1. System Specifications

	Design 1		Design 2	
Coils	two-coil	three-coil	two-coil	three-coil
Driver				
$D_{outD}(cm)$	3.8	3.8	4	4
$D_{inD}(cm)$	1.3	3.6	2	3.6
N_D	30	3	12	2
$L_d(\mu H)$	22.41	0.906	5.059	0.391
$R_{self}(\Omega)$	3.73	0.507	0.491	0.164
$Q_{unloaded}$	90.6	26.9	192.6	44.56
$R_{driver}(\Omega)$	5.3	5.3	5.1	5.1
$Q_{loaded}(Q_d)$	37.53	2.36	16.9	1.39
$C_d(nF)$	0.196	4.853	0.538	7.132
Wire (AWG)	28	28	44/100[1]	44/100
Transmitter				
$D_{outT}(cm)$		3.6		3.6
$D_{inT}(cm)$		1.3		2
N_T		27		10
$L_T(\mu H)$		19.01		3.96
$R_{self}(\Omega)$		3.527		0.4
$Q_{unloaded}$		81.3		187
$R_{driver}(\Omega)$		-		-
$Q_{loaded}(Q_t)$		81.3		187
$C_T(nF)$		0.228		0.706
Wire (AWG)		28		44/100
Load				
$D_{outL}(cm)$	0.5	0.5	1.5	1.5
$D_{inL}(cm)$	0.13	0.13	0.5	0.5
N_L	102	102	8	8
$L_L(\mu H)$	24	24	0.687	0.687
$R_{self}(\Omega)$	16.9	16.9	0.113	0.113
$Q_{unloaded}$	21.4	21.4	115	115
$R_{load}(\Omega)$	50.3	50.3	100	100
$Q_{loaded}(Q_l)$	5.38	5.38	7.24	7.24
$C_L(nF)$	0.183	0.183	4	4
Wire Type (AWG)	45	45	44/100	44/100
d (mm)	15	15	12	12
k_1 (or k)	0.016	0.47	0.074	0.5
k_2		0.015		0.065
k_4		0.012		0.05
f_{res} (MHz)	2.4	2.4	3	3
Load Type	Series	Series	Parallel	Parallel

For low coupling between the external and implant coils ($k \sim 0.05$), frequency bandwidth of uplink and downlink is limited by the Q-factor of the coils [18, 19]. Thus, a typical frequency bandwidth of about 10% of the carrier frequency is achieved to communicate between the external and the implanted device [4–7].

For two resonating oscillators, the frequency bandwidth is directly proportional to the coupling between the oscillators. Couple mode theory [20] can be used to explain the phenomenon of pole splitting due to the coupling between the resonating objects. Higher coupling causes higher pole splitting. Therefore using strongly coupled resonators, higher frequency bandwidth of the system can be obtained. The inductive link acts as a bandpass filter around its resonance frequency and its transfer function can be represented by V_{out}/V_{in}. Figure 2.4 shows that, by increasing the coupling between the two magnetically coupled resonators, the bandwidth of the inductive link increases. Similar observation was seen in [21]; however, the underlying phenomenon was not explained. In typical biomedical applications, the coupling between external and implant coil lies in the range of 0.01 to 0.07 [4, 5] and, for a given operating distance, the frequency bandwidth of a two-coil system is fixed due to fixed coupling between the driver and load coils. Compared to a two-coil system, a multi-coil system provides the possibility to achieve high coupling between the coils. Multi-coil systems use a high coupling k_1 between the driver coil and the transmitter coil (and in the case of a four-coil system, a high coupling k_3 between the receiver coil and the load coil) to improve the frequency bandwidth compared to two-coil systems of similar size for a given fixed operating distance.

Figure 2.5 shows that, for different operating distances (thus different coupling $k = k_2 = \{0.055, 0.065, 0.075\}$), the frequency bandwidth increases with increase in coupling. For *Design 2* (Table 2.1), a three-coil system achieves higher frequency bandwidth compared to that of an equivalent sized two-coil system for all coupling $k_1 > 0.2$. The bandwidth of the three-coil system increases linearly with increase in k_1 as depicted by the coupled mode theory.

Increasing the coupling k_1 also reduces the voltage gain. Figure 2.6 shows the gain-bandwidth product (GBP) of the two-coil and three-coil systems with different coupling $k = k_2 = \{0.055, 0.065, 0.075\}$. The GBP of the three-coils system is higher than the equivalent two-coil system's GBP and provides a design trade-off to tune the gain and the frequency bandwidth of a multi-coil system.

To demonstrate the data transfer for two-coil and multi-coil inductive link, FSK-based modulated data is used and the downlink data transfer is shown. As the inductive link is a linear and invertible system, the frequency bandwidth will be the same for both uplink and downlink communication. Figure 2.7 shows the schematics of the two-coil and three-coil systems based on the parameters *Design 2* (Table 2.1).

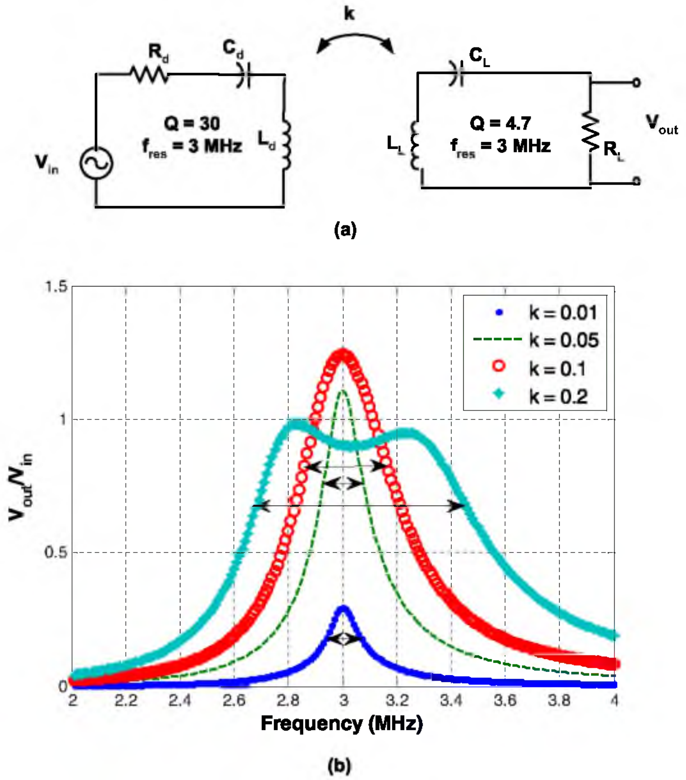

Figure 2.4. Voltage gain between two magnetically coupled resonators with the variation of frequency and coupling. (a) Schematics of two magnetically coupled resonators with same resonance frequency (3 MHz) (b) Bandpass response of the inductive link with the variation in coupling between the resonators.

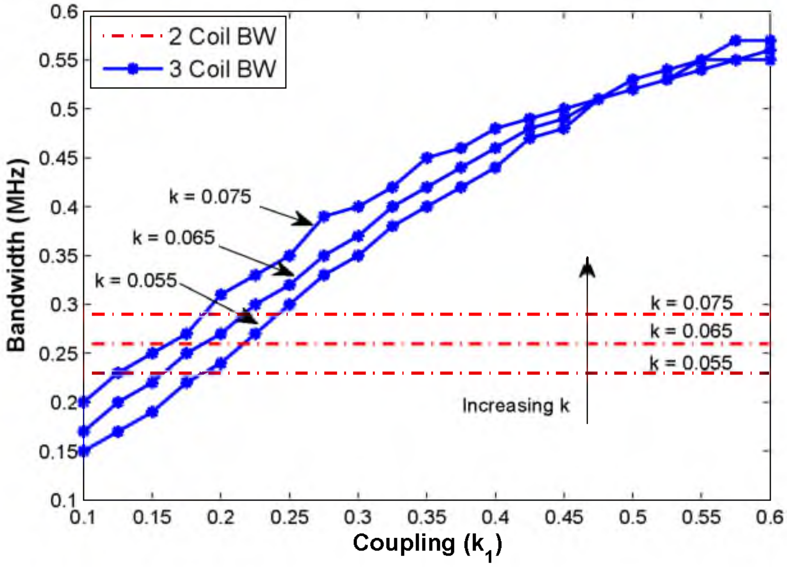

Figure 2.5. Channel bandwidth (*BW*) variation of the two-coil and its equivalent three-coil system with change in coupling k_1, and $k_2 = k$. The design parameters are based on *Design 2* (Table 2.1). For unity input voltage source $V_1 = 1V$, the 3-dB frequency bandwidth is calculated from the voltage gain versus frequency plot.

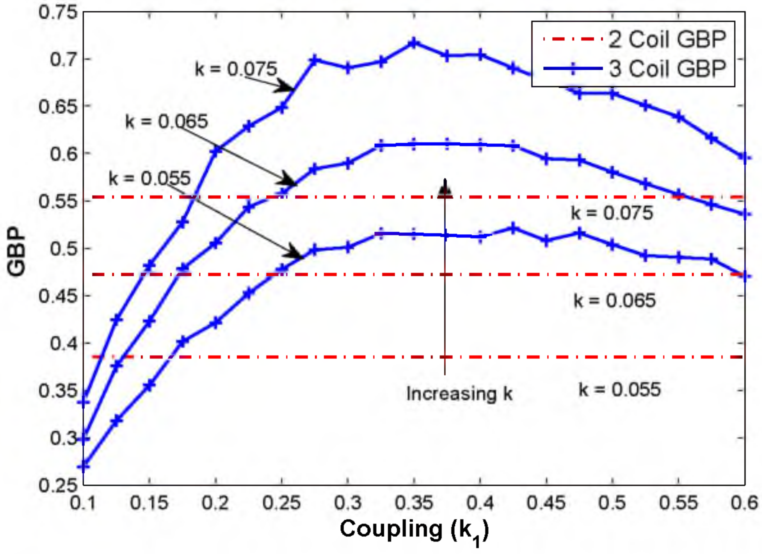

Figure 2.6. Gain-Bandwidth product (GBP) of a two-coil and its equivalent three-coil system with change in coupling k_1, and $k_2 = k$. The design parameters are based on *Design 2* (Table 2.1).

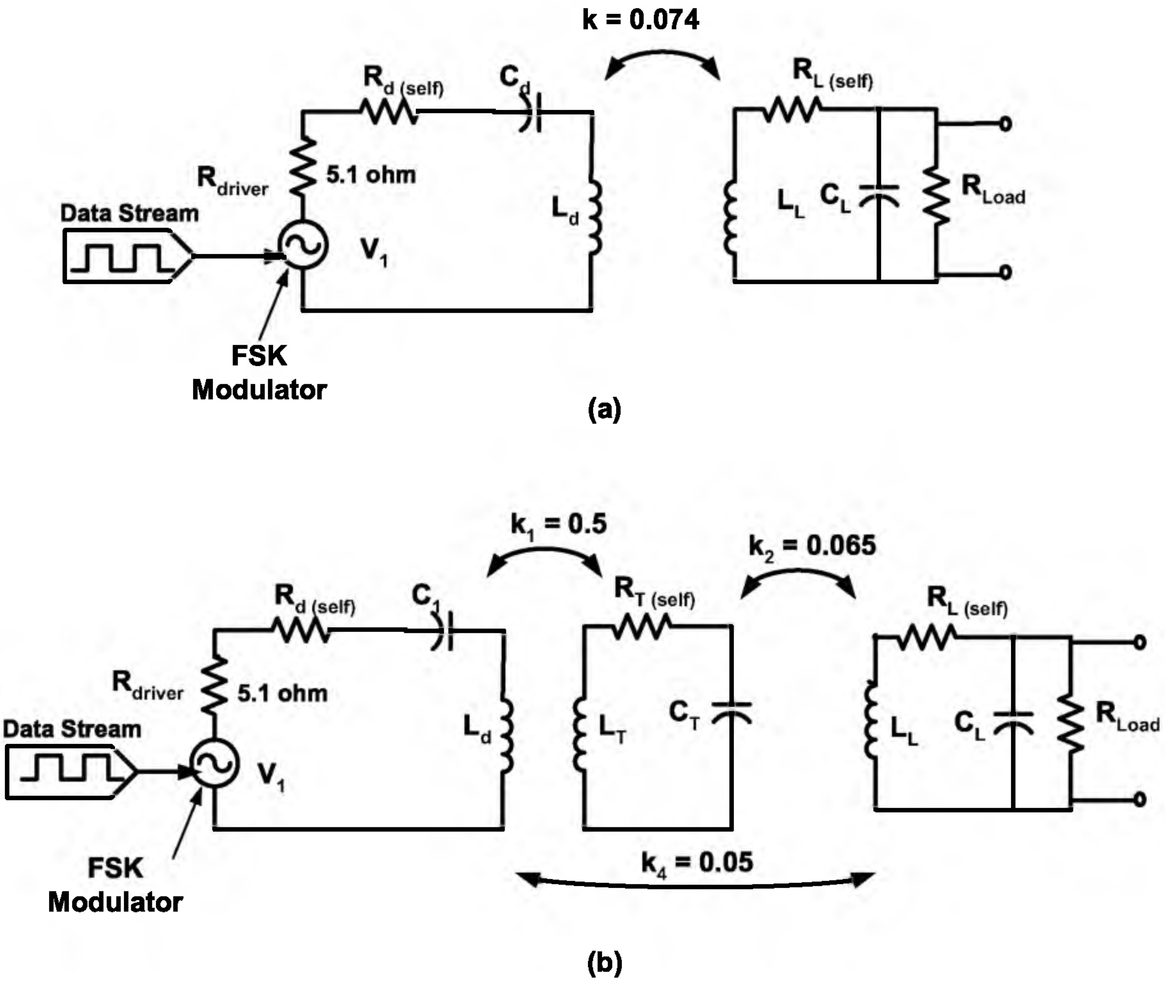

Figure 2.7. FSK modulation based data transfer system over (a) two-coil and (b) three-coil inductive link for *Design 2* (Table 2.1).

The modulation frequency is chosen based on the 3-dB frequency of the two-coil and three-coil system. In the example presented (*Design 2, Table 2.1*), the 3-dB points of the two-coil system are at 2.913 MHz and 3.17 MHz. Thus, for bit '1', the modulator generates the frequency of 2.913 MHz and, for bit '0', the modulator outputs frequency of 3.17 MHz. Similarity, the 3-dB points of the three-coil system are at 2.673 MHz and 3.194 MHz. For bit '1', the modulator of the three-coil system generates the frequency of 2.673 MHz and, for bit '0', the modulator outputs the frequency of 3.194 MHz. A data stream of 200 kbps is sent and received over the inductive link. Figure 2.8 shows the input data stream and the received modulated signals at the load (R_{load}) terminals.

To demonstrate the effectiveness of the multi-coil system to improve the frequency bandwidth, Fast Fourier Transforms (FFTs) of the received signals are shown in Figure 2.9. Due to higher channel spacing in the multi-coil system (3-dB bandwidth ~ 521 *kHz*) to represent bit '1' and '0', the multi-coil approach shows lower channel interference for high data rate of 200 kbps. Conversely, the channel spacing in the two-coil system is low (3-dB bandwidth ~ 257 *kHz*) and shows a significant interference between two data channels for 200 kbps data rate. From the spectrum of the received signal, due to the increase in frequency bandwidth using a three-coil system compared to its two-coil equivalent, multi-coil inductive link can therefore support higher data rate.

2.7 Maximum Power Transfer

For some devices, the input voltage of the driver coil is restricted by the supply voltage of the power source (e.g., power amplifier source voltage). In a wireless power transfer system, the load impedance can be seen as a reflected resistance on the input source. For a constant source voltage, the reflected impedance should be matched to the source resistance in order to deliver the maximum possible power to the load. Maximum power transfer condition limits the maximum PTE to 50%, as in the best case scenario half of the available power is dissipated at the source resistance. This section formulates the reflected impedance and resulting PTE for a two-coil and a multi-coil system.

2.7.1 Effective Resistance

Using the network model of the two-coil and the multi-coil system (Equations 2.1, 2.2, and 2.3), the reflected load impedance R_{eff} at the source can be calculated by V_1/I_1 and can be expressed as in Equations 2.27, 2.28 and 2.29. These equations show the total resistance seen by the source due to self impedance and input reflected load resistance as a function of the coil parameters.

For a two-coil system,

$$R_{eff} = R_1(1 + k^2 Q_d Q_l) \tag{2.27}$$

For a three-coil system,

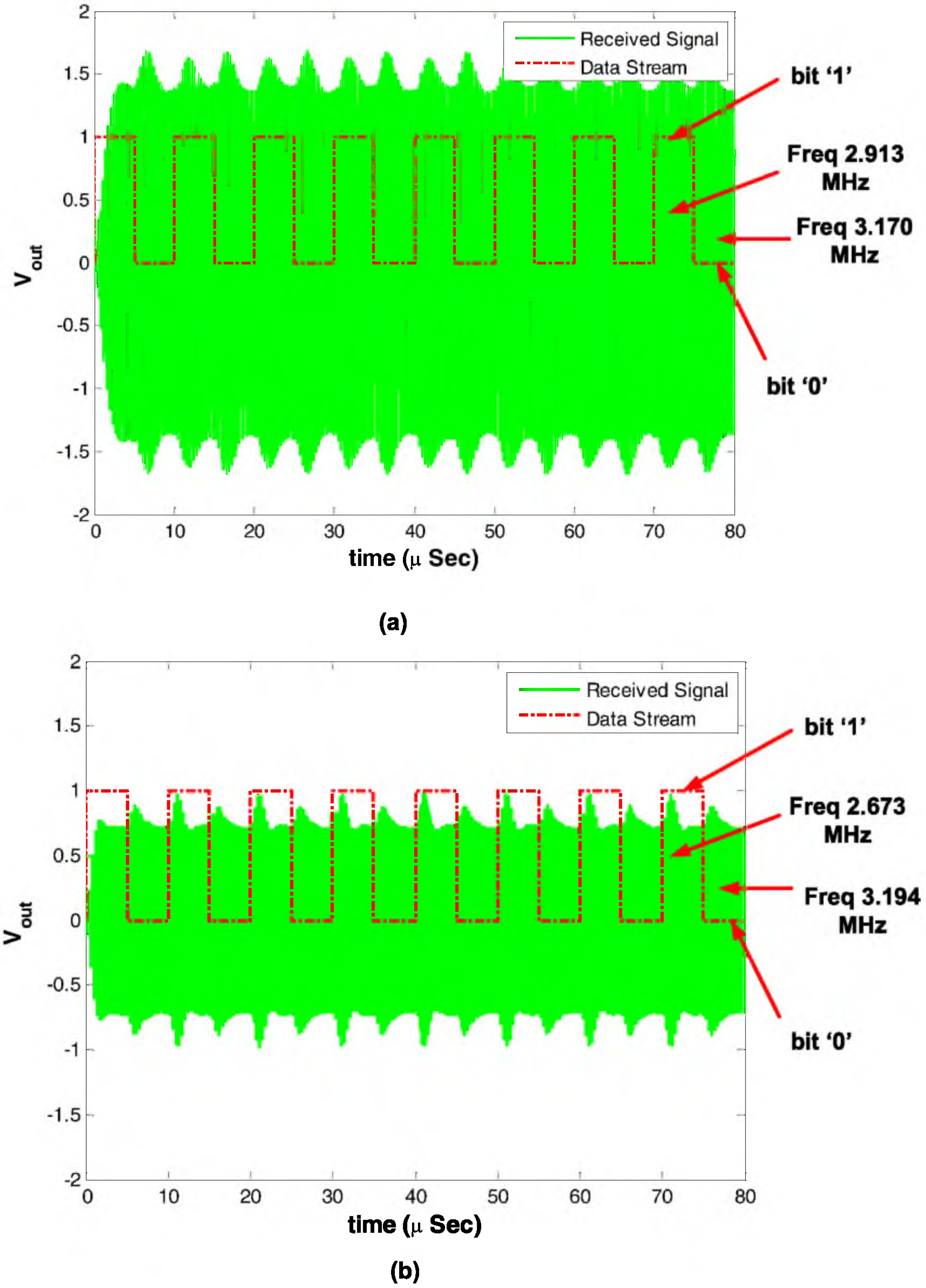

Figure 2.8. Transient response of (a) input data stream and received signal at two-coil load terminal (b) input data stream and received signal at three-coil load terminal. The design parameters are based on *Design 2* (Table 2.1).

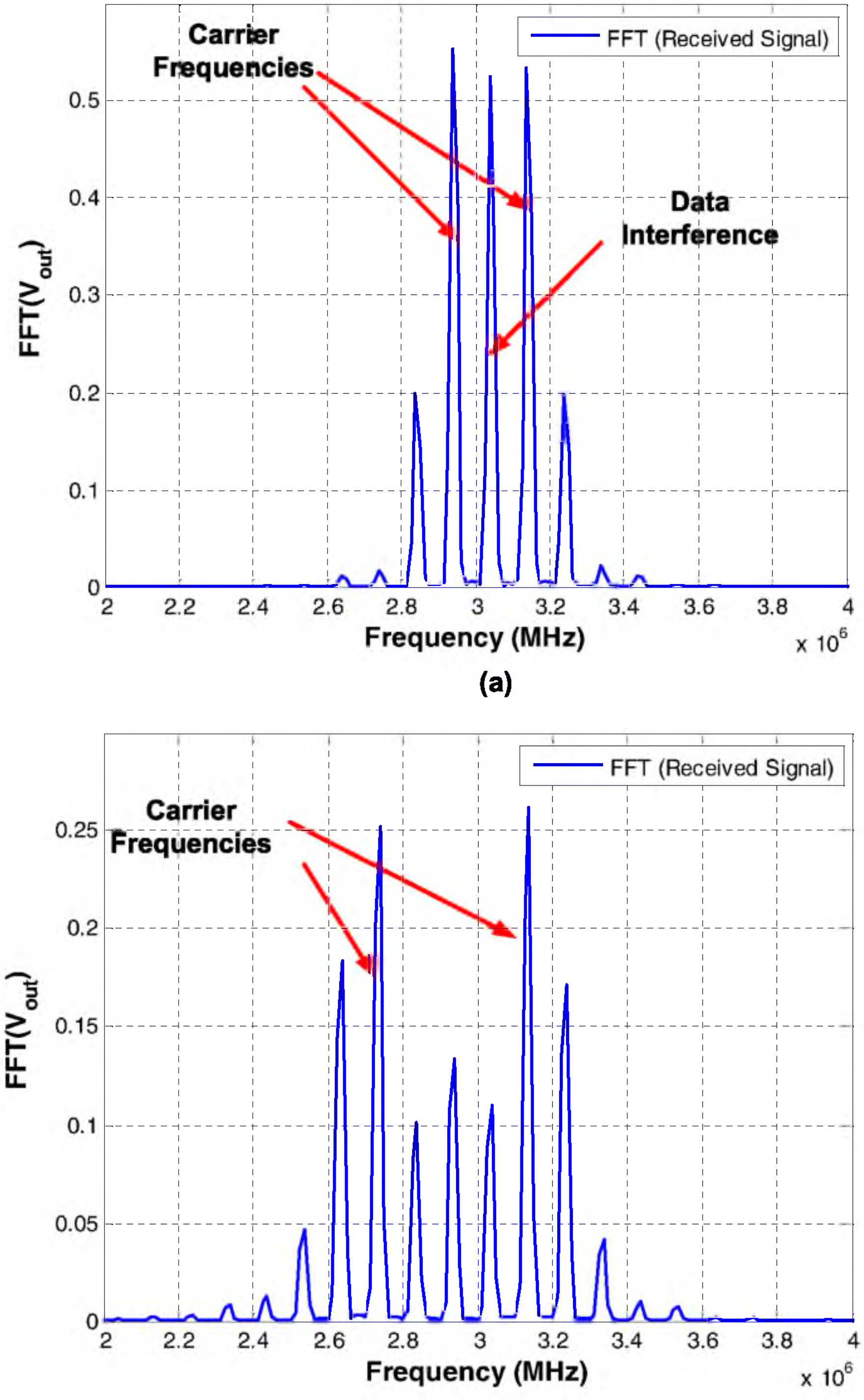

Figure 2.9. Frequency spectrum plot of received signal at (a) two-coil load terminal (b) three-coil load terminal. The design parameters are based on *Design 2* (Table 2.1).

$$R_{eff} = R_1 \left(1 + \frac{k_1^2 Q_d Q_t}{1 + k_2^2 Q_t Q_l} \right) \tag{2.28}$$

For a four-coil system,

$$R_{eff} = R_1 \left(1 + \frac{k_1^2 Q_d Q_t (1 + k_3^2 Q_r Q_l)}{1 + k_2^2 Q_t Q_r + k_3^2 Q_r Q_l} \right) \tag{2.29}$$

To quantify the loading effect of the load resistance and its matching to the source resistance, two terms namely "loading factor N" and "matching factor p" are introduced. The effective resistance R_{eff} can be written as a function of the loading factor N, which is used to define the matching factor p as in Equation 2.30. For all values of Q-factor and coupling, the loading factor N is a positive real number. For the two-coil, the three-coil and the four-coil systems, N is defined in Equations 2.31, 2.32, and 2.33, respectively. The matching factor p denotes the ratio of power delivered and the maximum deliverable power for a constant source voltage. For all values of N, matching factor p lies between 0 and 1. For perfect impedance matching to R_1, the loading factor N will be 1 and maximum power will be delivered to the load (p = 1).

$$\begin{aligned} R_{eff} &= R_1(1+N) \\ P_{in} &= \frac{V_{in}^2}{2R_{eff}} \\ P_{out} &= \eta P_{in} \\ p &= \frac{4N}{(1+N)^2}; \qquad 0 \leq p \leq 1 \end{aligned} \tag{2.30}$$

For a two-coil system:

$$N = k^2 Q_d Q_l \tag{2.31}$$

For a three-coil system:

$$N = \frac{k_1^2 Q_d Q_t}{1 + k_2^2 Q_t Q_l} \tag{2.32}$$

For a four-coil system:

$$N = \frac{k_1^2 Q_d Q_t (1 + k_3^2 Q_r Q_l)}{1 + k_2^2 Q_t Q_r + k_3^2 Q_r Q_l} \tag{2.33}$$

2.7.2 Impedance Matching

The PTE of the two-coil, three-coil, and four-coil systems (Equations 2.16, 2.17, and 2.19) can be rewritten in terms of the loading factor N and the matching factor p as in Equations 2.34, 2.35 and 2.36, respectively.

For a two-coil system, the loading factor N (Equation 2.31) is in the range 0.2 to 0.5 for all practical values [4, 5, 16] making it impossible to achieve the matching condition.

$$\begin{aligned} \eta &= [1-\frac{p}{2}\frac{1}{1+\sqrt{1-p}}]; \quad for \quad N \geq 1 \\ \eta &= [1-\frac{p}{2}\frac{1}{1-\sqrt{1-p}}]; \quad for \quad N < 1 \end{aligned} \tag{2.34}$$

In three-coil systems, for a given operating distance, the loading factor N can be controlled by varying k_1 and Q_d. This makes achieving the matching condition relatively easy. For example, given $k_1 = 0.25, Q_d = 0.44, Q_t = 160, Q_l = 7, k_2 = 0.055$, the loading factor and the matching factor are 1, resulting in a PTE η of 38.6%.

$$\begin{aligned} \eta &= [1-\frac{p}{2}\frac{1}{1+\sqrt{1-p}}]\eta_{23}; \quad for \quad N \geq 1 \\ \eta &= [1-\frac{p}{2}\frac{1}{1-\sqrt{1-p}}]\eta_{23}; \quad for \quad N < 1 \end{aligned} \tag{2.35}$$

where $\eta_{23} = \frac{k_2^2 Q_t Q_l}{1+k_2^2 Q_t Q_l}$.

Similarly, a four-coil system is also capable of achieving maximum power transfer condition by tuning Q_d, k_1 and k_3. For example, given $k_1 = 0.2, Q_d = 0.7, Q_t = 200, Q_r = 100, Q_l = 2.5, k_2 = 0.05, k_3 = 0.2$, the loading factor and the matching factor are 1, resulting in a PTE η of 37.4%.

$$\begin{aligned} \eta &= [1-\frac{p}{2}\frac{1}{1+\sqrt{1-p}}]\eta_{23}\eta_{34}; \quad for \quad N \geq 1 \\ \eta &= [1-\frac{p}{2}\frac{1}{1-\sqrt{1-p}}]\eta_{23}\eta_{34}; \quad for \quad N < 1 \end{aligned} \tag{2.36}$$

where $\eta_{23} = \frac{k_2^2 Q_t Q_r}{1+k_2^2 Q_t Q_r + k_3^2 Q_r Q_l}$ and $\eta_{34} = \frac{k_3^2 Q_r Q_l}{1+k_3^2 Q_r Q_l}$.

For a constant source voltage and a given operating distance, the output power to the load can be varied. The formulation of output power and its trade-off with the PTE provides an important tool to the designer to generate adequate output power in the load. As compared to the two-coil system, the multi-coil system offer higher number of tunable design parameters (Q factor and coupling) and thus it can easily achieve maximum power transfer condition to the load.

2.8 Experimental Results

To demonstrate the PTE and the frequency bandwidth improvement using a multi-coil telemetry system, two experiments were performed. The performance of a three- and a two-coil equivalent system were compared; in this, for the same type of wire, the equivalency is defined by the total number of turns of driver and transmitter coils in the the three-coil system being equal to the number of turns of the driver coil in the two-coil system. A small implant (load) coil, with dimensions published in [22], is chosen for Experiment 1. For the second experiment, a different small implant coil was built with dimensions listed in column *Design 2* of Table 2.1. Assuming that these coils were already implanted and could not be modified, two setups were considered using external single and double coils to create and compare a two-coil and a three-coil system. Two sets of experiments were performed to assess the efficiency improvement for different coil types, as well as the effect of the Q-factor on the overall system efficiency and bandwidth.

2.8.1 Experimental Setup

A 50 Ω sinusoidal source was used to generate a signal at the operating frequency. The PTE was calculated from the output terminal of the signal source to negate the effect of the source resistance. Instead, a resistance of 5.1Ω was used in series with the driver coil in order to emulate the typical source resistance of a power amplifier used for telemetry applications [15, 16] and to measure the input current in the driver coil to calculate the input power. The source resistance of the power amplifier is mainly governed by the ON-resistance of switching transistor and ESR (effective series resistance) of the lumped components (capacitances and RF choke) [13, 15, 16, 23]. Even if few MOSFETs provide much smaller ON-resistance ($\sim 0.05\Omega$), due to their size they can cause much higher input and output capacitance ($\sim 1000pF$) [24]. High input capacitance results in slow switching in input signal and high MOSFET output capacitance can restricts the optimum design parameters of the class-E amplifier [23]. Thus, selection of the switching transistor depends on the maximum drain-to-source voltage rating ($V_{ds(max)}$), ON-resistance, input and output capacitance of the switching transistor [25]. To use a wide range of supply voltage, low switching delays and low parasitic capacitances, MOSFETs with comparatively higher ESR ($\sim 1\Omega$) might be required [26]. For biomedical applications, moderate R_{on} and ESR of resonating capacitances can lead to a driver impedance of a few ohms [16].

Table 2.1 reports the measured electrical and mechanical parameters for the two designs considered here. The schematics of the two- and three-coil systems are similar to that shown in Figure 2.7. To demonstrate the wireless power and data transfer, the external and implant coils are separated by distance d as shown in Figure 2.10. Figure 2.11 shows the concentric transmitter and driver coil for *Design 1* and *Design 2*. Input power is calculated using measured input voltage and input current. Output power at the load resistance is calculated from the measured output voltage across load.

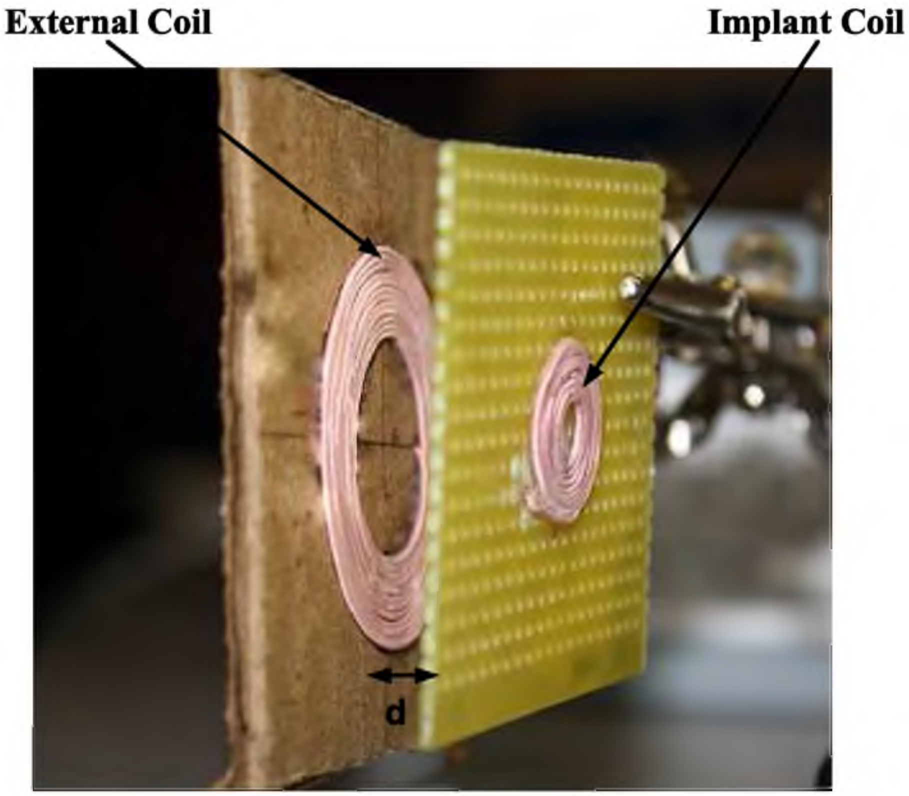

Figure 2.10. Experimental setup for the telemetry system for *Design 2* (Table 2.1) showing the relative positioning and distance *d* between the external and implant (load) coils.

2.8.1.1 Experiment 1

The first experiment compares the PTE, voltage gain and frequency bandwidth of a two-coil system and its three-coil equivalent. The external coils are coaxially aligned and positioned at a distance *d* from the implant (load) coil. Table 2.1 (column *Design 1*) provides the electrical, mechanical, and operating conditions of the two-coil and the three-coil systems. To achieve a fair comparison, the overall mechanical dimensions of both systems are equal. A small implant coil of diameter 0.5 cm is used for both cases. Figure 2.12 (a) shows the implanted coil for *Design 1*.

2.8.1.2 Experiment 2

Experiment 2 shows the effect of a high Q-factor transmitter coil on the system PTE when comparing the two-coil and the three-coil cases. The design parameters are detailed in Table 2.1 under the *Design 2* column. The coil is built using low resistance multi-strands Litz wire to improve the Q-factor [27]. Figure 2.12 (b) shows the implanted coil for this experiment.

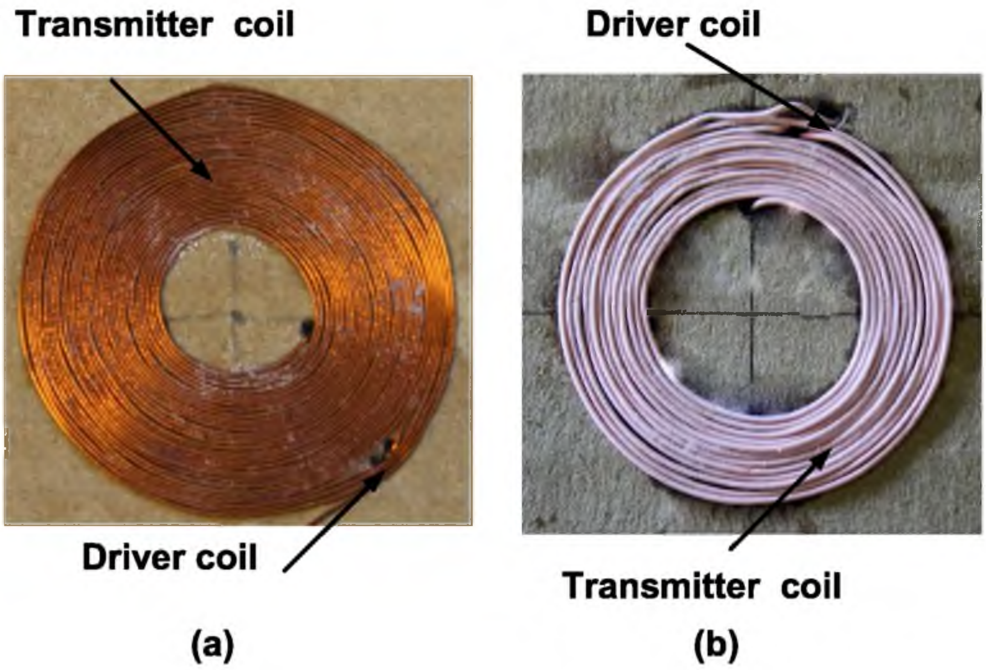

Figure 2.11. Co-centric, co-planar transmitter and driver coil for three-coil system used for (a) *Design 1* and (b) *Design 2* (Table 2.1), showing the relative positions of driver and transmitter coils.

2.8.2 Experimental Results

2.8.2.1 Experiment 1

Figure 2.13 shows the simulated and measured PTE for the two-coil and the three-coil systems for *Design 1*. The simulation is done with and without the consideration of k_4 on voltage gain and PTE which shows that, due to the small inductance value of driver coil, k_4 does not have a significant effect on the voltage gain and PTE. The three-coil system shows more than twice the PTE compared to the two-coil equivalent setup for the same operating conditions and system dimensions. The shift in the peak value of the PTE is only 10 kHz, which is caused by the difference in the value of the resonating capacitors from their ideal value (within 5 % tolerance limit).

Figure 2.14 shows the simulated and measured voltage gains of a two-coil and a three-coil system. The three-coil system shows higher frequency bandwidth than the two-coil system due to high coupling between the driver and the transmitter coil ($k_1 = 0.47$). As expected, due to high coupling k_1, the voltage gain of the three-coil system is smaller than the voltage gain of the two-coil system.

2.8.2.2 Experiment 2

Figure 2.15 shows the simulated and measured efficiency for a two-coil system and a three-coil system with high Q-factor transmitter coil. The simulation is done with and without the effect of k_4

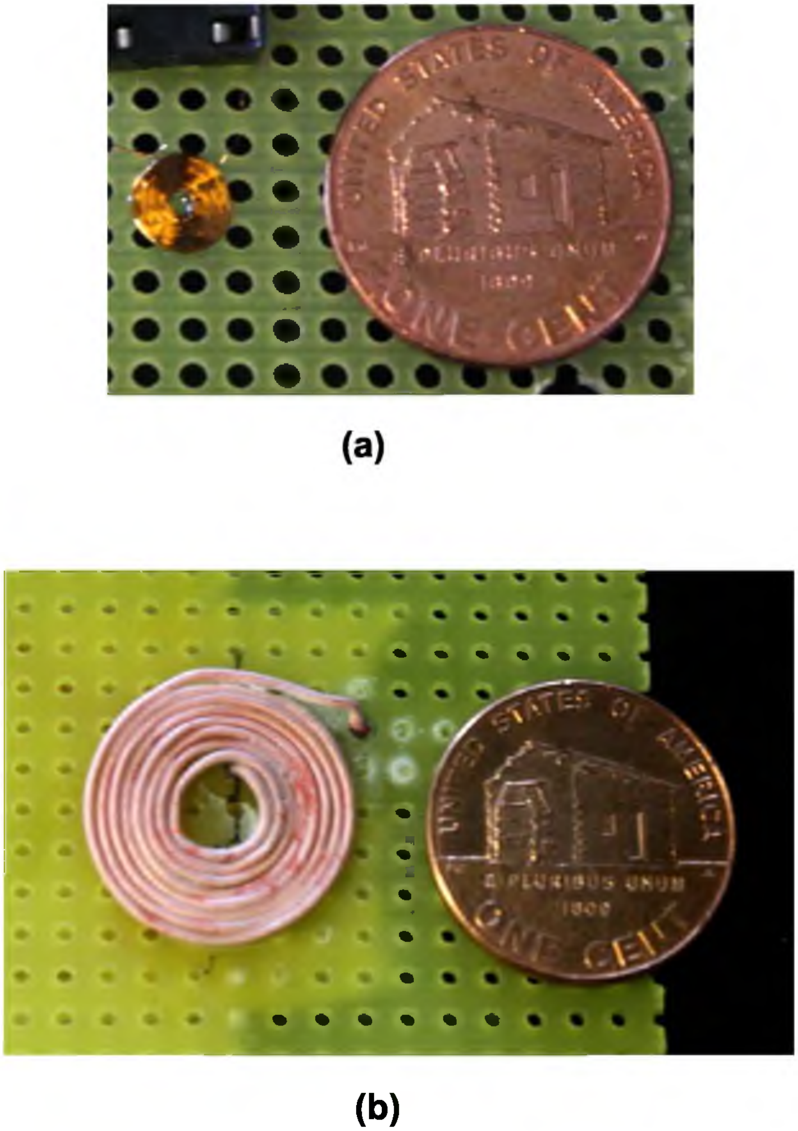

Figure 2.12. Implant (load) Coils used for (a) *Design 1* and (b) *Design 2* (Table 2.1) showing the relative dimensions of the coils with respect to 1-cent coin (USA)

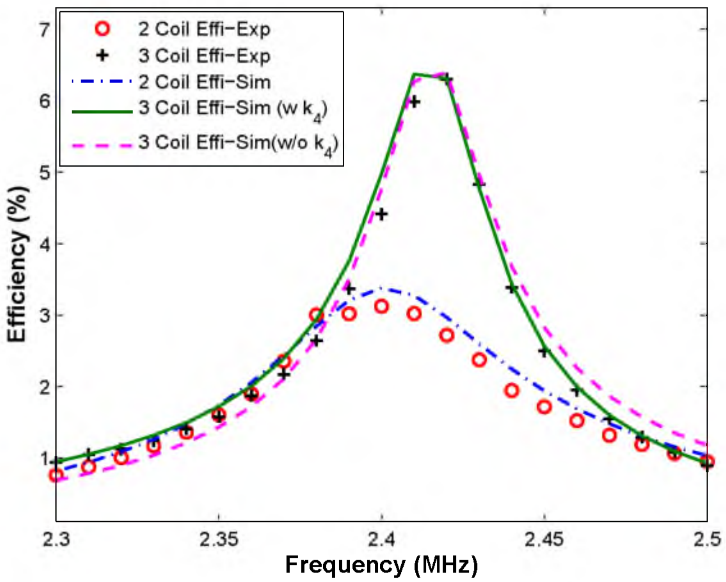

Figure 2.13. Simulated (Sim) and experimental (Exp) PTE of a two-coil and its three-coil equivalent system with respect to frequency for *Design 1* (Table 2.1). Simulation is done with (w k_4) and without (w/o k_4) the consideration of coupling between driver and load coils (k_4).

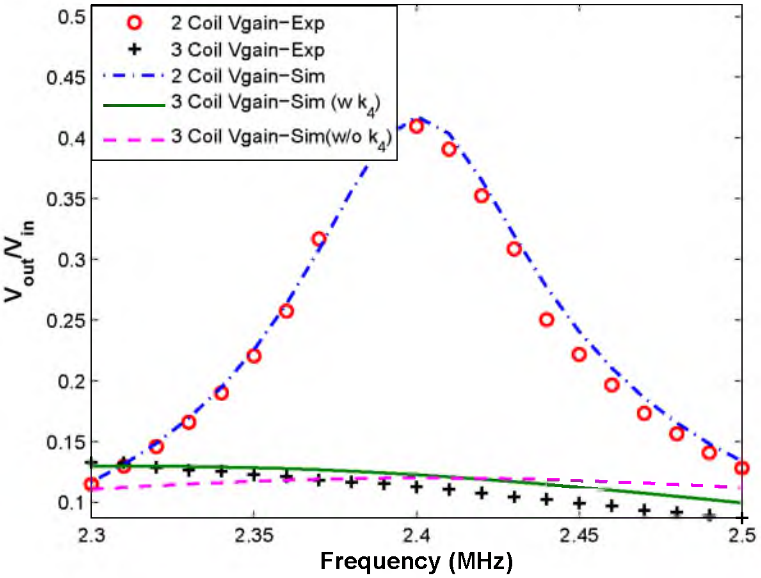

Figure 2.14. Simulated (Sim) and experimental (Exp) voltage gain of a two-coil and its three-coil equivalent system with respect to frequency for *Design 1* (Table 2.1). For unity input voltage source $V_1 = 1V$, the 3-dB frequency bandwidth is calculated from the voltage gain (Vgain) versus frequency plot. Simulation is done with (w k_4) and without (w/o k_4) the consideration of coupling between driver and load coils (k_4).

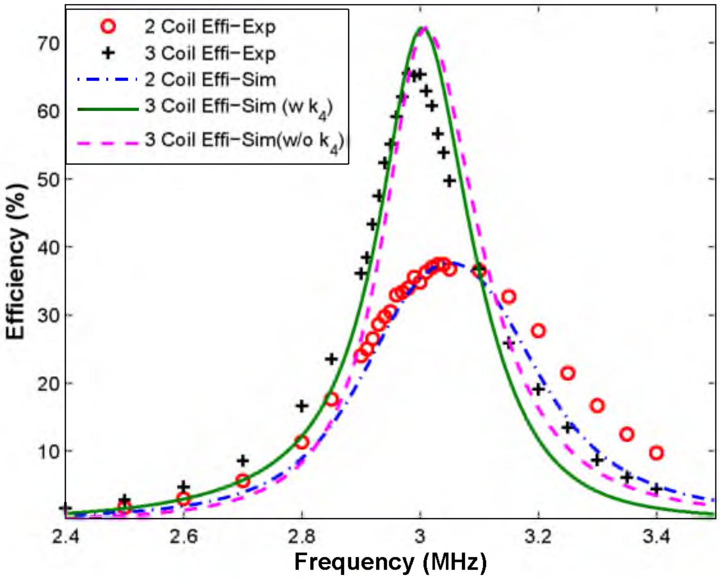

Figure 2.15. Simulated (Sim) and experimental (Exp) PTE of a two-coil and its three-coil equivalent system with respect to frequency for *Design 2* (Table 2.1). Simulation is done with (w k_4) and without (w/o k_4) the consideration of coupling between driver and load coils (k_4).

on voltage gain and PTE. From Figure 2.15, it can be seen that, due to the small inductance value of the driver coil, k_4 does not have appreciable effect on the voltage gain and PTE. Using Litz wire for all the external coils, the resistive loss in the coils is reduced. The three-coil system achieves a high PTE (65%) and approximately two times the efficiency of the equivalent two-coil system. The shift in the peak value of PTE is only 20 kHz which is also caused by the drift in resonating capacitors from their ideal value (within 5 % tolerance limit).

Figure 2.16 shows simulated and measured voltage gains of a two-coil and a three-coil system. The three-coil system shows higher frequency bandwidth compared to the two-coil system due to the high value of the coupling k_1 (~ 0.5).

2.9 Comparison

Catrysse et al. [5] defined a performance metric as a function of PTE, frequency bandwidth, and system dimensions (Equation 2.37). This metric allows simple comparison between different telemetry systems performance.

$$FOM = 10Log_{10}\left[\frac{d^2}{D_1 \times D_2}\frac{BW}{f_{res}} \times \eta\right] \tag{2.37}$$

In Equation 2.37, *d* is the distance between the external and the implant coil with D_1 and D_2 denoting as the diameter of the external and the implant coils, respectively. *BW* denotes the 3-dB

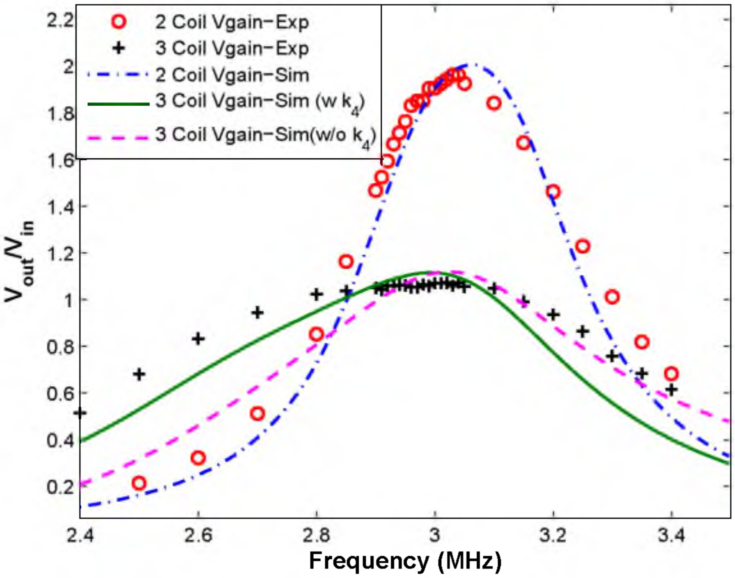

Figure 2.16. Simulated (Sim) and experimental (Exp) voltage gain of a two-coil and its three-coil equivalent system with respect to frequency for *Design 2* (Table 2.1). For unity input voltage source $V_1 = 1V$, the 3-dB frequency bandwidth is calculated from the voltage gain (Vgain) versus frequency plot. Simulation is done with (w k_4) and without (w/o k_4) the consideration of coupling between driver and load coils (k_4).

frequency bandwidth at resonant frequency f_{res}. η is the PTE of the system.

Due to the limited range of the input power source voltage, the voltage gain is also an important design parameter for the telemetry system. High voltage gain reduces the requirement of high source voltage. Therefore Equation 2.37 was modified to include the voltage gain factor *Gain* as shown in Equation 3.14.

$$FOM_n = 10Log_{10}\left[\frac{d^2}{D_1 \times D_2}\frac{BW}{f_{res}} \times \eta \times Gain\right] \tag{2.38}$$

Table 2.2 summarizes the performance metric of the two-coil and its three-coil equivalent systems for both the designs specified in Table 2.1. It can be seen that for all the designs the multi-coil system outperforms the two-coil system for both power and data transfer.

2.10 Conclusion

We have introduced a novel multi-coil based telemetry system for power and data transfer over an inductive link, and compared it with an equivalent system employing two coils. The network model and the two-port model for both the two-coil and the multi-coil system were described, analyzed and compared to provide insights about their performance in terms of power and data transfer. The analysis for the two-coil and the multi-coil (three-coil and four-coil) system shows that the multi-coil configuration can be used effectively to improve the PTE and gain-bandwidth product of the system. A multi-coil system provides additional tuning parameters to the designer. It is simpler to adjust a particular configuration for achieving the maximum power transfer in the multi-coil case than in the two-coil system.

In addition to the theoretical modeling, two experiments were conducted with two implant coils. For all considered designs, the experimental data show that the multi-coil (three-coil) configurations achieved more than twice the efficiency and higher gain-bandwidth-product compared to the equivalent two-coil system. Further, it is noted that all the simulation results are in close agreement with the experimental results. One significant advantage of the three-coil configuration is that it can be

Table 2.2. Experimental Results

	Design 1		Design 2	
	two-coil	three-coil	two-coil	three-coil
η(%)	3.12	6.3	35	65
BW(kHz)	60	332	240	580
Gain	0.42	0.125	1.9	1.07
GBP	25.2	41.5	456	620.6
FOM_n	-34.28	-28.8	-18.94	-14.91

used to upgrade two-coil systems already implanted in patients without any requirement to modify or replace the implanted coil, providing with a nonsurgical, cost-effective higher performance alternative.

2.11 References

[1] S. Smith, T. Tang, and J. Terry, "Development of a miniaturised drug delivery system with wireless power transfer and communication," *IET Nanobiotechnology*, vol. 1, pp. 80–86, Oct. 2007.

[2] C. Chestek, V. Gilja, P. Nuyujukian, R. Kier, F. Solzbacher, S. Ryu, R. Harrison, and K. Shenoy, "Hermesc: Low-power wireless neural recording system for freely moving primates," *IEEE Transactions on Neural Systems and Rehabilitation Engineering*, vol. 17, no. 4, pp. 330 –338, 2009.

[3] G. Yan, D. Ye, P. Zan, K. Wang, and G. Ma, "Micro-robot for endoscope based on wireless power transfer," in *International Conference on Mechatronics and Automation*, Aug. 5-8 2007, pp. 3577 – 3581.

[4] G. Wang, W. Liu, M. Sivaprakasam, M. Zhou, J. D. Weiland, and M. S. Humayun, "A dual band wireless power and data telemetry for retinal prosthesis," in *Conf Proc. IEEE EMBS*, Aug. 30-Sept.3 2006, pp. 28–38.

[5] M. Catrysse, B. Hermans, and R. Puers, "An inductive power system with integrated bidirectional data transmission," in *Proc. Eurosensors XVII*, Sept. 21-24 2003, pp. 843–846.

[6] M. Ghovanloo and K. Najafi, "A wireless implantable multichannel microstimulating system-on-a-chip with modular architecture," *IEEE Transactions on Neural Systems and Rehabilitation Engineering*, vol. 15, pp. 449–457, Sept 2007.

[7] G. Simard, M. Sawan, and D. Massicotte, "High-speed oqpsk and efficient power transfer through inductive link for biomedical implants," *IEEE Transactions on Biomedical Circuits and Systems*, vol. 4, no. 3, pp. 192 –200, 2010.

[8] M. Haider, S. Islam, S. Mostafa, M. Zhang, and T. Oh, "Low-power low-voltage current readout circuit for inductively powered implant system," *IEEE Transactions on Biomedical Circuits and Systems*, vol. 4, no. 4, pp. 205 –213, 2010.

[9] A. Bonfanti, M. Ceravolo, G. Zambra, R. Gusmeroli, A. Spinelli, A. Lacaita, G. Angotzi, G. Baranauskas, and L. Fadiga, "A multi-channel low-power system-on-chip for single-unit recording and narrowband wireless transmission of neural signal," in *Engineering in Medicine and Biology Society (EMBC), 2010 Annual International Conference of the IEEE*, 31 Aug.-4 Sept. 2010, pp. 1555 –1560.

[10] N. Neihart and R. Harrison, "Micropower circuits for bidirectional wireless telemetry in neural recording applications," *IEEE Transactions on Biomedical Engineering*, vol. 52, pp. 1950–1959, Nov. 2005.

[11] H. Chen, M. Liu, C. Jia, C. Zhang, and Z. Wang, "Low power IC design of the wireless monitoring system of the orthopedic implants," in *Conf Proc. IEEE EMBS*, Aug. 22-26 2007, pp. 5766–5769.

[12] A. K. RamRakhyani, S. Mirabbasi, and M. Chiao, "Design and optimization of resonance-based efficient wireless power delivery systems for biomedical implants," *IEEE Transactions on Biomedical Circuits and Systems*, vol. 5, no. 1, pp. 48 –63, 2011.

[13] M. Kiani, U.-M. Jow, and M. Ghovanloo, "Design and optimization of a 3-coil inductive link for efficient wireless power transmission," *IEEE Transactions on Biomedical Circuits and Systems*, vol. 5, no. 6, pp. 579 – 591, 2011.

[14] V. Singh, A. Roy, R. Castro, K. McClure, R. Dai, R. Agrawal, R. Greenberg, J. Weiland, M. Humayun, and G. Lazzi, "On the thermal elevation of a 60-electrode epiretinal prosthesis for the blind," *IEEE Transactions on Biomedical Circuits and Systems*, vol. 2, no. 4, pp. 289 –300, 2008.

[15] M. W. Baker and R. Sarpeshkar, "Feedback analysis and design of RF power links for low-power bionic systems," *IEEE Transactions on Biomedical Circuits and Systems*, vol. 1, pp. 28–38, March 2007.

[16] R. Harrison, "Designing efficient inductive power links for implantable devices," in *Proc. ISCAS*, 2007, pp. 2080–2083.

[17] A. Kumar, S. Mirabbasi, and M. Chiao, "Resonance-based wireless power delivery for implantable devices," in *IEEE Biomedical Circuits and Systems Conference(BioCAS)*, 26-28 Nov. 2009, pp. 25–28.

[18] M. Sawan, Y. Hu, and J. Coulombe, "Wireless smart implants dedicated to multichannel monitoring and microstimulation," *IEEE Circuits and Systems Magazine*, vol. 5, no. 1, pp. 21 – 39, 2005.

[19] N. Chaimanonart, M. Suster, and D. Young, "Two-channel passive data telemetry with remote rf powering for high-performance wireless and batteryless strain sensing microsystem applications," *IEEE Sensors Journal*, vol. 10, no. 8, pp. 1375 –1382, aug. 2010.

[20] H. Haus and W. Huang, "Coupled-mode theory," *Proc. of the IEEE*, vol. 79, pp. 1505–1518, Oct. 1991.

[21] G. B. Hmida, H. Ghariani, and M. Samet, "Design of wireless power and data transmission circuits for implantable biomicrosystem," *Biotechnology*, vol. 6, no. 2, pp. 153–164, 2007.

[22] S. Kim, R. Harrison, and F. Solzbacher, "Influence of system integration and packaging on its inductive power link for an integrated wireless neural interface," *IEEE Transactions on Biomedical Engineering*, vol. 56, no. 12, pp. 2927 –2936, dec. 2009.

[23] N. Sokal and A. Sokal, "Class `E-A` new class of high-efficiency tuned single-ended switching power amplifiers," *IEEE Journal of Solid-State Circuits*, vol. 10, no. 3, pp. 168 – 176, jun 1975.

[24] V. Siliconix, "N-channel 30-v (d-s) mosfet," 2011, `http://www.vishay.com/docs/68786/sie860df.pdf`.

[25] J. Casanova, Z. N. Low, and J. Lin, "Design and optimization of a class-e amplifier for a loosely coupled planar wireless power system," *IEEE Transactions on Circuits and Systems II: Express Briefs*, vol. 56, no. 11, pp. 830 –834, nov. 2009.

[26] ON-Semiconductor, "N-channel power mosfet 300 mamps, 20 volts," 2011, `http://www.onsemi.com/pub-link/Collateral/MMBF2201NT1-D.pdf`.

[27] N. E. W. Technology, "New `England` wire technologies - litz wire- technical.pdf," `http://www.newenglandwire.com/litz.asp`.

CHAPTER 3

MULTI-COIL FOR HIGH TOLERANCE WIRELESS POWER

3.1 Abstract

Inductive coupling based wireless power transfer (WPT) is commonly used for near field power and data transfer to implanted electronics. Some implanted coils undergo relative motion during device operation causing variation in magnetic coupling from their normal position. To ensure stable power transfer efficiency and frequency bandwidth, these WPT systems should have high tolerance with coupling variation and operation mode. In this work, a multi-coil based WPT system is utilized to achieve high tolerance for system power transfer efficiency and data bandwidth. It is demonstrated that for the coupling variation, a multi-coil WPT system can reduce variation by half in power transfer efficiency (PTE) and by one third in frequency bandwidth compared to a two-coil WPT system with the same dimensions and operating conditions. Moreover, power transfer efficiency of the multi-coil WPT system shows lower variation with the variation of driver (source) and load (implant) impedance.

3.2 Introduction

Wireless power transfer (WPT) is currently used as a mechanism to transfer power to implanted electronics, such as implanted sensors and neuro-stimulators. Traditional WPT systems utilize two-coil based systems in which power and data are transferred from the external coil to the implant coil based on magnetic induction. Figure 3.1(a) shows the block diagram of a typical two-coil WPT system indicating the magnetic coupling k between the coils. Performance (Power Transfer Efficiency, voltage gain, and bandwidth) of the telemetry systems is strongly dependent on the coupling between external and implant coils. Thus, with the relative motion of the implant (or external) coil with respect to its normal position, Power Transfer Efficiency (PTE), voltage gain and frequency bandwidth can be greatly affected [1]. An example of this situation is encountered in wirelessly powered retinal implants [2]. The movement and rotation of the eye causes the primary and secondary coils to be nonparallel and offset with respect to each other. To insure continuous powering and data transmission despite these natural movements of the eye of the blind patient, the telemetry link must retain its performance characteristics over a relatively broad rotation angle and offset [2] and should achieve a high tolerance in PTE and frequency bandwidth with the coupling variation during the operation of the system. Moreover, to improve the lifetime of a body-worn battery to power an implant wirelessly, biomedical implants have multiple power-saving modes. With the variation of required power for different power modes, the effective load resistance (R_L) varies causing variation in power transfer efficiency. Because efficiency is a strong function of driver resistance, the WPT system must also be more tolerable of driver (power amplifier) output resistance (R_d).

Recently, a multi-coil based WPT system was proposed to achieve higher efficiency and improved frequency bandwidth as compared to a two-coil WPT system with the same dimensions [3]. Figure 3.1(c) and (e) show block diagrams of multi-coil WPT systems with a three-coil and four-coil configuration, respectively [3]. In this work, a multi-coil based WPT approach is used to improve the tolerance in power transfer efficiency and link bandwidth of the WPT system without reducing the tolerance of voltage gain. A detailed analysis of the tolerance for the two-coil system and multi-coil system is presented, demonstrating that a multi-coil system can achieve a higher tolerance in efficiency and bandwidth. Similarly, tolerance analysis of a two-coil WPT system is done with the variation of driver and load resistance. To improve the tolerance and make the design more robust, a multi-coil WPT design approach is proposed. With the use of intermediate self-resonating passive coils, the multi-coil WPT system can reduce the dependence of R_d and R_L on the power transfer efficiency of the system. To the best of author's knowledge, such a study has not been done before.

3.3 Tolerance Analysis in Telemetry System with Coupling Variation

During device operation, the distance between external and implanted coils can vary from its nominal values and cause decay in the coupling between the coils. Therefore, the wireless power

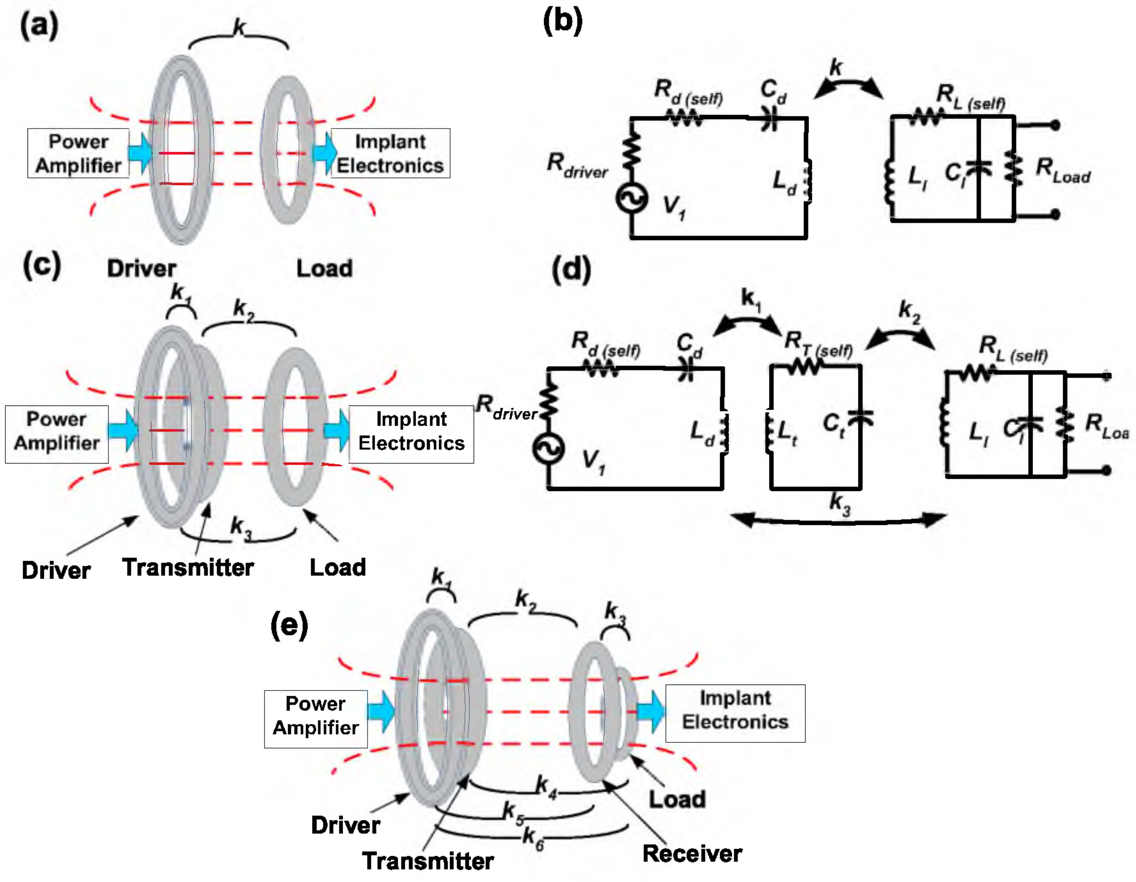

Figure 3.1. Block diagram of (a) two-coil and multi-coil ((c) three-coil (e) four-coil) wireless power transfer system. Electrical model of a (b) two-coil and (d) three-coil telemetry system

link should have high tolerance with the change in coupling k (or k_2 (Figure 3.1(c) and (e)). At any orientation (respective coupling k), the parametric tolerance of the telemetry system can be calculated by $\frac{1}{P}\frac{\partial P}{\partial k}$ where P is the considered performance parameter. In the following section, tolerance is formulated for key performance parameters of a telemetry systems including PTE, voltage gain and frequency bandwidth. To demonstrate the difference in a practical telemetry system, such as that in a dual unit artificial retina system, the theoretical analysis is applied to a sample two-coil and three-coil telemetry link (Table 3.1).

Table 3.1. System Specifications

Coils	Two-coil System	Three-coil System
Driver Coil		
$D_{outD}(cm)$	3.6	3.6
N_D	12	2
$L_d(\mu H)$	5.23	0.354
$C_d(nF)$	0.424	6.98
$R_{dl}(\Omega)$	0.72	0.21
$R_{driver}(\Omega)$	4.7	4.6
$Q_{d(unloaded)}$	154	35.86
$Q_{d(loaded)}$	20.13	1.56
Transmitter Coil		
$D_{outT}(cm)$		3.2
N_T		10
$L_t(\mu H)$		3.18
$C_t(nF)$		0.702
$R_t(\Omega)$		0.621
$Q_{unloaded}$		108.4
$Q_{t(loaded)}$		108.4
Load Coil		
$D_{outL}(cm)$	1.5	1.5
N_L	8	8
$L_l(\mu H)$	0.6	0.6
$C_l(nF)$	3.61	3.61
$R_{cl}(\Omega)$	0.09	0.09
$Q_{l(unloaded)}$	141	141
$Q_{l(loaded)}$	8.15	8.15
$R_{Load}(\Omega)$	110	110
Wire (AWG)	Litz 100/44	Litz 100/44
d (mm) ($\phi = 0$)	10	10
k_1 (or k) ($\phi = 0$)	0.10	0.5
k_2 ($\phi = 0$)		0.10
k_3 ($\phi = 0$)		0.096
f_{res} (MHz)	3.37	3.37

3.3.1 Power Transfer Efficiency with Variation in Coupling

In our previous work [3, 4], resonating coils were used for efficient power transfer between external and implanted coils. To improve the power transfer efficiency, the Q-factor of the coils should to be maximized [3]. To formulate the variation in power transfer efficiency with respect to coupling k (or k_2) variation, efficiency tolerance for a two-coil, three-coil, and four-coil system is given by Equations 3.2, 3.4 and 3.6, respectively. Due to the high quality factors of the transmitter and receiver coils, the multi-coil system efficiency η has a lower rate of change compared to the two-coil equivalent. Using expression for the efficiency η found in [3], for a two-coil WPT system we have:

$$\eta = \frac{k^2 Q_d Q_l}{1+k^2 Q_d Q_l} \tag{3.1}$$

$$\frac{1}{\eta}\frac{\partial \eta}{\partial k} \simeq \frac{2}{k(1+k^2 Q_d Q_l)} . \tag{3.2}$$

For a three-coil WPT system, we have instead:

$$\eta \simeq \frac{k_1^2 Q_d Q_t}{1+k_1^2 Q_d Q_t}\frac{k_2^2 Q_t Q_l}{1+k_2^2 Q_t Q_l} \tag{3.3}$$

$$\frac{1}{\eta}\frac{\partial \eta}{\partial k_2} \simeq \frac{2}{k_2(1+k_2^2 Q_t Q_l)} , \tag{3.4}$$

while for a four-coil WPT system, we can write:

$$\eta \simeq \frac{k_1^2 Q_d Q_t}{1+k_1^2 Q_d Q_t}\frac{k_2^2 Q_t Q_r}{1+k_2^2 Q_t Q_r}\frac{k_3^2 Q_r Q_l}{1+k_3^2 Q_r Q_l} \tag{3.5}$$

$$\frac{1}{\eta}\frac{\partial \eta}{\partial k_2} \simeq \frac{2}{k_2(1+k_2^2 Q_t Q_r)} \tag{3.6}$$

Figure 3.2 (a) shows the simulated change in efficiency η (normalized for k(or k_2) = 0.1) with variation in coupling between the external and implant coils for coil parameters given in Table 3.1, which can be used for retinal implant systems. For the nominal operating range ($k \subseteq [0.03, 0.1]$), the three-coil based system has lower variation in efficiency.

3.3.2 Voltage Gain with Variation in Coupling

For wireless power transfer, voltage gain is an important design parameter when considering what voltage level is sufficient for operating the implanted device reliably. Voltage gain (V_{out}/V_{in}) is a function of coupling and coil quality factors. Equations 3.7, 3.9 and 3.11 give the voltage gain of two-coil, three-coil and four-coil based systems, respectively [3].

To ensure reliable device operation, the rate of change of voltage at the implant's terminal should be small with coupling variation. Equations 3.8, 3.10 and 3.12 provide the voltage gain variation

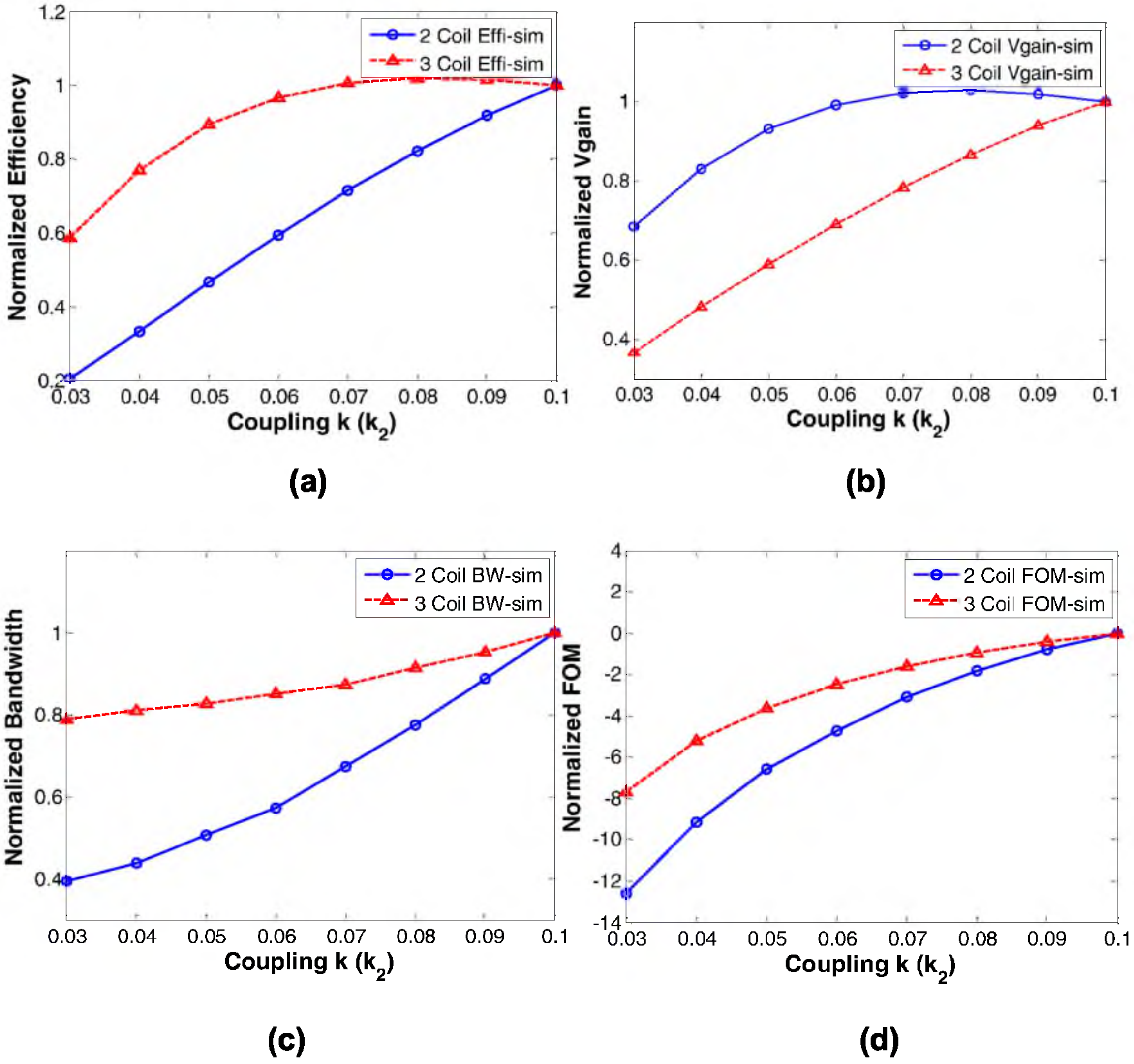

Figure 3.2. Simulated (a) efficiency (b) voltage gain (c) bandwidth and (d) FOM of the two-coil and its three-coil equivalent system normalized for coupling k(or k_2) = 0.1 for the design example (Table 3.1). Efficiency tolerance can be calculated from the slope of the curve.

for the two-coil, three-coil and four-coil WPT systems, respectively. For a two-coil WPT system, we have:

$$G_2 = j\sqrt{\frac{R_L}{R_d}}\frac{k\sqrt{Q_dQ_l}}{1+k^2Q_dQ_l} \tag{3.7}$$

$$\frac{\partial G}{\partial k} = j\sqrt{\frac{R_L}{R_d}}\sqrt{Q_dQ_l}\frac{1-k^2Q_dQ_l}{(1+k^2Q_dQ_l)^2} \tag{3.8}$$

For the three-coil WPT system, we have:

$$G_3 \sim -\sqrt{\frac{R_L}{R_d}}k_2\sqrt{Q_tQ_l}\frac{1}{k_1\sqrt{Q_dQ_t}} \tag{3.9}$$

$$\frac{\partial G}{\partial k_2} \sim -\frac{1}{k_1\sqrt{Q_dQ_t}}\sqrt{\frac{R_L}{R_d}}\sqrt{Q_tQ_l} \tag{3.10}$$

and for the four-coil WPT system, we have instead

$$G_4 \sim -j\sqrt{\frac{R_L}{R_d}}k_2\sqrt{Q_tQ_l}\frac{1}{k_1\sqrt{Q_dQ_t}}\frac{1}{k_3\sqrt{Q_rQ_l}} \tag{3.11}$$

$$\frac{\partial G}{\partial k_2} \sim -j\frac{1}{k_1\sqrt{Q_dQ_t}}\frac{1}{k_3\sqrt{Q_rQ_l}}\sqrt{\frac{R_L}{R_d}}\sqrt{Q_tQ_r} \tag{3.12}$$

For moderate coupling in a two-coil WPT system ($k^2Q_dQ_l \ll 1$), Equations 3.8, 3.10 and 3.12 can be simplified to

$$\frac{1}{G_n}\frac{\partial G}{\partial k_2} \simeq \frac{1}{k_2}; n \in \{2,3,4\} \tag{3.13}$$

Figure 3.2(b) shows that, for the presented two-coil design, voltage gain variation is minimal while operating the system close to the critical coupling ($k \sim 0.071$). However for large distance between the external and implant coil (coupling $k \leq 0.055$), the two-coil and three-coil WPT systems show a similar rate of change in voltage gain with coupling variation, which is expected from Equation 3.13.

3.3.3 Frequency Bandwidth with Variation in Coupling

In telemetry applications [5], moderate data bandwidth is essential for sending/controlling vital sign signals to/from the implanted device. Multi-coil systems use high coupling between the driver and transmitter coils (k_1) (and/or receiver to load coil (k_3)) to improve the data bandwidth compared to a two-coil equivalent system for a given operating distance. Bandwidth increases with the increase in coupling k_1 [3].

For telemetry applications, to keep sufficient data bandwidth with coupling variation, bandwidth should be independent of coupling k (or k_2). In a multi-coil system, due to high coupling between the driver and the transmitter coils (or between the receiver and the load coil), the bandwidth is dominated by k_1 (or k_3). With change in the coupling k (or k_2), a multi-coil system shows small variation in bandwidth. Figure 3.2 (c) shows the bandwidth variation (normalized for k (or k_2) = 0.1) for the three-coil and two-coil system, which depicts that the three-coil system's bandwidth remains almost constant with the change in coupling between external and implanted coils.

To compare different WPT systems, a figure of merit (FOM) was proposed to include PTE, voltage gain, frequency bandwidth, system dimensions and operating conditions as shown in Equation 3.14 [3]. Figure 3.2 (d) shows that, for all coupling values, the multi-coil WPT system has lower variation in FOM than the two-coil WPT system with the same dimensions.

$$FOM = 10Log_{10}\left[\frac{d^2}{D_1 \times D_2}\frac{BW}{f_{res}} \times \eta \times Gain\right] \tag{3.14}$$

where d is the operating distance of telemetry system, with D_1 and D_2 as the diameter of the external and the implant coils respectively. BW denotes the 3-dB frequency bandwidth at resonant frequency f_{res}.

3.3.4 Design Example

As mentioned in the previous section, to demonstrate the system's performance variation during the operation of the device, a retinal implant is considered. In this, the implant coil rotates with the movement of eye [1]. To minimize changes of the existing retinal implants, which are currently using two-coil systems, and to incorporate the multi-coil WPT design, its multi-coil equivalent must share the same implant coil specifications (Figure 3.1(b)). For fair comparison, three-coil and two-coil WPT systems share the same overall external coil's dimensions. The following section provides the experimental setup and experimental results of the two-coil and three-coil WPT systems.

3.3.4.1 Experimental Setup

To compare the system tolerance improvement due to a multi-coil based approach, a typical implant coil size of $\sim$ 1.5 cm is chosen. Figure 3.3(a) shows the block diagram and 3.3(d) actual image of the experimental setup. Figures 3.3(b) and (c) show the image of hand wound coils used for two-coil and three-coil telemetry systems. To mimic the rotation of the eye, the implant coil is mounted on a sphere of diameter 36 mm. The eye model is rotated along its axis from -30^o to 30^o in steps of 5^o. Due to symmetry of the implant and the external coil along its center axis, the vertical motion of the eye does not vary the coupling between external and implant coils, thus it is not considered in current setup. Under normal operating conditions, the implant and external coils are coaxial and are at the operating distance d of 10 mm. Eye rotation causes the implant and external coils to be misaligned, resulting in lower coupling than under the normal operating conditions. Figure 3.1(b), (d) shows the electrical model of the two-coil and three-coil WPT systems.

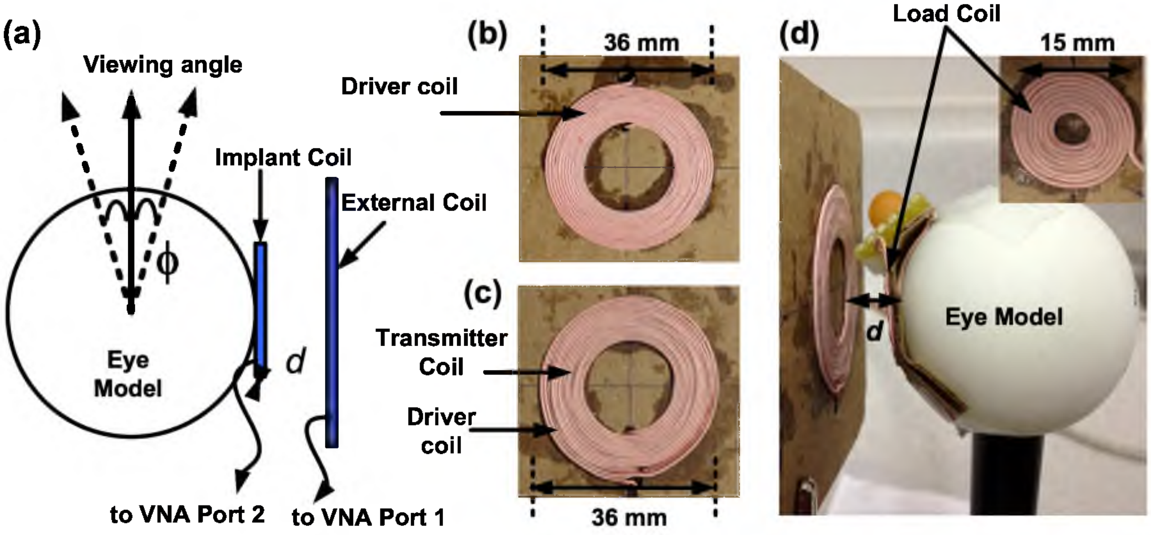

Figure 3.3. Experimental setup. (a) Eye model for WPT performance's variation in two-coil and three-coil system. Electrical model of the (b) two-coil and (c) three-coil WPT systems are based on the design example(Table 3.1)

To measure the efficiency, voltage gain and bandwidth, a two-port impedance model of the WPT system is incorporated based on [3]. A VNA is used to measure the efficiency and voltage gain as a function of frequency [3]. A resistance of $\sim 4.7\Omega$ is used in series with the driver coil to emulate the typical source resistance([3, 6]) of the power amplifier.

Table 3.1 provides the electrical and mechanical parameters for the two-coil WPT system and its three-coil equivalent. Total dimensions of the external coils of the three-coil system are the same as the two-coil system's external coil. However, the transmitter coil of the three-coil design can achieve much higher loaded Q factor of $Q_t \sim 108$ due to source resistance decoupling, compared to $Q_d \sim 20$ for the two-coil equivalent.

3.3.4.2 Experimental Results

To compare the performance of the power transfer system with change in coil misalignment between the external and the implanted coil, Figure 3.4 shows the experimental results for efficiency, voltage gain, frequency bandwidth and FOM variation with respect to coil rotation angle.

To compare the two-coil and three-coil WPT system performance variation on the same scale, Figure 3.5 shows the normalized efficiency, voltage gain, bandwidth and FOM of the three-coil and two-coil system. For the three-coil WPT system, due to the high Q factor of the transmitter coil (Q_t), the effect of coupling variation on PTE is compensated by Q_t. It shows that with respect to the reference position ($\phi = 0^o$), variation in the three-coil system's efficiency is much smaller than the

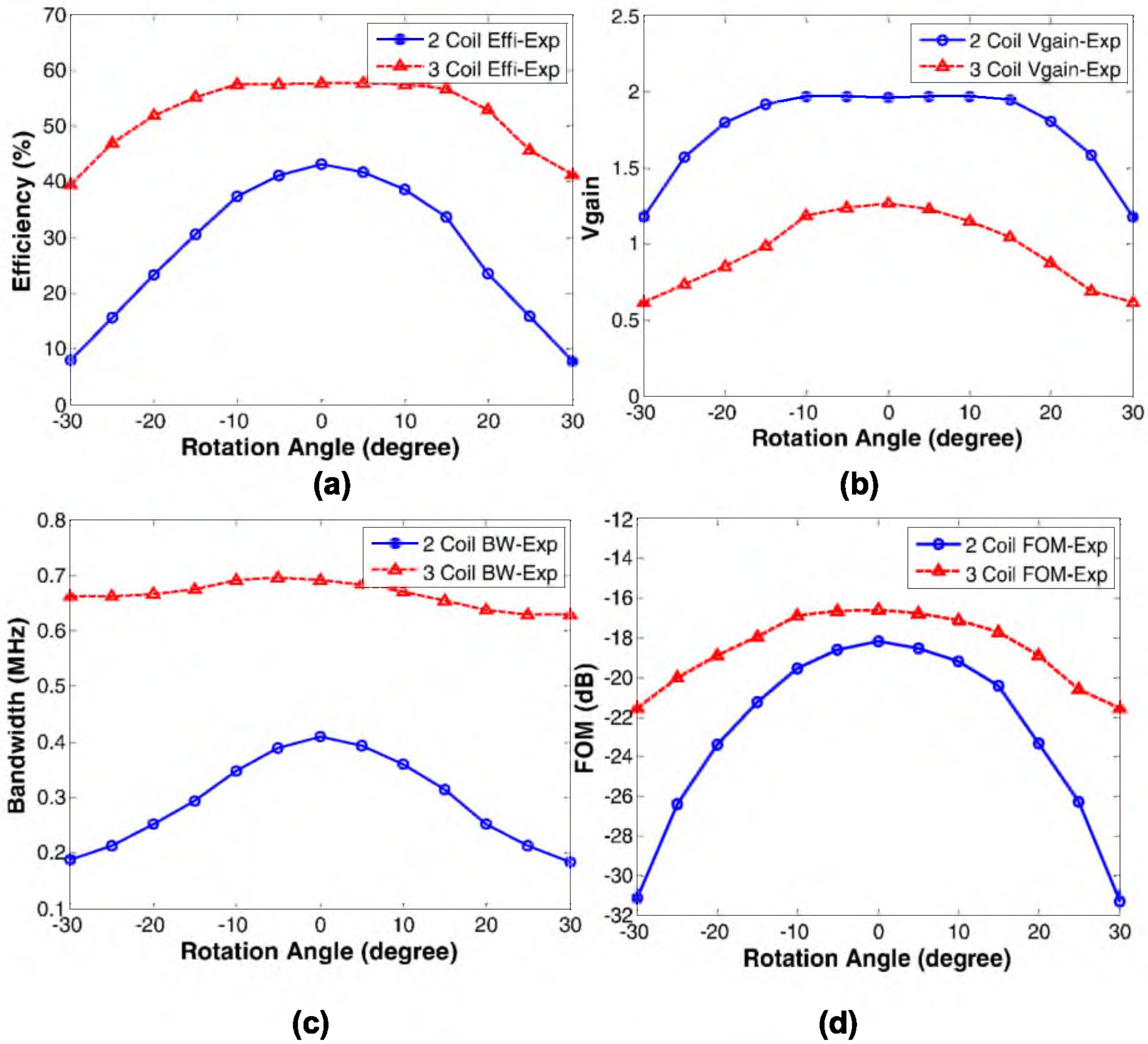

Figure 3.4. Measured (a) efficiency (b) voltage gain (c) bandwidth and (d) FOM of the two-coil and its three-coil equivalent system for eye rotation from -30^o to 30^o in step of 5^o (design example, Table 3.1)

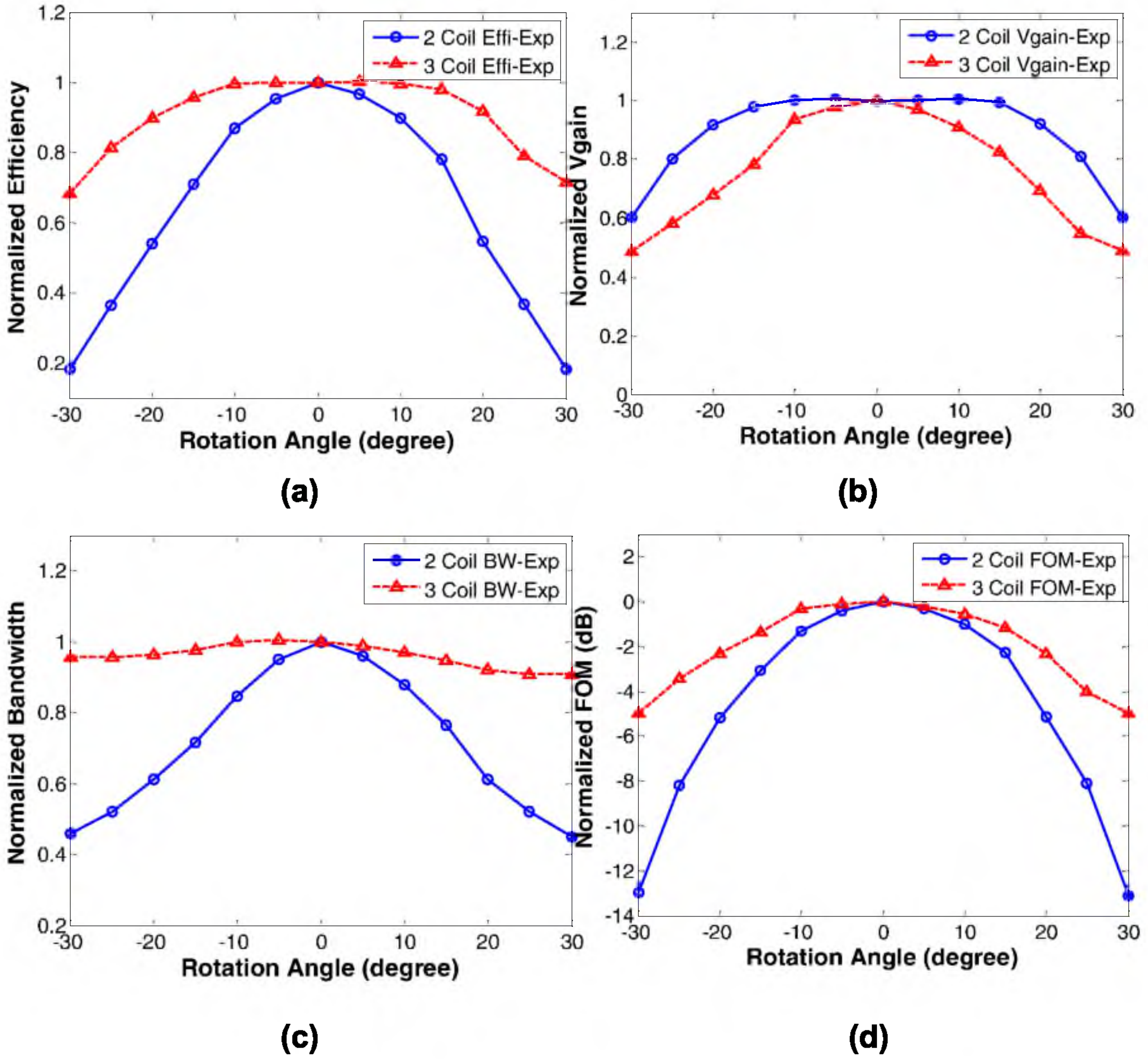

(a)

(b)

(c)

(d)

Figure 3.5. Measured (a) efficiency (b) voltage gain (c) bandwidth and (d) FOM of the two-coil and its three-coil equivalent system normalized with respect to 0^o eye position for the design example (Table 3.1). For normalized parametric value P, tolerance for angle $\phi = 0$ can be calculated using $\frac{P_0 - P_\phi}{\phi}$.

two-coil equivalent (Figure 3.5 (a)).

In the presented design example, normal operating condition ($\phi = 0^o$) is close to the critical coupling condition ($k^2 Q_d Q_l = 1$). Due to critical coupling near $k \sim 0.71$ the voltage gain variation of the two-coil is smaller. However, for higher misalignment $|\phi| > 20^o$, rate of change in the two-coil's voltage gain is similar to the rate for the three-coil system (Figure 3.5 (b)).

Multi-coil utilizes high coupling between driver and transmitter coils ($k_1 \sim 0.5$) to improve the frequency bandwidth of the system which is unaffected from the eyeball rotation. Figure 3.5 (c) shows that due to k_1 being a key parameter in controlling the bandwidth in the three-coil system, frequency bandwidth of the three-coil system is almost constant with the misalignment of the external and implant coils.

3.4 Tolerance Analysis with Source and Load Variation

The efficiency of a WPT system depends on the driver resistance and the effective resistance of the implant. In different operation modes of implant electronics, the effective load resistance varies causing significant variation in efficiency. In the following sections, a multi-coil based WPT system is proposed to improve the tolerance of the power transfer efficiency due to the variation in source and implant resistance. For the same physical dimensions, the multi-coil system shows twice the better efficiency tolerance compared to a traditional two-coil based WPT system.

3.4.1 Efficiency with Respect to Source Resistance

Driver resistance of a WPT system depends on the ON-resistance of the switching transistor and the residual resistance of the parasitic components. It is desirable to use WPT systems seamlessly with a variety of different amplifiers. Thus, it is important to improve the tolerance of power transfer efficiency with respect to the different driver resistance. Equation 3.15, 3.16, and 3.17 show the analytical formulation for the rate of change in efficiency $\frac{\partial\eta}{\partial R_1}$ with driver resistance and tolerance of efficiency $\frac{1}{\eta}\frac{\partial\eta}{\partial R_1}$. For a multi-coil design (three-coil/ four-coil), the effect of the high-Q factor transmitter coil ($\sim$150) is in the denominator of these formulations which reduces the value of $\frac{\partial\eta}{\partial R_1}$ and $\frac{1}{\eta}\frac{\partial\eta}{\partial R_1}$ significantly as compared to two-coil design.

$$\frac{\partial\eta}{\partial R_1} = \frac{\partial\eta}{\partial Q_1}\frac{\partial Q_1}{\partial R_1} = -\frac{Q_1}{R_1}$$

For two-coil WPT system,

$$\begin{aligned}\frac{\partial\eta}{\partial R_1} &= -\frac{1}{R_1}\frac{k^2Q_dQ_l}{(1+k^2Q_dQ_l)^2}\\ \frac{1}{\eta}\frac{\partial\eta}{\partial R_1} &= -\frac{1}{R_1}\frac{1}{1+k^2Q_dQ_l}\end{aligned} \tag{3.15}$$

For three-coil WPT system,

$$\begin{aligned}\frac{\partial\eta}{\partial R_1} &= -\frac{1}{R_1}\eta_{23}\frac{\partial\eta_{12}}{\partial R_1}\\ \frac{1}{\eta}\frac{\partial\eta}{\partial R_1} &= -\frac{1}{R_1}\frac{1}{1+k_1^2Q_dQ_t}\end{aligned} \tag{3.16}$$

For four-coil WPT system,

$$\begin{aligned}\frac{\partial\eta}{\partial R_1} &= -\frac{1}{R_1}\eta_{23}\eta_{34}\frac{\partial\eta_{12}}{\partial R_1}\\ \frac{1}{\eta}\frac{\partial\eta}{\partial R_1} &= -\frac{1}{R_1}\frac{1}{1+k_1^2Q_dQ_t}\end{aligned} \tag{3.17}$$

3.4.2 Efficiency with Respect to Load Resistance

In general, implant electronics is parallel configuration with the load coil [4]. With the variation in different power-saving modes in a biomedical implant, the Q-factor of the load coil (Q_l) varies significantly and causes variation in the WPT systems power transfer efficiency. Analytical formulation for the rate of change $\frac{\partial\eta}{\partial R_2}$ and tolerance $\frac{1}{\eta}\frac{\partial\eta}{\partial R_2}$ with respect to change in load resistance is done for the two-coil and multi-coil designs. Due to the large Q-factor transmitter coil Q_t (three-coil system) and receiver coil Q_r (four-coil system), the tolerance of efficiency can be reduced (Equation 3.18, 3.19, and 3.20).

For two-coil WPT system,

$$\begin{aligned}\frac{\partial\eta}{\partial R_2} &= -\frac{1}{R_1}\frac{k^2Q_dQ_l}{(1+k^2Q_dQ_l)^2}\\ \frac{1}{\eta}\frac{\partial\eta}{\partial R_2} &= -\frac{1}{R_2}\frac{1}{1+k^2Q_dQ_l}\end{aligned} \tag{3.18}$$

For three-coil WPT system,

$$\frac{1}{\eta}\frac{\partial\eta}{\partial R_3} = -\frac{1}{R_3}\frac{1}{1+k_2^2Q_tQ_l} \tag{3.19}$$

For four-coil WPT system,

$$\frac{1}{\eta}\frac{\partial\eta}{\partial R_4} = -\frac{1}{R_4}\frac{1}{1+k_3^2Q_rQ_l} \tag{3.20}$$

3.4.3 Design Example

To demonstrate an improvement in efficiency tolerance using the multi-coil approach, a three-coil WPT system and its equal sized two-coil WPT system are designed. Table 3.2 provides the key parameters of both systems. The implant coil remains the same for both the designs. For the same system dimensions and driver resistance of 5.1 Ω, the three-coil system achieves much higher Q_t of 174 at 2.8 MHz operating frequency as compared to Q_d of 15.9 for the two-coil design.

Figure 3.6 shows the variation of power transfer efficiency for the two-coil and three-coil WPT systems with change in driver resistance. As expected, the three-coil design's efficiency has a slower rate of change (0.64 % per ohm) than its two-coil equivalent (1.47 % per ohm). Similarly, with the load resistance varying from 300 -1000 Ω the three-coil system shows stable power transfer

Table 3.2. Design Specifications

	D_{ext} (cm)	D_{imp} (cm)	L_d (μH)	L_t (μH)	L_l (μH)	Q_d	Q_t	Q_t $(R_L = 650\Omega)$	k_1	$k(k_2)$
two-coil	4.0	1.5	5.06	-	6	15.9	-	5.24	-	0.074
three-coil	4.0	1.5	0.39	3.96	6	15.9	-	5.24	-	0.065

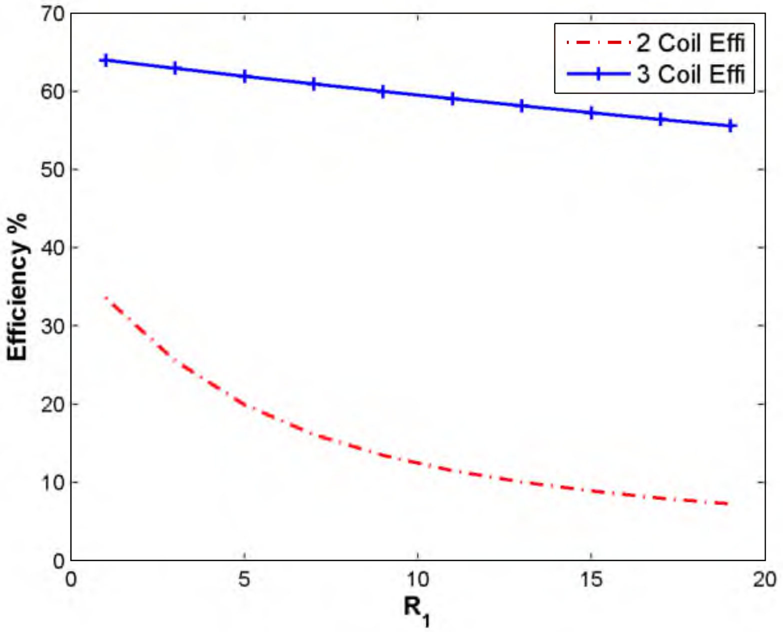

Figure 3.6. Variation of power transfer efficiency with variation in source resistance (@ R_L = 650 Ω) based on Table 3.2.

efficiency (variation 0.009% per ohm) as shown in Figure 3.7 which is desirable to ensure an efficient wireless power link for different operating modes of implanted electronics.

3.5 Conclusion

In this work, it is shown that a multi-coil WPT system can achieve high tolerance for the variation in magnetic coupling between an external and implant coil during WPT system operation. For the presented design example, with the same system dimensions and operating conditions, a three-coil system achieves more than 40 % improvement in efficiency and 62.5 % improvement in frequency bandwidth as compare to a two-coil WPT system. Due to the high Q-factor of the transmitter coil (Q_t) three-coil systems showed lower variation (average -0.6 % per degree rotation) in efficiency with eye model rotation. Similarly, the three-coil design achieved a higher tolerance (average 2.2 khz per degree rotation) for frequency bandwidth as compared to variation of 7.5 khz per degree (averaged) rotation in the two-coil equivalent. However, variation in voltage gain of the two-coil (average -0.0264 per degree) and the three-coil (average -0.0217 per degree) WPT system are similar.

Moreover, a multi-coil based WPT system is proposed to improve the efficiency tolerance for the variation in driver and load resistance. It is demonstrated that due to the high Q-factor transmitter coil in the three-coil system, variation in driver and load resistance causes lesser variation

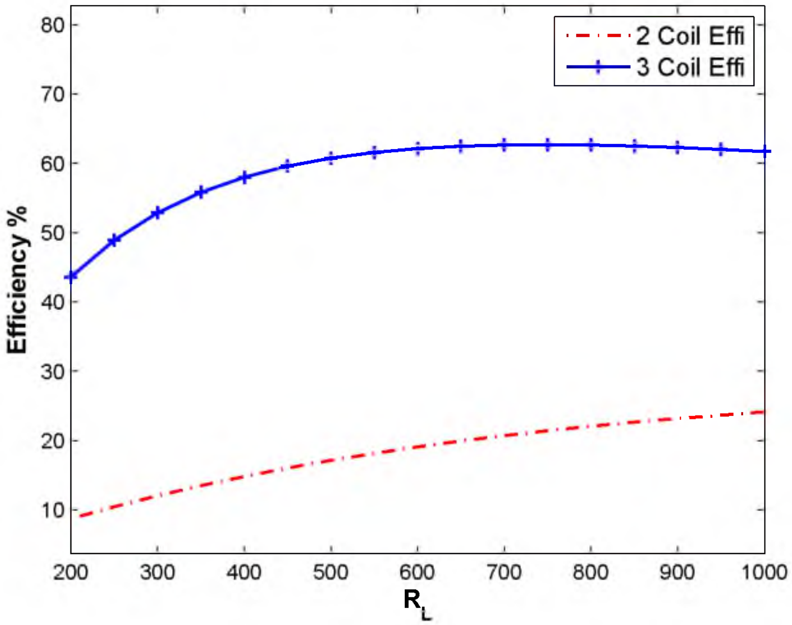

Figure 3.7. Variation of power transfer efficiency with variation in load resistance (R_d = 5.1 Ω) based on Table 3.2.

in efficiency. Simulation of the presented two-coil and three-coil systems showed that the three-coil system efficiency has less than half of the variation of the two-coil design.

3.6 References

[1] K. Chen, Z. Yang, L. Hoang, J. Weiland, M. Humayun, and W. Liu, “An integrated 256-channel epiretinal prosthesis,” *IEEE Journal of Solid-State Circuits*, vol. 45, no. 9, pp. 1946 –1956, Sept. 2010.

[2] D. Yanai, J. D. Weiland, M. Mahadevappa, R. J. Greenberg, I. Fine, and M. S. Humayun, “Visual performance using a retinal prosthesis in three subjects with retinitis pigmentosa,” *American Journal of Ophthalmology*, vol. 143, no. 5, pp. 820 – 827, 2007.

[3] A. K. RamRakhyani and G. Lazzi, “On the design of efficient multi-coil telemetry system for biomedical implants,” *IEEE Transactions on Biomedical Circuits and Systems*, vol. 7, no. 1, pp. 11–23, Feb. 2013.

[4] A. K. RamRakhyani, S. Mirabbasi, and M. Chiao, “Design and optimization of resonance-based efficient wireless power delivery systems for biomedical implants,” *IEEE Transactions on Biomedical Circuits and Systems*, vol. 5, no. 1, pp. 48 –63, 2011.

[5] G. Wang, W. Liu, M. Sivaprakasam, M. Zhou, J. D. Weiland, and M. S. Humayun, “A dual band wireless power and data telemetry for retinal prosthesis,” in *Conf. Proc. IEEE EMBS*, Aug. 30-Sept.3 2006, pp. 28–38.

[6] R. Harrison, “Designing efficient inductive power links for implantable devices,” in *Proc. ISCAS*, 2007, pp. 2080–2083.

CHAPTER 4

MULTI-COIL APPROACH TO REDUCE ELECTROMAGNETIC ENERGY ABSORPTION FOR WIRELESSLY POWERED IMPLANTS

© 2014 IET. Reprinted, with permission, from: Anil Kumar RamRakhyani, Gianluca Lazzi, "Multi-Coil Approach to Reduce Electromagnetic Energy Absorption for Wireless Powered Implants," in IET Healthcare Technology Letters, vol.1, no.1, pp.21-25, March 2014.

4.1 Abstract

Near-field inductive coupling is a commonly used technique for wireless power transfer (WPT) in biomedical implants. Due to the close proximity of the implant coil(s) with the tissue ($\sim$ 1 mm) and high current ($\sim$ 100-300 mA) in the magnetic coil(s), a significant induced electric field can be generated for the operating frequency (1-20 MHz). In this work, a multi-coil based WPT technique is proposed to selectively control the currents in the external and implant coils to reduce the Specific Absorption Rate (SAR). A three-coil WPT system that can achieve 26% reduction in peak 1-gram SAR and 15 % reduction in peak 10-gram SAR, as compared to a two-coil WPT system with the same dimensions, is implemented and used to demonstrate the effectiveness of the proposed approach. To achieve the seamless design for the external and implant electronics, the multi-coil system achieves the same voltage gain and bandwidth as the two-coil design with 46 % improvement in the power transfer efficiency (PTE).

4.2 Introduction

Wireless power transfer (WPT) has proven to be a viable and necessary technology to power implantable electronics [1–3]. To accommodate the advances in prostheic systems [2, 3], the power requirement of the implanted device can vary hundreds of milli-watts [2–5]. To ease the mobility of the patient, most of these devices use body-worn batteries as a power source. This requires an efficient wireless powered system to improve the battery life. Traditionally, a two-coil based inductive link is commonly used to design a wireless power system [2, 4, 5] . Such systems require a power amplifier to drive a resonating driver (external) coil and cause a time-varying magnetic field. The load (implant) coil is connected to the implant electronics. The power transfer efficiency (PTE) of the two-coil based WPT depends on the magnetic coupling and loaded Q-(quality) factor of the magnetic coils.

For many prosthesis devices such as an epiretinal prosthesis [4, 5], the driver coil (3-5 cm) is much larger than the implant coil (0.5-2 cm) to achieve sufficient magnetic coupling over a long operating distance (0.5-1.8 cm) between the coils. Moreover, the driver and implant coils are in close proximity to the tissue, which can cause a significant induced electric field and eddy currents in tissues. The induced electric field is directly proportional to the currents in the magnetic coils. Thus, to design a safe electromagnetic WPT system, currents in the magnetic coils may need to be reduced. Traditionally, a two-coil WPT system provides only few parameters (Q-factors and coupling k, Figure 4.1) to tune the currents in the magnetic coils, which need to be optimized to achieve sufficient PTE (>30 %) under design constraints and operating conditions [4, 5].

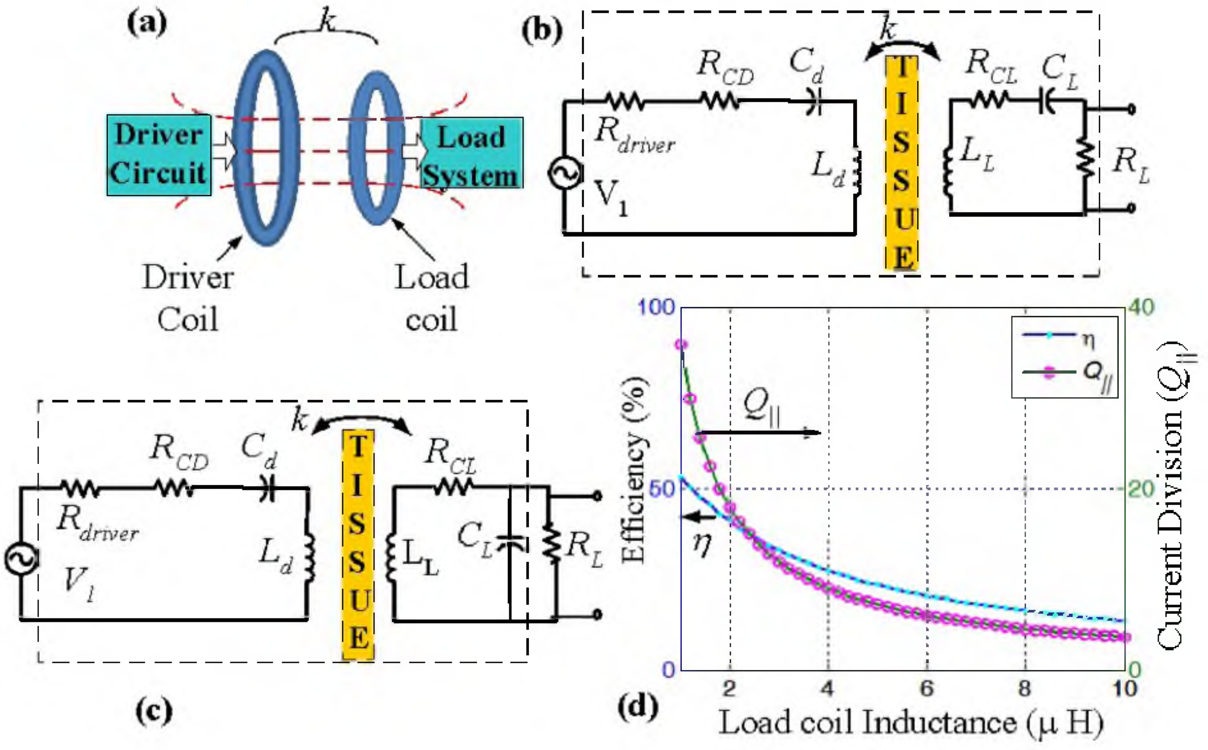

Figure 4.1. Two-coil WPT system. (a) Magnetically coupled two-coil WPT system with coupling k (b) Schematic of the WPT system with load coil (L_L) in series with load resistance R_L (c) Schematic of the WPT system with load coil (L_L) in parallel with load resistance R_L. (d) Effect of load coil inductance L_L on the efficiency η and $Q_{||}$ of the two-coil WPT system (Table 4.1).

Recently, a multi-coil based wireless powered system was proposed to achieve high wireless power transfer efficiency between external and implant electronics [6, 7]. The multi-coil WPT system can achieve more than twice the power transfer efficiency as compared to the two-coil design under the same size restrictions and operating conditions [7]. Multi-coil WPT systems utilize intermediate coils to improve the PTE and result in a high number of design parameters (k_{1-3}, Q_d, Q_t, Q_l, Figure 4.2) that can be used to control the current in each magnetic coil. In this work, a multi-coil based WPT system is demonstrated to achieve the same system performance (voltage gain and bandwidth) as a two-coil WPT design under the same size restrictions and operating conditions. It is shown that without any change in the driver or implant electronics, this new multi-coil WPT system can replace the traditional two-coil system requiring the same dimensions. The current in each coil can be selectively tuned to reduce the induced electric field in tissue. Formulation and demonstration of a multi-coil WPT system, which can reduce the specific absorption rate (SAR) in telemetry systems, are the main contributions of this work.

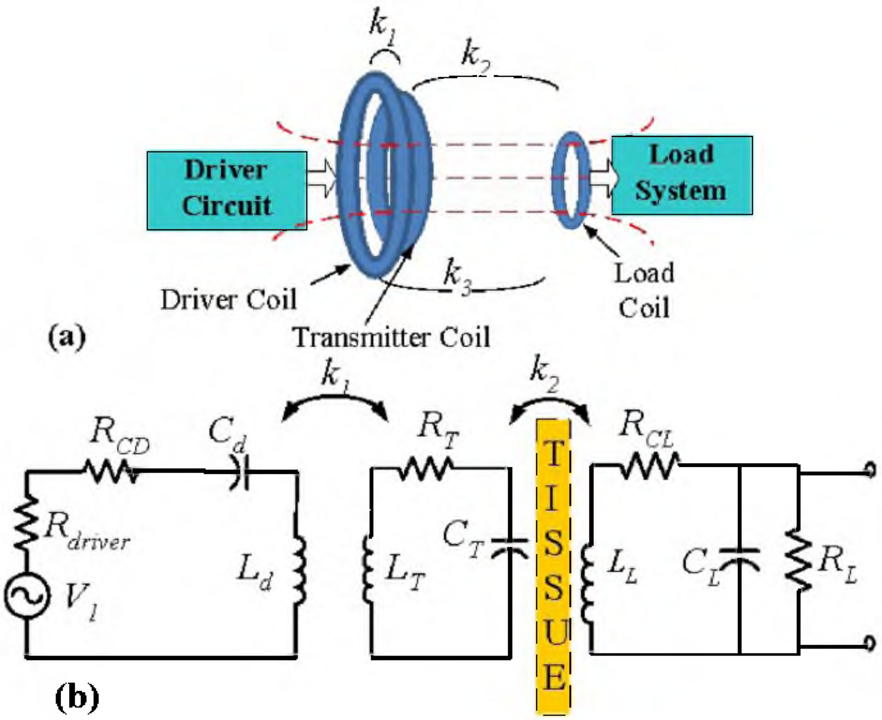

Figure 4.2. Three-coil WPT system. (a) Block diagram and (b) schematics of the three-coil (multi-coil) based WPT system showing the coupling k_{1-3} between each coil.

4.3 Safety Aspects

Specific absorption rate (SAR) is a standard quantity used to provide a measure of the electromagnetic energy deposited in the conductive tissue (Equation 4.1). Absorbed energy can be a key contributor of thermal [8] or nonthermal effect [9] in tissue. At low frequencies, induced electric field is linearly proportional to the current in the magnetic coil [8].

$$SAR = \frac{\sigma(r)|E_{rms}(r)|^2}{\rho(r)} \tag{4.1}$$

where, at location r, $\sigma(r)$ is the tissue electrical conductivity of the tissue, $E_{rms}(r)$ is the RMS peak induced electric field, and $\rho(r)$ is the tissue density in Kg/m^3.

SAR increases with the conductivity of the tissue and current in the magnetic coils. Therefore, current of the coil near high conductivity tissue needs to be minimized to keep the absorbed power in tissue well within the safety standards. In the following sections, an analytical formulation is presented to identify the key parameters that can be utilized to tune the current in the individual coils for the traditional two-coil WPT system and multi-coil systems.

4.4 Currents in the Two-coil WPT System

Two-coil wireless power transfer system is a traditional technique for transferring energy from the external source to the implant coil. Figure 4.1(a) shows the basic block diagram of this system. Current in the driver coil (Equation 4.2) and load coil (Equation 4.3) can be calculated based on the coupling k, resistance $R_d = R_{driver} + R_{CD}$, (where R_{CD} is self resistance of the driver coil), and Q-factors Q_d (driver coil) and Q_l (load coil). R_d and R_l are the effective series resistances connected to the driver and load coils, respectively.

$$I_d = \frac{1}{R_d(1+k^2Q_dQ_l)}V_1 \tag{4.2}$$

$$I_l = -j\frac{k\sqrt{Q_dQ_l}}{\sqrt{R_dR_l}(1+k^2Q_dQ_l)}V_1 \tag{4.3}$$

The load resistance R_L depends on the current and the voltage requirements of the implant electronics. Depending on the value of R_L and load inductance L_L, there are two popular topologies (series and parallel) to connect R_L with the resonating load coil. In a series load configuration (Figure 4.1(b)), the Q-factor of the load coil is inversely proportional to R_l ($Q_l = \omega L_L/R_l$, $\omega = 2\pi f_{res}$), where $R_l = R_L + R_{CL}$ (R_{CL} is self resistance of the load coil). From Equation 4.4, it can be seen that the required driver current increases with the reduction in coupling k. Due to the small inductance of the implant coil (below 10 μH), only a small load resistance (below 100 Ω) can achieve a moderate Q_l of 3 to 6 for f_{oper} below 10 MHz.

$$\left|\frac{I_d}{I_{load}}\right| = \frac{R_l}{\omega M} = \frac{R_l}{\omega k\sqrt{L_d L_L}}; \quad \left|\frac{I_l}{I_{load}}\right| = 1 \tag{4.4}$$

where M is the mutual inductance between the driver and the load coil. L_d and L_L are the self-inductance of the driver coil and load coil, respectively.

For a large load resistance R_L (200 Ω -10kΩ), a parallel load configuration utilizes an impedance transform mechanism to achieve smaller effective resistance $R_l = R_L/Q_{||}^2 + R_{CL}$ (where $Q_{||} = R_L/\omega L_L$). The current of the load coil I_l gets divided between the resonating capacitor (C_L) and R_L (Figure 4.1(c), Equation 4.7). For a fixed R_L, increasing the load coil inductance L_L reduces $Q_{||}$ and increase R_l, limiting the value of Q_l. The power transfer efficiency for the two-coil WPT system increases monotonically with Q factors (Q_d, Q_l) and coupling k between the coils (Equation 4.5). Therefore, L_L needs to be adjusted to achieve a moderate $Q_{||}$ (below 15) to reduce the current division and sufficient Q_l to achieve PTE above 30% (Equation 4.5 and 4.6) (Figure 4.1(d)).

$$\eta = \frac{k^2 Q_d Q_l}{1 + k^2 Q_d Q_l} \tag{4.5}$$

$$Q_l = \frac{\omega L_L}{(\omega L_L)^2/R_L + R_{CL}} \tag{4.6}$$

$$\left|\frac{I_d}{I_{load}}\right| \simeq \frac{Q_{||} R_l}{\omega M}; \quad \left|\frac{I_l}{I_{load}}\right| \simeq Q_{||} \tag{4.7}$$

where M is the mutual inductance between the driver and the load coil; L_d and L_L are the self-inductance of the driver coil and load coil, respectively.

For most biomedical implants, R_L lies in a higher value range (200 Ω -10kΩ) [1–3], making a parallel load configuration as a practical topology to achieve sufficient power transfer efficiency above 30% [4, 5]. However, care needs to be taken in designing a load coil to achieve trade-off between the efficiency and current division (Figure 4.1(d)). In the following sections, our focus is to reduce the current division without losing the power transfer efficiency of the wireless power link.

4.5 Currents in a Multi-coil WPT System

Recently, we proposed a multi-coil wireless power system for the biomedical applications [7]. The proposed design utilizes intermediate transmitter and(or) receiver coils to decouple the effect of the source and(or) load resistances and achieve high Q factor external and(or) implant coils. Figure 4.2(a) shows the block diagram of three-coil system. At resonance, Equation 4.8 can be used to calculate the current in each coil.

$$\begin{bmatrix} I_d \\ I_t \\ I_l \end{bmatrix} = \begin{bmatrix} R_d & j\omega M_{dt} & j\omega M_{dl} \\ j\omega M_{dt} & R_t & j\omega M_{tl} \\ j\omega M_{dl} & j\omega M_{tl} & R_l \end{bmatrix}^{-1} \begin{bmatrix} V_1 \\ 0 \\ 0 \end{bmatrix} \tag{4.8}$$

where M_{dt}, M_{tl} and M_{dl} are the mutual inductances between the driver and transmitter coil, the transmitter and load coil and the driver and load coil, respectively.

In multi-coil design, M_{dl} is many orders smaller than M_{tl}, allowing us to ignore M_{dl} in the current calculation [7]. To generate the unit current in the load resistance, the current ratio of the driver, transmitter, and load (implant) coils can be calculated as shown in Equations 4.9 and 4.10:

$$\left|\frac{I_d}{I_{load}}\right| = \sqrt{\frac{R_l}{R_d}}\frac{1+k_2^2Q_tQ_l}{k_1k_2\sqrt{Q_dQ_t}\sqrt{Q_tQ_l}} \tag{4.9}$$

$$\left|\frac{I_t}{I_{load}}\right| \simeq \frac{Q_{||}R_l}{\omega M_{tl}}; \quad \left|\frac{I_l}{I_{load}}\right| \simeq Q_{||} \tag{4.10}$$

where k_1, k_2, and k_3 are the coupling between the driver coil and transmitter coil, the transmitter and load coil, and the driver and load coil, respectively. Q_d, Q_t and Q_l are the Q-factors of the driver, transmitter and load coil, respectively.

Figure 4.2 (b) shows the schematic of the three-coil based wireless power transfer system. The load resistance is connected to the load coil in parallel to achieve sufficient Q factor and to sustain PTE above 30 %. However, multi-coil WPT can reduce $Q_{||}$ significantly compared to its two-coil equivalent and the effect of the low Q-factor load coil Q_l on the PTE is compensated using a high Q-factor transmitter coil [7].

4.6 Simulation Model and Methods

To model a practical wireless powered implant, an epiretinal prosthesis is taken as a design example [4, 8]. The traditional design uses two-coil based WPT system [3–5]. Thus, to improve the PTE and to reduce the absorbed energy in the tissue, a three-coil based WPT system is selected. Table 4.1 shows the electrical and mechanical properties of two-coil and three-coil equivalent systems. For both designs, the physical dimensions of the external coil and implant coil are identical to ensure fair comparison (Figure 4.3(c)). However, the inductance of the load coil in two-coil system is optimized to achieve $\eta > 30\%$ and $Q_{||} < 15$ (Figure 4.1(d)). For the three-coil WPT system, $Q_{||}$ is reduced by 40% compared to its two-coil equivalent and its effect on the system's PTE is compensated by high Q-transmitter coil ($Q_t \sim 178$). The driver coil is fed with a voltage source with amplitude 3 V and operating frequency of 2 MHz. Implant electronics is modeled as a resistive load of 450 Ω, which requires a load current of 22.3 mA to generate 10 V across implant [2]. To achieve maximum coupling, the external coil is positioned parallel to the surface of the head (Figure 4.3 (c)) and wireless power is transferred over the operating distance of 15 mm. In both designs, a driver resistance R_{driver} of 8 Ω is used to emulate the practical power-amplifier output resistance [12].

Table 4.1. System Specifications

	Two-Coil		Three-Coil		
Parameters	Driver	Load	Driver	Tx	Load
$D_{out}(cm)$	4.0	1.5	1.2	4.0	1.5
N_{coil}	12	12	4	12	15
$L_{coil}(\mu H)$	5.68	2.58	0.39	5.68	4.2
$R_{coil}(\Omega)$	0.4	0.22	0.1	0.4	0.45
$R_{driver}(\Omega)$	8	-	8		
$R_{load}(\Omega)$	-	450			450
$Q_{(loaded)}$	8.5	12.7	0.6	178	7.95
Litz [13]	100/44	3/22/48	100/44	100/44	33/48
d (mm)	15		15		
f_{res} (MHz)	2		2		
Load Type	Parallel		Parallel		
coupling	k = 0.072		$k_1 = 0.33$, $k_2 = 0.072$, $k_3 = 0.04$		

For our simulation, we took the heterogeneous tissue model of the human head [14] with 1 mm x 1 mm x 1 mm resolution. For the frequency range of 1-10 MHz, the conductivity of most tissues (skin, sclera, retina, muscle) vary between 0.01-1.5 S/m [15]. Figure 4.3(d) shows the conductivity map for different tissues at the operating frequency of 2 MHz [15]. As the implant coil is in close proximity to the high conductive vitreous humor (1.5 S/m), the implant coil contributes highly to the absorbed energy.

Figures 4.3(a), (b) and (c) show the head model, 3-D simulation model and cross-section of the simulation model, showing the external and implant coils. Figure 4.3(c) shows the position of the external coil parallel to the head surface and implant coil next to the eye sclera. For both designs, an external coil with diameter 40 mm and an implant coil with diameter 15 mm are used (Table 4.1). The equivalent three-coil system consists of external coils (driver and transmitter coil) and an implant coil as shown in Figure 4.2(b). For the two-coil WPT system and its equivalent three-coil WPT system, the induced electric field is calculated using the impedance method [16] for current carrying coils to determine the absorbed power in the tissue.

4.7 Results and Comparison

For the two-coil system, Equations 4.2 and 4.3 can be used to calculate the currents in the driver coil, the load coil and the load resistance. Similarly, for the three-coil system, current in each coil can be calculated based on Equations 4.9 and 4.10. Table 4.2 shows the current in each coil and load resistance for the two-coil and three-coil WPT systems. Table 4.2 also shows that the current

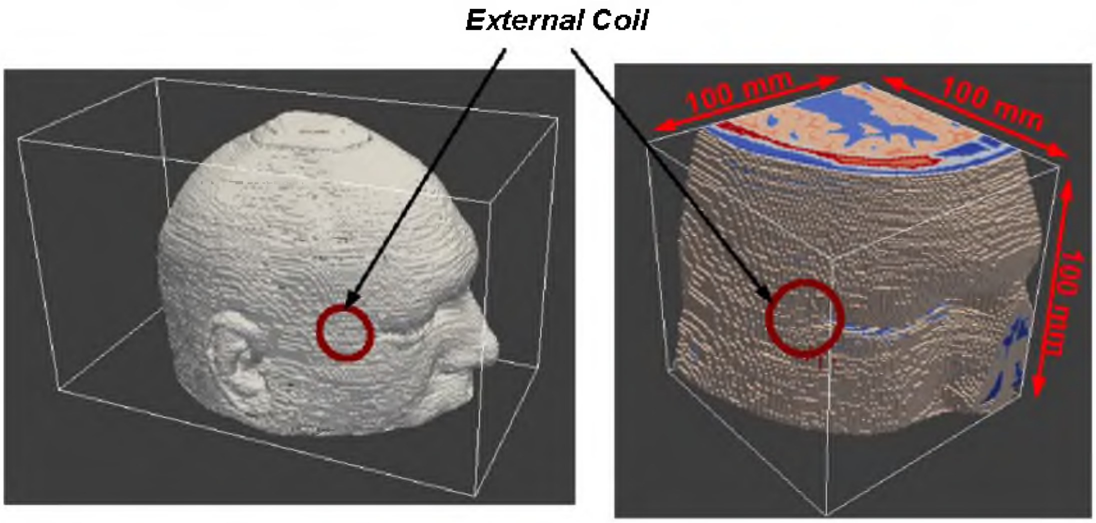

(a) Head Model for the Epiretinal Prothesis

(b) Simulation model (Head Section)

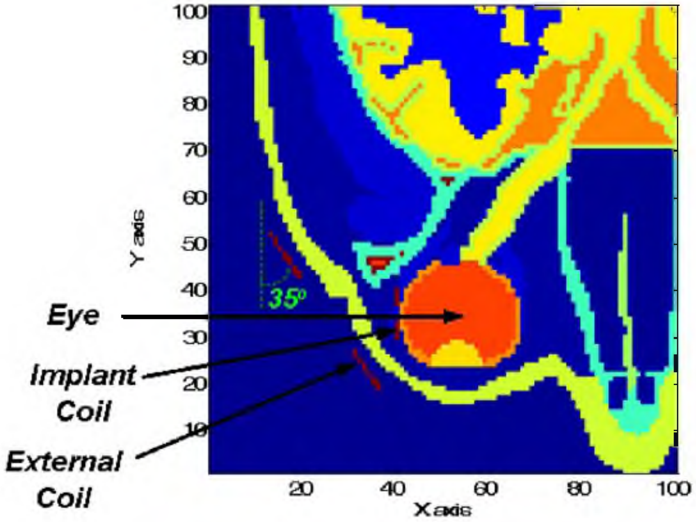

(c) Cross-section of head model with position of magnetic coils

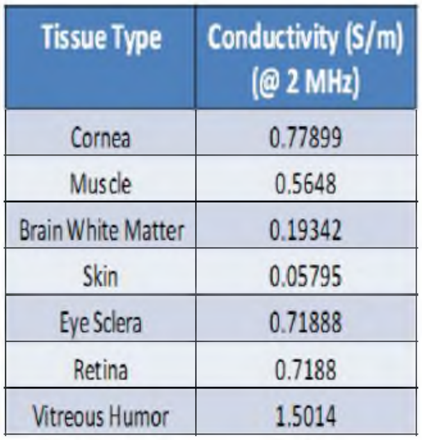

Tissue Type	Conductivity (S/m) (@ 2 MHz)
Cornea	0.77899
Muscle	0.5648
Brain White Matter	0.19342
Skin	0.05795
Eye Sclera	0.71888
Retina	0.7188
Vitreous Humor	1.5014

(d) Tissue type and its conductivity @ 2 MHz

Figure 4.3. Simulation model: (a) Head model for the Epiretinal prosthesis with external coil position (b) Simulation model with 1 mm x 1 mm x 1 mm resolution including tissue heterogeneity (c) Positions of the implant and the external coil with respect to eye (cross-section model) (d) Conductivities of different tissues types at 2 MHz [15].

Table 4.2. Coil Current

Coil	Driver I_d(mA)	Transmitter I_t(mA)	Load I_l(mA)	R_L I_{load}(mA)
Two-coil	229.5		310.6	22.32
Three-coil	156.2	282.35	190.9	22.24

in the implant coil is significantly reduced as compared to the two-coil design to generate the same load current of $\sim$ 22.3 mA.

Figure 4.4(a) and 4.4(b) show the cross section view of the induced electric field due to the two-coil and the three-coil WPT system, respectively. For the two-coil system, due to the large current in the implant coil (Table 4.2), the induced field near the implant coil is maximum (Figure 4.4(a)). For tissue density of 1000 kg/m^3, the peak 1-gram SAR and peak 10-gram SAR are calculated based on the FCC (Federal Communications Commission) [10] and IEC (International Electrotechnical Commission) [11] standards for SAR, respectively. Figure 4.4(c) and (d) show the distribution of SAR due to two-coil and three-coil WPT system, respectively.

To evaluate the performance of the new three-coil WPT system, the system performance is characterized based on the power transfer efficiency (PTE), the voltage gain and the bandwidth [7]. Figure 4.5(a) shows that the proposed three-coil WPT system can achieve significant PTE improvement over two-coil design as expected from the multi-coil design approach [7]. The new three-coil design achieves the same voltage gain over frequency as the initial two-coil design without change in driver electronics, implant electronics, or system dimensions (Figure 4.5(b)). Therefore it can be seamlessly incorporated into existing two-coil WPT systems.

Table 4.3 show the significant reduction in absorbed electromagnetic energy by using three-coil WPT over a traditional two-coil design.

4.8 Conclusion

Two-coil based WPT systems only have a few factors (k, Q_d, Q_L) to control the current in each coil. However, multi-coil WPT systems utilize multiple coils to improve the PTE and result in a high number of design parameters (k_{1-3}, Q_d, Q_t, Q_l) that can be used to control current in each magnetic coil. For the proposed design example, a reduction of 26% in peak 1-gram SAR and a reduction of 15 % in peak 10-gram peak are achieved with the improvement of 46 % in power transfer efficiency (PTE). A two-coil WPT system and its three-coil equivalent are demonstrated to achieve the same voltage gain and frequency bandwidth over the same operating distance. While the presented design example used the typical dimensions for biomedical WPT system, the design approach is valid for any near field WPT system to reduce the absorbed electromagnetic field in tissue.

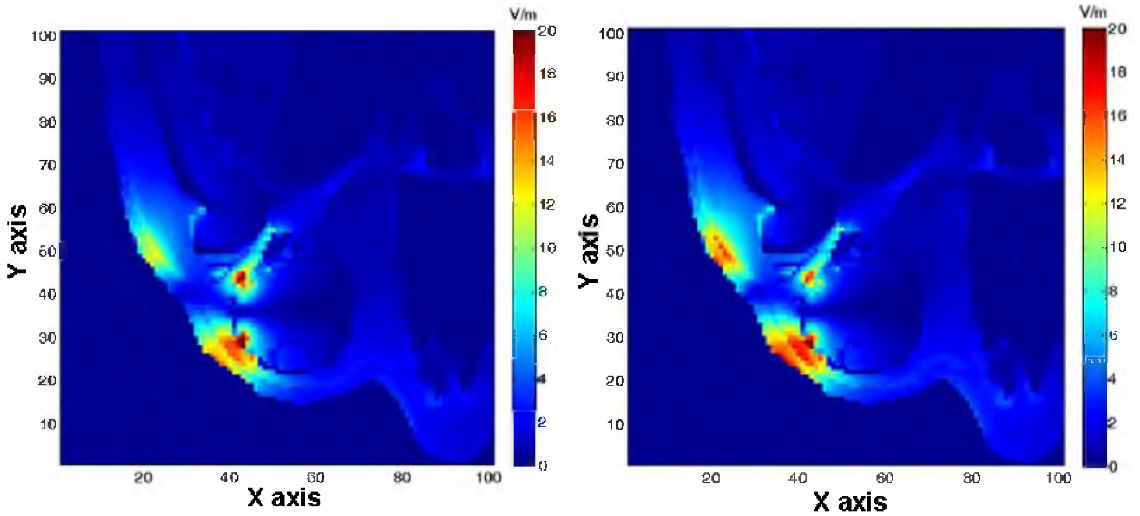

(a) Induced E-field due to 2-Coil WPT system

(b) Induced E-field due to 3-Coil WPT system

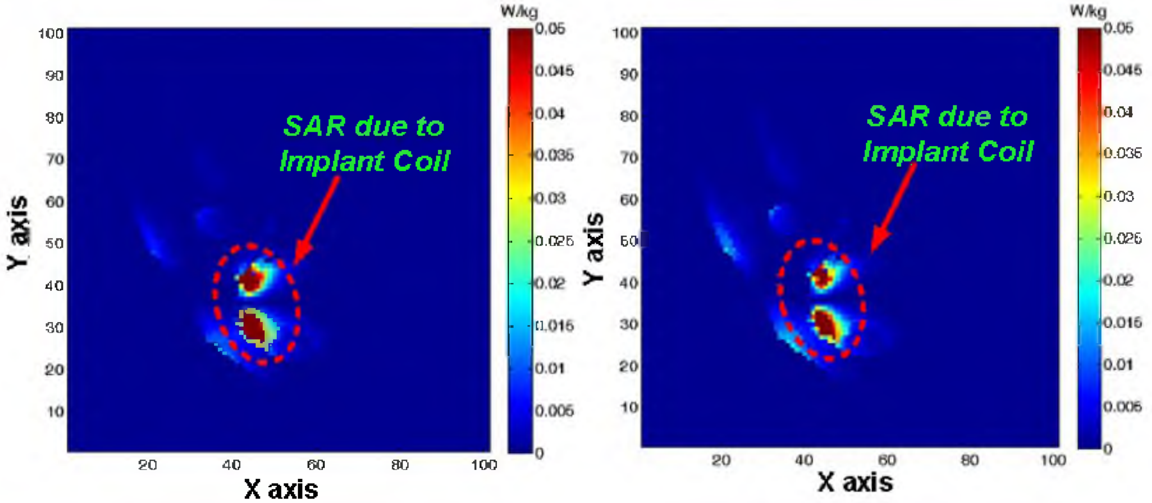

(c) SAR (2-Coil WPT system)

(d) SAR (3-Coil WPT system)

Figure 4.4. Cross section view of the induced electric field due to (a) two-coil and (b) three-coil WPT system. Distribution of the Specific absorption rate (SAR) due to (c) two-coil and (d) three-coil WPT system. Coil currents are based on Table 4.2.

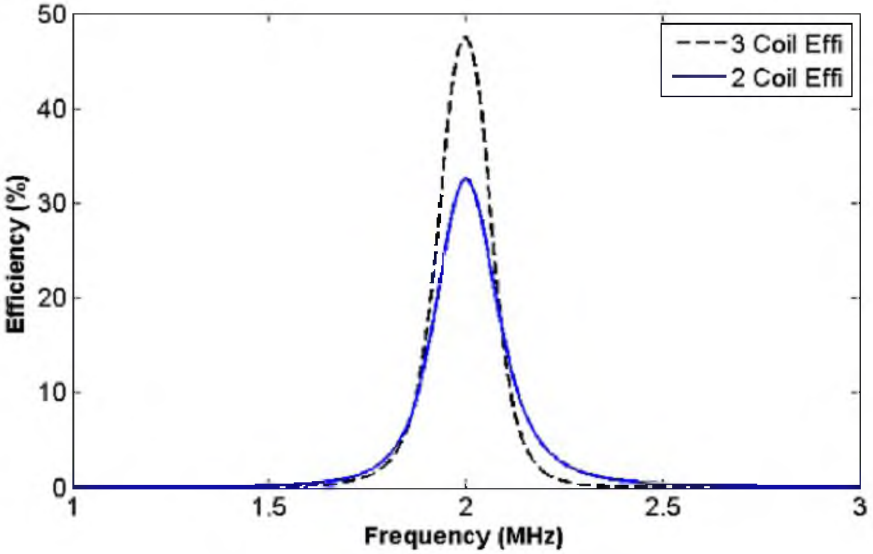

(a) Efficiency Comparison (2-coil, 3-coil)

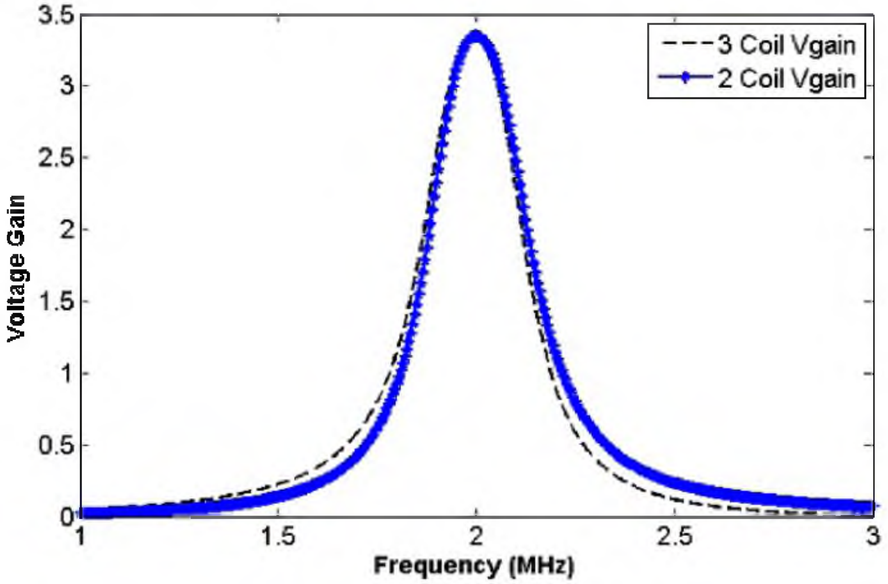

(b) Voltage Gain (2-coil, 3-coil)

Figure 4.5. System performance: (a) Power transfer efficiency of two-coil and three-coil system (b) voltage-gain of two-coil and three-coil system.

Table 4.3. System Performance

	1-gram SAR (mW/Kg)	10-gram SAR (mW/Kg)	Efficiency (%)	Voltage gain	Bandwidth (khz)
Two-coil	48.2	15.1	32.5	3.348	209
Three-coil	35.7	12.8	47.5	3.336	207
Variation	-26 %	-15.2%	+46%	<1 %	<1%

4.9 References

[1] C. Chestek, V. Gilja, P. Nuyujukian, R. Kier, F. Solzbacher, S. Ryu, R. Harrison, and K. Shenoy, "Hermesc: Low-power wireless neural recording system for freely moving primates," IEEE Transactions on Neural Systems and Rehabilitation Engineering, vol. 17, no. 4, pp. 330-338, 2009.

[2] M. S. Humayun, E. D. Juan, G. Dagnelie, R. J. Greenberg, R. H. Propst, and H. Phillips, "Visual perception elicited by electrical stimulation of the retina in blind humans," Arch. Ophthalmology, vol. 114, pp. 40-46, 1996.

[3] Kuanfu Chen, Yang, Zhi, Linh Hoang, J. Weiland, M. Humayun, and Wentai Liu, "An Integrated 256-Channel Epiretinal Prosthesis," IEEE Journal of Solid-State Circuits, vol. 45, no. 9, pp. 1946-1956, Sept. 2010

[4] G. Wang, W. Liu, M. Sivaprakasam, M. Zhou, J. D. Weiland, and M. S. Humayun, "A dual band wireless power and data telemetry for retinal prosthesis," in Conf. Proc. IEEE EMBS, Aug. 30-Sept. 3 2006, pp. 28-38.

[5] L. Wu, Z. Yang, E. Basham, and W. Liu, "An efficient wireless power link for high voltage retinal implant," in Proc. BioCAS, 2008, pp. 101-104.

[6] A. K. RamRakhyani, S. Mirabbasi, and M. Chiao, "Design and optimization of resonance-based efficient wireless power delivery systems for biomedical implants," IEEE Transactions on Biomedical Circuits and Systems, vol. 5, no. 1, pp. 48-63, 2011.

[7] A. RamRakhyani and G. Lazzi, "On the design of efficient multi-coil telemetry system for biomedical implants," IEEE Transactions on Biomedical Circuits and Systems, vol. 7, no. 1, pp. 11-23, 2013.

[8] V. Singh, A. Qusba, A. Roy, R. Castro, K. McClure, R. Dai, R. Greenberg, J. Weiland, M. Humayun, and G. Lazzi, "Specific absorption rate and current densities in the human eye and head induced by the telemetry link of an epiretinal prosthesis," IEEE Transactions on Antennas and Propagation, vol. 57, no. 10, pp. 3110 -3118, oct. 2009.

[9] Challis LJ., "Mechanisms for interaction between RF fields and biological tissue," Bioelectromagnetics 26(suppl 7):S98-S106, 2005.

[10] Federal Communications Commission, "Wireless devices and health concerns," [Online]. Available: http://www.fcc.gov/guides/wireless-devices-andhealth-concerns

[11] International Electrotechnical Commission, "Human exposure to radio frequency fields from hand-held and body-mounted wireless communication devices," [Online]. Available: http://webstore.iec.ch/webstore/webstore.nsf/artnum/033746

[12] R. Harrison, "Designing efficient inductive power links for implantable devices," in Proc. IEEE ISCAS, 2007, pp. 2080-2083.

[13] N. E. W. Technology, "New England wire technologies - litz wiretechnical.pdf," [Online]. Available: http://www.newenglandwire.com/litz.asp.

[14] The National Library of Medicine, "The Visible Human Project," 2000 [Online]. Available: http://www.nlm.nih.gov/research/visible/

[15] Italian National Research Council, "Dielectric properties of body tissue," 1997-2007 [Online]. Available: http://niremf.ifac.cnr.it/tissprop/

[16] N. Orcutt and O. P. Gandhi, "A 3-D impedance method to calculate power deposition in biological bodies subjected to time varying magnetic fields," IEEE Transactions on Biomedical Engineering, vol. 35, no. 8, pp. 577-583, Aug. 1988

CHAPTER 5

INTERFERENCE FREE WIRELESS POWER TRANSFER SYSTEM FOR BIOMEDICAL IMPLANTS USING MULTI-COIL APPROACH

© 2014 IET, Reprinted, with permission from: Anil Kumar RamRakhyani, Gianluca Lazzi, "Interference Free Wireless Power Transfer System for Biomedical Implants using Multi-Coil Approach," in IET Electronics Letters, vol.50, no.12, pp.853-855, June 2014.

5.1 Abstract

Low frequency (1-20 MHz) inductive coupling is a leading technique to power biomedical implants wirelessly. Even though these are nonradiating systems, the external and the implant coils can cause sufficient radiated electric field to exceed the federal standards for communication. In this work, a multi-coil based wireless power transfer (WPT) technique is developed to selectively control the currents in the external and implant coils to reduce radiated electric field. A four-coil WPT system that can achieve more than 37% reduction in radiated electric field as compared to a two-coil WPT system with the same dimensions and design constraints is implemented and used to demonstrate the effectiveness of the proposed approach.

5.2 Introduction

Wireless power transfer (WPT) is commonly used to power implantable devices such as sensors, actuators, and neural stimulators [1]. Traditionally, two-coil based design is used to transfer power from the external (driver) coil to the implant coil using time varying magnetic field (Figure 5.1 (a)). Using a large driver coil (3-5 cm), sufficient magnetic coupling ($k \sim$ 0.01-0.1) to the implant coil (0.5-2 cm) is achieved over a long operating distance (0.5-1.8 cm) between the coils [1, 4]. Due to the small size of the magnetic coils, as compared to operating frequency wavelength, WPT systems are poor radiators. To reduce the interference with other operating devices, the federal regulators, such as the Federal Communications Commission (FCC), restrict the total electric field generated by the nonradiating device to be less than 30 μV measured at 30 meters (FCC 47 CFR

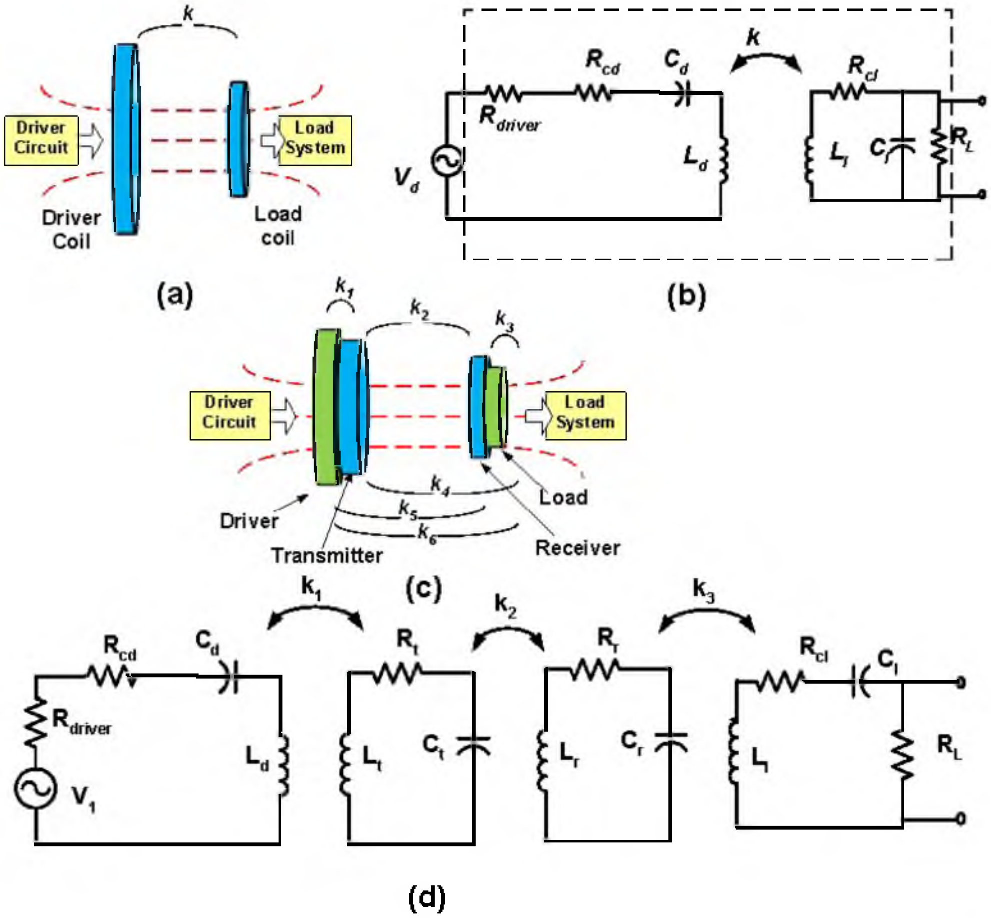

Figure 5.1. Block diagram of (a) the two-coil and (c) the four-coil wireless power transfer system including the magnetic coupling between different coils. Circuit model of (b) the two-coil and (d) the four-coil wireless power transfer system [4].

Ch. I [2]). Depending on the design and application, transferring power of hundreds of milliwatts to the implanted device may require a large current (1-2 A) in the external coil. Far-field radiated field depends on the current in the driver and implant coils. Thus, few commercial biomedical implants violate these limits by using a midsized coil (4 cm diameter), carrying current of 1 A at 3 MHz and require special waiver for commercialization [3]. Therefore, to comply with the federal regulation for future nonradiating devices, the WPT system should ensure no interference with other radiating/nonradiating devices. Recently, we proposed a multi-coil based wireless powered system to achieve high wireless power transfer efficiency [4]. In this work, a four-coil based WPT system is proposed to achieve the same system performance (voltage gain) as a two-coil WPT design under the same size restrictions and operating conditions. The current in each coil is selectively tuned to reduce the radiated electric field. Formulation and demonstration of a multi-coil WPT system, which can reduce the radiated field in telemetry systems, are the main contributions of this work.

5.3 Radiated energy

In general, spiral coils are used for wireless power applications [1, 4]. For a spiral coil, radiated E field is proportional to the current and area of the coil (Equation 5.1) [5].

$$E_\phi = \sum_{i=1}^{N} Z_{air} \left(\frac{2\pi}{\lambda}\right)^2 \frac{e^{-j\beta r}}{4\pi r} sin(\theta) A_i I_0 \tag{5.1}$$

where I_0 is the current in the magnetic loop, N is the number of turns in spiral coil, Z_{air} is the wave impedance of air (377 Ω), λ is the free space wavelength at operating frequency, A_i is the area of turn i, and r is the distance of observation point from the radiator. For low frequency of operation (below 10 MHz), conductive tissue with conductivity σ less than 1.5 S/m has negligible effect on the radiated field. To validate it, a 12-turn spiral coil with outer diameter 49 mm is simulated in FDTD (finite-difference time-domain) based numerical solver to calculate the radiated E-field at 30 meters. The coil is placed 3 mm from the conductive tissue block (σ = 0.5 S/m) and driven by 1 A current at 3 MHz. Using Equation 5.1, radiated field is calculated to be 43.78 μV/m which is very close to the simulated value of 44.4 μV/m. Radiated power increases with the current in the magnetic coils. Therefore, currents need to be minimized to keep the radiated field well within interference standards. In the following sections, we propose a multi-coil WPT system to reduce current values in external coils to generate same load current into the load resistance.

5.4 Currents in Two-coil based Wireless Power Transfer System

For most biomedical implants, load resistance R_L lies in a higher value range (200 Ω -10$k\Omega$), making a parallel load configuration as practical topology to achieve sufficient power transfer efficiency [1] over 25% (Figure 5.1(b)). For R_L (200 Ω -10$k\Omega$), a parallel load configuration utilizes an impedance transform mechanism to achieve smaller effective resistance $R_l = R_L/Q_{||}^2 + R_{cl}$ (where $Q_{||} = R_L/\omega L_l$). The current of the load coil I_l gets divided between the resonating capacitor (C_l) and R_L (Figure 5.1(b), Equation 5.3). For a given R_L, increasing the load coil inductance L_l reduces $Q_{||}$ and increases R_l, limiting the value of Q_l. Therefore, L_l needs to be adjusted to provide moderate $Q_{||}$ (below 5) to reduce the current division and sufficient Q_l to achieve PTE above 25% (Equation 5.2). From Equation 5.4, it can be seen that as the coupling k decreases, the required driver current increases to generate the desired load current.

$$\begin{aligned} Q_l &= \frac{\omega L_l}{(\omega L_l)^2/R_L + R_{cl}} && (5.2) \\ I_{load} &\simeq I_l/Q_{||} && (5.3) \\ \left|\frac{I_d}{I_{load}}\right| &\simeq \frac{Q_{||}R_l}{\omega M} = \left(R_L/Q_{||} + Q_{||}R_{cl}\right)\frac{1}{\omega k\sqrt{L_d L_l}} && (5.4) \end{aligned}$$

where M is the mutual inductance between the driver and the load coil. L_d and L_l are the self-inductance of the driver coil and load coil, respectively. In the following sections, our focus is to achieve a series connected load coil to reduce the current division without losing the power transfer efficiency of the wireless power link.

5.5 Currents in Four-coil based Wireless Power Transfer System

Figure 5.1(c) and (d) show the typical block diagram and the schematics of a four-coil system consisting of a driver, transmitter, receiver and load coil [4]. At resonance, Equation 5.5 can be used to calculate the current in each coil.

$$\begin{bmatrix} I_d \\ I_t \\ I_r \\ I_l \end{bmatrix} = \begin{bmatrix} R_d & j\omega M_{dt} & j\omega M_{dr} & j\omega M_{dl} \\ j\omega M_{dt} & R_t & j\omega M_{tr} & j\omega M_{tl} \\ j\omega M_{dr} & j\omega M_{tr} & R_r & j\omega M_{rl} \\ j\omega M_{dl} & j\omega M_{tl} & j\omega M_{rl} & R_l \end{bmatrix}^{-1} \begin{bmatrix} V_1 \\ 0 \\ 0 \\ 0 \end{bmatrix} \qquad (5.5)$$

where M_{dt}, M_{tr} and M_{rl} the are mutual inductance between the driver and transmitter coil, the transmitter and receiver coil and the receiver and load coil, respectively. Generally for a four-coil WPT system, mutual inductance M_{dl} (between driver and load coil), M_{tl} (between transmitter and load coil) and M_{dr} (between driver and receiver coil) are of small value as compared to M_{dt}, M_{tr} and M_{rl}. This allows us to neglect M_{dl}, M_{tl} and M_{dr} for further calculation and simplifies the current equations.

Equation 5.6 can be used to approximately estimate the current in the external coil I_t (transmitter coil) to generate unit load current in the load resistance. As expected, the required current I_t is inversely proportional to coupling k_2 between the transmitter and receiver coil. From Equation 5.6, it can be seen that I_t is independent of R_L and by reducing k_3 the current ratio can be reduced. To generate the same load current in a two-coil and its four-coil equivalent, the ratio of current in the transmitter coil (of four-coil design) and driver coil (of two-coil design) can be calculated using Equation 5.7. In general, $R_L/Q_{||} \gg Q_{||}R_{cl}$ and $M_{tr(4-coil)} \approx M_{dl(2-coil)}$ (for four-coil design and its equivalent two-coil system). This allows us to simplify the current ratio of the four-coil and two-coil design using Equation 5.8

$$\left|\frac{I_t}{I_{load}}\right| \simeq \frac{k_3}{k_2}\sqrt{\frac{L_l}{L_t}} = \frac{M_{rl}}{M_{tr}} \tag{5.6}$$

$$\frac{|I_t/I_{load}|_{4-coil}}{|I_d/I_{load}|_{2-coil}} = \left(\frac{M_{rl}}{M_{tr}}\right)_{4-coil} \left(\frac{\omega M_{dl}}{Q_{||} R_l}\right)_{2-coil} \tag{5.7}$$

$$\frac{|I_t/I_{load}|_{4-coil}}{|I_d/I_{load}|_{2-coil}} = k_3\sqrt{\frac{(L_r L_l)_{4-coil}}{L^2_{l(2-coil)}}} \tag{5.8}$$

where k_3 is the coupling between the receiver and load coil and is less than 1. For proper selection of L_r and L_l in a four-coil WPT system, transmitter coil current I_t can be significantly reduced as compared to two-coil equivalent.

5.6 Design Example

To validate the efficacy of the multi-coil approach for radiation reduction, a retinal prosthesis based design is considered. According to the federal regulations, the emitted radiation needs to be tested for the extreme operation of the system. For retinal prosthesis, due to eye movement, the implant coil undergoes rotation, and magnetic coupling is minimum ($k = 0.025$) for the extreme rotation of the eye ($\phi = 30^0$) (Figure 5.2(a)). Table 5.1 shows the electrical and mechanical properties of the two-coil and four-coil equivalent chosen based on the specifications of retinal prosthesis design [1, 3]. The physical dimensions of the external coil and implant coil are the same for fair comparison (Figure 5.2(b) and (c)). Implant electronics is modeled as a resistive load of 450 Ω and requires a load current of 23.11 mA, which results in a supply voltage of $\sim$ 10 V across the load [1]. Wireless power is transferred over an operating distance of 15 mm. Figure 5.1(b) and (d) show the schematics of the two-coil and four-coil, respectively. The two-coil system is optimized to achieve $Q_{||} \leq 5$ to achieve low current division (Equation 5.3) and PTE more than 25% for normal operating condition ($\phi = 0^0$, $k = 0.072$).

Table 5.2 shows the current requirements for each coil in the two-coil and its four-coil equivalent (same dimension) WPT system to generate 23.1 mA current in the load resistance. Figure 5.3 shows that performance (efficiency, voltage gain and bandwidth) of the two-coil and its four-coil equivalent WPT system. It shows that using multi-coil approach the high power transfer efficiency can be achieved without changing the driver and load electronics for the system. Table 5.3 tabulates the system performance for both designs and shows two-coil WPT design exceed the federal limit of radiated field. However, four-coil WPT system reduces the radiated electric field by 37 % and can easily comply with the federal regulations.

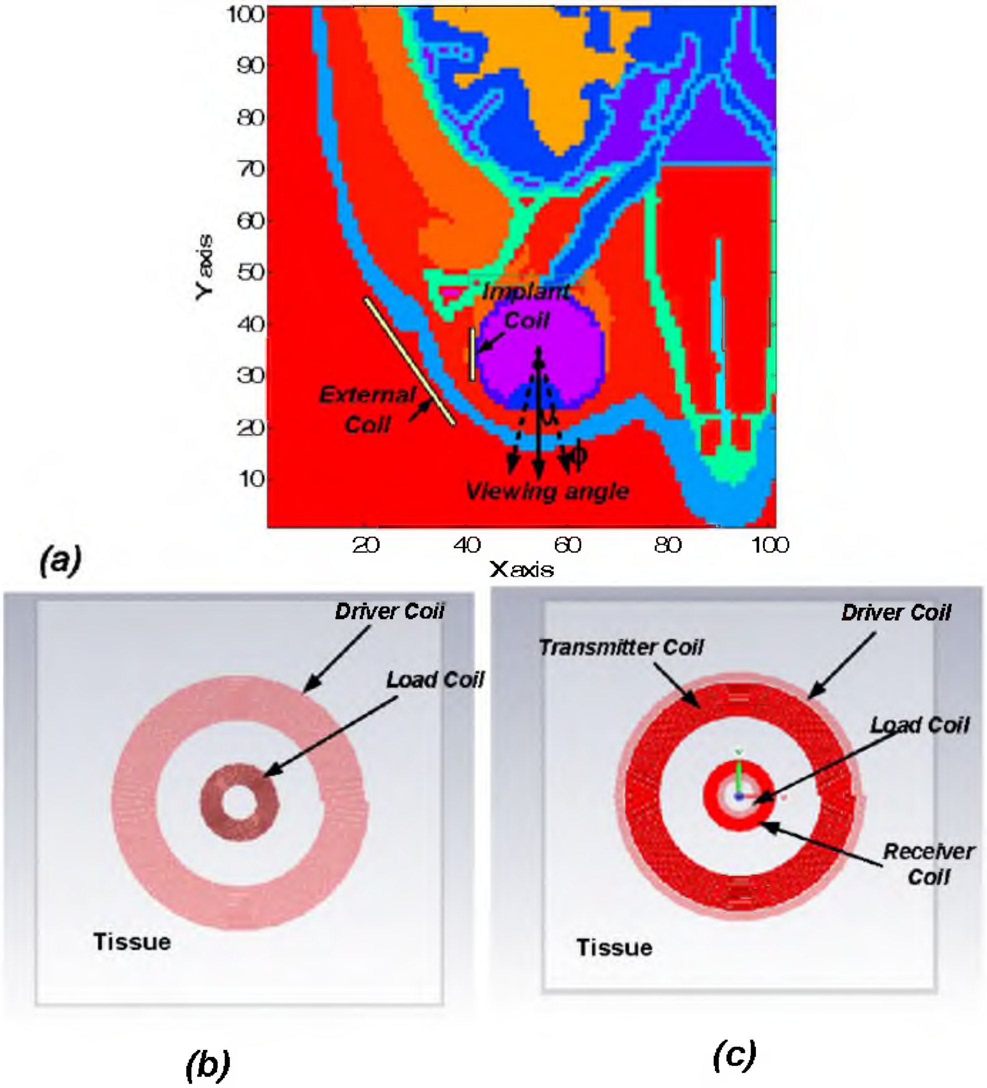

Figure 5.2. Simulation model: (a) Position of the external and implant coil for retinal prosthesis. The implant coil rotates with the movement of eye during the device operation (b) top view of external and implant coil for two-coil WPT system (c) top view of concentric external coils (driver and transmitter) and implant coils (receiver and load) for four-coil WPT system.

Table 5.1. System Specifications

	Two-Coil		Four-Coil			
Parameters	Driver	Load	Driver	Tx	Rx	Load
$D_{out}(cm)$	4.0	1.5	4.0	3.8	1.5	1.2
N_{coil}	12	20	2	10	14	17
$L_{coil}(\mu H)$	5.29	4.09	0.38	3.82	4.27	5.03
$R_{coil}(\Omega)$	0.4	0.3	0.1	0.4	0.55	1.07
$R_{driver}(\Omega)$	5.8	-	5.8			
$R_{load}(\Omega)$	-	450				450
$Q_{(loaded)}$	16.92	4.26	1.24	185	151	0.22
Wire (Litz)	100/44	3/22/48	100/44	100/44	26/48	12/48
d, ϕ	(15 mm, 30^0)		(15 mm, 30^0)			
f_{res} (MHz)	3.1		3.1			
Load Type	Parallel		Series			
coupling	k = 0.025		$k_1 = 0.37$, $k_2 = 0.0255$, $k_3 = 0.52$			
			$k_4 = 0.015$, $k_5 = 0.018$, $k_6 = 0.013$			

Table 5.2. Coil Current

Coil	Driver I_d(mA)	Transmitter I_t(mA)	Receiver I_r(mA)	Load I_l(mA)	R_L I_{load}(mA)
Two-coil	857			124	23.1
Four-coil	78.9	591	223	22.95	22.95

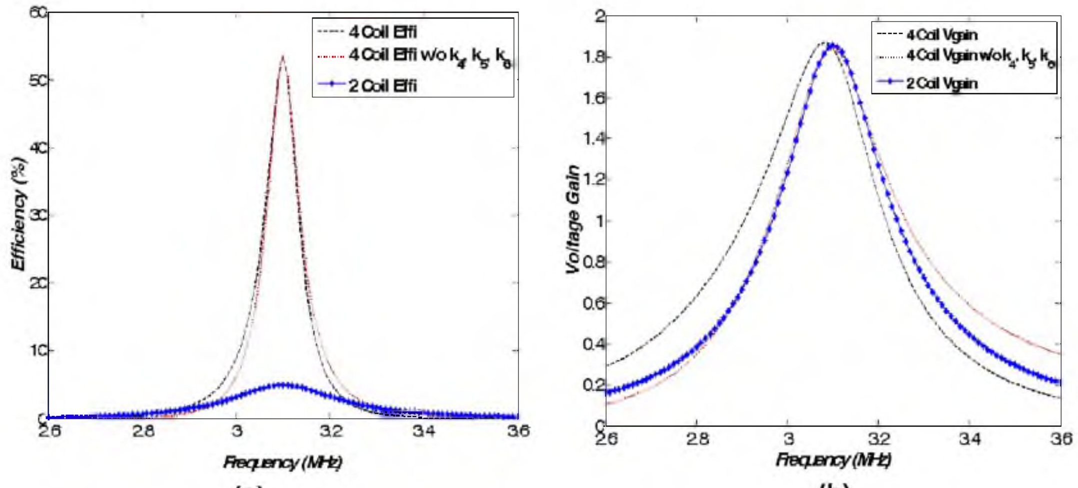

(a) (b)

Figure 5.3. System performance: (a) Power transfer efficiency and voltage gain of the two-coil and its four-coil equivalent WPT system (with and without effect of k_4, k_5, k_6).

Table 5.3. WPT System Performance

	Efficiency (%)	Voltage Gain	Bandwidth (kHz)	E-field @30 m (μV/m)
Two-coil	4	1.855	196	31.3
Four-coil	53.5	1.835	209	19.66
Gain	+1200%	< 1%	+6%	-37.2 %

5.7 Conclusion

In this work, 37 % reduction in the radiated field is achieved using multi-coil wireless power transfer (WPT) system instead of traditional two-coil WPT design. The four-coil WPT design achieves higher power transfer efficiency and demonstrates the same voltage gain and frequency bandwidth with its two-coil equivalent WPT system over the same operating distance. This ensures the new WPT system can be seamlessly integrated with the existing electronics to reduce the time of design cycle and clinical trial of new design.

5.8 References

[1] Kuanfu Chen, Zhi Yang, Linh Hoang, J. Weiland, M. Humayun, and Wentai Liu, "An integrated 256-channel epiretinal prosthesis," IEEE Journal of Solid-State Circuits, vol. 45, no. 9, pp. 1946-1956, Sept. 2010.

[2] Federal Communications Commission, "47 cfr 15.209 radiated emission limits; general requirements," 2002, http://www.gpo.gov/fdsys/pkg/CFR-2002-title47-vol1/pdf/CFR-2002-

title47-vol1-sec15-209.pdf.

[3] Federal Communication Commission, “Second sight medical products, inc. request for waiver letter,” 2011, http://www.fcc.gov/document/second-sight-medicalproducts-inc-request-waiver-letter.

[4] A. RamRakhyani and G. Lazzi, “On the design of efficient multi-coil telemetry system for biomedical implants,” IEEE Transactions on Biomedical Circuits and Systems, vol. 7, no. 1, pp. 11-23, 2013.

[5] C. A. Balanis, Antenna Theory: Analysis and Design. Wiley-Interscience, 2005.

CHAPTER 6

ON THE DESIGN OF MICROFLUIDIC IMPLANT COIL FOR FLEXIBLE TELEMETRY SYSTEM

© 2014 IEEE. Reprinted, with permission, from: A. Qusba, A. K. RamRakhyani, J.-H. So, G. J. Hayes, M. D. Dickey, and G. Lazzi, “On the Design of Microfluidic Implant Coil for Flexible Telemetry System,” IEEE Sensors Journal, vol.14, no.4, pp.1074-1080, April 2014.

6.1 Abstract

This paper describes the realization of a soft, flexible, coil fabricated by means of a liquid metal alloy encased in a biocompatible elastomeric substrate for operation in a telemetry system, primarily for application to biomedical implantable devices. Fluidic conductors are in fact well suited for applications that require significant flexibility as well as conformable and stretchable devices, such as implantable coils for wireless telemetry. A coil with high conductivity, and therefore low losses and high unloaded Q factor, is required to realize an efficient wireless telemetry system. Unfortunately, the conductivity of the liquid metal alloy considered - eutectic gallium indium (EGaIn) - is approximately one order of magnitude lower than gold or copper. The goal of the present work is to demonstrate that, despite the lower conductivity of liquid metal alloys such as EGaIn compared to materials such as copper or gold, it is still possible to realize an efficient biomedical telemetry system employing liquid metal coils on the implant side. A wireless telemetry system for an artificial retina to restore partial vision to the blind is used as a testbed for the proposed liquid metal coils. Simulated and measured results show that power transfer efficiency of 43 % and 21 % are obtained at operating distances between coils of 5 mm and 12 mm, respectively. Further, liquid metal based coil retains more than 72 % of its performance (voltage gain, resonance bandwidth, and power transfer efficiency) when physically deformed over a curved surface, such as the surface of the human eye. This study demonstrate that liquid metal-based coils for biomedical implant provide an alternative to stiff and uncomfortable traditional coils used in biomedical implants.

6.2 Introduction

Flexible coils are important for a number of applications that require wireless telemetry for power and/or data transmission, including implantable devices such as retinal prostheses [1–3]. Conventional implant coils are often fabricated using biocompatible metal (e.g., gold) and are characterized by their unloaded Q factor (quality factor), which is a measure of the resistive losses in the coil within the resonance bandwidth. Unfortunately, traditional wireless telemetry coils tend to be stiff and are not easily comformable to surfaces inside or outside the human body, such as the eye in the case of a retinal prosthesis. Further, their stiffness makes them difficult to handle and position well during surgery and could result in subsequent discomfort for the patient.

Our approach to the realization of soft and flexible coils for wireless biomedical telemetry, presented in this paper, relies on injecting a micromoldable liquid metal composed of an eutectic alloy of gallium and indium (EGaIn) into elastomeric microfluidic channels. In this work, we first show that it is possible to fabricate fluidic coils that have sufficiently low resistance, and therefore large unloaded Q factor, by varying the cross-sectional area of the microchannels that define the shape of the coil without altering the footprint of the coil. The potential of utilizing coils thus fabricated in biomedical implant systems is demonstrated by implementing a telemetry link for wireless power/data transfer between external units and biomedical implants. We selected a specific application - that of a retinal prosthesis to restore partial vision to the blind - to provide realistic parameters for a wireless telemetry test-bed. Specifically, we demonstrate that a wireless telemetry link whose secondary coil is made of liquid metal alloy can achieve comparable system-level performance (frequency bandwidth, voltage gain, and power transfer efficiency) as the metal based implant coil.

6.3 Background and Motivation

Typically, application requirements of the implant dictate the geometry of telemetry coils and the performance metrics like bandwidth and power transfer efficiency. In this paper, we focus on telemetry coils for implantable devices: in particular, we focus on a retinal prosthesis application described in [1, 2] as a case study. The motivation behind the development of a retinal prosthesis, which has been the focus of the work of some of the members of our research team for the past 15 years, is that blind patients have been shown to regain some form of vision by means of a systematic electrical stimulation [1]. The primary goal of this work is to demonstrate that liquid metal alloy coils, when employed as receiving (implanted) coils, can achieve reasonable power transfer efficiency and, therefore, be used in an inductively coupled wireless telemetry system, such as that of a retinal prosthesis system, or any other biomedical implant or sensor requiring wireless power/data transmission.

Current prototypes of the retinal prosthesis system utilize a wearable camera which captures images that are subsequently transmitted wirelessly to a receiver coil (secondary coil) implanted inside the eye. This secondary coil receives both power and data signal via an inductively coupled wireless telemetry link and sends the signal to a processing chip, which in turn stimulates the retina by an electrode array placed against the retinal surface [4].

While the retinal prosthesis application provides an example of the design constraints (dimensions of the footprint, operating distance between the telemetry coils) for the coils considered in this work, the approach and conclusions extend to other coil geometries and different applications.

To maximize the power transfer efficiency over the operating range of implanted electronics, the secondary (or implant) coil can be the largest component of the prosthetic implant and often needs to be conformal to tissue or organ. As a result, highly-flexible coils (Figure 6.1) that can bend, stretch and reversibly deform without loss of function facilitate the surgical implantation and conform more readily to the surface of the organ - the eye in the particular case of a retinal implant.

When subjected to flexing, conventional solid metallic structures can crease, fatigue, or deform, which can disrupt electrical functionality. The liquid metal alloy encapsulated in an elastomeric substrate (e.g., silicones) flows in response to stress, and is therefore not prone to fatigue or permanent deformation [5]. Injecting liquid metal into microfluidic channels offers a simple approach to shaping them into useful structures, such as coils.

Figure 6.1 demonstrates the highly stretchable and flexible nature of these coils. Less information is known about the biocompatibility of the metals that compose the alloy (gallium and indium) and their long term behavior in the body, although they are believed to have low toxicity [6]. The implant coil could be simply composed of gallium since its melting point is below body temperature. Gallium has been used in dental fillings and gallium salts have been used for MRI imaging agents and pharmaceuticals [7, 8]. Further research into the toxicity of EGaIn needs to be undertaken before it could be considered for implantation in a human body; however, through this study we demonstrate that EGaIn based coils have all the characteristics desirable for prosthetic implants and these support the future in-vivo and in-vitro testing of the devices.

Traditionally liquid metal alloys, such as EGaIn, have been shown by our group and others to be useful in dipole antennas [5], [9–11], planar antennas [12], and patch antennas [13]. These antennas consist of radiating structures composed of liquid metal alloy injected into microfluidic channels of an elastomeric polydimethylsiloxane (PDMS) substrate. The performance metric of these radiating elements doesn't significantly depend on the conductivity of the liquid metal alloy. Thus, a feasibility study need to be done to utilize the similar liquid metal for wireless power/data

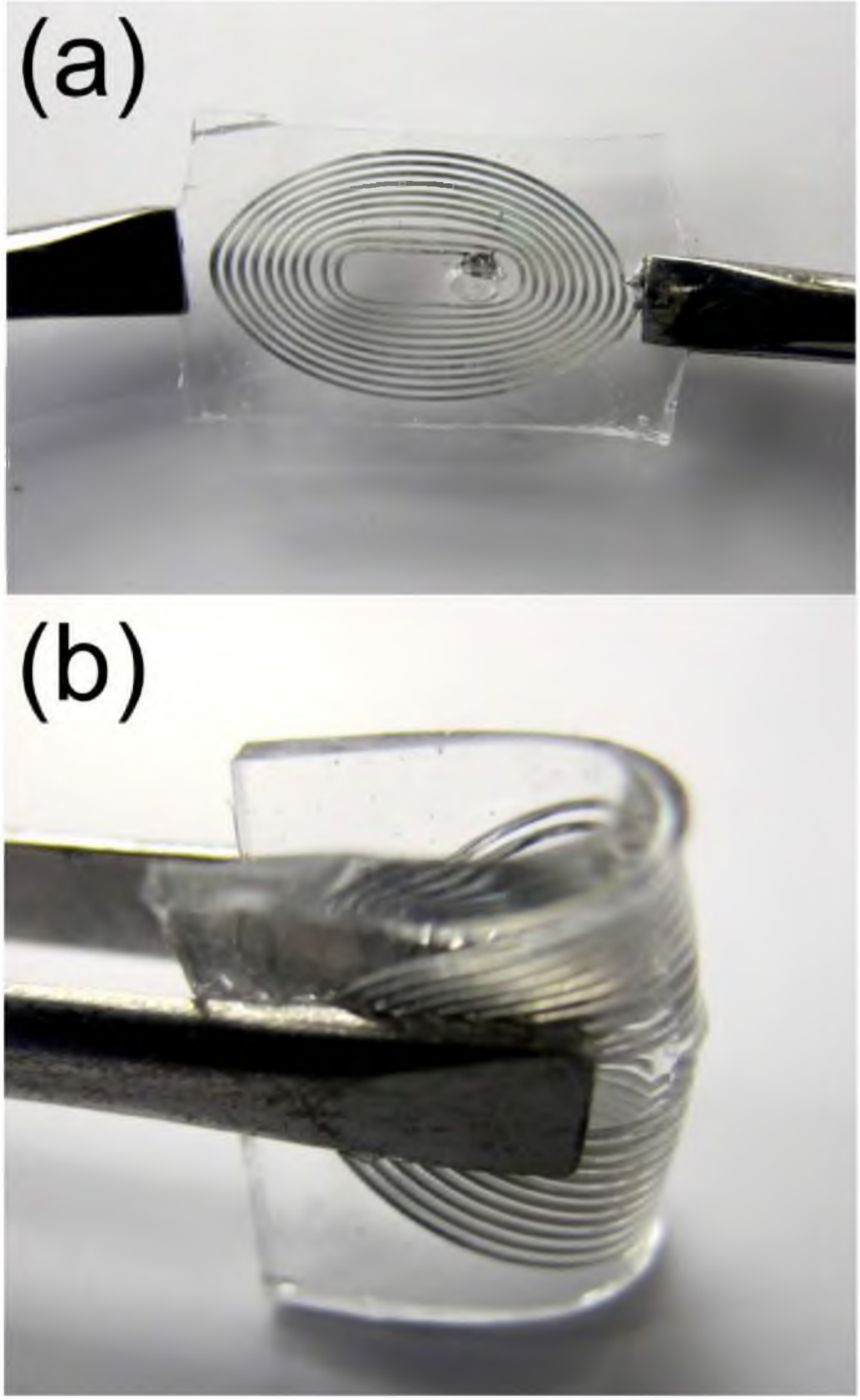

Figure 6.1. Soft and flexible coil antenna composed of liquid metal alloy encased in biocompatible elastomeric PDMS. Metal tweezers deform the coils. (a) Stretching the coils and (b) folding the coils.

transfer. To estimate the resistive losses due to the coil, we measure the unloaded Q_{ul} factor of the coil which is inversely proportional to the resistance of the coil (Equation 6.1).

$$Q_{ul} = \frac{2\pi f L}{R} \tag{6.1}$$

where f is frequency of operation, L is the self-inductance of the coil and R is the effective series resistance of the coil. The series resistance is proportional to the conductivity of the liquid metal alloy in the micro-channel; thus, the Q factor is an appropriate parameter to quantify the effects of introducing new materials into a coil. To compensate for the lower conductivity of EGaIn ($\sigma = 3.4 \times 10^4 Scm^{-1}$) which is about one order of magnitude lower than that of gold ($\sigma = 4.57 \times 10^5 Scm^{-1}$) and copper ($\sigma = 5.96 \times 10^4 Scm^{-1}$), we hypothesized that increasing the cross-sectional area of the fluidic channels in the coil would decrease the wire resistance and thereby increase the unloaded Q factor of the coil. The cross-sectional area is varied primarily by altering the aspect ratio (height:width) of the microfluidic channel. Once the Q factor is optimized, we quantify the performance of the liquid metal alloy coil as a secondary coil in an inductively coupled telemetry link.

6.4 Liquid Metal Coil Design, Fabrication and Characterization

In the case of a retinal prosthesis, the anatomy of the eye limits the length of the secondary coil to approximately 15 mm and the position of the lateral rectus muscle of the eye favors smaller width [14]. Thus, elliptical coils are geometrically favored shapes of secondary coil in this application. Figure 6.2 illustrates the footprint of the secondary coil in this example, relative to a US coin (cent).

While the length could be longer in principle, the endmost portions of the secondary coil (i.e., that beyond 15-16 mm) curl away from the primary coil due to the curvature of the eye ball and, therefore, do not contribute significantly to the mutual coupling. Furthermore, the use of larger coils could complicate the surgical implantation procedure.

We limited the secondary coil to have no more than 10 turns because additional turns would decrease the pitch (i.e., the spacing between adjacent turns), resulting in undesirable parasitic capacitance. The geometrical model of our slightly deformed elliptical secondary coil is formulated based on an expression presented in [15].

We fabricated the secondary coil by injecting EGaIn into microfluidic channels composed of PDMS [5, 9]. We controlled the cross-sectional dimensions using soft lithography (i.e., by replica molding photolithographic features using PDMS). An appeal of this approach is the simplicity of the fabrication and the ease by which the dimensions may be varied. We used PDMS for

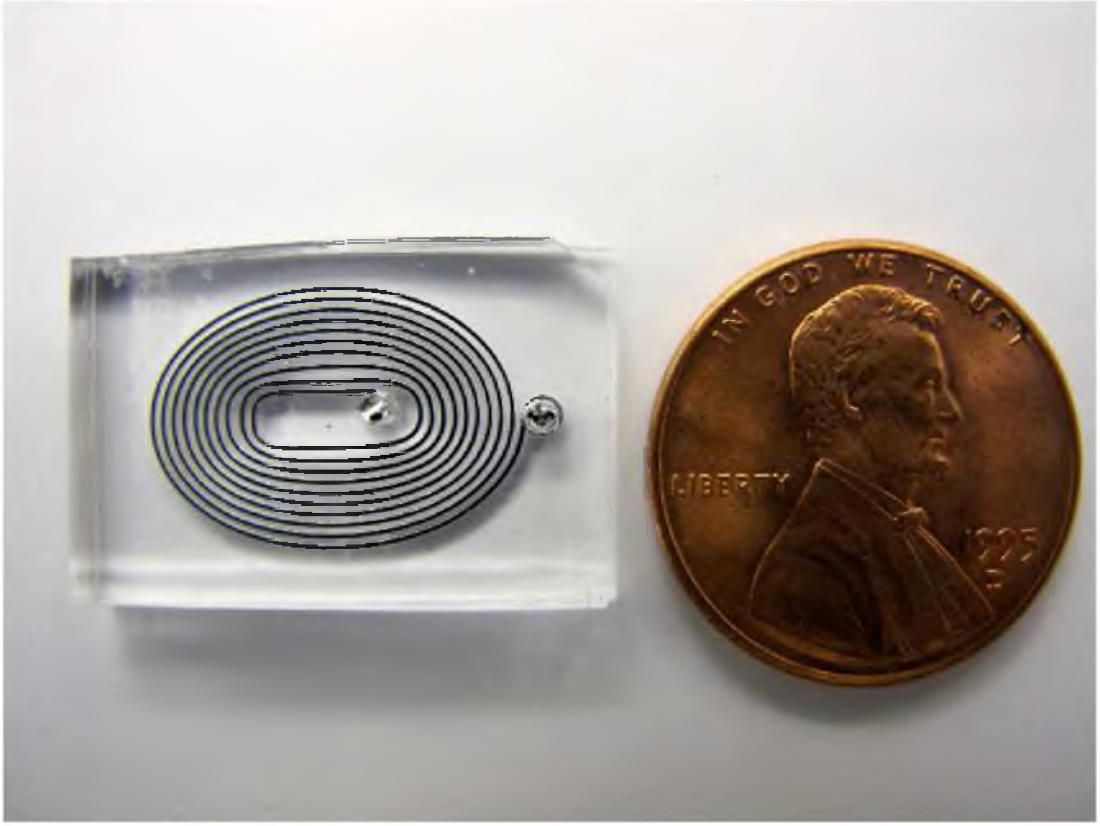

Figure 6.2. Photograph of the secondary coil of the RF telemetry link. EGaIn is injected into the microchannels of this coil using a syringe pump. The wire cross-section of this coil is $200\mu m \times 640\mu m$ and it is encased in PDMS.

the microfluidic channels because it is commercially available, biocompatible, easy to process, elastomeric, and has low dielectric loss properties [16, 17].

Coils with a range of wire cross-sections were fabricated. An Agilent E5071B ENA series vector network analyzer measured the impedance properties of the fabricated secondary coils. The target operation frequency for our testbed was 4 MHz, even though it can be chosen to be anywhere in the range of 2-10 MHz [1]. Resistance and self-inductance of the liquid metal alloy coil are measured at operating frequency and Equation 6.1 is used to determine the unloaded Q factor at 4 MHz. Table 6.1 summarizes the results of these experiments and compares the performance of liquid metal based implant coils with the metal (e.g., gold) based coils of the same physical footprint.

In Table 6.1, Q_L provides the loaded Q-factor of the coil due to effective resistance of the implant electronics, which can be calculated using Equation 6.1 and 6.3. It can be seen that, for a given load resistance R_{load}, the Q_L of liquid metal and metal based coils do not differ significantly. In fact,

$$R_{eff} = Q_{ul}^2 R_{coil} || R_{load} \tag{6.2}$$

$$Q_L = \frac{R_{eff}}{2\pi f L_s} \tag{6.3}$$

where R_{coil} and L_s are the self resistance and self inductance of the secondary (implant) coil, respectively.

As expected, increasing the cross-sectional area decreases the resistance of the coil while lowering the inductance by about half. The results in Table 6.1 show that the unloaded Q factor of the secondary coil (Q_{ul}) increases with larger cross sectional area, for a given footprint and number of turns. We limited the width of the conductors to 200 μm to maintain the geometric requirements of the coil. We also limited the aspect ratio of the microfluidic channels to 3:1 (height to width) since the PDMS features can collapse at larger aspect ratios. The coils with the largest cross-sectional area

Table 6.1. Comparison: EGaIn and Metal Coils at 4 MHz (R_{load} = 217 Ω)

		EGaIn			Gold		
Secondary Coil Cross-section Width × Height	L_{coil} (μH)	R_{coil} (Ω)	Q_{ul}	Q_L	R_{coil} (Ω)	Q_{ul}	Q_L
$40\mu m \times 72\mu m$	2.03	33.64	1.52	1.12	3	17	3.40
$200\mu m \times 100\mu m$	1.40	4.81	7.31	3.35	0.57	62	5.60
$200\mu m \times 200\mu m$	1.32	2.38	14.25	4.45	0.42	79	6.04
$200\mu m \times 640\mu m$	0.86	1.26	17.19	6.33	0.13	166	9.46

($200\mu m \times 640\ \mu m$) are used in this study to demonstrate the feasibility of an inductively coupled wireless link that employs a liquid metal alloy implantable coil.

6.5 Design of Inductively Coupled Telemetry Link

In an inductively coupled telemetry link, the modulation of current/voltage in the primary coil changes the current/voltage in the secondary coil. The effectiveness of the electromagnetic coupling between the primary and the secondary coil is characterized by three parameters: power transfer efficiency (η), bandwidth, and voltage gain.

6.5.1 Power Transfer Efficiency (η)

The power transfer efficiency is the most important metric for a wireless telemetry link because it determines how much useful power the telemetry link delivers to the implant circuit per unit power supplied to the primary coil. The power transfer efficiency η of the telemetry link increases as the unloaded Q factor of the coils increases (by, for example, reducing the resistive losses of the coils). The power transfer efficiency is defined by the ratio of power at the secondary coil, P_{out}, to the power input to the primary coil, P_{in}:

$$\eta = \frac{P_{out}}{P_{in}} = \frac{k^2 Q_p Q_s}{1 + k^2 Q_p Q_s} \frac{R_{load}}{R_{load} + R_{parasitic}} \tag{6.4}$$

where $R_{parasitic}$ is the effective resistance due to the finite conductivity of the coil. Q_p and Q_s are the loaded Q factors of the primary (external) and secondary (implant) coil, respectively.

6.5.2 Voltage Gain

The voltage gain of the telemetry system is one of the key performance parameters to generate sufficient voltage across the implant electronics under the operating distance. In an application such as the retinal prosthesis, the output of the secondary coil feeds a rectifier and then to a voltage regulator to generate the voltage supply to the implant. As a result, voltage gain at the output of the secondary coil is desirable so that signal from secondary coil can be rectified to generate a higher average DC reference. Depending on the operating voltage and current in the implant, the electronics can be represented as an effective load resistance R_{load} (Figure 6.3(a)).

6.5.3 Bandwidth

A high Q factor results in lower frequency bandwidth. Thus, a trade-off exists between power transfer efficiency and resonance frequency bandwidth for a practical wireless telemetry link. Signals transmitted through an inductive link are typically narrowband (with common bandwidths ranging from tens to few hundreds of kHz). It is desired that voltage gain is maximum or close to maximum over the entire bandwidth of the transmitted signals. Thus, the 3 dB resonance bandwidth is an important metric in a practical telemetry link as beyond this bandwidth induced voltage will be less than half of maximum voltage at resonance [18].

6.5.4 Wireless Power/Data Link

The power transfer efficiency of the telemetry link circuit can be computed using the circuit diagram and the two-port model shown in Figure 6.3 [19]. In Figure 6.3(a), the key variables are self-inductance (L_p) and capacitance (C_p) of the primary coil, self-inductance (L_s) and capacitance (C_s) of the secondary coil, the primary coil series resistance (R_p) and the secondary coil series resistance (R_s). L_p and L_s can be estimated using the partial inductance modeling method, described in [20, 21].

The two-port model (Figure 6.3(b)) utilizes two-port measurements from a vector network analyzer to measure $Z_{21(eff)}$ and $Z_{11(eff)}$. Reference [19] shows that the power transfer efficiency η and voltage gain can be computed using Equations 6.5 and 6.6.

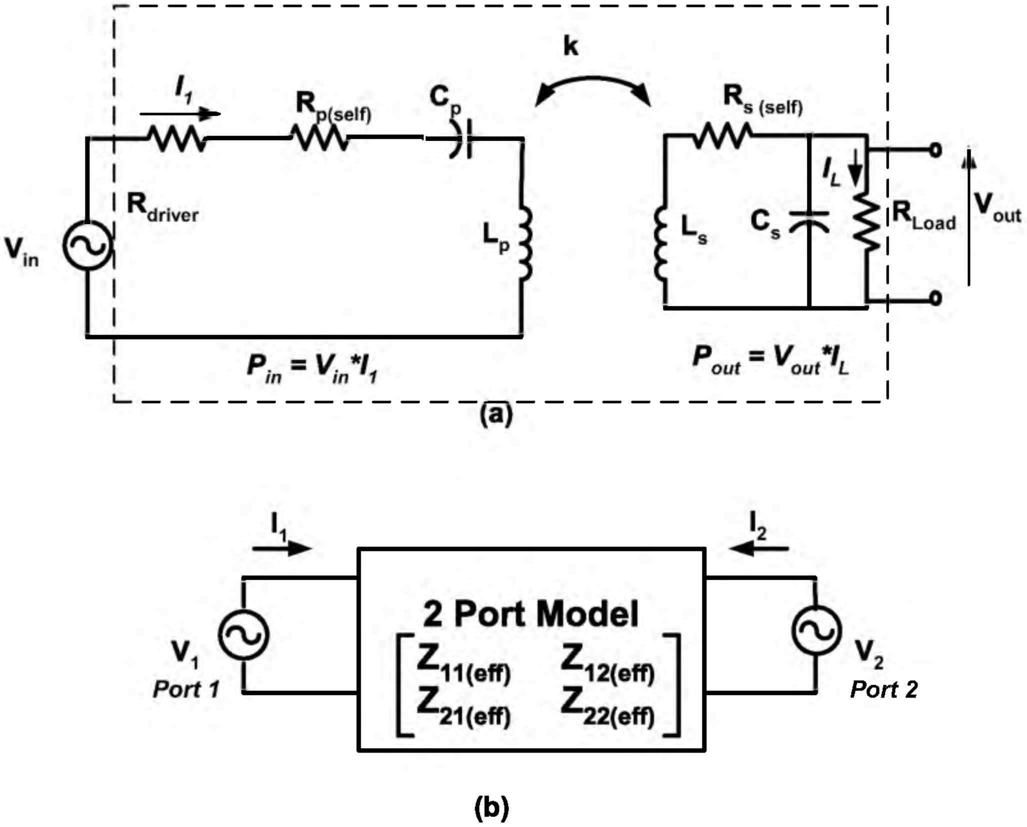

Figure 6.3. System model: (a) Circuit model of wireless power transfer and telemetry system. (b) Two-port model of inductive link using Z_{eff} [19] for efficiency and voltage gain measurement.

$$\eta = \frac{P_{out}}{P_{in}} = \frac{|Z_{21(eff)}(f)|^2}{R_{load}|Z_{11(eff)}(f)|} \tag{6.5}$$

$$Gain(f) = \frac{|V_{out}|}{V_{in}} = \frac{|Z_{21(eff)}(f)|}{|Z_{11(eff)}(f)|} \tag{6.6}$$

6.6 Experimental Results

To demonstrate the liquid metal coil based wireless power and data link, we conducted multiple experiments. The first experiment characterizes power transfer efficiency, voltage gain and frequency bandwidth of the inductive link for an axial separation of 12 mm between the coils. The second experiment characterizes the variation in power transfer efficiency and voltage gain as a function of coil separation and the third experiment identifies the effect of coil's curvature on the power transfer efficiency. Table 6.2 lists the specifications of the measurement setup. Figure 6.3(a) shows the circuit model of the telemetry link. C_p is the capacitance required to resonate the inductance of the primary and the secondary coils at 4 MHz. Q_{loaded} is the quality factor of the circuit when resistance from the driver (R_{driver}) and the load (R_{load}) are taken into account to calculate losses in the primary and the secondary coil circuits, respectively [22–24]. The assumed distance between the coils for retinal prosthesis system considered here is 12 mm [14]. The goal of the telemetry system is to be able to deliver more than 100 mW power to the high density retinal implant electronics, which presents an effective load electronics resistance close to 220 Ω [25]. To

Table 6.2. System Specifications

	Primary Coil	Secondary Coil
Coil Type	Circular	Elliptical
Outer Diameter $D_{outD}(mm)$	37	16×10
Inner diameter $D_{inD}(mm)$	19	8.5×3.5
Number of turns N_D	12	10
Self inductance $L_d(\mu H)$	4.98	0.862
Series resistance $R_{self}(\Omega)$	0.5	1.26
$Q_{unloaded}$	250	17.19
$R_{driver}(\Omega)$	5.3	
$R_{Load}(\Omega)$		217
Q_{loaded}	21.57	6.32
$C_d(nF)$	0.319	1.82
Wire (AWG) Type	44/100^1	EGaIn liquid coil $200\mu m \times 640\mu m$
Load Type		Parallel

simulate the coil inductance and coupling, the partial inductance method is used. The simulation of the telemetry system is performed using a network model based on our previous work, found in [19].

6.6.1 Power Transfer Efficiency (η)

Figure 6.4 shows the measured and calculated power transfer efficiency of the telemetry link as a function of frequency. As expected, the maximum power transfer efficiency occurs at the resonance frequency of the system (4 MHz). Figure 6.4 also contains a plot of Equation 6.5. The parameters for Equation 6.5 were obtained by extracting mutual and self-inductances of the two coils using the partial inductance model of the two coils [15, 20]. The numerically calculated results obtained using Equation 6.5 agree well with the measured results. The link achieved 21 % power transfer efficiency at 12 mm separation between primary and secondary coils, which is in the higher range of acceptable efficiency values [24]. By using the same footprint and the same operating conditions, a power transfer efficiency of 39 % can be achieved by employing a traditional metal (Gold) implant coil (Figure 6.4).

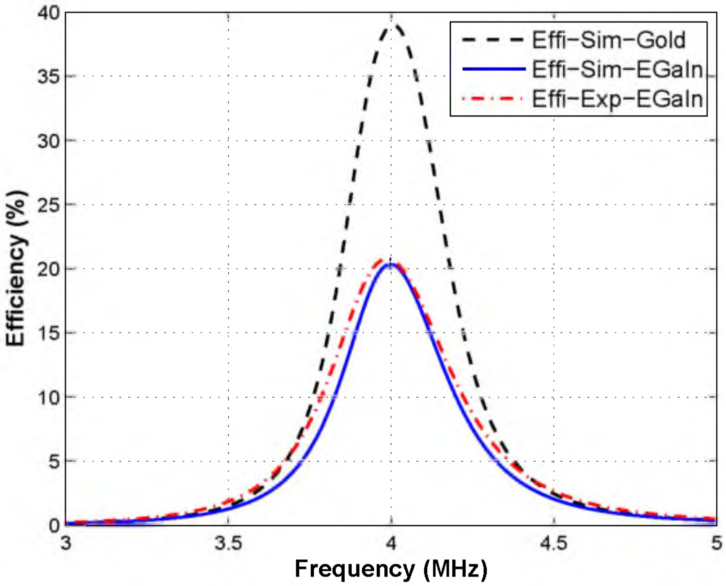

Figure 6.4. Simulated and experimental power transfer efficiency of liquid coil based telemetry link as a function of frequency compared to telemetry link with metal based implant coil. The operating distance is set to 12 mm. The design parameters are based on Table 6.2.

6.6.2 Bandwidth and Voltage Gain

Figure 6.5 shows the measured and numerically calculated voltage gain as a function of frequency. The design shows a 3 dB frequency bandwidth of 230 KHz (5.75 % fractional bandwidth), which is wide enough to support moderate data rate of 100 kbps to transmit narrowband signals such as control and data to/from the implant over the inductively coupled wireless telemetry systems. The numerical model matches the voltage gain of the experimental results. Due to higher resistive losses in EGaIn, liquid metal based telemetry link achieves voltage gain value 23 % below the voltage gain of metal (Gold) based telemetry link (Figure 6.5).

Figure 6.6 shows the power transfer efficiency variation as a function of coil separation. Decrease in separation between the coils only increases the coupling between the primary and the secondary coils. Calculated results and measurements of efficiency as a function of coil separation are in very close agreement. As expected, the power transfer efficiency increases as the primary and secondary coils approach each other (due to higher coupling coefficients).

Since liquid metal alloy coils can flex and conform to surfaces, we present in Figure 6.7 a comparison of power transfer efficiency for a planar secondary coil and a coil conformal to a sphere (radius of curvature of 36 mm). Figure 6.8 shows a picture of the experimental setup.

Figure 6.7, shows that power transfer efficiency decreases from 21 % to 15 % when flexible secondary coil is nonplanar. This reduction is due to reduction in coupling between coils when the

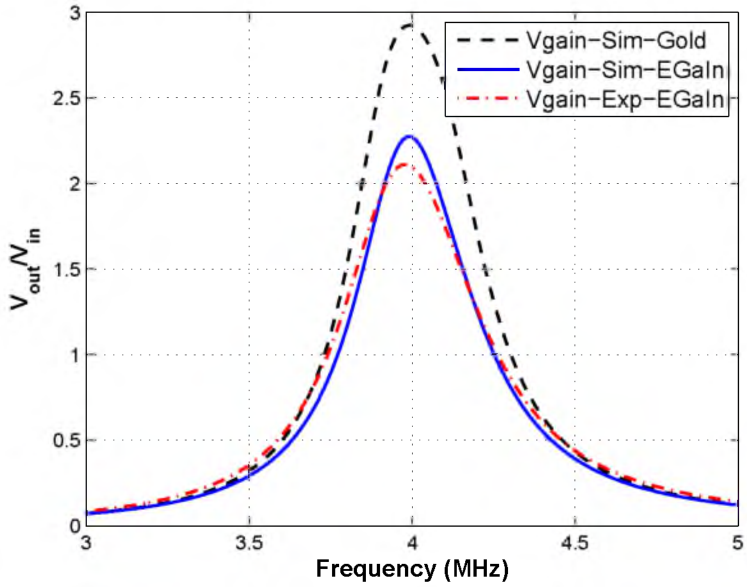

Figure 6.5. Simulated and experimental voltage gain of liquid coil based telemetry link as a function of frequency compared to telemetry link with metal based implant coil. The operating distance is set to 12 mm. The design parameters are based on Table 6.2.

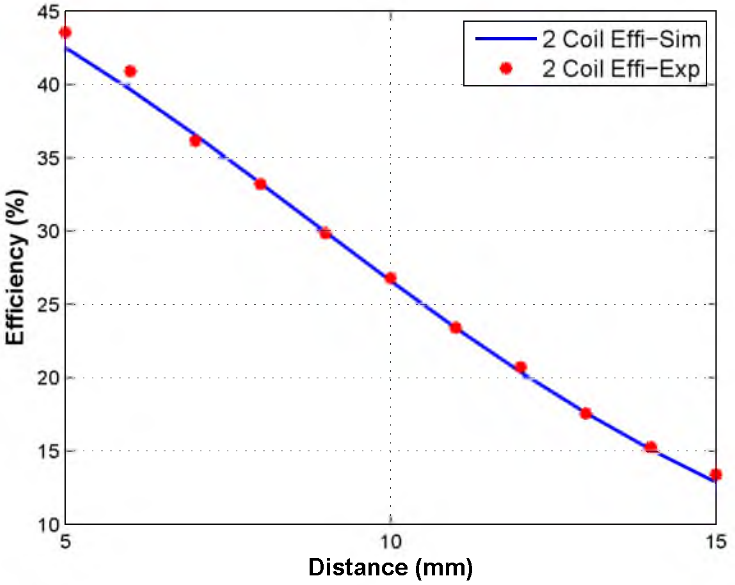

Figure 6.6. Simulated and experimental power transfer efficiency of liquid coil based telemetry link as a function of coil separation. The operating frequency is set to 4 MHz. The design parameters are based on Table 6.2.

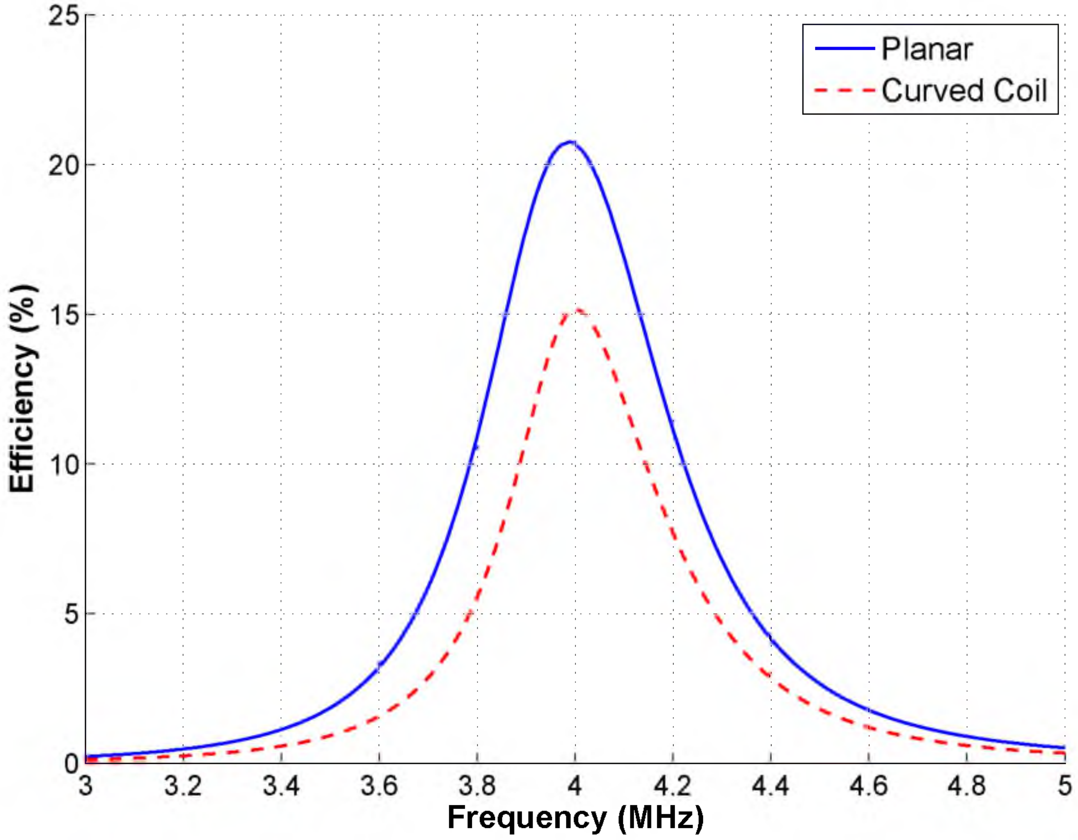

Figure 6.7. Comparison of power transfer efficiency when the flexible secondary coil is planar (solid blue) and curved (red dash dot) around a sphere of diameter 36 mm. The separation between the primary and the secondary coil centers was maintained as 12 mm in both cases.

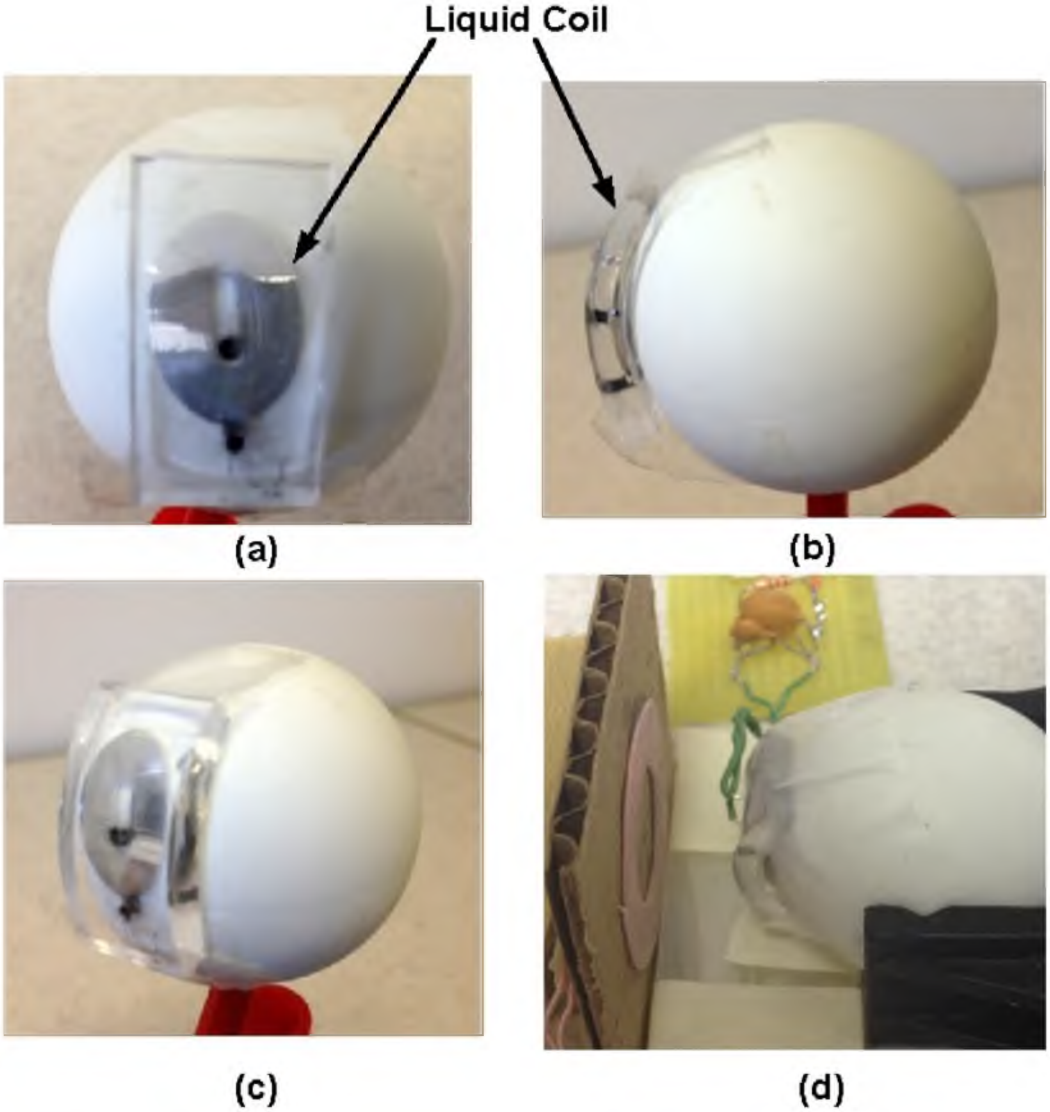

Figure 6.8. Photographs of the telemetry coil setup. (a) Front view (b) side view and (c) perspective view of the curved liquid coil on the sphere of diameter 36 mm. (d) Telemetry link setup consists of primary and liquid metal based secondary coil.

secondary coil curves away from the primary coil. Similar percentile reductions are observed with traditional metal-based coils.

6.7 Conclusions

Applications such as the retinal prosthesis often require biocompatible flexible coils for wireless telemetry links that can be deformed during implantation and conformed to the tissue. In this work, we reported the fabrication of soft and flexible telemetry coils for the wireless, near field, transfer of data and power. The coils described here are elastomeric (i.e., stretchable) and encased by a biocompatible polymer. Despite the relatively low conductivity of the liquid metal (relative to gold or copper), we achieved sufficient Q factor (for a given footprint) by varying the cross-sectional geometry of the wire. This liquid metal based coil can be successfully employed in a telemetry system used to deliver power to the implant coil efficiently, with the added benefit of being flexible, stretchable, and conformable. We demonstrated the use of a liquid metal coil in an inductively coupled wireless telemetry link with a power transfer efficiency of 21 % and a fractional bandwidth of 5.75 % which is at the higher end of acceptable efficiency range for a 12 mm separation between coils [1]. Under the same operating conditions and footprint, the proposed flexible coil results in an acceptable degrade in power transfer efficiency (PTE) (reduction by 46 %) compared to metal based implant coils, while achieving high flexibility and stretchability for implantation and operation.

While we focused in this work on the design of a wireless telemetry for a retinal prosthesis system, there are many other applications that use inductively coupled coils for wireless power and data transfer including wireless battery chargers, cardiac implants, glucose monitoring implants, near field communication coils in smart phones and RFIDs that could find this technology useful. In such applications the geometrical restrictions on the design of the telemetry coils are not as stringent and may utilize different number of turns, foot print size, and pitch. Our work suggests that the cross-section of the liquid metal alloy wire can be used to improve effective power transfer efficiency without varying other geometric parameters.

6.8 References

[1] V. Singh, A. Qusba, A. Roy, R. Castro, K. McClure, R. Dai, R. Greenberg, J. Weiland, M. Humayun, and G. Lazzi, “Specific absorption rate and current densities in the human eye and head induced by the telemetry link of an epiretinal prosthesis,” *IEEE Transactions on Antennas and Propagation*, vol. 57, no. 10, pp. 3110 –3118, Oct. 2009.

[2] V. Singh, A. Roy, R. Castro, K. McClure, R. Dai, R. Agrawal, R. Greenberg, J. Weiland, M. Humayun, and G. Lazzi, “On the thermal elevation of a 60-electrode epiretinal prosthesis for the blind,” *IEEE Transactions on Biomedical Circuits and Systems*, vol. 2, no. 4, pp. 289 –300, Dec. 2008.

[3] K. Chen, Z. Yang, L. Hoang, J. Weiland, M. Humayun, and W. Liu, "An integrated 256-channel epiretinal prosthesis," *IEEE Journal of Solid-State Circuits*, vol. 45, no. 9, pp. 1946 –1956, Sept. 2010.

[4] M. S. Humayun, E. D. J. Jr., G. Dagnelie, R. J. Greenberg, R. H. Propst, and H. Phillips, "Visual perception elicited by electrical stimulation of the retina in blind humans," *Arch. Ophthalm.*, vol. 114, pp. 40–46, 1996.

[5] M. Dickey, R. Chiechi, R. Larsen, E. Weiss, D. Weitz, and G. Whitesides, "Eutectic gallium-indium (egain): A liquid metal alloy for the formation of stable structures in microchannels at room temperature," *Advanced Functional Materials*, vol. 18, pp. 1097–1104, 2008.

[6] W. M. Haynes, *CRC Handbook of Chemistry and Physics, 92nd Edition.* CRC Press/Taylor and Francis, Boca Raton, FL, 2012.

[7] F. J. Shaini, R. M. Shelton, P. M. Marquis, and A. C. Shortall, "In vitro evaluation of the effect of freshly mixed amalgam and gallium-based alloy on the viability of primary periosteal and osteoblast cell cultures," *Biomaterials*, vol. 21, pp. 113–119, 2000.

[8] A. Drasima, L. Maffioli, M. Gasparini, G. Savelli, E. Pauwels, and E. Bobardieri, "Gallium-67 as a tumor-seeking agent in lymphomasa review," *Tumori*, vol. 84, pp. 434–441, 1998.

[9] J.-H. So, J. Thelen, A. Qusba, G. J. Hayes, G. Lazzi, and M. D. Dickey, "Reversibly deformable and mechanically tunable fluidic antennas," *Advanced Functional Materials*, vol. 19, no. 22, pp. 3632–3637, 2009.

[10] M. Kubo, X. Li, C. Kim, M. Hashimoto, B. J. Wiley, D. Ham, and G. M. Whitesides, "Stretchable microfluidic radiofrequency antennas," *Advanced Materials*, vol. 22, no. 25, pp. 2749–2752, 2010.

[11] M. Rashed Khan, G. Hayes, J.-H. So, G. Lazzi, and M. Dickey, "A frequency shifting liquid metal antenna with pressure responsiveness," *Applied Physics Letters*, vol. 99, no. 1, pp. 13 501–13 503, 2011.

[12] S. Cheng, A. Rydberg, K. Hjort, and Z. Wu, "Liquid metal stretchable unbalanced loop antenna," *Applied Physics Letters*, vol. 94, no. 14, pp. 144 103–144 105, April 2009.

[13] G. J. Hayes, J.-H. So, A. Qusba, M. D. Dickey, and G. Lazzi, "Flexible liquid metal alloy (egain) mircrostrip patch antenna," *IEEE Transactions on Antennas and Propagation*, vol. 60, no. 10, pp. 2151–2156, May 2012.

[14] A. Qusba, "Design of flexible coils in an inductively-coupled telemetry system for the epiretinal prosthesis," Ph.D. dissertation, North Carolina State University, Raleigh, NC, 2011.

[15] J. Gielis, "Generic geometric transformation that unifies a wide rage of natural and abstract shapes," *American Journal of Botany*, vol. 3, no. 90, pp. 333–338, 2003.

[16] N. Tiercelin, P. Coquet, R. Sauleau, V. Senez, and H. Fujita, "Polydimethylsiloxane membranes for millimeter-wave planar ultra flexible antennas," *Journal of Micromechanics and Microengineering*, vol. 16, no. 11, pp. 2389–2395, 2006.

[17] H. Cong and T. Pan, "Microfabrication of conductive pdms on flexible substrates for biomedical applications," in *Proc. of IEEE International Conference on Nano/Micro Engineered and Molecular Systems, 2009*, Jan. 2009, pp. 731 –734.

[18] T. H. Lee, *The Design of CMOS Radio-frequency Integrated Circuits*. New York: Cambridge University Press, 2004.

[19] A. K. RamRakhyani and G. Lazzi, "On the design of efficient multi-coil telemetry system for biomedical implants," *IEEE Transactions on Biomedical Circuits and Systems*, no. 1, pp. 11–23.

[20] M. Beattie and L. Pileggi, "Inductance 101: modeling and extraction," in *Design Automation Conference, 2001. Proceedings*, 2001, pp. 323 – 328.

[21] A. E. Ruehli, "Inductance calculations in a complex integrated circuit environment," *IBM Journal of Research and Development*, vol. 16, no. 5, pp. 470 –481, Sept. 1972.

[22] F. E. Terman, *Radio Engineering Handbook*. New York: McGraw-Hill, 2005.

[23] A. Djemouai and M. Sawan, *Prosthetic Power Supplies*. John Wiley & Sons Inc., 2001.

[24] R. Harrison, "Designing efficient inductive power links for implantable devices," in *Proc. ISCAS*, 2007, pp. 2080–2083.

[25] K. Chen, Z. Yang, L. Hoang, J. Weiland, M. Humayun, and W. Liu, "An integrated 256-channel epiretinal prosthesis," *IEEE Journal of Solid-State Circuits*, vol. 45, no. 9, pp. 1946–1956, 2010.

CHAPTER 7

STUDY OF CORE'S NONLINEARITY FOR MAGNETIC NEURAL STIMULATION

Anil Kumar RamRakhyani, Gianluca Lazzi, "Numerical Modeling of Cores Nonlinearity for Magnetic Neural Stimulation," submitted to IET Healthcare Technology Letters.

7.1 Abstract

This paper is motivated by the need to correctly predict the voltage across terminals of mm size coils, with ferrite core, to be employed for magnetic stimulation of the peripheral neural system. In such applications, which rely on a capacitive discharge on the coil to realize a transient voltage curve of duration and strength suitable for neural stimulation, the correct modeling of the nonlinearity of the ferrite core is critical. In this work, we demonstrate how a Finite-Difference model of the considered coils, which include a model of the current-controlled inductance in the coil, can be used to correctly predict the time-domain voltage waveforms across the terminals of a test coil. Five coils of different dimensions, loaded with ferrite cores, have been fabricated and tested; measured magnitude and width of the induced pulse are within 10 % of simulated values.

7.2 Introduction

Magnetic fields cover an important role in several biomedical devices and diagnostic equipment. From the point of view of neurostimulation, transcranial magnetic stimulation is one of the non-invasive techniques for the stimulation of the central nervous system. It uses time-varying magnetic fields to induce eddy currents in the tissue and elicit neural stimulation [1]. Compared to an electrical stimulator, a magnetic neurostimulator can provide reliable stimulation over a long period due to its contact-less stimulation mechanism. In the literature, several approaches have been considered to employ magnetic core based coils to generate high induced electric fields using small dimension coils (diameter 4-12 mm) [1, 2]. Traditionally, these designs use expensive magnetic cores with high permeability ($\mu_r \sim 20000$) and high magnetic field saturation (~ 2 Tesla). Despite the advances in the use and analysis of relative large coils for neurostimulation, external to the human body, the development of small coils for possible implantation still faces significant challenges. Among these challenges, the behavior of small ferrite loaded coils to be used in implants and, in particular, the effect of saturation on the waveform of these neurostimulators has not been well studied.

Most magnetic materials (iron, ferrite) are nonlinear and dispersive. Their relative magnetic permeability (μ_r) varies with the applied magnetic field intensity ($\overrightarrow{H}$) and operating frequency. Due to changes in the μ_r with respect to field intensity, inductors with a magnetic core show a nonlinear inductance as a function of applied current. In the case of small size, ferrite-loaded, coils for neurostimulation a linear inductor model is no longer valid [3], and the correct prediction of the nonlinear effect in the inductor is critical to determine the potential effectiveness of these coils for magnetic stimulation. In fact, for magnetic stimulation, the calculation of electric field distributions (spatial and temporal) in the proximal region of the stimulus coil is required to predict the stimulation site and to optimize the design under system constraints. Therefore, numerical modeling of the system is required to predict the field distribution of magnetic core based magnetic stimulator.

In this work, we demonstrate how a Finite-Difference model of the considered coils, which include a model of the current-controlled inductance in the coil, can be used to correctly predict the time-domain voltage waveforms across the terminals of a test coil. We employ a nonlinear ferromagnetic core [4] and the time domain numerical simulation incorporates the nonlinearity of μ_r as the function of current in the coil. The correct knowledge of the voltages and fields associated with the small implantable coils is critical for the prediction of the effectiveness of these coils for neuromagnetic stimulation.

7.3 Magnetic Coils with Ferrite Core

Magnetic stimulation is based on the electromagnetic induction principle. The magnetic field intensity $\vec{B}$ can be written in terms of magnetic vector potential $\vec{A}$ [5]. Induced eddy current $\vec{J}(r,t)$ at location r in the tissue can be calculated using conductivity $\sigma(r)$ and magnitude of the electric field $\vec{E}(r,t)$.

$$\begin{aligned} \vec{\nabla}\times\vec{E} &= -\frac{\partial\vec{B}}{\partial t} = -\frac{\vec{\nabla}\times\vec{A}}{\partial t} && (7.1)\\ \vec{E}(r,t) &= -\frac{\partial\vec{A}(r,t)}{\partial t} - \vec{\nabla}V(r,t) && (7.2)\\ \vec{J}(r,t) &= \sigma(r)\vec{E}(r,t) && (7.3) \end{aligned}$$

where $\vec{\nabla}V(r,t)$ is the electric field contribution by the surface charge.

The neural stimulation threshold generally depends on the strength and the duration of the induced electric field pulse. In general, and within a certain operating window, the threshold is inversely proportional to the pulse duration of the induced electric field. Therefore, to design an efficient magnetic stimulator, the induced electric fields should be maximized while maintaining a sufficient pulse width. For a fixed current in the coil, a magnetic material based coil is expected to increase the magnetic field generated in close proximity of the coil, as compared to an air-cored coil. However, due to high currents in the coil, these magnetic cores may saturate, deteriorating the performance of the system.

Figure 7.1 shows a typical configuration of the magnetic stimulator, which requires a charging capacitor. At the stimulation instant, the charge stored in the capacitor causes a time-varying current in the coil. For an inductor L_i (constant or current dependent) and capacitor C, a pulse discharge circuit can be solved to compute the capacitor voltage V_c and current I in the coil (Figure 7.1 (a)).

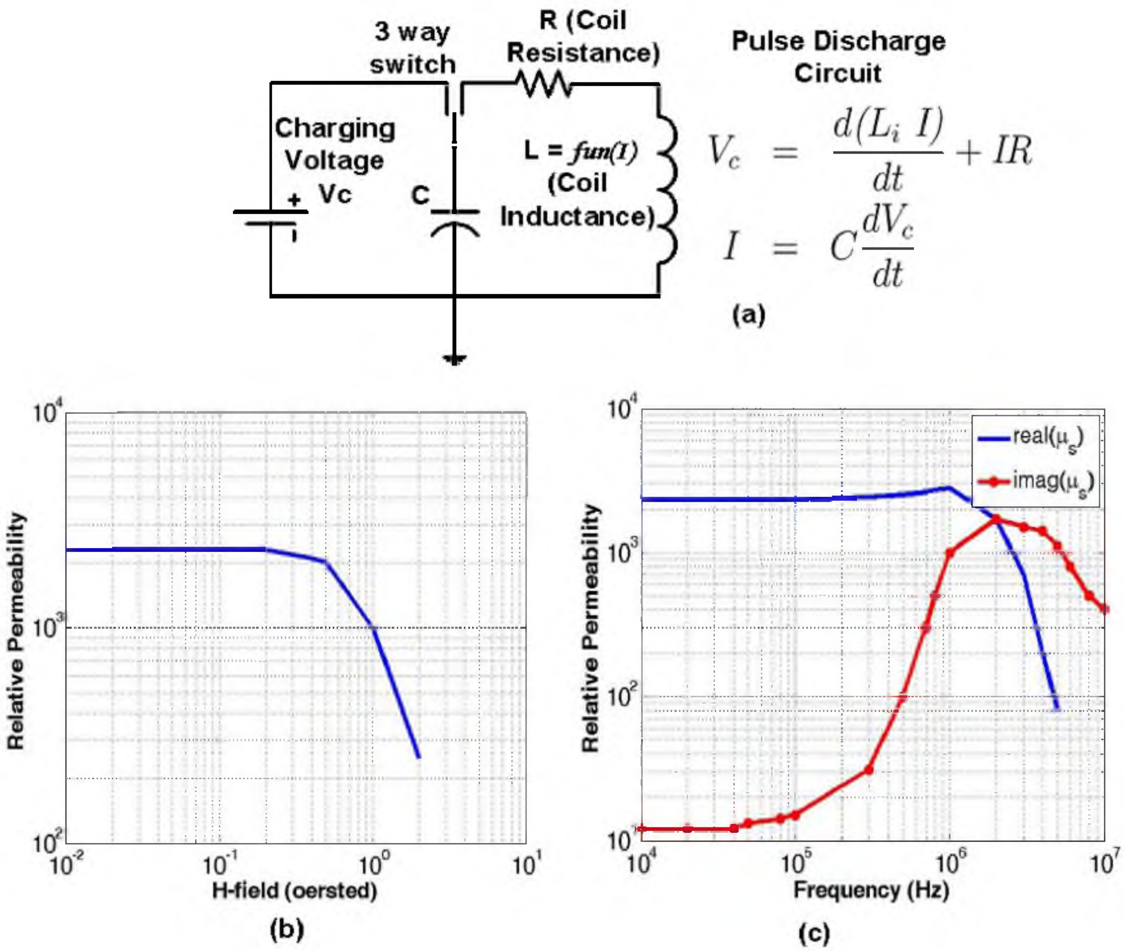

Figure 7.1. Magnetic stimulator model: (a) Simplified schematic of a pulse-discharged based magnetic stimulator. Variation of the core's permeability with respect to (b) H-field and (c) operating frequency [6].

7.4 Numerical Modeling

As compared to a toroid coil, solenoid coils provide more flexibility to position the magnetic coil near the stimulation site. For solenoid coils, the current-carrying wire is wrapped over a circular magnetic core. Figure 7.2 (a) shows the block diagram of a fabricated coil. The typical pulse width of the magnetic stimulator is on the order of 100-500 μs, which restricts the frequency component of the current pulse into sub-kHz region. Thus, for small dimension magnetic coils at sub-kHz operating frequency, quasi-static approximation is reasonably valid for the field simulation.

For a solenoid coil, the current is in the $\vec{a}_\phi$ direction resulting in a single component vector potential $\vec{A}_\phi$. We developed a finite difference model and a Poisson equation solver to simulate the electric and magnetic field distribution near the magnetic coil (Equation 7.4, [7]). The $\vec{B}$-field is calculated by taking the curl of $\vec{A}_\phi$ (Equation 7.5) [7].

$$\frac{\partial}{\partial z}\left(\frac{1}{\mu_r(r,z)r}\frac{\partial(r\vec{A}_\phi)}{\partial z}\right)+\frac{\partial}{\partial r}\left(\frac{1}{\mu_r(r,z)r}\frac{\partial(r\vec{A}_\phi)}{\partial r}\right)=-\mu_0\vec{J}_\phi(r,z) \tag{7.4}$$

$$\vec{B}=\frac{1}{r}\left(\frac{\partial(r\vec{A}_\phi)}{\partial z}\right)\vec{r}-\frac{1}{r}\left(\frac{\partial(r\vec{A}_\phi)}{\partial r}\right)\vec{z} \tag{7.5}$$

An empirical model of the magnetic material's permeability as a function of $\vec{H}$-field is developed from the manufacturer's specification [6] (Figure 7.1 (b)). A 3-dimensional finite difference model of the solenoid coil is created to include the coil wires and magnetic core (Figure 7.2 (a)). Figure 7.2 shows the induced vector potential $\vec{A}_\phi(r,z)$ and $\vec{B}$-field distribution by solving Equation 7.4 and 7.5 for one of solenoid coil (A9, Table 7.1).

To model the effect of the current in the coil on the core's saturation, the proposed electric field solver is used and the coil's inductance is modeled as a function of the current in the magnetic coil ($L_{coil}=fn(I)$). For the time domain simulation, the pulse discharge circuit (Figure 7.1) is defined using the charging capacitance C, the current controlled coil inductance $L_{coil}(I)$, the coil's resistance R and the DC voltage V. Time step is linearly varied until the maximum simulation time. For each time step $K+1$, the coil current and the capacitor voltage are calculated by solving the differential equation given by Equation 7.6. With the calculated value of the current, the new value of the magnetic coil's inductance is calculated using the derived empirical formulation of the inductance of the coil ($L_{coil}=fn(I)$).

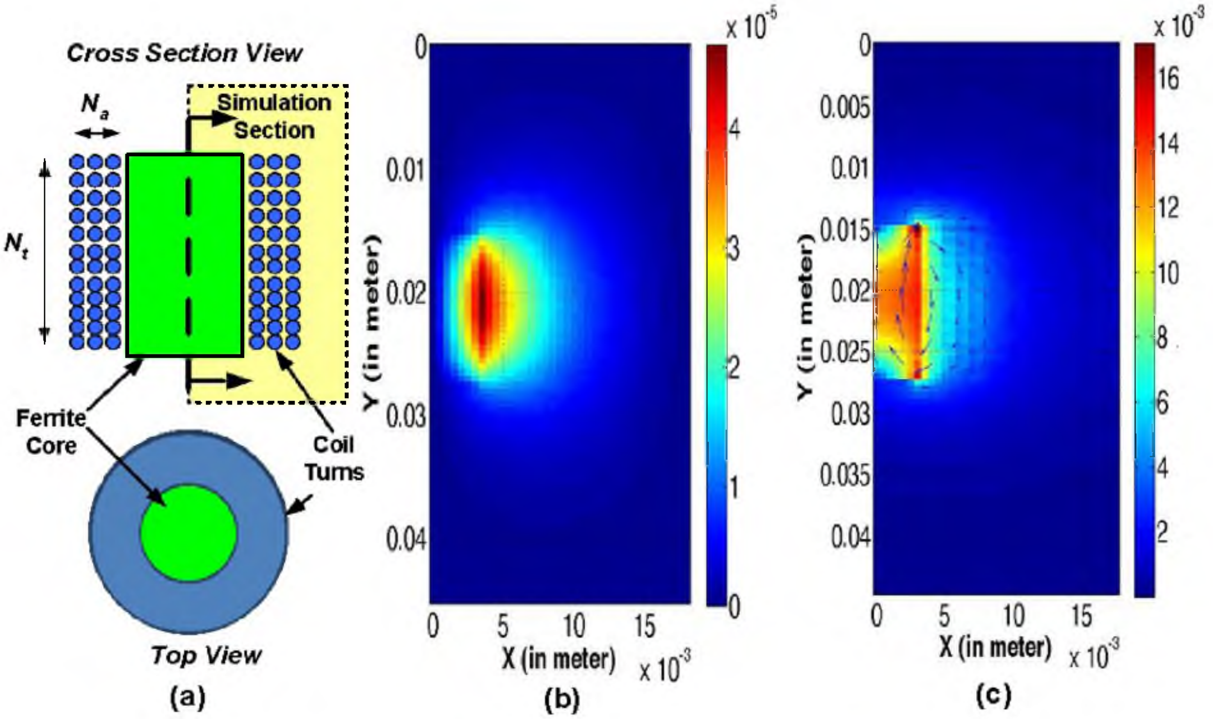

Figure 7.2. Numerical modeling: (a) Block diagram of solid coil (Top and cross section view) (b) Magnetic vector potential and (c) B-field due to coil *A*9 for unity current and unity frequency. Vector potential is V.s/m and B-field is in Tesla.

Table 7.1. Mechanical Dimensions

Coil Number	(O.D.,I.D) (mm)	Length (mm)	Turns per layer	Core
A1	(12,6)	18	(15,15,14)	Ferrite
A2	(12,7)	15	(15,15,15)	Wood
A3	(14,6)	12	(12,11,10,9)	Ferrite
A4	(9,6)	12	(12,11)	Ferrite
A9	(16,6)	12	(12,12,11,12,9)	Ferrite
Test	(9,8)	4	(4)	air

$$\begin{aligned}
V(t) &= \frac{d(L_i\,I)}{dt} + IR = I\frac{dL_{coil}(I))}{dt} + L_{coil}(I)\frac{dI}{dt} + IR \\
I(K+1) &= I(K)\left[2 - \frac{L(K+1)}{L(K)} - \frac{R\Delta t}{L(K)}\right] + \frac{V(K)\Delta t}{L(K)} \\
V(K+1) &= V(K) - \frac{I(K+1)\Delta t}{C} \qquad (7.6)
\end{aligned}$$

Using the developed hybrid solver for the spatial and temporal distribution of the induced electric field, the effect of the nonlinear inductor can be included in the optimization step to design a magnetic neural stimulator.

7.5 Experimental Validation

To validate the accuracy of the numerical models, five inductors were fabricated using different core types and with a different number of turns (Table 7.1). Using two techniques (inductance measurements and induced voltage in a test coil), the accuracy of the simulated spatial and temporal distributions of the induced electric field is validated.

7.5.1 Inductance Calculation

Four coils have been built using a ferrite magnetic core, while one coil is built using a non-magnetic material core. For the calculation of the inductance, a unity test current of 1 A at a frequency 1 Hz is used to calculate the coil's inductance with vector potentials ($L = \vec{A}.\vec{dl}$). Table 7.2

Table 7.2. Electrical Properties

Coil Number	Inductance (μH) (calculated)	Inductance (μH) (measured)	core	Resistance Ω
A1	38.25	43	Ferrite	0.057
A2	8.91	9.2	Wood	0.065
A3	31.28	31.54	Ferrite	0.047
A4	10.479	11.19	Ferrite	0.028
A9	52.41	54.21	Ferrite	0.071

shows that all measured values of the inductances are in close agreement with the simulated values, with a maximum error of 10%, which is primarily attributable to the uniformity of the coil winding.

7.5.2 Induced Electric Field Simulation

To design an optimum magnetic stimulator, the induced field strength needs to be maximized with a reasonably wide pulse width ($\sim$ 100-500 μs). Figure 7.3 shows the magnetic stimulator board (PCB) that utilizes an electrolytic capacitor ($C = 2200$ μF) with the timing and driver electronics. The PCB traces cause a stray impedance of 0.1 Ω in the discharge path of the capacitor. The magnetic coil is attached to the stimulator board to create time-varying current and thus a time varying $\vec{B}$ field. To validate the simulated induced E-field values, a test coil (Table 7.1) is positioned in close proximity to the magnetic coil as shown in Figure 7.3. The induced voltage in the test coil, which is linearly proportional to the induced electric field, is recorded by an oscilloscope.

For a high power magnetic stimulator, the magnetic core is prone to saturate, affecting the induced electric field configuration. Thus, peak-induced voltage in the test coil, time of core saturation, and pulse width are considered the three key features of the stimulus pulse. Figures

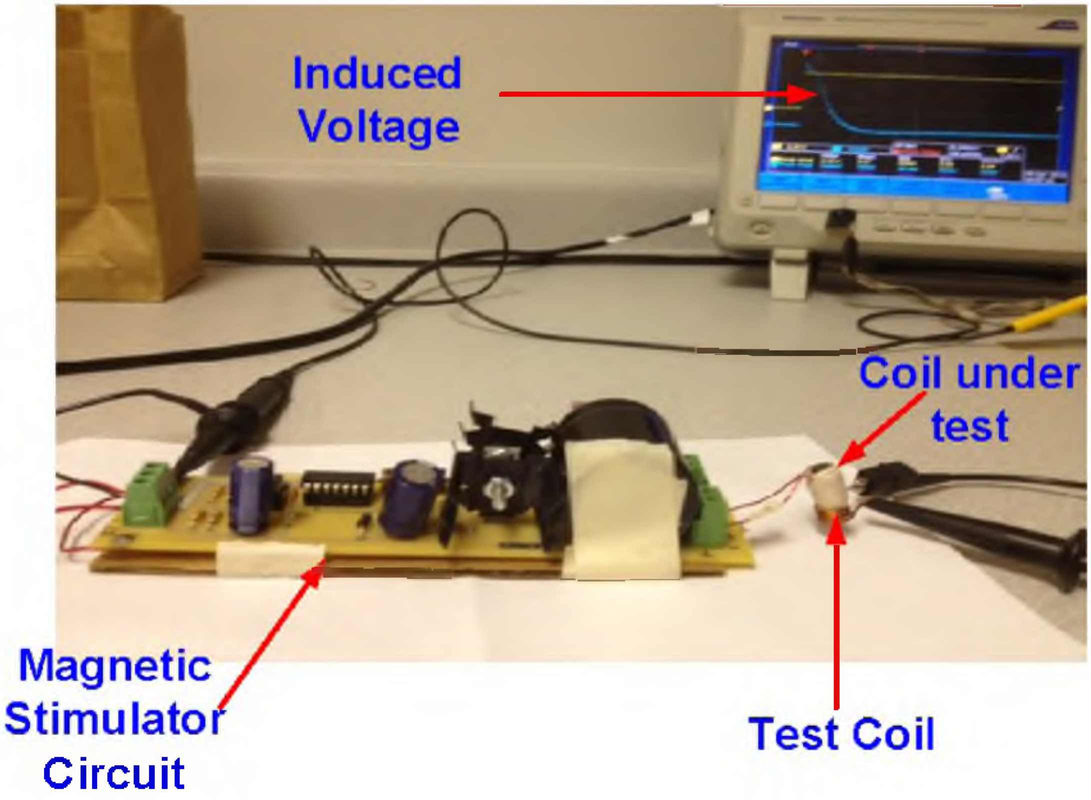

Figure 7.3. Magnetic stimulator test setup consisting of stimulator board, coil under test, and test coil.

7.4 and 7.5 show the simulated and experimental induced voltages at the test coil terminal due to change in the current of the magnetic coil. A difference in the induced waveform after the saturation point, which is caused by the low-pass behavior of the permeability as a function of frequency, can be observed. It should be noted that, in the simulation, the permeability of the ferrite core is considered independent of the operating frequency, which is not realistic for the practical ferrite cores. Figure 7.1 (c) shows the variation of μ_r as a function of the frequency. The permeability of the magnetic core shows a low pass-filter response as a function of frequency and, therefore, does not allow a fast change in its value. However, for the key features of the magnetic stimulation, such as the peak induced voltage, the time of saturation, and the zero crossing (pulse duration), the simulated and the measured waveform are in good agreement.

7.5.2.1 Effect of Charging Voltage

To identify the peak value of the induced voltage as a function of the capacitor charging voltage, the induced voltage in the test coil is simulated and measured for capacitor charging voltages of 5 V, 10 V, 15 V, and 25 V (Figure 7.4 (a), (b)). It can be seen that the peak induced voltage varies linearly with the change in the capacitor's initial voltage. Since the coil's current is proportional to the initial voltage of the capacitor, increasing the voltage causes the magnetic core to saturate faster. Table 7.3 shows the simulated saturation time of coil-$A9$ as a function of input voltage and shows that the saturation time decreases linearly with increasing voltage. Due to fast saturation of the core with the increase in voltage, the pulse width (zero-crossing) also decreases. Table 7.3 shows the comparison between the simulation and experimental results: the simulation can accurately predict the key design parameters of the magnetic stimulator, including peak E-field, saturation point, and zero-crossing time.

7.5.2.2 Effect of Coil Configuration

Figure 7.5(a), (b) show the simulated and measured induced voltage across the test coil for different coils, and provides different peak induced voltage, saturation time, and zero crossing time. For the same capacitor, a low inductive magnetic coil shows a faster decay rate due to the faster change in the coil current. It can be seen that, before saturation, the rate of decay in the induced voltage reduces with the increase in the inductance of the coil. For example, coil $A9$ shows slower decay with time in the induced voltage as compared to coil $A4$. After saturation of the core, ferrite-cored coils behave as air-cored coils and cause a faster decay in the induced voltage. Thus, coils with a lower number of turns show a faster decay rate after saturation.

Table 7.4 compares the performance of each coil on the basis of peak induced voltage, saturation time, and zero-crossing time. Coil $A9$ shows the highest pulse width with moderate peak induced

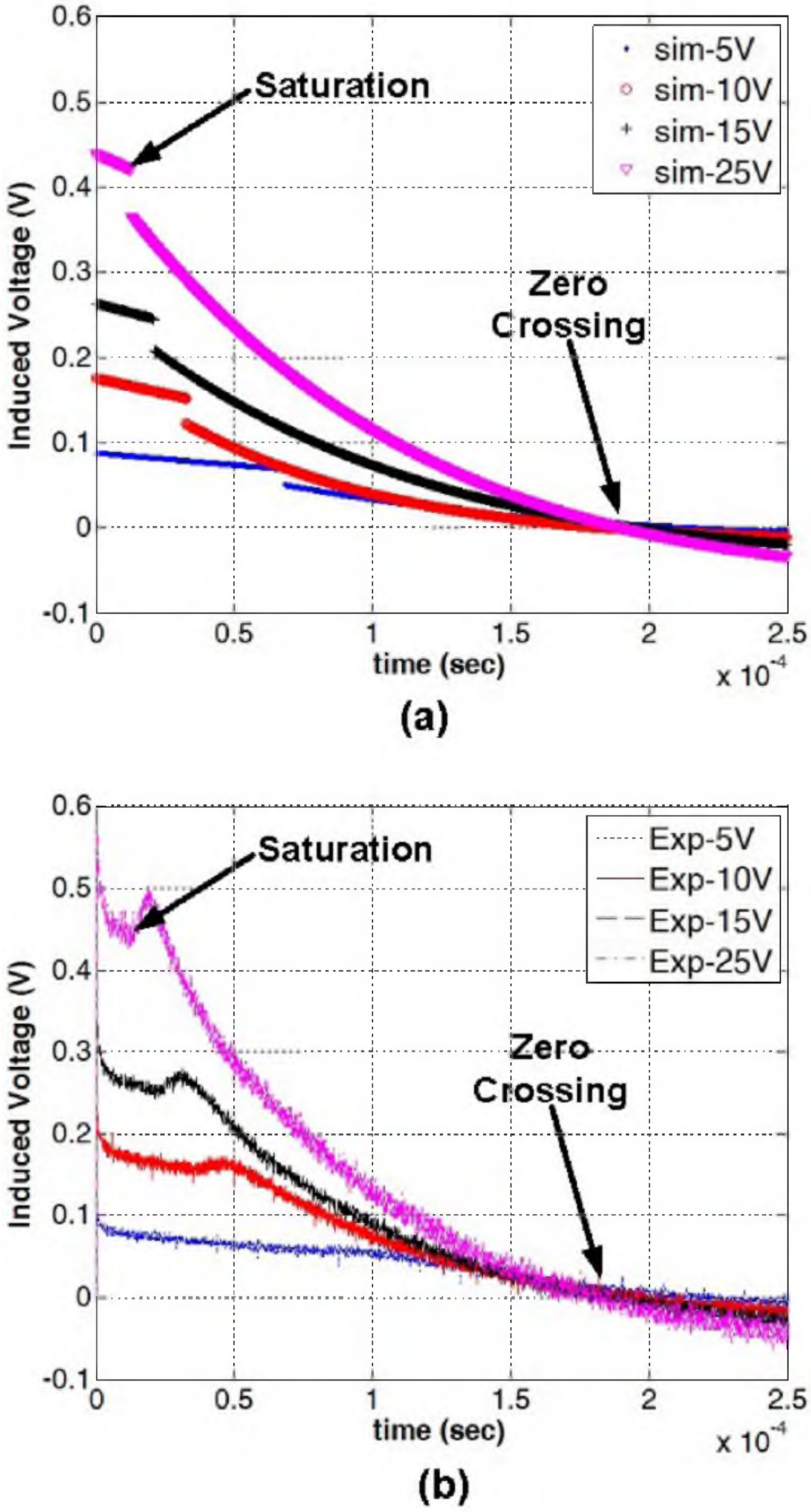

Figure 7.4. Effect of charging voltage: (a) Simulated and (b) measured induced voltage waveforms due to coil *A*9 across the test coil terminals with varying charging voltage.

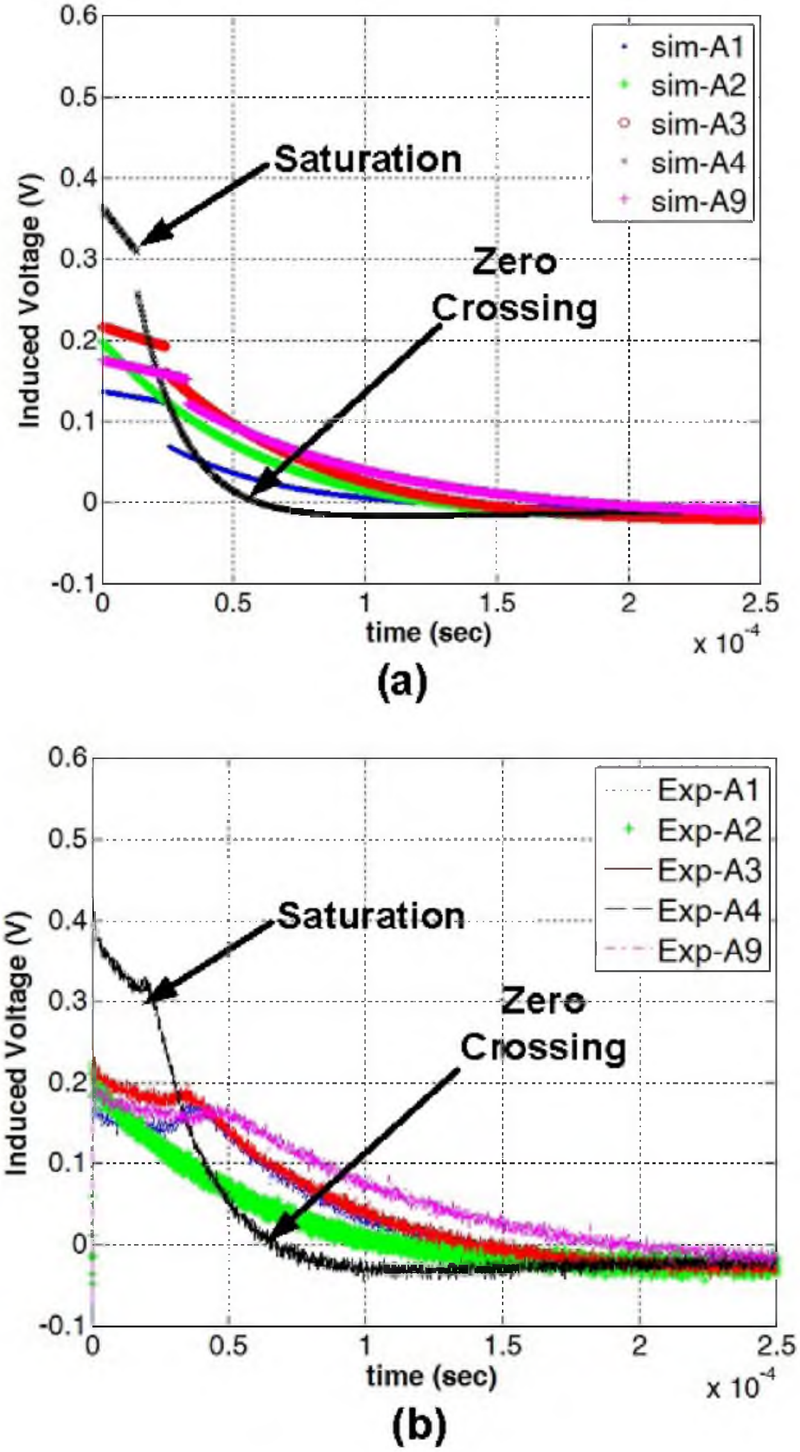

Figure 7.5. Effect of coil configuration: (a) Simulated and (b) measured induced voltage waveforms due to different coil configurations with charging voltage of 10 V.

Table 7.3. Coil A9- Pulse Properties

Capacitor Voltage	Peak Induced Voltage(sim,meas)	Saturation time (sim,meas)	Zero Crossing (sim,meas)
5 V	(0.09 V, 0.09 V)	(68.2μs, 70μs)	(215μs, 216μs)
10 V	(0.18 V, 0.19 V)	(31.8μs, 34μs)	(199μs, 195μs)
15 V	(0.27 V, 0.28 V)	(20.8μs, 23.5μs)	(194μs, 190μs)
25 V	(0.44 V, 0.45 V)	(12.2μs, 13μs)	(190μs, 186μs)

Table 7.4. Coil Pulse Properties @10 V

Coil Number	Peak Induced Voltage(sim,meas)	Saturation time (sim,meas)	Zero Crossing (sim,meas)
A1	(0.136 V, 0.16 V)	(25.4μs, 24μs)	(121.5μs, 128μs)
A2	(0.2 V, 0.21 V)	(no saturation)	(127μs, 120μs)
A3	(0.217 V, 0.218 V)	(23.8μs, 26μs)	(138μs, 140μs)
A4	(0.365 V, 0.39 V)	(13.2μs, 16μs)	(59.5μs, 68μs)
A9	(0.18 V, 0.19 V)	(31.8μs, 34μs)	(199μs, 195μs)

voltage, while coil $A4$ has highest induced voltage but decays faster and results in smaller pulse width.

7.6 Conclusion

In this work, the nonlinear effect of the magnetic core of small coils to be used for implantable magnetic neurostimulation is studied. Five ferrite-loaded coils, of different dimensions, are fabricated and tested. The implemented numerical solver demonstrates to be able to accurately predict the amplitude and waveform of the induced electric fields. For all magnetic coils, measurements show close agreement ($< 10\%$ difference) with the simulated values. The capability of these models to also correctly predict the effects of initial voltages of the capacitors on the induced field intensity and saturation time is instrumental in developing an effective magnetic neuostimulator. In fact, it is confirmed that due to the saturation of the core, the inductance of the coil changes drastically from its nonsaturated value, which causes faster decay in the induced voltage and, ultimately, negatively affects the neurostimulator.

7.7 References

[1] S. Ueno, “Studies on magnetism and bioelectromagnetics for 45 years: From magnetic analog memory to human brain stimulation and imaging,” *Bioelectromagnetics*, vol. 33, no. 1, pp. 3–22, 2012.

[2] K. Davey, L. Luo, and D. Ross, “Toward functional magnetic stimulation (fms) theory and experiment,” *IEEE Transactions on Biomedical Engineering*, vol. 41, no. 11, pp. 1024 –1030,

Nov. 1994.

[3] J. Gomand, G. Remy, A. Tounzi, P.-J. Barre, and J.-P. Hautier, “Impact of permanent magnet field on inductance variation of a pmlsm,” in *Proc. of European Conference on Power Electronics and Applications*, Sept. 2007, pp. 1–9.

[4] I. Sirbu, “A new technique for the determination of magnetic field distribution in a ferromagnetic core,” in *Proc. of 3rd International Students Conference on Electrodynamics and Mechatronics (SCE III)*, Oct. 2011, pp. 127–132.

[5] D. Cai, Y. Fang, X. Cao, X. Zhang, and J. Tang, “Transcranial magnetic stimulation: Modeling, calculating and system design,” in *Biomedical Engineering and Informatics, 2009. BMEI ’09. 2nd International Conference on*, 2009, pp. 1 –5.

[6] Fair-rite, “78 materials characteristics,” [Online] Available: http://www.fair-rite.com/newfair/materials78.htm.

[7] S. software, “Magnetic potential,” [Online] Available: http://simion.com/info/magneticpotential.html.

CHAPTER 8

USE OF AIR-CORE COILS FOR THE EX-VIVO MAGNETIC STIMULATION OF FROG'S SCIATIC NERVE

8.1 Abstract

Air-core based magnetic coils are commonly used for magnetic neural stimulation. As compared to the magnetic-core based coil, which are prone to saturation, air-core based coils provide constant inductance over the pulse duration. In this chapter, design and optimization for the air-core solenoid coil are presented. Some of these coils (solenoid and figure-8) are used for ex-vivo magnetic stimulation of the sciatic nerve. In frogs, it is demonstrated that a solenoid coil with outer diameter as small as 23.5 mm can elicit muscle activity for the threshold voltage of $\sim$115 V in the charging capacitor of 2.2 mF. A detailed analysis of the individual experiment is presented to establish the understanding of magnetic stimulation.

8.2 Introduction

Due to high magnetic field density requirement ($\sim$ 1-2 Tesla) [1–5] for magnetic stimulation, only closed magnetic structures, such as toroids, have been used to successfully demonstrate ex-vivo magnetic stimulation of the sciatic nerve of frog [6]. However, implantation of toroidal structure is a design challenge due to the requirement of nerve placement inside the toroid. Therefore, planar or solenoid type coils are better suited for the in-vivo magnetic stimulation [7–9]. In our previous work (Chapter 7), we demonstrated that, due to fast saturation of the magnetic core, a coil wrapped around a cylindrical magnetic core does not provide any advantage over a air-core coil. Therefore, we focus our work on the design and optimization of an air-core coil. Traditionally, magnetic coils have been designed for transcranial magnetic stimulation (TMS) applications [3, 4, 10, 11]. The design objectives for given coils include high penetration depth and focal stimulation. Therefore, round [8], figure-8 [2], slinky [12, 13], and clover leaf [14] topologies were proposed to improve the focalization of the induced field. Some special configurations, such as Crown/C coils, which utilizes the curvature of the head, were also proposed to increase the depth of the stimulation [15].

Due to use of magnetic coils outside the body for TMS applications, dimensions of the coil were not considered a driving constraint in the design. However, to design an implantable magnetic stimulator for peripheral nerve stimulation, the volume of the magnetic coil and its projected area over the nerve need to be minimized. Figure-8 and slinky coils occupy larger volume and projected area on the stimulation site than solenoid coils. Therefore, we limited our design to a solenoid configuration for which system performance can be optimized as a function of the coil diameter (inner D_{in} and outer D_{out}), number of layers (L), and turns per layer (N).

Stimulation threshold of the nerve fibers depends on the strength and duration of the induced electric field caused by the magnetic coil [16, 17]. Thus, magnetic coils are designed based on their ability to induce a high electric field magnitude and its pulse width at the stimulation site. In the following sections, the design algorithm for the magnetic coils is presented. Some coils are used for the ex-vivo magnetic stimulation of the frog's sciatic (peripheral) nerve. Stimulation conditions and field simulations are also presented to establish the understanding of the underlying principles of magnetic stimulation.

8.3 Design of the Magnetic Coil

Selection for the magnetic coil depends on the ability to induce high electric field ($\sim$ 40-50 V/m) with sufficient pulse width ($\sim$ 100-200 μs) [16]. Threshold requirements for induced field depend on the underlying animal model, pulse width of the induced field, coil position with respect to stimulation site, and its surrounding media. Traditionally, a strength-duration (S-D) curve is established for the nerve, which demonstrates the inverse relation of stimulation threshold with respect to pulse width (Equation 8.1) [16]. The S-D curve is modeled using two parameters E_{th} and time constant τ, which depend on the coil configurations and the animal model.

$$E_{threshold} = \frac{E_{th}}{1 - e^{-\frac{PW}{\tau}}} \tag{8.1}$$

Design and optimization of the magnetic coil for neural stimulation requires inclusion of information of the S-D curve, system constraints, and design limitations. Some of the constraints for the coil design include the maximum and minimum dimensions of the coil, current carrying capability of the coil and switches, and maximum temperature rise in the coil. Therefore, we propose an algorithm to select all the coil configurations based on the these parameters and constraints. Figure 8.1 shows the flow of the proposed design algorithm for the solenoid-configuration-based magnetic coil.

The algorithm includes the design constraints of the coil dimensions and coil current for the solenoid-based magnetic coil. However, it can be easily extended to the different coil configurations

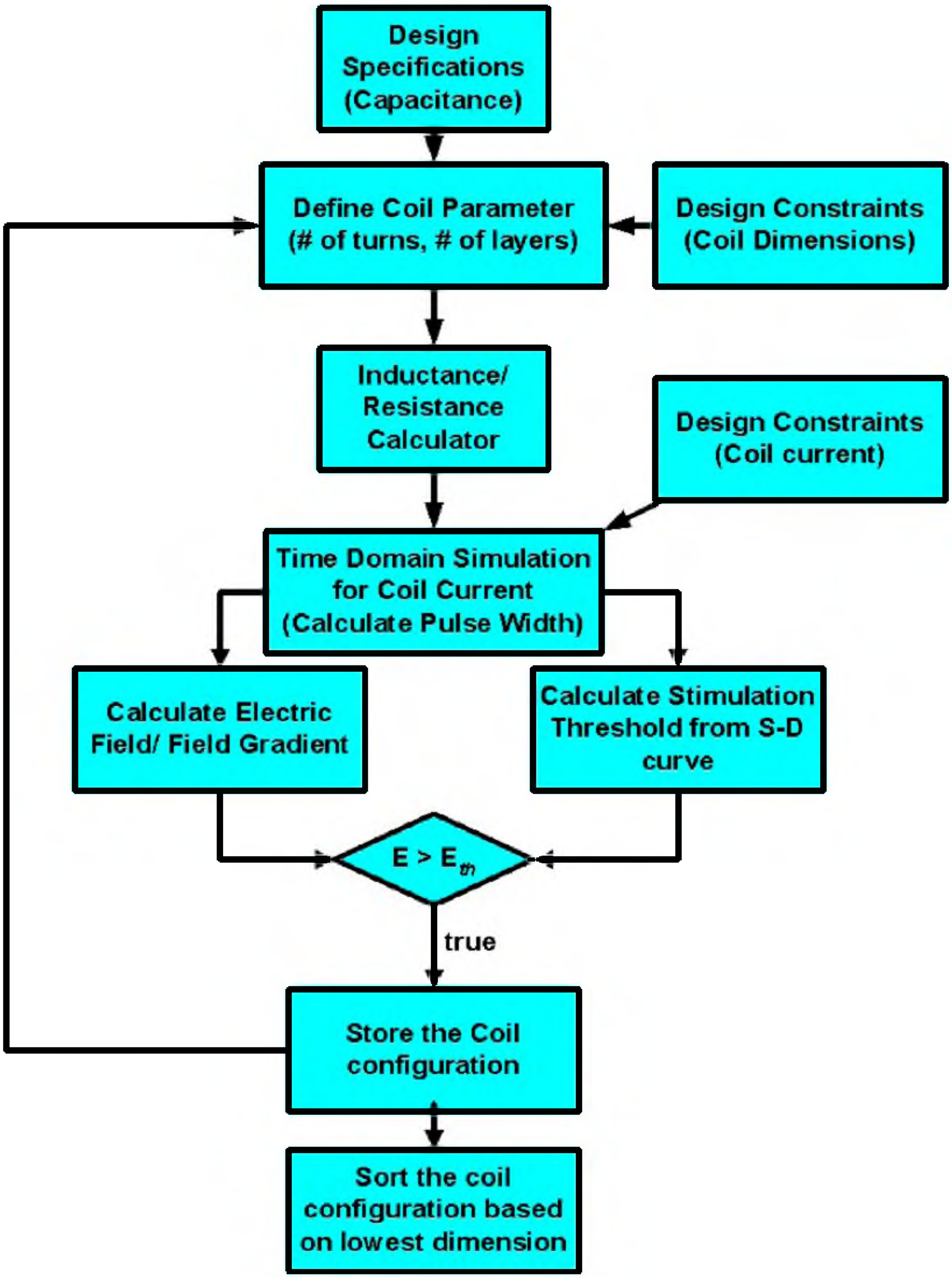

Figure 8.1. Flow chart for the brute-force search algorithm to optimize the magnetic coil. The algorithm also includes the design goals, system paramaters, and its constraints.

such as planar and curved coils. The algorithm uses a “brute-force” search to sequentially increment the number of layers, number of turns per layer, and inner radius of the coil. For the fixed charging capacitor, the pulse width of the induced field depends on the coil inductance and parasitic resistance due to the coil and circuit. The coil inductance can be calculated based on the analytical solution for the self inductance (Equation 8.2) and mutual inductance (Equation 8.3) of the circular coils.

The self inductance of a coil with loop radius a and wire radius R (assuming $\frac{R}{a} \ll 1$) is approximated by Equation 8.2. Mutual inductance of the two parallel single turn coils with loop radius a and b can be approximated by Equation 8.3. In these, d and ρ are relative distance and lateral misalignment, respectively, between the two coils. Thus:

$$L(a,R) = \mu_o a \left[ln\left(\frac{8a}{R}\right) - 2 \right] \tag{8.2}$$

$$\begin{aligned} M(a,b,\rho,d) = \pi\mu_o\sqrt{ab}\int_0^{\infty} J_1\left(x\sqrt{\frac{a}{b}}\right) J_1\left(x\sqrt{\frac{b}{a}}\right) \\ \times J_0\left(x\frac{\rho}{\sqrt{ab}}\right) exp\left(-x\frac{d}{\sqrt{ab}}\right) dx \end{aligned} \tag{8.3}$$

where J_0 and J_1 are zeroth and first-order Bessel functions .

For a solenoid coil with N_t turns per layer and N_a coaxial layers, total self-inductance can be expressed by Equation 8.4.

$$\begin{aligned} L_a = Nt\sum_{i=1}^{Na} L(a_i,R) \\ + \sum_{i=1}^{Na}\sum_{j=1}^{Na}\sum_{k=1}^{Nt}\sum_{l=1}^{Nt} M(a_{ik}, a_{jl}, \rho = 0, d = d_l|k-l|) \\ \times(1-\delta_{ij})(1-\delta_{kl}) \end{aligned} \tag{8.4}$$

where $\delta_{ij}(or\delta_{kl}) = 1$ for $i = j(ork = l)$ and $\delta_{ij}(or\delta_{kl}) = 0$ otherwise. d_l is the minimum distance between two consecutive turns.

Traditionally, the current pulse generated by the magnetic stimulator contains low frequency components (500 Hz - 10 kHz). Therefore, the coil resistance is primarily contributed by the DC resistance of the coil. The coil resistance is calculated based on the length of the copper wire used for the coil and its cross sectional area. Due to the high current requirement (1 kA-4 kA) in the coil, a pulse discharge circuit is used to generate the time-varying magnetic field [18]. The switches control the flow of energy and store it in the charging capacitor. The discharge cycle is controlled through a thyristor-based switch, and current handling capability of the system depends on the current rating of wire and the thyristor. For the solenoid coil with N_a layers and N_t turns per layer, the induced electric field $\vec{E}$ in $\vec{\phi}$ direction can be calculated based on the analytical formulation of magnetic vector potential $\vec{A}$ (Equation 8.5 and 8.6).

$$\vec{A}(t) = \sum_{i=1}^{N_a} \sum_{j=1}^{N_t} \frac{\mu_0 I(t) a_{ij}}{\pi} \int_0^{\pi/2} \frac{(2sin^2\phi - 1)}{\sqrt{(a_{ij}+\rho_{ij})^2 + z_{ij}^2 - 4a_{ij}\rho_{ij}sin^2\phi}} d\phi \vec{a}_\phi \tag{8.5}$$

$$\vec{E}(r,t) = -\frac{\partial \vec{A}(r,t)}{\partial t} \tag{8.6}$$

where μ_0 is the magnetic permeability of air. ρ_{ij} and z_{ij} are the radial and lateral distance of the turn $i-j$ (with radius a_i) from the observation point r, respectively.

During the optimization step, the induced electric field and field gradient are calculated for the coil configuration and compared with the field threshold, which is computed based on the strength-duration curve and the pulse width. If the generated field value is higher than the threshold value, the coil's configurations are stored. The trade-off between the different coil configurations is based on the dimensions, voltage, and energy requirements for the stimulation.

8.4 Optimization of Magnetic Coil

To design a practical magnetic coil for the magnetic stimulation, cm-sized dimensions are used as shown in Table 8.1. For the charging voltage of 300 V, the induced electric field is calculated at a distance z = 1.5 mm from the coil end as shown in Figure 8.2 (a).

Based on the optimization parameters, the pulse width and the peak of the induced electric field are computed. The coil current, based on the discharge capacitor and parasitic resistance, is compared with the current rating of the thyristor and coil wire. Out of 546 combinations of the coil

Table 8.1. Optimization Parameters

Parameters	Values
Capacitor	2284 μF
DC (direct current) voltage	300 V
Number of Layers (range)	1:1:6
Number of Turns/layer (range)	1:1:13
Inner Diameter D_{in} (range)	4:4:28 mm
E_{th}	24.29 V/m
τ	420 μ Sec
Coil current (max)	3000 A
Pulse width (min)	100 μs
Parasitic resistance	50 mΩ
Wire diameter	1.15 mm

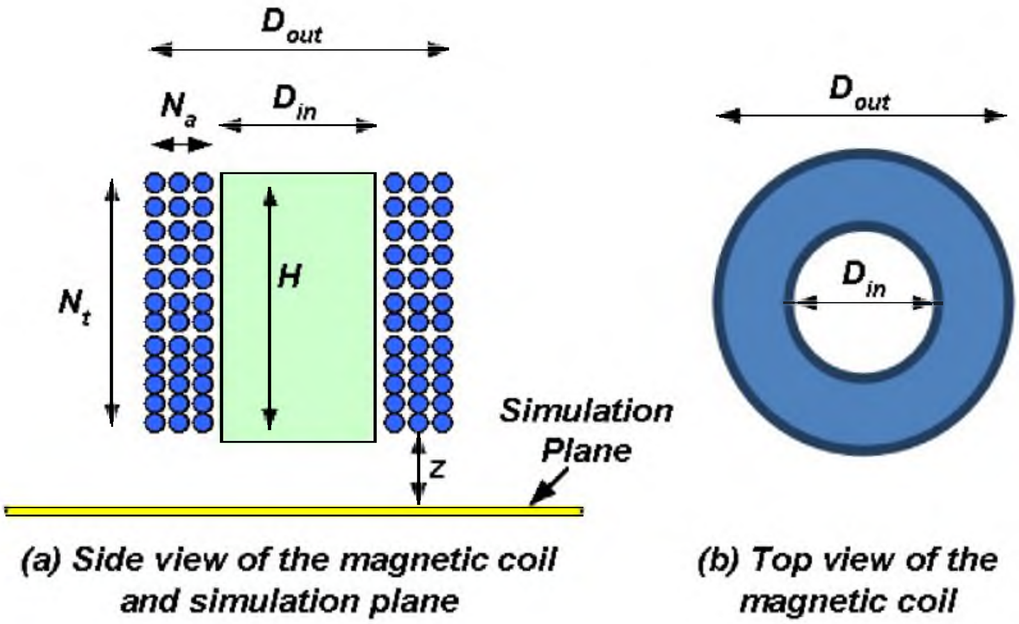

Figure 8.2. Solenoid coil structure: (a) Cross section view of the solenoid coil with coil windings. Flat surface of the coil is positioned parallel to the simulation plane. (b) Top view of the solenoid coil describing the inner and outer diameter.

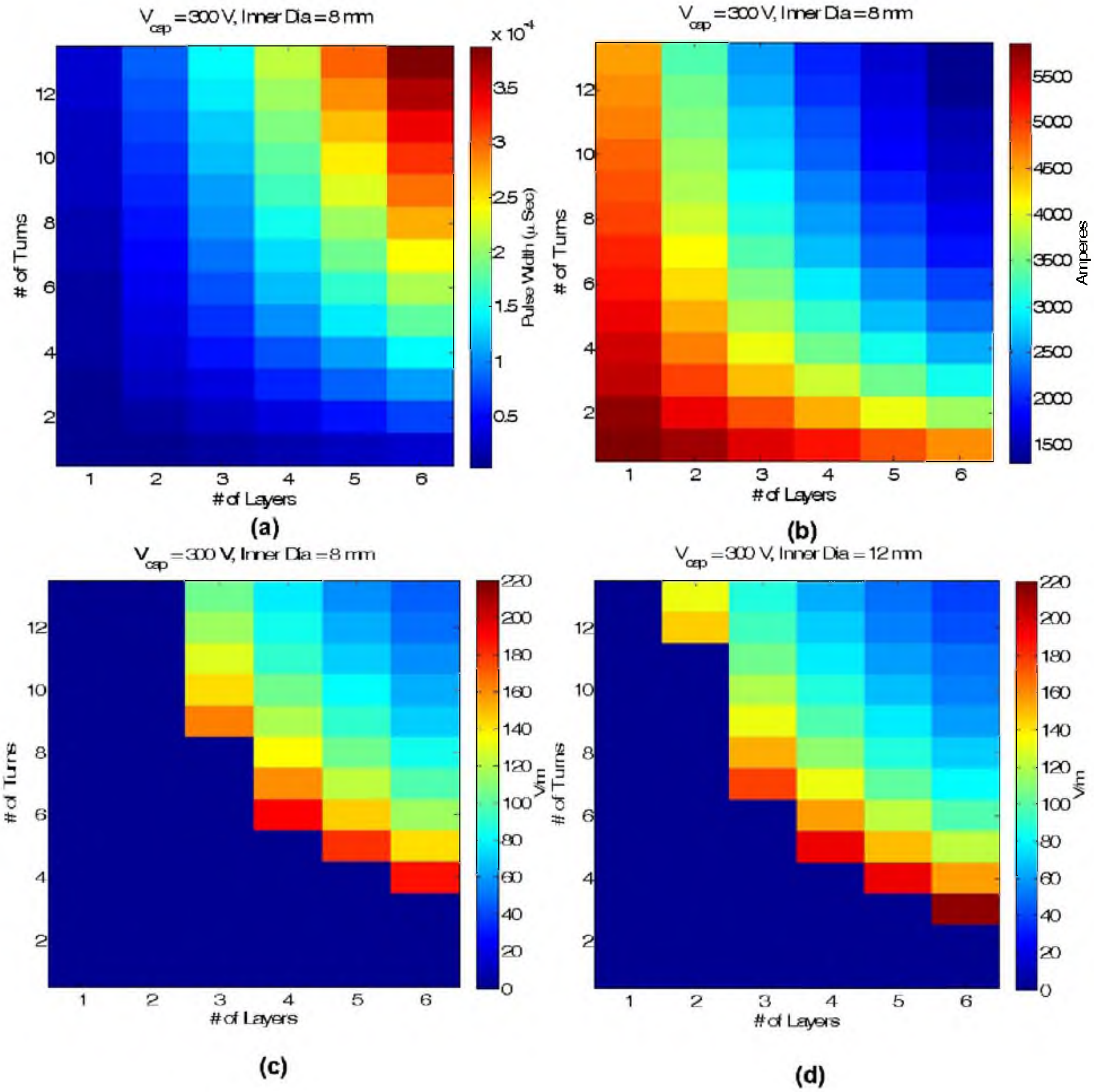

Figure 8.3. Effect of number of layers and turns per layer on the (a) pulse width, (b) coil current, and (c) induced electric field for the solenoid coil with inner diameter 8 mm. (d) Solenoid coil with inner diameter 12 mm shows a higher number of configurations to meet the threshold requirements.

parameters, 286 configurations can induce electric field higher than the threshold value that results in neural stimulation. Figure 8.3 (a) and (b) show the pulse width and coil current as a function of the number of layers and number of turns per layer, respectively. It shows that, by increasing the number of turns and layers, the inductance increases, which results in increased pulse width and decreased coil current. Figure 8.3 (c) and (d) show the peak of of induced electric field for a coil diameter of 8 mm and 12 mm, respectively. Due to the larger inner diameter of the coil configuration in Figure 8.3 (d), more coil configurations can achieve the threshold value of the electric field value for the stimulation.

To validate the performance of the simulated magnetic coils in experiments, we fabricated coils based on our understanding of the optimization cycle. As the optimization depends on the animal model and stimulation conditions, we extended the scope of the coil selection. Table 8.2 shows the electrical and mechanical properties of the fabricated coils. Coil RC1-RC5 are fabricated with different inner diameters D_{in}, height H, and turns N_t, while keeping the same number of layers (N_a) and inductance. Similarly, coils C1-C5 are fabricated with varying coil dimensions, number of layers, and turns. As shown in Table 8.2, the simulated value of inductances and coil resistances are very similar to the experimental values, and can be used to estimate the pulse width of the induced electric field. Comparison between coil C5 and RC1 shows that even if both coils have a similar outer diameter, coil C5 can achieve stimulation with smaller coil volume and lower inductance. The proposed optimization includes few design constraints (e.g., dimensions, maximum coil current, and minimum pulse width). However, the algorithm can be easily extended to include further constraints, such as maximum energy requirement and maximum temperature rise in the coil.

8.5 Magnetic Stimulator Design

Our simulations show that for the inductance range between 4-25 μH, coil current can exceed 3500 A (Figure 8.3 (b)). Therefore, we designed a system that can operate on high pulsed current values. Figure 8.4 (a) shows the block diagram of the pulse discharge circuit, which is controlled by a timing circuit. During the charging cycle, the energy is stored through the IGBT-based switch to the charging capacitor. At the time of stimulation, the energy stored in the capacitor is discharged through the magnetic coil and thyristor, which results in a monophasic or biphasic current pulse based on the system parameters. Our in-house developed magnetic stimulator can be operated up to 420 V. Figure 8.4 (b) shows our current implementation of the stimulator design, which demonstrates the placement of different components and boards.

To characterize the temporal distribution of the induced electric field, a test wire is attached to a high impedance (10 $M\Omega$) probe to monitor the induced voltage. The test wire is placed in

Table 8.2. Coil Configurations

Coil	O.D (mm)	I.D. (mm)	H (mm)	N_t	N_a	L_{exp} (μ H)	R_{exp} (mΩ)	L_{sim} (μ H)	R_{sim} (mΩ)
RC1	18.3	9	38.1	27	3	22.3	63	21.74	59
RC2	20.75	12.56	25.72	18	3	21.03	51	20.1	48
RC3	24.5	15.75	21.2	14	3	19.5	46	19.6	45
RC4	27.2	19.2	16.5	12	3	21.7	46	21.8	44
RC5	31.2	22.9	14.95	10	3	20.5	44	20.5	43
C1	23.5	9.35	8.75	6	5	10.32	30	9.83	26.1
C2	26.35	10	9.31	6	5	10.75	28.5	10.91	28.9
C3	20	9.58	8.96	7	3	4.45	17.28	4.38	16.4
C4	17.39	9.22	15.26	11	3	7.19	23	7.022	23.2
C5	16.4	8	13.3	9	3	4.28	17.28	4.32	19.4

close proximity to the magnetic coil to improve the coupling of the magnetic coil and test wire. Figure 8.5 shows the typical waveforms of the thyristor control signal and the induced voltage. As compared to the control signal, the induced voltage is delayed due to the on-time of the thyristor. As shown in Figure 8.5, the temporal distribution of the induced voltage can be subdivided into three components, the rise time, the pulse width, and the thyristor-off time. The rise time of the induced voltage is due to the nonlinearity of the thyristor during the turn-on cycle. Nerve depolarizes during the positive cycle of the induced electric field. Therefore, “pulse width” is the key component of the induced field (or voltage), and is the defined by the time to zero-crossing. The third component is the thyristor-off time which is due to the fall of coil current below the thyristor’s holding current.

8.6 Coil Characterization and Effect of Coil Orientation

The induced voltage across the test wire is linearly proportional to the induced electric field. Therefore, we can validate the efficacy of the field simulation by comparing the simulated and experimental induced voltage across the test wire. To study the effect of coil configurations on the induced electric field, some of the fabricated coils are driven with the magnetic stimulator. Figure 8.6 (a) and (b) shows the positioning of the magnetic coil (RC1) and the test wire in perpendicular and parallel orientation, respectively. In our system, we define the “coil orientation” as the placement of the coil’s flat surface with respect to the plane carrying the test wire (or nerve). It should be noted from Table 8.2 that the coils RC1-RC5 are designed to achieve similar inductances by varying inner diameters and number of turns. This results in a different aspect ratio for each coil. Each coil is driven in two orientations as shown in Figure 8.6 (a) and (b). Figure 8.6 (c)

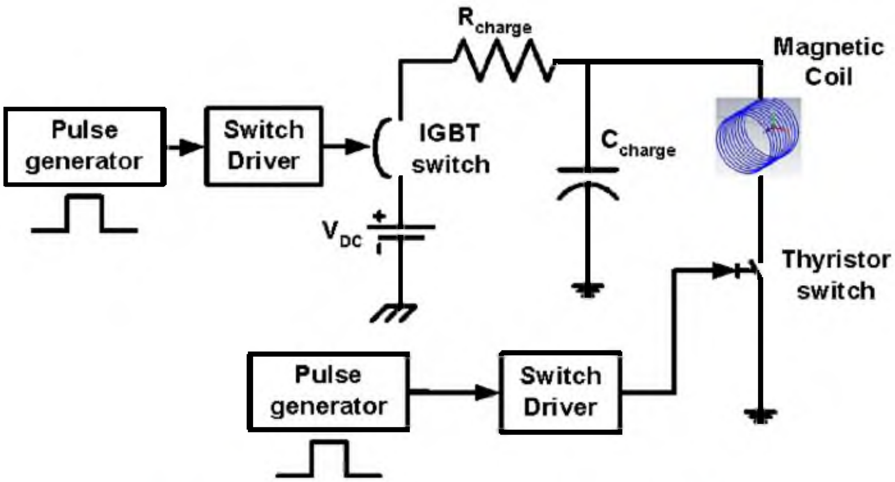

(a) Block diagram of Magnetic stimulator

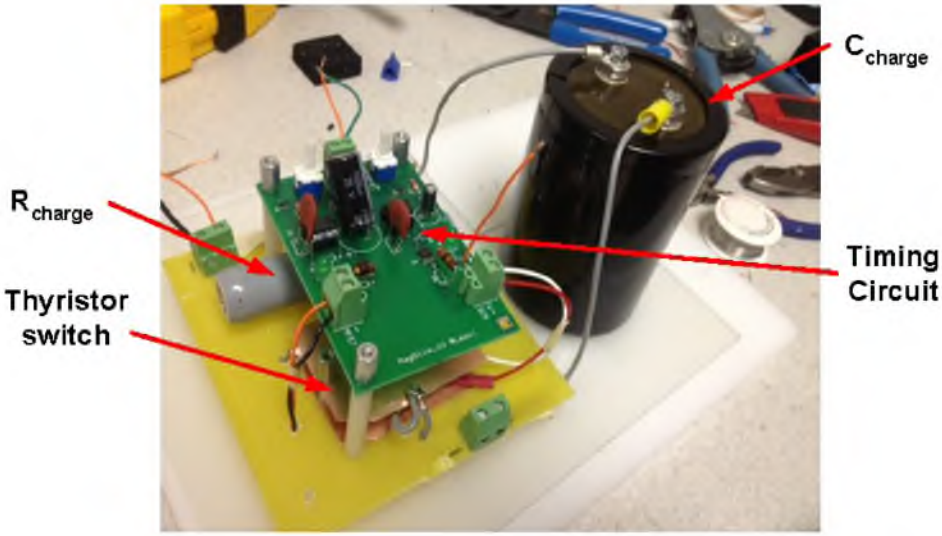

(b) Implementation of magnetic stimulator circuit

Figure 8.4. Stimulator design: (a) Schematics of the pulse discharge circuit for magnetic neural stimulation. (b) Implementation of the magnetic stimulator using high voltage charging capacitor and control circuits.

and (d) show the spatial distribution of the induced electric field for perpendicular and parallel orientation, respectively. To validate the simulation, the magnitude and pulse parameters of the induced voltage in the test wire are recorded and compared with the simulated induced field (or voltage) and pulse width. The results are presented in Table 8.3, which shows a good agreement between the simulation and experimental results. It can be seen that, for high aspect ratio coils (e.g., RC1), the perpendicular orientation induces higher electric field (or voltage) compared to the parallel orientation. By reducing the aspect ratio of the coil (RC1 → RC5) while keeping the similar

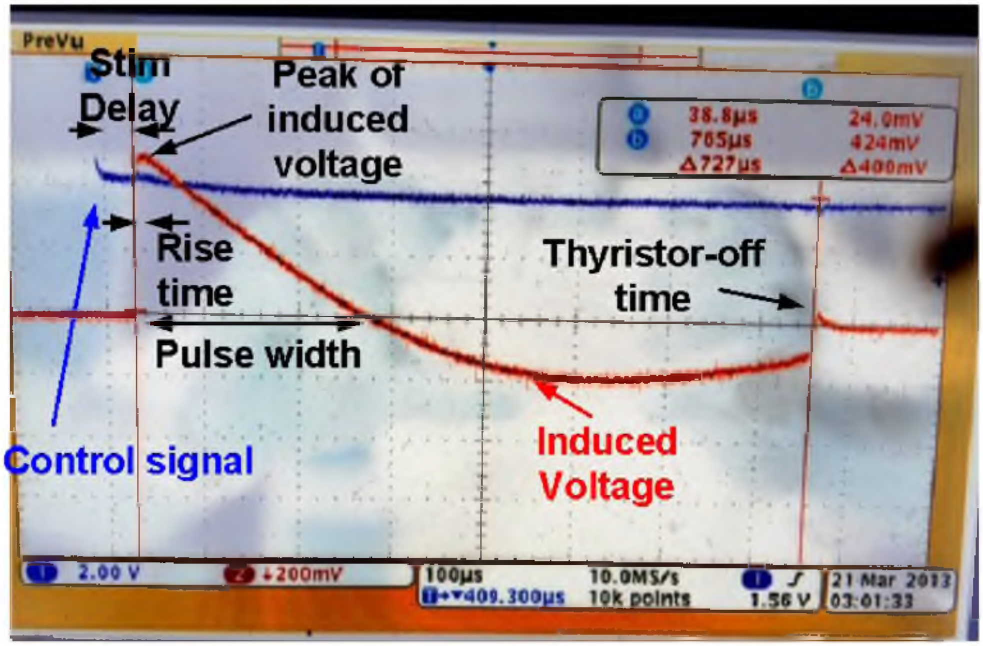

Figure 8.5. Captured waveform of (a) the input control signal to the thyristor (blue), and (b) induced voltage (red) in the test wire due to the current pulse in magnetic coil. The induced electric field is directly proportional to the induced voltage in the test wire.

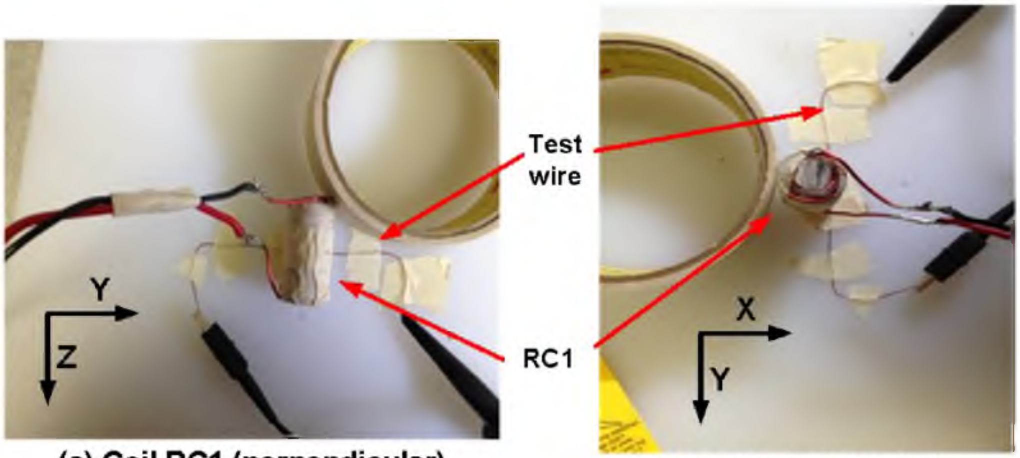

(a) Coil RC1 (perpendicular)

(a) Coil RC1 (parallel)

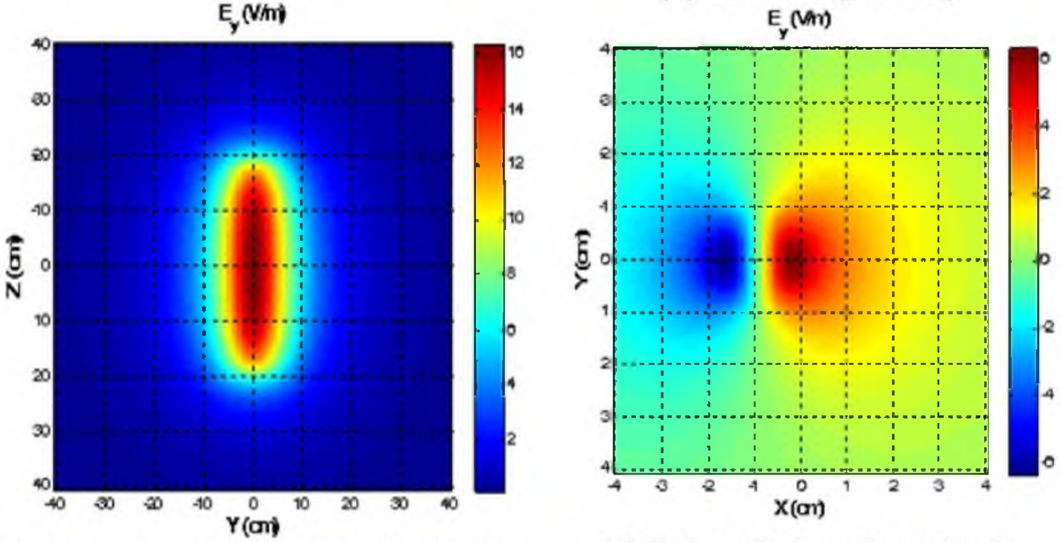

(c) E_y (perpendicular configuration)

(d) E_y (parellel configuration)

Figure 8.6. Placement of the solenoid coil RC1 in (a) perpendicular and (b) parallel orientation with respect to the test wire. Induced electric field distribution along the test wire for (c) perpendicular and (d) parallel orientation. All electric fields are in V/m.

inductances, the parallel orientation increases the induced electric field. Thus, the higher axial ratio (height/radius) coils achieve higher ratio of the induced voltage for perpendicular versus parallel configuration.

Table 8.3 shows the temporal parameters of the induced electric field. T_{rise} is the time required for the induced voltage to reach its maximum. Ideally, $T_{rise} = 0$; however, due to the nonlinearity in the thyristor's turn-on condition, the current in the coil has zero gradient at time t=0. T_{pulse} is the time from peak of the induced pulse ($V_{induce}= 0$) to the zero crossing of the induced voltage. All magnetic coils RC1-RC5 have almost same pulse width (255 +/- 5 us) due to the similar inductances. $T_{thyristor}$ is the time when thyristor turns off, which is observed when the coil current falls below the

Table 8.3. Performance of the Magnetic Coil

Coil	$\frac{Height}{radius}$	Config.	T_{rise} (μSec)	T_{pulse} (μSec)	$T_{thyristor}$ (μSec)	StimDelay (μSec)	V_{Exp} (mV)	Ratio $\frac{V_{per}}{V_{parallel}}$	PW_{Exp} (μSec)	V_{sim} (mV)	PW_{sim} (μSec)
RC1	8.5	perpendicular	6.41	259	792	42	288		265	320	267
		parallel					25	11.52		43	
RC2	4.1	perpendicular	8	252	747	41	372		260	412	265
		parallel					40	9.3		57	
RC3	2.7	perpendicular	6.3	253	718	40	432		259	481	256
		parallel					98	4.41		88	
RC4	1.7	perpendicular	6	253	744	40	496		259	533	273
		parallel					140	3.54		106	
RC5	1.3	perpendicular	6	250	725	39	504		256	600	265
		parallel					140	3.6		152	

holding current of the thyristor.

8.7 Ex-vivo Experiments with Frog's Sciatic Nerve

To design and optimize an in-vivo magnetic stimulator, the underlying principle of magnetic stimulation needs to be identified. In previous studies [7, 16, 20] of magnetic stimulation, different animal models (e.g., frog, rabbit, pig) were used. However, most of these studies used ex-vivo stimulation of frog's sciatic nerve [6, 7, 19, 21–24]. One study included the in-vivo magnetic stimulation of the rabbit sciatic nerve [16], and stimulus threshold was identified as a function of stimulus voltage and electric field at the stimulation site. With change in the magnetic coil, the field distribution along the nerve varies and requires establishment of a new stimulation threshold. Traditionally, figure-8 coils have been used to improve the localization of the induced electric field. Therefore, we built a figure-8 coil using two 33 mm diameter solenoid coils. In our study, we performed multiple experiments using figure-8 (Figure 8.7 (a)) coils and solenoid (Figure 8.7 (c)) coils. Figure 8.7 (b) and (d) show the magnitude of the electric field induced by the figure-8 and solenoid coil, respectively. To characterize the stimulation threshold, the E_{max} position of the magnetic coil is defined as the location in the nerve-carrying plane at which induced electric field is maximum along the nerve (x-direction). To reduce the mechanical vibration due to pulse discharge and to ensure stable positioning of the magnetic coil, a coil holder is used to place the coils in parallel orientation only.

To study the mechanism of magnetic stimulation and identify the key parameters that affect the stimulation threshold, we magnetically excited the sciatic nerve of euthanized bullfrogs (Rana catesbiana). The sciatic (and the tibial nerve branch) was extracted from the spinal cord to the innervation of the gastrocnemius muscle. The nerve was placed in a plastic Petri dish (thickness $\sim$1.5 mm) with saline (Frog Ringers Solution, FRS), and the Achilles tendon was suspended vertically to a force transducer. Additionally, we inserted two fine wire electrodes into the gastrocnemius muscle

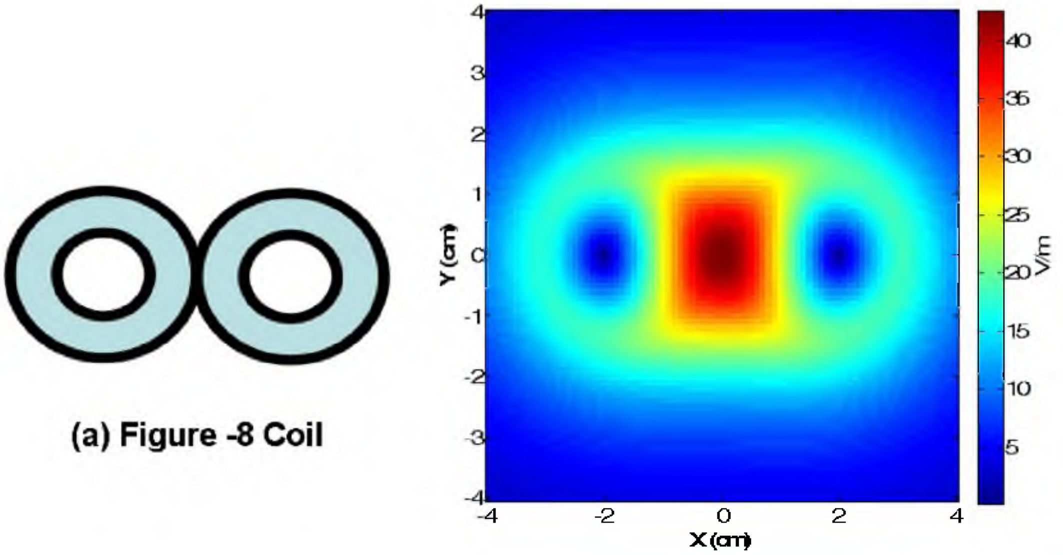

(a) Figure -8 Coil

(b) E-field (magnitude)

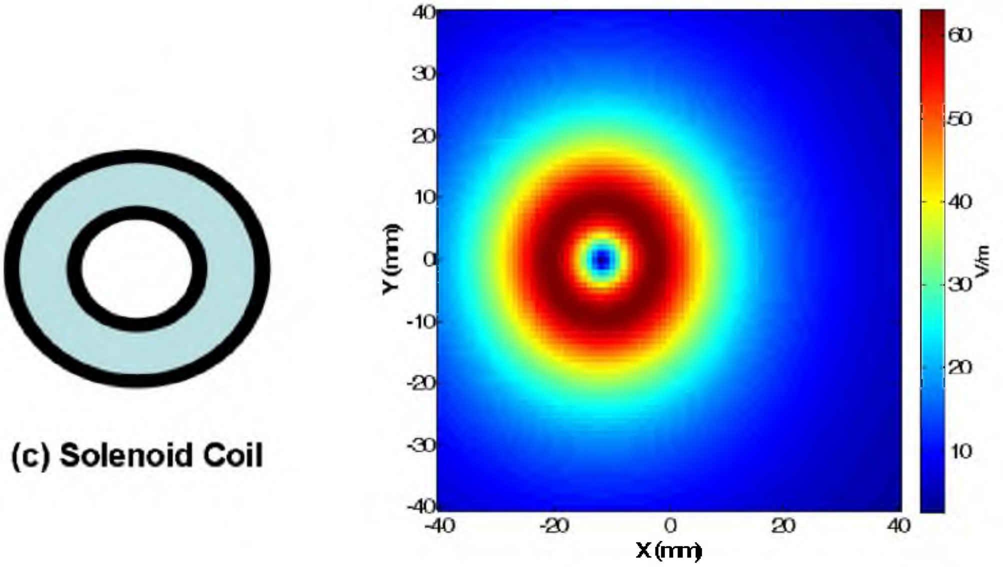

(c) Solenoid Coil

(d) E-field (magnitude)

Figure 8.7. Block diagram of the (a) figure-8 and (c) solenoid coil. Distribution of the induced electric field magnitude by (b) figure-8 and (d) solenoid coil in the plane of nerve.

to record the electromyogram (EMG). Both figure-8 and solenoid magnetic coils were fabricated and were used to induce an electric field. Coils were driven with an in-house designed magnetic stimulator that can source up to 420 V across the coil. These coils were placed under the Petri dish to assure electrical isolation. It was previously identified that electric field along the nerve as well its spatial derivative contributes to the stimulation. Moreover, for most of the studies, stimulation thresholds are presented in terms of electric field without providing the effect of surrounding media and nerve conditions. Therefore, the focus of our research is to identify the location of stimulation, stimulation threshold, effect of surrounding media, and strength-duration curve for the frog's sciatic nerve. In the following sections, five experiments are discussed to establish the key findings of the magnetic stimulation.

8.7.1 Experiment 1: Stimulation Using Figure-8 Coil

The first magnetic ex-vivo stimulation experiment was performed with the figure-8 coil. Figure 8.8 (a) shows the experimental setup for the magnetic stimulation. The magnetic stimulator uses a charging capacitor of 2.2 mF and can be operated up to 300 V. Figure 8.8 (b) shows the placement of the magnetic coil with respect to the nerve and muscle. The nerve is submerged in the FRS solution.

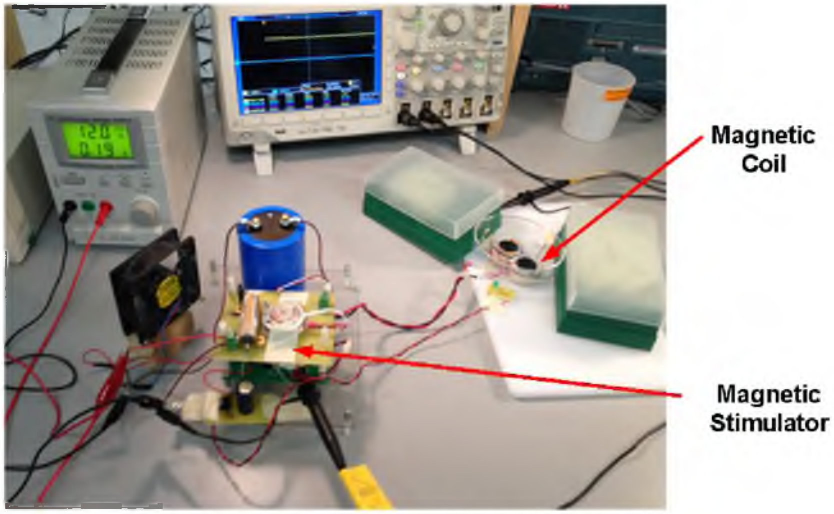

(a) Experimental setup for in-vitro stimulation

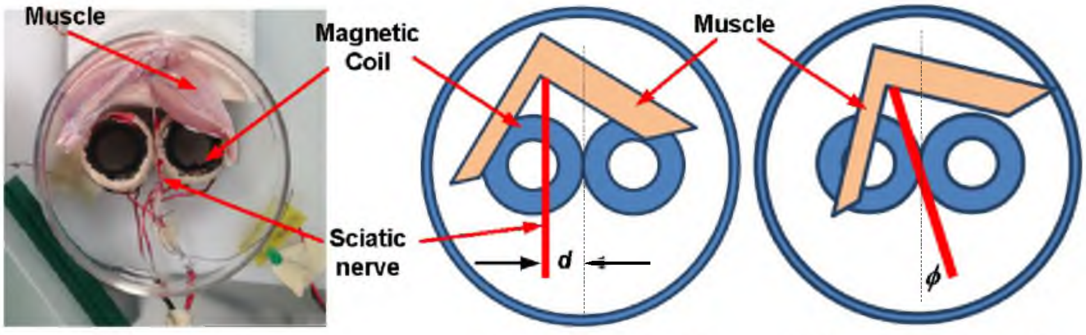

(b) Stimulation with Figure-8 Coil

(c) Placement of the nerve away from the coil's centroid

(d) Angular rotation of the nerve from the coil's centroid

Figure 8.8. Experimental setup: (a) Experimental setup for the magnetic neural stimulation of the frog's sciatic nerve. (b) Placement of magnetic (figure-8) coil with respect to the nerve. Block diagram of the (c) nerve position and (d) nerve orientation with respect to the figure-8 coil.

In this experiment, the nerve end is sutured to create high impedance at the end point. The nerve end is located ∼20 mm from the centroid (location of the peak electric field) of the figure 8-coil. Multiple sets of experiments were performed to identify the effect of nerve position d (Figure 8.8 (c)) and orientation ϕ (Figure 8.8 (d)) on the stimulation threshold.

Table 8.4 presents the stimulation thresholds for different positions and orientations of the nerve. The thresholds were identified based on the minimum charging voltage for which the stimulator caused visible muscle twitch. Table 8.4 shows that the minimum threshold is achieved when the nerve is submerged in the FRS solution and is placed at $d = 0$ and $\phi = 0$. As expected from the electric field simulation, the stimulation threshold increased with the increase in the separation from the center of the figure-8 coil. Similarly, increasing the angle ϕ (Figure 8.8 (d)) between $0^0 - 90^0$ requires higher threshold voltage. While placing the nerve at $\phi = 0$, the induced electric field along the nerve approaches zero, producing a stimulation threshold greater than 300 V. Table 8.4 also provides the simulated value of induced electric field at the nerve end depicting the $E_{threshold}$ requirement of 20-25 V/m.

8.7.2 Experiment 2: Recruitment Curve and Effect of Coil Separation

The second experiment is focused on capturing the recruitment curve of the magnetic stimulation using a figure-8 coil. The sciatic nerve is placed in the petri dish (thickness ∼1.5 mm). The nerve end is sutured and located at ∼15 mm away from the peak electric field location of the magnetic coil. EMG electrodes and force transducers are attached to the muscle to capture the muscle activity and generated force in response to the magnetic pulse. Figure 8.9 shows the typical waveform for the generated force and EMG signal during magnetic stimulation. It can be seen that the generated force

Table 8.4. Experiment 1: Stimulation Threshold Versus Nerve Position

Test No.	d (mm)	ϕ (degree)	Conditions	$V_{threshold}$ (V)	$E_x@Nerve-end$ (V/m)
1	0	0	Saline, Suture	190	19.85
2	1	0	Saline, Suture	190	19.8
3	3	0	Saline, Suture	225	23
4	5	0	Saline, Suture	300	29
5	0	180	Saline, Suture	190	19.85
6	0	10	Saline, Suture	200	-
7	0	45	Saline, Suture	250	-
8	0	90	Saline, Suture	> 300	-
9	0	0	No saline, Suture	> 300	-

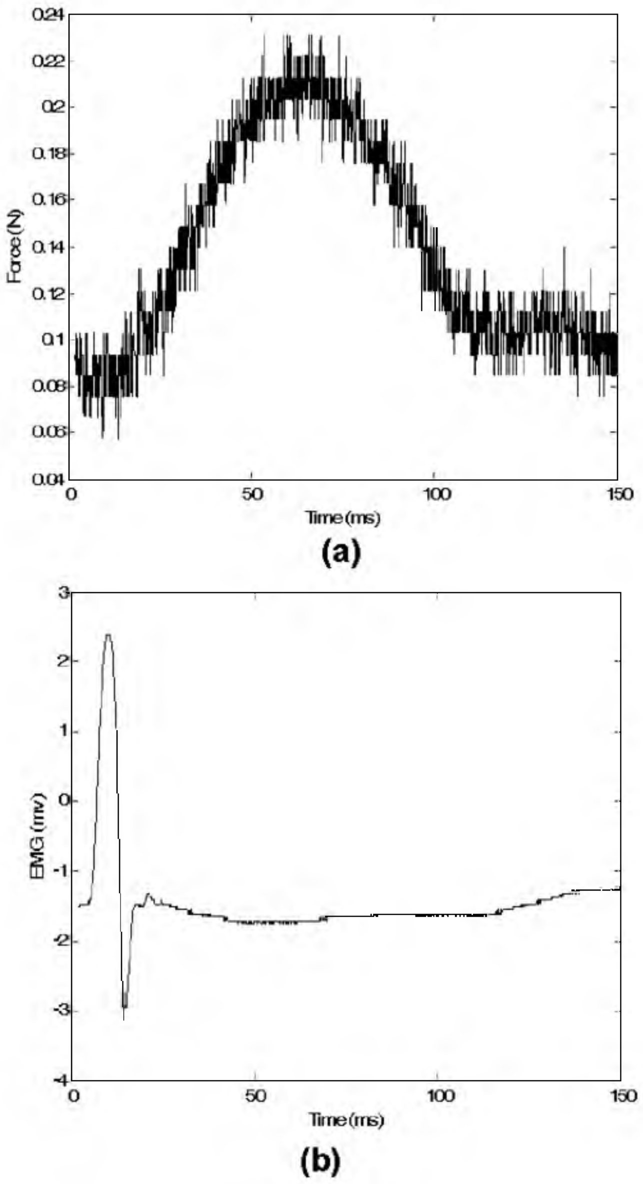

Figure 8.9. Neural activity: (a) Generated force and (b) EMG signal in the muscle in response to magnetic pulse.

varies slowly (20-100 ms), while the EMG signal is generated within 5-10 ms after the stimulation pulse. These waveforms are very similar (e.g. latency and temporal distributions) to the generated force and EMG signal from electric stimulation.

For all neural stimulation techniques (e.g., magnetic, electrical), the generated force and EMG signal is a nonlinear function of the stimulation magnitude. Below threshold, no neural activity can be recorded. However, operating the stimulator above the stimulation threshold increases the number of axons that can be excited. This results in a graded response of the generated force and

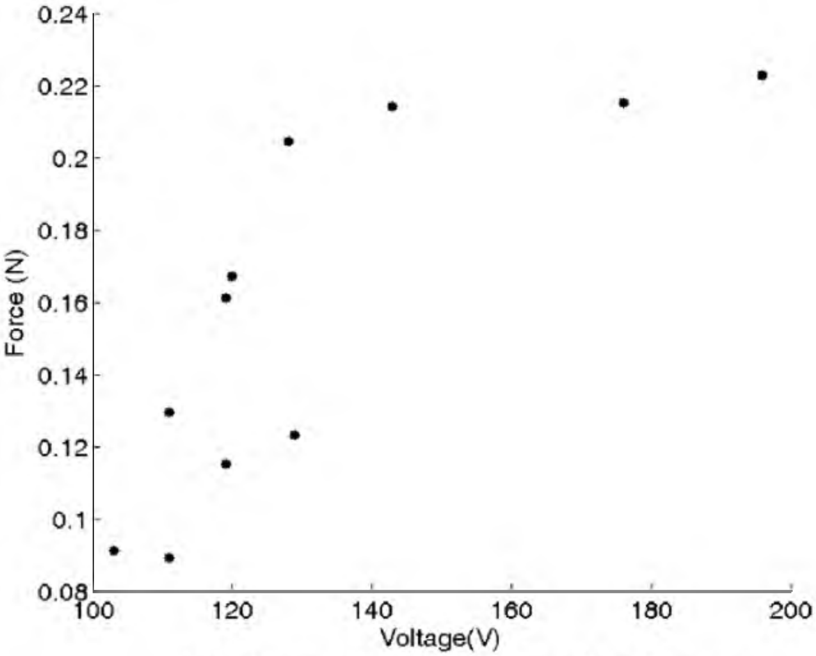

(a) Recruitment curve for force

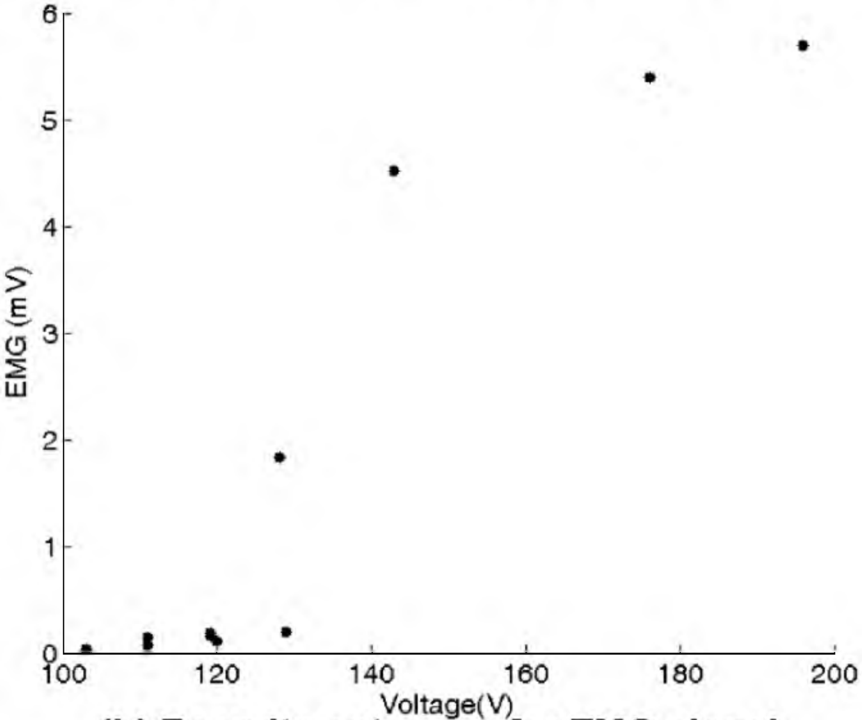

(b) Recruitment curve for EMG signal

Figure 8.10. Recruitment curve of (a) the generated force and (b) EMG signals in the muscle due to the magnetic pulse.

EMG signal as a function of the stimulation amplitude. By increasing the stimulation magnitude 1.5-3 times the threshold, the force and EMG signals approach a stable value. Figure 8.10 shows the recruitment curve for the force and EMG signal with a magnetic coil placed just below the petri dish. It shows the graded response of the muscle activity as a function of capacitor voltage.

To identify the operating distance of the magnetic coil and its impact on the stimulation threshold, the magnetic coil was vertically displaced from the petri dish, and threshold voltages were recorded for each distance. Table 8.5 shows the stimulation threshold (voltage and induced electric field) as a function of magnetic coil vertical separation from the nerve-carrying petri dish (petri dish thickness = 1.5 mm).

8.7.3 Experiment 3: Effect of Coil Position to the Nerve End

The third experiment was performed to study the impact of distance between the nerve end and the E_{max} position of the magnetic coil. Figure 8.11 shows the relative position of the nerve end with the solenoid based magnetic coil. For solenoid coils, E_{max} is located at the midpoint of the inner and outer radius of the coil (Figure 8.11(a)). However, for the figure-8 coil, the E_{max} is positioned at the center point of the two coils. The magnetic coil was placed under the petri dish and repositioned along the nerve during the experiment. As shown in Figure 8.11 (b), the distance d is characterized as the position of E_{max} with the nerve end. For this experiment, the nerve end was kept nonsutured to create a low-impedance end node.

Table 8.6 presents the threshold variation for the figure-8 and solenoid coil C1. It shows that the threshold voltage increases with the increase in the distance d. Electric field simulation depicts that, for the nerve placed in the x-direction, the threshold E_x (nerve end) reduces with the increase in d. The same trend is seen for the experiment with the solenoid coil C1. These data conclude that the magnetic stimulation not only depends on the induced E-field at the nerve end, but also the spatial

Table 8.5. Experiment 2: Threshold Variation with the Coil Separation

Test No.	h (mm)	ϕ (degree)	Conditions	$V_{threshold}$ (V)	$E_x@Nerve-end$ (V/m)
1	0	0	Saline, Suture	111	16.5
2	3	0	Saline, Suture	143	17.3
3	5	0	Saline, Suture	187	19.6
4	7	0	Saline, Suture	215	19.5
5	9	0	Saline, Suture	266	20.9
6	13	0	Saline, Suture	410	24.4

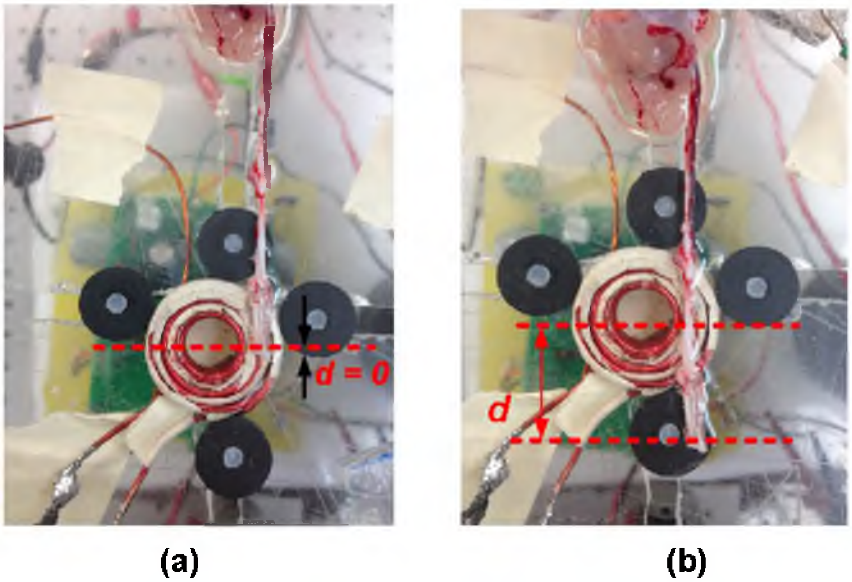

(a) (b)

Figure 8.11. Position of the nerve end with respect to the E_{max} location of the magnetic coil. The coil is moved along the nerve (a) to align the coil's E_{max} to the nerve end. (b) The coil is moved along the nerve to separate the coil's E_{max} at distance d from the nerve end.

Table 8.6. Experiment 3: Effect of Coil Position to the Nerve End

Test No.	Coil No.	d (mm)	Conditions	$V_{threshold}$ (V)	$E_x@Nerve-end$ (V/m)
1	Figure-8	0	13 ml saline, No suture	95	26.8
2	Figure-8	15	13 ml saline, No suture	100	15.42
3	Figure-8	25	13 ml saline, No suture	185	13.66
4	C1	0	13 ml saline, No suture	115	43.4
5	C1	10	13 ml saline, No suture	170	31.6
6	C1	20	13 ml saline, No suture	295	14.5
7	C1	30	13 ml saline, No suture	315	5.47
8	C1	40	13 ml saline, No suture	> 350	2.73

distribution of the electric field along the nerve.

8.7.4 Experiment 4: Effect of Surrounding Media and Position of Nerve End

During our ex-vivo experiments (Experiment 1), we found that the amount of FRS (saline) solution can modify the stimulation threshold. Therefore, this experiment consisted of a study to identify the impact of the amount of FRS in the petri dish on the stimulation threshold. Figure 8.12 (a) shows the experimental setup of the magnetic stimulation.

During the experiment, we used a plastic petri dish with diameter 15 cm. The volume of FRS (saline) was controlled during the experiment using a syringe. Table 8.7 shows the variation

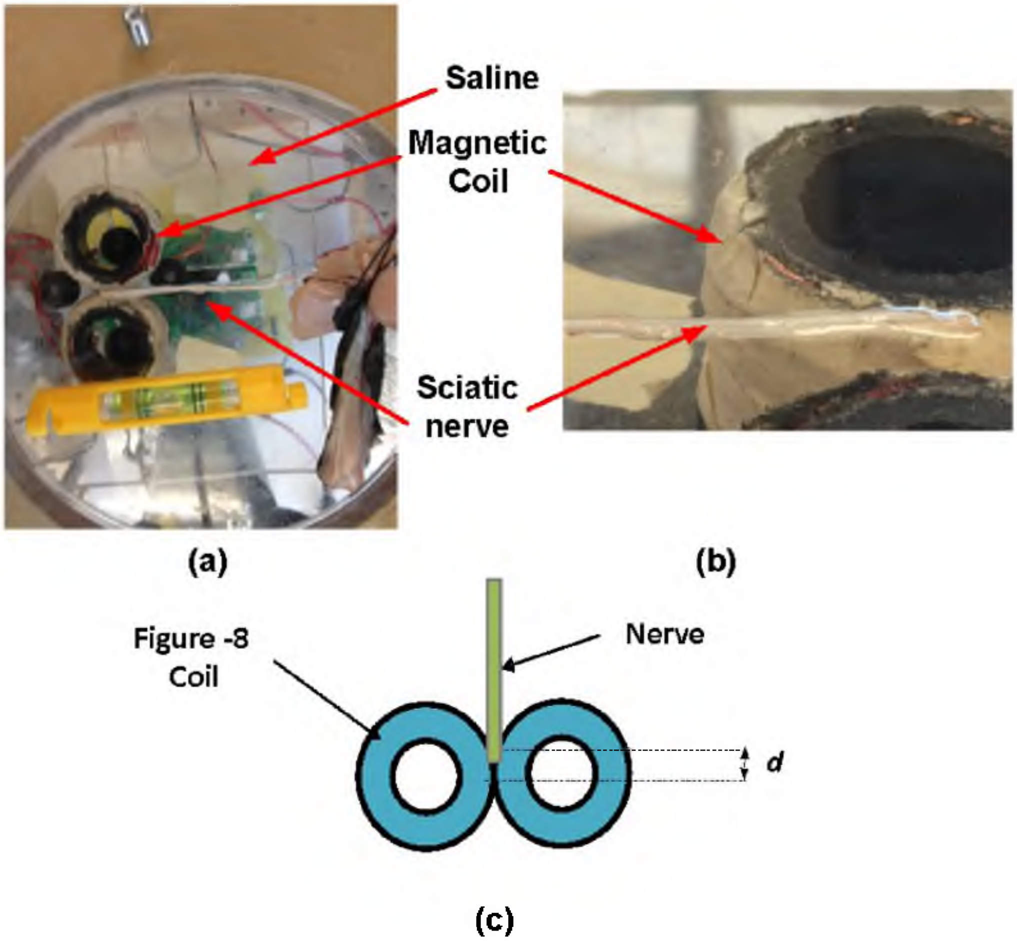

Figure 8.12. Experimental setup: (a) Placement of the magnetic coil with respect to the sciatic nerve. The petri dish is placed flat to insure uniformity of the saline. (b) zoomed version near the nerve end to show the height of saline with respect to the nerve (c) block diagram for the nerve end position with the E_{max} location.

Table 8.7. Experiment 4: Effect of Saline Height

Test No.	Coil No.	Saline Height (mm)	Conditions	$V_{threshold}$ (V)	$E_x@Nerve-end$ (V/m)
1	Figure-8	0.392	7 ml saline, No suture	207	58.4
2	Figure-8	0.28	5 ml saline, No suture	307	86.6
3	Figure-8	0	0 ml saline, No suture	> 420	> 118.5

of stimulation threshold for three different volumes. The stimulation threshold was at minimum when the sciatic nerve (diameter ~0.4-0.5 mm) was submerged in the uniformly distributed 7 ml FRS (Figure 8.12 (b)). For 0 ml FRS, we did not observe any neural response up to 420 V. This experiment suggests that the surrounding conductive media (height of FRS) affects the the stimulus threshold (induced electric field).

To validate whether the neural activity starts at the end-point of the nerve, the magnetic coil was moved equally in positive and negative directions (Figure 8.12 (c)). As the induced electric field is symmetrical with respect to E_{max} location along the nerve. Therefore, it was expected that in the case of end-point stimulation, the threshold would not vary while the coil is placed at varying distance along the nerve. Table 8.8 shows that for figure-8, as well solenoid coil C4, the stimulation threshold was not symmetric along the +ve and -ve value of d. We conclude that, for the nerve with no-suture, the stimulation threshold not only depends on the electric field at the end-point, but also its distribution along the nerve.

8.7.5 Experiment 5: Strength-duration Curve

As indicated in Section 8.3, to design and optimize the magnetic coils, the strength-duration (S-D) curve needs to be included in the optimization step. In this experiment, we intended to characterize the parameters of the strength-duration curve. To achieve different pulse widths for the same magnetic coil, we used a 3-capacitor based bank which can be connected in five configurations.

Table 8.8. Experiment 4: Effect of Nerve End Position

Test No.	Coil No.	d (mm)	Conditions	$V_{threshold}$ (V)	$E_x@Nerve-end$ (V/m)
1	Figure-8	+5 (towards muscle)	7 ml saline, No suture	172	40.1
2	Figure-8	0 (end point)	7 ml saline, No suture	185	52
3	Figure-8	-5 (away from muscle)	7 ml saline, No suture	214	> 50
4	C4	+5 (towards muscle)	7 ml saline, No suture	206	66.64
5	C4	0 (end point)	7 ml saline, No suture	264	66.4
6	C4	-4 (away from muscle)	7 ml saline, No suture	> 336	> 92.8

By operating multiple equally sized capacitors in series and parallel, equivalent capacitance values of 760 μF, 1142 μF, 2284 μF, 4564 μF, and 6852 μF are achieved. Ideally, for the fixed animal model, the S-D curve is independent of the electrode configuration. However, during our last ex-vivo experiments (1-4), we found that the stimulation threshold not only depends on the induced electric field at the nerve end, but also on its distribution along the nerve. Therefore, we characterized the S-D curve for the solenoid coil C1, which has smaller dimensions (outer diameter 23 mm) than the figure-8 coil.

For this experiment, a nerve with a nonsutured end was placed in the 10 ml FRS media. Table 8.9 shows the recorded threshold for different configurations of the capacitor bank. As expected, the stimulation threshold reduces with the increased effective capacitance (C_{eff}) value.

Figure 8.13 (a) shows the experimental value of the threshold voltage for coil C1. Figure 8.13 (b) shows the simulated electric field while the nerve end is located $\sim$ d = +3 mm away from the E_{max} position along the nerve. To identify the S-D curve parameters, the data are fitted using the empirical formulation ($V_{threshold} = \frac{V_{th}}{1-exp(-pulsewidth/\tau)}$ and $E_{threshold} = \frac{E_{th}}{1-exp(-pulsewidth/\tau)}$). For both the curves, the fitted empirical models achieve R-square value above 0.97. V_{th}, E_{th} and τ are the coefficients of the empirical models and based on the fitted data, V_{th} = 62.23 V, E_{th} = 22.27 V/m and τ = 420 μSec.

8.8 Discussion

In the previous sections, design and optimization of magnetic coils were presented, including five ex-vivo experiments performed to cause neural stimulation of the frog's sciatic nerve. All of the experiments were designed to identify the control parameters of the stimulation. Experiment 1 used a figure-8 magnetic coil and characterized the stimulation threshold for different positions and orientations. It was shown that minimum threshold is achieved when the nerve is placed over the centerline (midline of the two coils) of the figure-8 coil. Using a figure-8 magnetic coil (L = 18.5 μH, pulse width = 259 μSec @ charging capacitor = 2284 μF), stimulation was achieved for an

Table 8.9. Experiment 5: Stimulation Threshold Versus Pulse Width

Test No.	Capacitor Configuration	C_{eff} (mF)	Pulse Width (μ Sec)	$V_{threshold}$ (V)	$E_x@Nerve-end$ (V/m)
1	3-series	0.76	104	303	107
2	2-series	1.142	129	226	81
3	1-capacitor	2.284	185	164	59.5
4	2- parallel	4.584	238	137	49.6
5	3-parallel	6.852	273	129	46.7

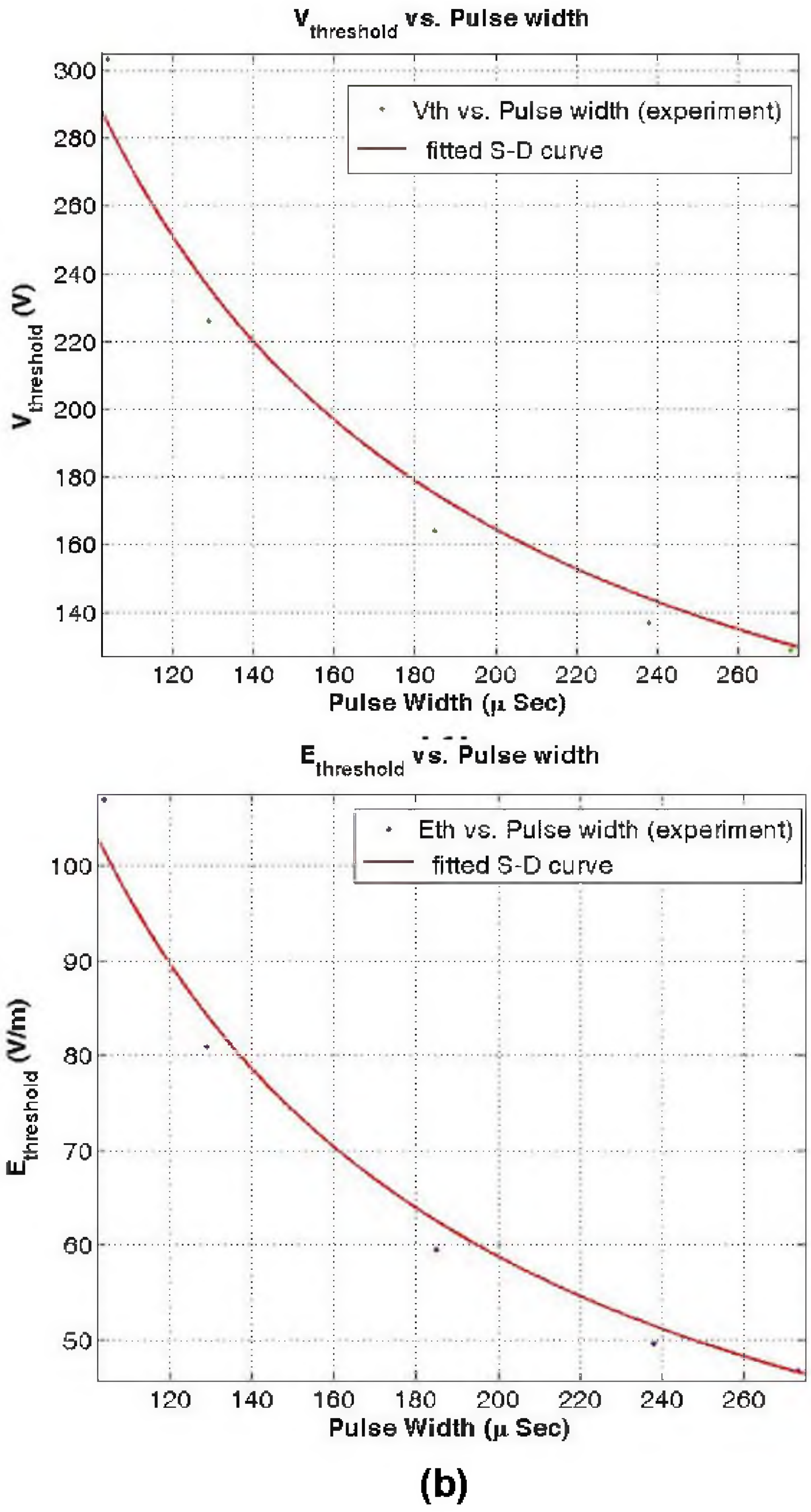

Figure 8.13. Strength-duration curves for the magnetic coil C1. The empirical models are created as a function of (a) voltage and (b) induced electric field at the nerve end.

induced electric field of ~20-25 V/m at the nerve end. Experiment 2 provided a systematic approach for capturing the recruitment curve for the frog sciatic nerve. The experiment also validated that the neural response (EMG and generated force) due to pulsed magnetic field is similar that of the electric simulation. In both experiments (1 and 2), the nerve end was sutured to create a high impedance termination. For Experiment 3, the nerve end was kept open, resulting in a low impedance node. Two magnetic coils (figure-8 and solenoid C1) were used for the experiment. The results show that when the coil is positioned close to the muscle, higher threshold voltage is required. For each configuration, the calculated electric field value at the nerve end shows that $E_{threshold}$ is different. It also concludes that by varying the coil's position along the nerve, stimulation can be started away from the nerve end. Therefore, the stimulus threshold depends on the induced electric field and its distribution along the nerve. For experiment 3, the threshold for the figure-8 coil was found higher than in experiment 2, which can be due to the low impedance (no-suture) versus high impedance (suture) nerve end and preparation of the nerve. Experiment 4 was designed to study the effect of surrounding media on the stimulation threshold. It is shown that stimulation threshold increases as the FRS level is decreased below the nerve height, which indicates that the induced electric field in the nerve depends on the surrounding conductive media. Experiment 5 was performed to estimate the parameters of the strength-duration curve of the frog's sciatic nerve for the solenoid coil C1. The stimulation threshold for experiment 5 was higher than the threshold value in experiment 4, which can be caused by the condition of the nerve during the experiment.

Based on the different ex-vivo experiments, some conclusions can be drawn:

1. The magnetic stimulation elicits similar neural responses (e.g., EMG and generated force) to electric stimulation (Experiment 2).
2. The stimulation threshold depends on the position of the nerve end with respect to the E_{max} location (position at which the induced field along the nerve is maximum) (Experiment 1 and 3).
3. High impedance nodes can be created by placing sutures at the nerve end. The nerve termination can alter the stimulation site and threshold (Experiment 1 and 3).
4. Distribution of the surrounding conductive media with respect to the nerve plays an important role in the generation of the induced electric field (Experiment 1 and 4).
5. Similar to electrical stimulation, magnetic stimulation can also be characterized based on the strength-duration curve (Experiment 5). The parameters of the S-D curve depend on the coil, the animal model, and the experimental setup.

Our experiments show that the medium heterogeneity at the stimulation site and the impedance of the nerve termination can alter the stimulation threshold. All the neural structures are heterogeneous medium and consist of different conductivity boundaries. They limit the accuracy of the analytical estimation of induced electric field [25–27]. Therefore, we intend to use numerical methods to estimate the distribution of induced electric field inside the nerve. In the following Chapter 9, we use the Impedance-Method based field simulator [28] to study the impact of tissue heterogeneity on the induced electric field.

8.9 Conclusion

In this work, design and optimization of air-core based magnetic coils was presented. The fabricated coils were used for ex-vivo experiments with the frog's sciatic nerve. Using a 23.5 mm diameter solenoid coil, successful stimulation of the frog's sciatic nerve was achieved at 115 V charging voltage. We also discussed the stimulation thresholds for five magnetic neural stimulation experiments to study different design parameters. It was shown that magnetic stimulation elicited similar neural activity as electrical stimulation, and its efficacy can be characterized by the recruitment curve of the recorded EMG and resultant muscle force. Similar to electrical stimulation, magnetic stimulation threshold also follows a strength-duration curve. Thus, for the derived S-D curve, the coils can be optimized under the limitation of dimensions, energy requirements, and system constraints. Moreover, it is shown that the stimulation threshold strongly depends on the surrounding conductive media and nerve position with respect to the magnetic coil.

8.10 References

[1] A. Rotem and E. Moses, "Magnetic stimulation of one-dimensional neuronal cultures," Biophys J, 94 (12) (2008), pp. 50655078.

[2] F.S. Salinas, J.L. Lancaster, and P.T. Fox, " Detailed 3D models of the induced electric field of transcranial magnetic stimulation coils," Phys. Med. Biol. 52, 28792892, 2007.

[3] AT Barker, R Jalinous, and IL Freeston, "Non-invasive magnetic stimulation of human motor cortex," The Lancet 325 (8437): 1106-1107, 1985.

[4] H. M. Roth and A. Zangen, "A coil design for transcranial magnetic stimulation of deep brain regions," J Clin Neurophysiol., vol. 19, pp. 361-70, Aug 2002.

[5] D. Cai, Y. Fang, X. Cao, X. Zhang, and J. Tang, "Transcranial magnetic stimulation: Modeling, calculating and system design," in Proc. of 2nd International Conference on Biomedical Engineering and Informatics, 2009, pp. 1-5.

[6] K. Davey, L. Luo, and D. Ross, "Toward functional magnetic stimulation (fms) theory and experiment," IEEE Transactions on Biomedical Engineering, vol. 41, no. 11, pp. 1024-1030, nov, 1994.

[7] S.S. Nagarajan and D. Durand, “Determination of excitation sites during magnetic stimulation of nerve fibers,” in Proc. of 14th Annual International Conference of Engineering in Medicine and Biology Society, Oct. 29 1992-Nov. 1 1992, pp. 1426-1427.

[8] I.N. Hsiao and V. Weh-Hau Lin, “Improved coil design for functional magnetic stimulation of expiratory muscles,” IEEE Transactions on Biomedical Engineering, vol. 48, no. 6, pp. 684-694, June 2001.

[9] L. Cret, M. Plesa, D. D. Micu, and R. Ciupa. ,“Magnetic coils design for focal stimulation of the nervous system,” in Proceedings of EUROCON 2007, 9-12 September 2007, Warsaw, Poland, pp. 1998-2003.

[10] Liu Jicheng, Lu Jiqing, Liu Cui, and Hu Yayi, “Coil arrays modeling and optimization for transcranial magnetic stimulation,” in Proc. of 2nd International Conference on Biomedical Engineering and Informatics, 17-19 Oct. 2009, pp.1-5.

[11] Guizhi Xu, Yong Chen, Shuo Yang, Mingshi Wang, and Weili Yan, “The optimal design of magnetic coil in transcranial magnetic stimulation,” in Proc. of 27th Annual International Conference of theEngineering in Medicine and Biology Society, 17-18 Jan. 2006, pp. 6221-6224.

[12] Ren Chunye, Peter P. Tarjan, and D.B. Popovic, “A novel electric design for electromagnetic stimulation-the Slinky coil,” IEEE Transactions on Biomedical Engineering, vol. 42, no. 9, pp. 918-925, Sept. 1995.

[13] V.W.-H. Lin, I.N. Hsiao, and V. Dhaka, “Magnetic coil design considerations for functional magnetic stimulation,” IEEE Transactions on Biomedical Engineering, vol. 47, no. 5, pp. 600-610, May 2000.

[14] K.-H. Hsu, S. Nagarajan, and D. Durand, “Analysis of efficiency of magnetic stimulation,” IEEE Transactions on Biomedical Engineering, vol. 50, no. 11, pp. 1276-1285, 2003.

[15] Zhi-De Deng, A.V. Peterchev, and S.H. Lisanby, “Coil design considerations for deep-brain transcranial magnetic stimulation (dTMS),” in Proc. of IEEE EMBS 2008, pp. 5675-5679, 20-25 Aug. 2008.

[16] Masuhiro Yamaguchi, Satoshi Yamada, Nobuo Daimon,Isao Yamamoto, Tadashi Kawakami, and Toshibumi Takenaka, “Electromagnetic mechanism of magnetic nerve stimulation,” Journal of Applied Physics , vol. 66, no. 3, pp. 1459-1465, Aug 1989.

[17] WG Friedli and M. Meyer, “Strength-duration curve: a measure for assessing sensory deficit in peripheral neuropathy,” J Neurol Neurosurg Psychiatry. 1984, vol. 47, no. 2, pp. 184-189.

[18] D. McRobbie, “Design and instrumentation of a magnetic nerve stimulator,” J. Phys. E: Sci. Instrum., 1985, vol. 18, no. 4, pp. 74-78.

[19] A. Rotem and E. Moses, “Magnetic stimulation of curved nerves,” IEEE Transactions on Biomedical Engineering, vol. 53, no. 3, pp. 414-420, March 2006.

[20] Lontis, E.R.; Nielsen, K.; Struijk, J.J., “In Vitro Magnetic Stimulation of Pig Phrenic Nerve With Transverse and Longitudinal Induced Electric Fields: Analysis of the Stimulation Site,” IEEE Transactions on Biomedical Engineering, vol. 56, no. 2, pp. 500-512, Feb. 2009.

[21] SS Nagarajan, DM Durand, and K. Hsuinghsu, “ Mapping location of excitation during magnetic stimulation effects of coil position,” Ann Biomed Eng 1997, vol. 25, no. 1, pp. 112-125.

[22] S.S. Nagarajan, D.M. Durand, E.N. Warman, “Effects of induced electric fields on finite neuronal structures: a simulation study,” IEEE Transactions on Biomedical Engineering, vol. 40, no. 11, pp. 1175-1188, Nov. 1993.

[23] E. Basham, Zhi Yang, and Wentai Liu, “Circuit and coil design for in-vitro magnetic neural stimulation systems,” IEEE Transactions on Biomedical Circuits and Systems, vol. 3, no. 5, pp. 321-331, Oct. 2009.

[24] S. S. Nagarajan, D. M. Durand, and Kai Hsuing-Hsu, “Mapping location of excitation during magnetic stimulation: Effects of coil position,” Annals of Biomedical Engineering January/February 1997, vol. 25, no. 1, pp 112-125.

[25] Bradley J. Roth and P.J. Basser, “A model of the stimulation of a nerve fiber by electromagnetic induction,” IEEE Transactions on Biomedical Engineering, vol. 37, no. 6, pp. 588-597, June 1990.

[26] Basser PJ, Roth BJ. ,“Stimulation of a myelinated nerve axon by electromagnetic induction,” Med Biol Eng Comput 1991, vol. 29, no. 3, pp. 261-268.

[27] B. J. Roth, L. G. Cohen, M. Hallett, W. Friauf, and P. J. Basser, “A theoretical calculation of the electric field induced by magnetic stimulation of a peripheral nerve,” Muscle Nerve, vol. 13, pp. 734-741, 1990.

[28] N. Orcutt and O. P. Gandhi, “A 3-D impedance method to calculate power deposition in biological bodies subjected to time varying magnetic fields,” IEEE Transactions on Biomedical Engineering, vol. 35, no. 8, pp. 577-583, Aug. 1988.

CHAPTER 9

NUMERICAL MODELING FOR THE MAGNETIC NEURAL STIMULATION OF THE PERIPHERAL NERVE

9.1 Abstract

To deduce the effect of surrounding conditions and nerve anatomy on the stimulation threshold, accurate computational models are required. In this work, we report an impedance-method-based field solver to study the effect of conductive media around nerve, and the impact of nerve termination on stimulation. Using a μm-resolution numerical model of the frog's sciatic nerve, the effect of axon density and impact of myelination node are studied. To simulate the transmembrane current due to cm-sized magnetic coils, a multiresolution impedance method was developed and the effect of axon distribution inside the nerve was studied. It is shown, due to the axon distribution, axons with $\sim$20 μm separation can differ more than 8% in induced electric field.

9.2 Introduction

With advancements in computational algorithms, numerical methods have been proven as key design and optimization tools for studying the mechanics of magnetic neural stimulation [1]. Transcranial magnetic stimulation (TMS) has been studied to evaluate the distributions of induced current and electric field [2, 3] inside the human head model. To improve the accuracy of the study, some simulations used anatomical models, which were created based on MRI scanning of human [2, 3] and rat [4] head. To increase the localization of the induced electric field, some studies were performed to design and optimize the magnetic coil (e.g., figure-8, coil array) for TMS application [5, 6]. Moreover, simulation models were also created for peripheral nerve magnetic stimulation to study the effect of tissue heterogeneity on the induced electric field [7].

Traditionally, finite-element [2, 4, 7, 8] and impedance [3, 6, 10] methods are used to solve the induced electric field in conductive media. The finite-element (FEM) algorithm is a generalized numerical method to solve boundary value problems for differential equations. It is well adopted by commercial software (e.g., SEMCAD, CST microwave studio, HFSS), which discretizes the 3-D simulation space into tetrahedral voxels and apply a governing equation to each element.

Compared to the impedance method, FEM has higher implementation complexity, and generally requires longer development time. Impedance method is well suited [3, 10] for studying magnetic stimulation. It solves for the induced electric field $\vec{E}$ by solving Faraday's induction law. Due to reduced implementation complexity, an impedance method based numerical solver is implemented in the following sections to compute the induced electric field in biological tissue.

9.3 Impedance Method for Electric Field Simulation

The impedance method was proposed and implemented to compute the absorbed electromagnetic energy in response to the incident magnetic field [13]. It is a frequency-domain solver that solves for an induced electric field $\vec{E}$ along a segment $\vec{dl}$ by solving Faraday's induction law ($\oint \vec{E}.\vec{dl} = -\frac{\partial \phi}{\partial t}$, ϕ is the magnetic flux). To represent a complex structure, the impedance method divides the solution space into cuboid voxels. Figure 9.1 shows a typical voxel, which is built using impedances at individual branches. The value of each impedance depends on the voxel dimensions and its conductivity. To represent the voxel in terms of lumped elements, quasi-static conditions need to be satisfied, which require the dimensions of the voxel to be much smaller the operating wavelength of the magnetic field. Moreover, the effect of the induced electric field needs to be negligible on the magnetic field source in order to decouple Ampere's law and Faraday's law of induction.

To solve the induced electric field in the x-, y-, and z- directions, the impedance method requires the evaluation of magnetic field intensity H_x, H_y, and H_z perpendicular to the faces of individual voxels. To evaluate the branch currents for each voxel, loop currents at each face can be calculated, which is an intermediate step of the algorithm. Figure 9.1 shows the orientation of the loop currents $iix(i,j,k)$, $iiy(i,j,k)$, and $iiz(i,j,k)$ at the voxel (i,j,k) face.

Branch currents of I_x(i,j,k), I_y(i,j,k), and I_z(i,j,k) flow in the branch impedances $Z_x(i,j,k)$, $Z_y(i,j,k)$ and $Z_z(i,j,k)$ in the x-, y- and z- directions, respectively. Equations 9.1, 9.2 and 9.3 formulate Faraday's induction law for the current loop in response to the magnetic field intensity of H_x, H_y, and H_z perpendicular to face in x-, y-, and z- directions, respectively.

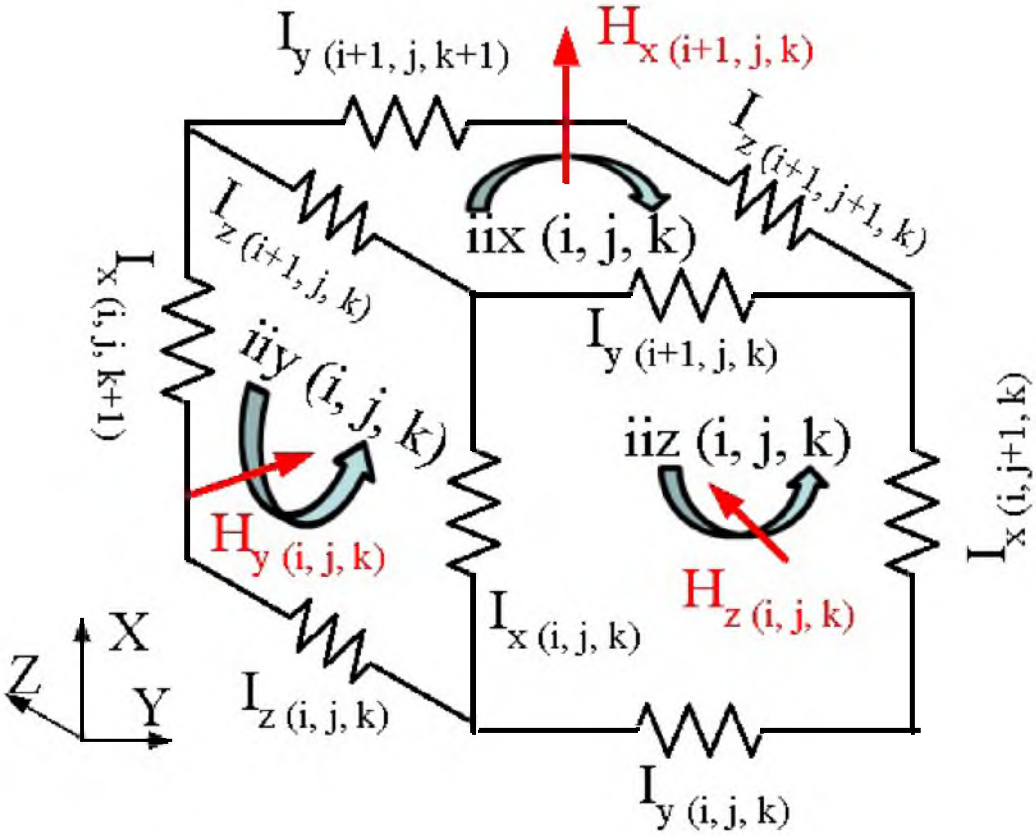

Figure 9.1. 3-D voxel used for the impedance method. Loop current is calculated at each face of the cuboid in response to the time-varying magnetic field.

$$
\begin{aligned}
&-I_y(i,j,k)Z_y(i,j,k)-I_z(i,j+1,k)Z_y(i,j+1,k)\\
&+I_y(i,j,k+1)Z_y(i,j,k+1)+I_z(i,j,k)Z_z(i,j,k) = -2j\pi f\mu_0 H_x(i,j,k)S_yS_z \qquad (9.1)\\
&I_x(i,j,k)Z_x(i,j,k)+I_z(i+1,j,k)Z_z(i+1,j,k)\\
&-I_x(i,j,k+1)Z_x(i,j,k+1)-I_z(i,j,k)Z_z(i,j,k) = -2j\pi f\mu_0 H_y(i,j,k)S_xS_z \qquad (9.2)\\
&-I_x(i,j,k)Z_x(i,j,k)-I_y(i+1,j,k)Z_y(i+1,j,k)\\
&+I_x(i,j+1,k)Z_x(i,j+1,k)+I_y(i,j,k)Z_y(i,j,k) = -2j\pi f\mu_0 H_z(i,j,k)S_xS_y \qquad (9.3)
\end{aligned}
$$

where f is the operating frequency. S_x, S_y and S_z are the length of each voxel in x-, y-, and z-directions, respectively.

Branch currents I_x, I_y, and I_z can be formulated based on the loop currents $iix(i,j,k)$, $iiy(i,j,k)$, and $iiz(i,j,k)$, respectively (Equations 9.4, 9.5, and 9.6).

$$I_x(i,j,k) = iiy(i,j,k-1)-iiy(i,j,k)+iiz(i,j,k)-iiz(i,j-1,k) \qquad (9.4)$$

$$I_y(i,j,k) = iix(i,j,k)-iix(i,j,k-1)+iiz(i-1,j,k)-iiz(i,j,k) \qquad (9.5)$$

$$I_z(i,j,k) = iix(i,j-1,k)-iix(i,j,k)+iiy(i,j,k)-iiy(i-1,j,k) \qquad (9.6)$$

Faraday's induction law (Equations 9.1, 9.2 and 9.3) and the branch currents in Equations 9.4, 9.5, and 9.6 show that loop currents are coupled to each other. Therefore, for the impedance network, loop analysis is performed by solving the coupled loop currents for each voxel. Loop currents, at the x-, y- and z- faces of the voxel (Figure 9.1), are solved using a successive over relaxation (SOR) method [13]. Branch currents are calculated for each voxel using loop currents. For the voxel conductivities (units S/m) of σ_x, σ_y and σ_z in x-, y- and z-directions, the induced electric field components (E_x, E_y, and E_z) are derived using Equations 9.7, 9.8, and 9.9, respectively.

$$E_x(i,j,k) = \frac{i_x(i,j,k)}{\sigma_x(i,j,k)S_yS_z} \qquad (9.7)$$

$$E_y(i,j,k) = \frac{i_y(i,j,k)}{\sigma_y(i,j,k)S_xS_z} \qquad (9.8)$$

$$E_z(i,j,k) = \frac{i_z(i,j,k)}{\sigma_z(i,j,k)S_xS_y} \qquad (9.9)$$

9.4 Validation of the Impedance Method

To validate this implementation of the impedance method, two design examples were chosen. For the first design, a figure-8 configuration was used for the magnetic coil. For the second design, a circular coil was placed perpendicular to the air-tissue interface. For both the examples, numerical solutions are compared with analytical solutions.

9.4.1 Example 1: Figure-8 Coil Parallel to Tissue

Due to wide use of figure-8 magnetic coils for magnetic stimulation, this configuration was modeled as an impedance network. The figure-8 coil was constructed using two four-turn spiral coils. Each coil had an outer and inner diameter of 33.5 mm and 25 mm, respectively. Figure 9.2 shows the simulation model and induced electric field distributions. A tissue (conductivity 0.5 S/m) model with dimensions 80 mm x 80 mm x 80 mm was created (Figure 9.2 (a) and (b)), and the 3-D electric field was simulated using the impedance method. Figure 9.2 (d) and (f) show the induced electric field components E_x (x-direction) and E_y (y- direction) in the observation plane parallel (1.5 mm away) to the coil. Due to the parallel configuration, the electric field component in the z-direction is zero.

For the same coil configuration (spiral coils), the induced electric field can be calculated based on the analytical formulation of the magnetic vector potential represented in cylindrical coordinates (Equation 9.10 and 9.11). Due to the parallel placement of the coil to the observation plane, the induced field is in the observation plane only ($\phi - \rho$ plane).

$$\vec{A}(\rho,z,t) = \sum_{i=1}^{N_a} \frac{\mu_0 I(t) a_j}{\pi} \int_0^{\pi/2} \frac{(2sin^2\phi - 1)}{\sqrt{(a_i+\rho_i)^2 + z_i^2 - 4a_i\rho_i sin^2\phi}} d\phi\vec{a}_\phi \tag{9.10}$$

$$\vec{E}(r,t) = -\frac{\partial \vec{A}(r,t)}{\partial t} \tag{9.11}$$

where a_i, ρ_i and z_i are the radii, radial distance location ρ, and vertical (z-direction) distance from the turn i.

Comparing the induced electric field in the x- (Figure 9.2 (c) and (d)) and y- (Figure 9.2 (e) and (f)) direction using the impedance method (finite boundaries) and analytical solution (infinite boundaries), a good agreement ($\frac{\textit{Average difference between the numerical and analytical model}}{\textit{Peak E-field value over simulation model}} < 3\%$) between the two methods is clear. The difference reduces below 1% by increasing (more than four times) the simulation model of the impedance method to approach infinite boundary conditions. This example demonstrates that the impedance method is an effective simulation algorithm for calculating the induced electric field in the simple tissue structure (homogeneous model).

9.4.2 Example 2: Coil Perpendicular to Tissue

Nerve is a heterogeneous medium and causes discontinuity in the tissue conductivity perpendicular to the induced electric field. This results in surface charge at the interface [18]. For time-varying magnetic field, the surface current contributes to the induced electric field. Therefore, to validate the use of the impedance method for medium discontinuity, a coil in the perpendicular configuration is chosen. Figure 9.3 (a) shows the block diagram of the coil position to the conductive tissue. As

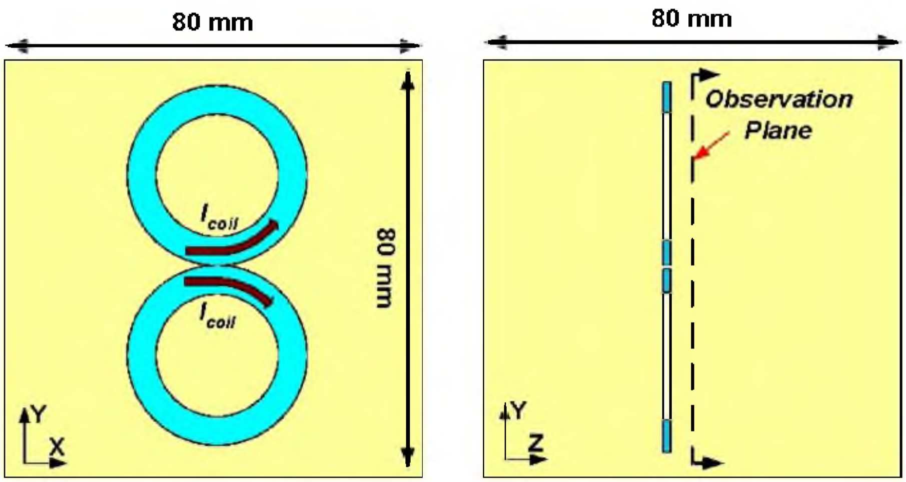

(a) Top View (X-Y Plane)

(b) Side View (Y-Z Plane)

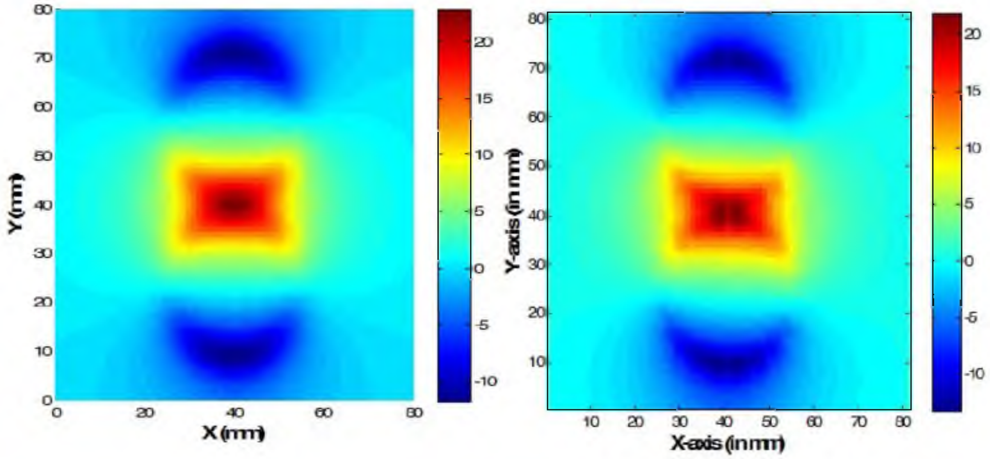

(c) E_x - Analytical Solution

(d) E_x - Impedance Method

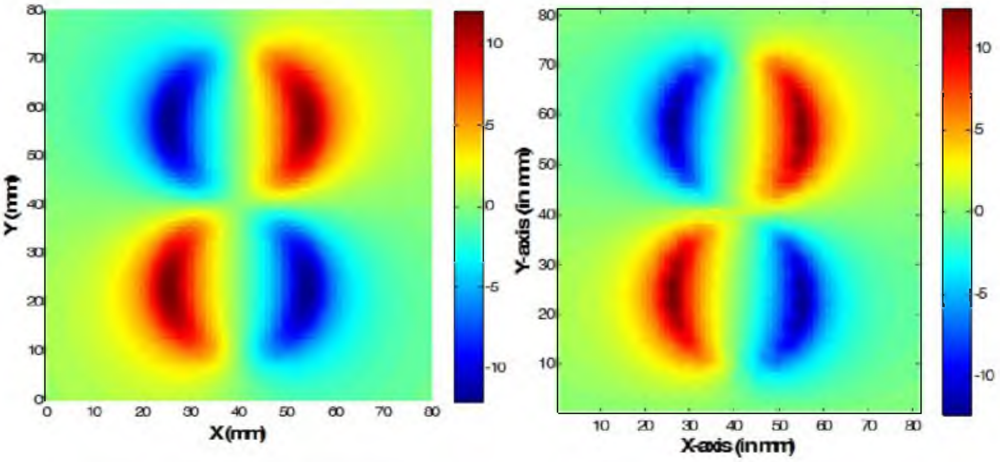

(e) E_y - Analytical Solution

(f) E_y - Impedance Method

Figure 9.2. Numerical modeling: (a) Top and (b) side view of the numerical model. Calculation of the electric field (magnitude) components (c) E_x and (e) E_y are done using analytical solution and compared with the impedance method solution (d), (e). All electric field values are in V/m.

shown, a circular single turn coil with diameter 5 mm was placed 4.5 mm (center to the tissue) away from the surface. A numerical tissue model with dimensions 80 mm x 80 mm x 80 mm was created. Electric field was simulated for the coil current of 600 A at 2 kHz. Using the impedance method, the induced electric field was simulated in x-, y-, and z- directions. The results are compared with the analytical solutions for the simulation model, which was presented for the air-tissue (semi-infinite) interface located at $z = 0$ [12]. Equations 9.12, 9.13 and 9.14 formulate the induced electric field in the conductive tissue (location (x, y, z)) due to the current segment $\vec{dl}$ (where $\vec{dl} = dl_x\vec{x} + dl_y\vec{y} + dl_z\vec{z}$) located at (x_0, y_0, z_0). At the observation point, the fields from each current segment are integrated over the loop to calculate the total induced field due to the coil.

$$\begin{aligned} d\vec{E}_x &= -\frac{\mu_0}{4\pi}\frac{\partial I}{\partial t}\left[\frac{dl_x}{R} + \frac{x dl_z}{\rho^2}\left(1 - \frac{z_0 - z}{R}\right)\right]\vec{x} \qquad (9.12) \\ d\vec{E}_y &= -\frac{\mu_0}{4\pi}\frac{\partial I}{\partial t}\left[\frac{dl_y}{R} + \frac{y dl_z}{\rho^2}\left(1 - \frac{z_0 - z}{R}\right)\right]\vec{y} \qquad (9.13) \\ d\vec{E}_z &= 0\,\vec{z} \qquad (9.14) \end{aligned}$$

where I and μ_0 are the current in the current segment and magnetic permeability of the free space, $\rho = \sqrt{(x-x_0)^2 + (y-y_0)^2}$ and $R = \sqrt{(x-x_0)^2 + (y-y_0)^2 + (z-z_0)^2}$.

Figures 9.3 (b) and (d) show the simulated electric field distribution using the impedance method in x- and y- directions. Figures 9.3 (c) and (e) show the calculated electric field using an analytical solution. As compared to the analytical value of E_z equal to zero, the peak E_z using the impedance method achieves a very small value ($\sim$ 0.07 V/m). The results show a good agreement between the simulated and calculated field components. The small difference ($\sim$ 8%) between the simulated (numerical model) and calculated (analytical) is primarily contributed by the finite length of the tissue model for the impedance method.

Using two examples it is shown that the impedance method can be used effectively to simulate the induced electric field in the presence of tissue boundaries. The good agreement between the simulation and analytical solutions validates the efficacy of the implemented impedance method to study the effect of conductivity discontinuity on the induced electric field.

9.5 Numerical Models for Ex-vivo Experiments

As discussed in Chapter 8 during the ex-vivo experiment on the frog's sciatic nerve, multiple phenomena were seen which are not predictable using homogeneous modeling of the induced electric field [11]. In the following sections, simulation models are developed to study the effect of saline volume in the petri dish. The second study is performed to analyze the effect of nerve termination on the stimulation site.

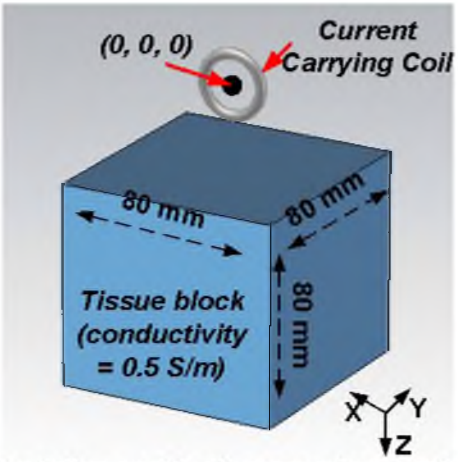

(a) Simulation model with perpendicular coil

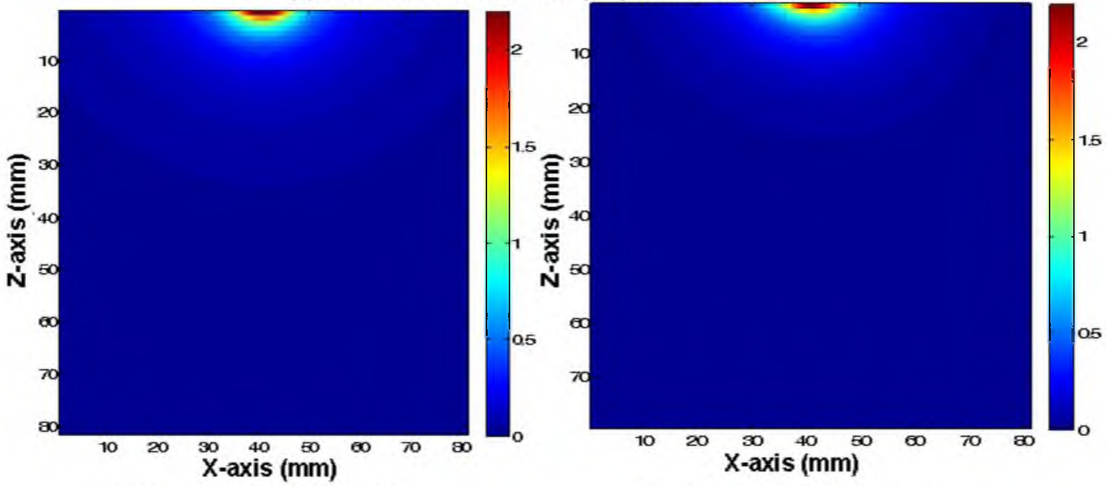

(b) E_x - Analytical Solution

(c) E_x - Impedance Method

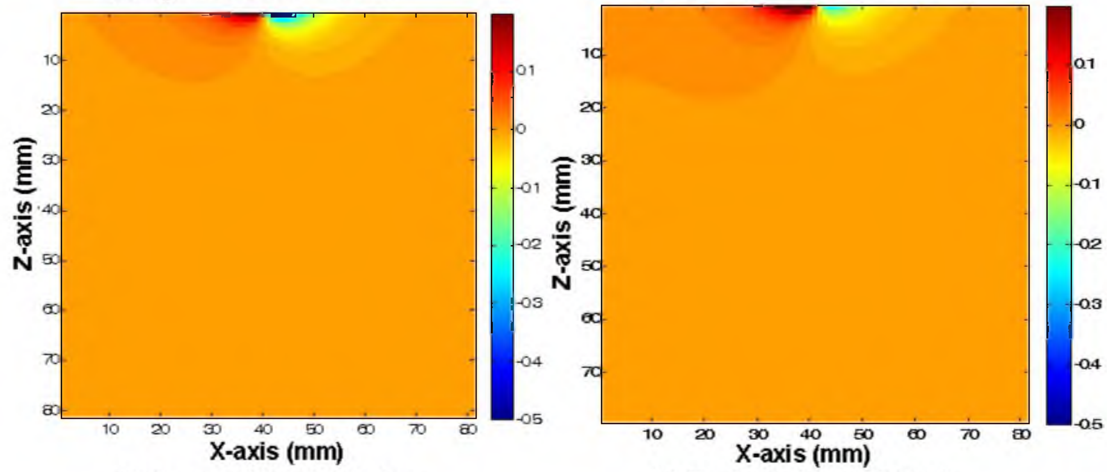

(d) E_y - Analytical Solution

(e) E_y - Impedance Method

Figure 9.3. Induced electric field due to a figure-8 magnetic coil. Calculation of the electric field components E_x (b, d) and E_y (c, e) are done using analytical solution (Equations 9.12 and 9.13) and impedance method. Due to a finite simulation boundary, E_z (max) = 0.07 V/m. All electric field values are in V/m.

9.5.1 Effect of Saline Volume on Stimulation Threshold

During Experiment 4 in Chapter 8, the stimulation threshold for different saline volumes was recorded. It was shown that for the saline height below the nerve diameter, the stimulation threshold increases with the reduction of saline height in the petri dish. Therefore, to study the effect of surrounding conductive medium (saline) on the induced electric field, a numerical model was created to include different conductive boundaries.

Figures 9.4 (a) and (b) show the side and top view of the simulation model. An impedance network was created to include the petri dish, saline and a cylindrical nerve. Figure 9.4 (c) shows the cross-section view of the nerve's numerical model. For the simulation, a figure-8 coil with individual coil's outer diameter 33 mm and inner diameter 25 mm was used. Each coil was fed with a sinusoidal current of 600 A at 2 kHz in reverse direction to maximize the induced electric field at the center of the figure-8 coil. The magnetic coil was placed 1.5 mm from the petri dish (dimension of 80 mm x 80 mm). A cylindrical nerve with an elliptical (1 mm x 0.9 mm) cross-section and length 45 mm is used for the model creation and is placed along the x- direction. The numerical model uses the spatial resolution of 0.5 mm, 0.1 mm, and 0.1 mm in x-, y-, and z- directions, respectively, and achieves ~2.7 millions voxels for simulation.

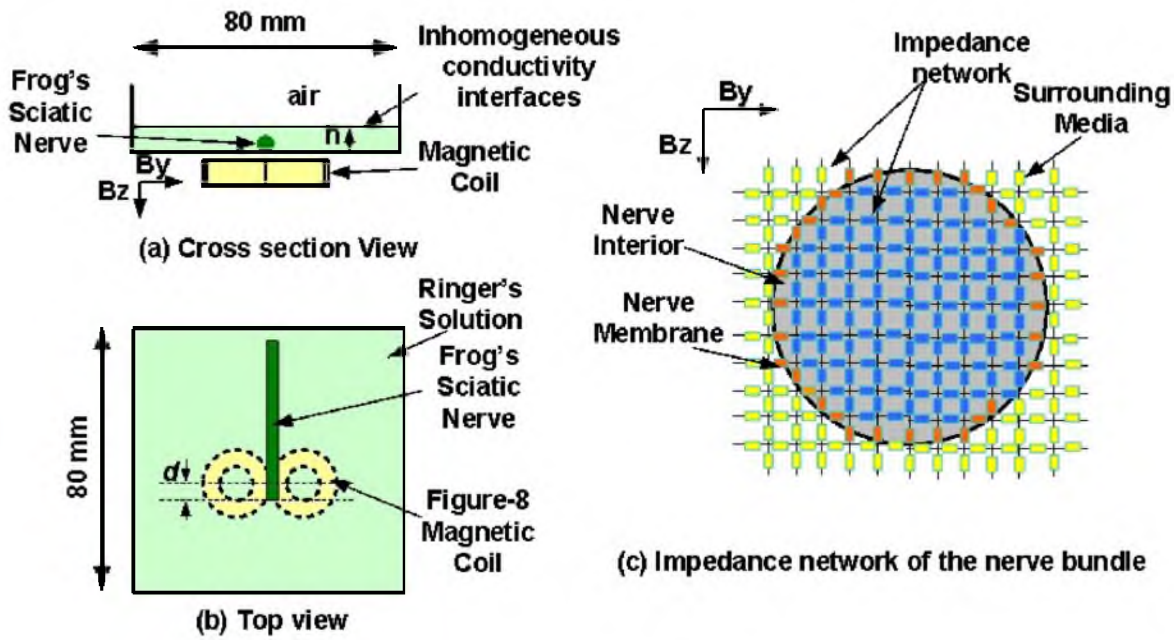

(a) Cross section View

(b) Top view

(c) Impedance network of the nerve bundle

Figure 9.4. Simulation model to characterize the effect of Ringers solution on the induced electric field. (a) Cross-section (Y-Z) and (b) Cross-section (X-Y) views of the simulation model. (c) Impedance network model of nerve bundle submerged in the ringer (saline) solution.

To study the effect of surrounding conductive media (saline) on the induced electric field, multiple numerical models were created to include the individual saline height for the range of 0 mm to 1.9 mm in steps of 0.1 mm. To include the heterogeneity of the nerve, the outer layer of the nerve bundle was considered as membrane with conductivity of 0.02 S/m. The interior part of the nerve was considered as the isotropic intracellular space with conductivity 0.91 S/m. Petri dish is modeled as an insulator with conductivity 1x10^{-11} S/m, and saline with conductivity 0.5 S/m was used for the model.

Figure 9.5(a) shows the average and standard deviation of the induced electric field (E_x) across the cross-section of the nerve end. The induced field is simulated as a function of saline height. For zero-mm saline in the petri dish, the average value of the induced field is zero. Therefore, it requires a high voltage threshold to cause the neural activity. Figure 9.5(a) indicates that the induced electric field in the nerve increases with the increase in saline height. For the saline height below the nerve diameter, the induced electric field increases faster than the induced field increment rate above nerve height. Figure 9.5(b) shows the cross-section view of the induced electric field along nerve (x- direction) for saline height of 0.5 mm.

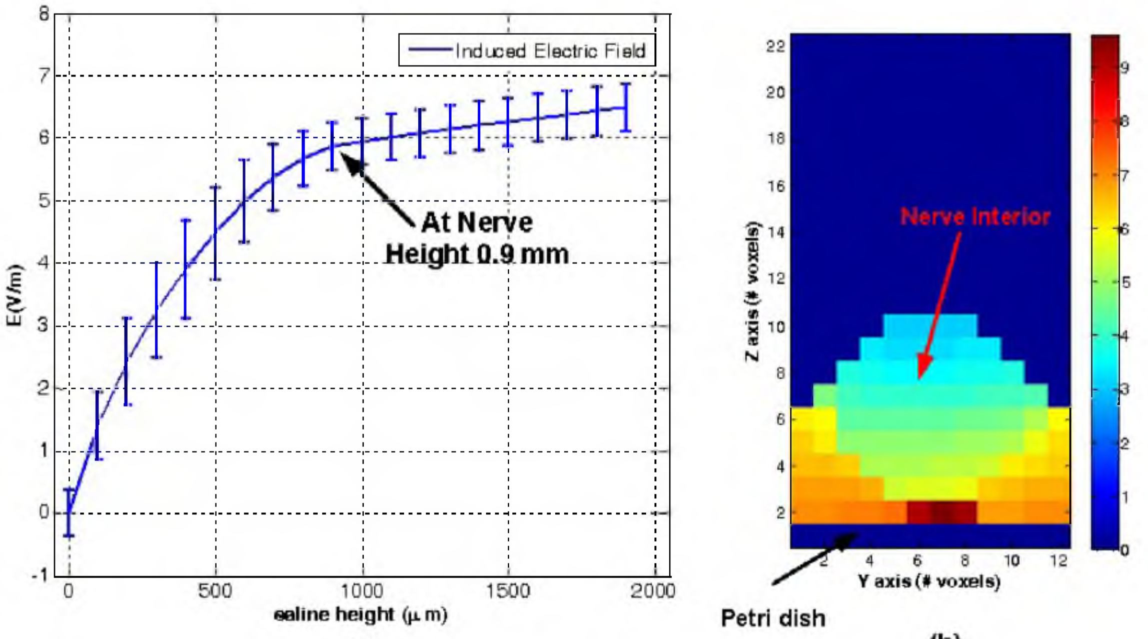

(a) (b)

Figure 9.5. Simulated electric field: (a) Average and variation of the induced electric field (Ex) at the nerve termination. Field values are averaged over the nerve cross-section (Y-Z). (b) Distribution of the induced electric field in nerve bundle and surrounding media due to the magnetic coil. All fields are in V/m.

The proposed numerical models indicate that the induced electric field inside the nerve can be greatly affected by the amount of saline in the petri dish. Petri dish with low saline volume will require higher threshold voltage to evoke the neural activity. This phenomenon is validated during the ex-vivo experiment on the frog's sciatic nerve (Experiment 4, Chapter 8), which shows that by reducing the saline height below the nerve diameter, the stimulation threshold increases.

9.5.2 Effect of Nerve Termination on the Stimulation Site

It was commonly believed that for the coil position close to the nerve termination (end-point stimulation), the action potential initiates at the nerve end [14]. Therefore, the stimulation threshold should be lowest for the positioning of coil E_{max} near the nerve end. Moreover, the threshold should be symmetric along the nerve for the +ve and -ve positioning of the E_{max} location to the nerve termination. In Experiment 4 (Chapter 8), the stimulation threshold was lowest for the d = +5 mm (Figure 9.6 (a) and (b)), which is contrary to the condition for the end-point stimulation. For the current system, d is defined as the distance of the coil E_{max} to the nerve end. The value of d will be +ve when the magnetic coil E_{max} location is moved towards the muscle (Figure 9.6 (a)).

To study the effect of nerve termination, a passive model of the nerve was created to estimate the variation of the transmembrane potential along the nerve in response to the induced electric field. Ranvier nodes of axon were represented by parallel $R-C$ networks, defining the transmembrane resistance r_m and capacitance c_m, and the nerve ends were represented by the termination impedance of r_{seal}. Figure 9.7 shows the network model of the axon including the intracellular resistance r_a, transmembrane resistance r_m, and transmembrane capacitance c_m. Due to the large dimension of the extracellular space, the extracellular impedance between the nodes is zero. To solve the change in the transmembrane voltage due to the magnetic stimulation, the passive model of the axon was solved as a function of intracellular induced electric field (E_x). For the n-node axon, Equation 9.15 formulates the correlation between the transmembrane voltage V_m and the induced electric field E_x for intermediate nodes. For the nerve terminations node 1 and node n, Equations 9.16 and 9.15 can be used to solve for the V_1 and V_n, respectively.

$$j\omega c_m V(N) + \frac{V(N)}{r_m} - \frac{V(N-1) - 2V(N) + V(N+1)}{r_a} + \frac{V(N)}{r_{seal}} = \frac{1}{r_a}(E_x(N) - E_x(N+1))dx (9.15)$$

$$j\omega c_m V(1) + \frac{V(1)}{r_m} + \frac{V(2) - V(1)}{r_a} + \frac{V(1)}{r_{seal}} = \frac{1}{r_a}E_x(1)dx (9.16)$$

$$j\omega c_m V(n) + \frac{V(n)}{r_m} - \frac{V(n-1) - V(n)}{r_a} + \frac{V(n)}{r_{seal}} = \frac{1}{r_a}E_x(n)dx (9.17)$$

Value of the nerve termination impedance (r_{seal}) varies based on the suture, no-suture, or self-sealing condition. Therefore, the equations were solved for the value of r_{seal}/r_m 0.1 and 1, which

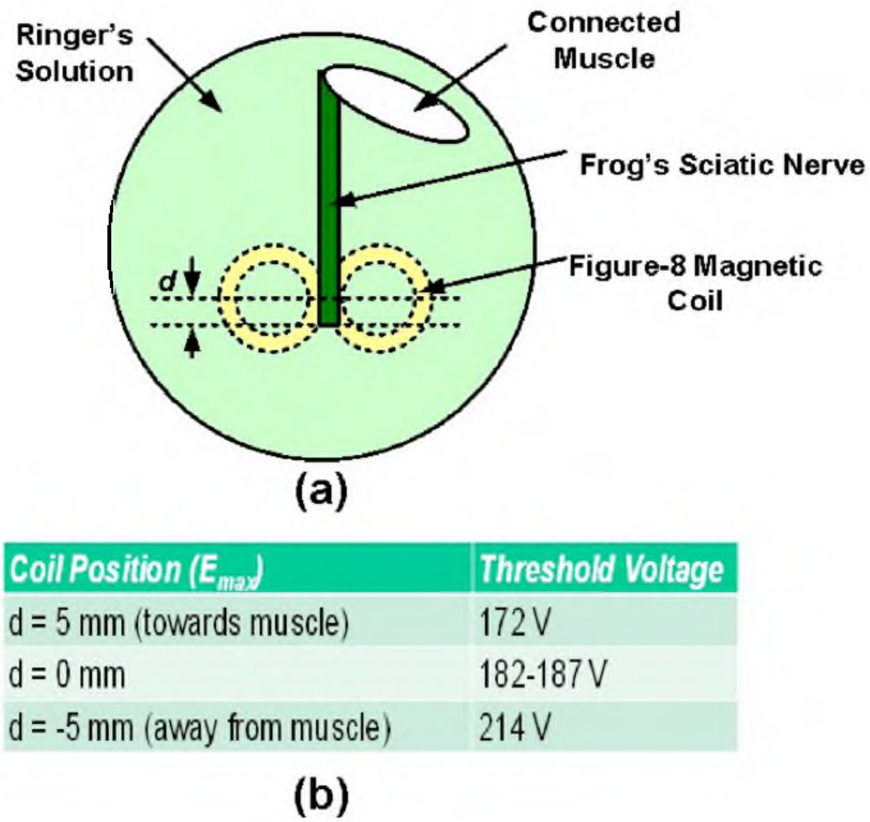

Coil Position (E_{max})	Threshold Voltage
d = 5 mm (towards muscle)	172 V
d = 0 mm	182-187 V
d = -5 mm (away from muscle)	214 V

Figure 9.6. Effect of nerve position: (a) Position of nerve termination with respect to magnetic coil. d is the distance of nerve end from the figure-8 center. (b) Threshold variation due to nerves end location with the E_{max} of the magnetic coil during Experiment 4 (Chapter 8).

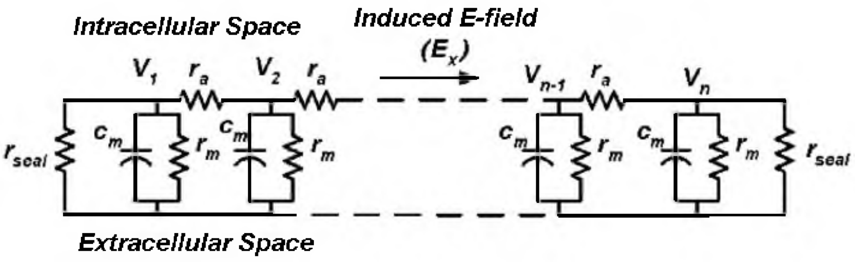

Figure 9.7. Passive model of the axon using lumped elements. The end points are terminated using sealing resistance.

represents a leaky (low impedance) and sealed (high impedance) termination, respectively. Coil's E_{max} location is varied for 3 locations (d = -5 mm, 0 mm and +5 mm) with respect to nerve end. For each condition, electric fields are calculated along the nerve. Simulation was performed for a figure-8 coil (coil outer diameter =33 mm) with a coil current of 600 A at 2 kHz. For the simulations, 20 μm diameter axon was used with an internodal distance of 0.5 mm. The axon has membrane conductance G_{na} of 120 mS/cm^2, and node capacitance C_m of $1\mu F/cm^2$. Figure 9.8 shows the variation of transmembrane potential along the axon as a function of d and r_{seal}. Figure 9.8(a) shows that for $r_{seal} = r_m$, the peak V_m is achieved at position x = 0. For the same stimulation current, V_m peaked for d = 0 mm. This condition initiates end-point stimulation. However, for the leaky termination ($r_{seal} = 0.1{*}r_m$), the membrane potential at the nerve end (x = 0 mm) is shorted and the peak membrane potential is reached at the point away from the end (midpoint stimulation).

For midpoint stimulation, Figure 9.8(b) shows that for the same stimulation current, V_m increases with d. A similar trend is seen in Experiment 4 (Chapter 8) as tabulated in Figure 9.6(b) which indicates the midpoint stimulation of the frog's sciatic nerve. It also demonstrates that by using the passive axon model, the effect of the axon property and nerve termination (leaky or sealed) can be studied for the magnetic stimulation.

9.6 Numerical Model of Frog's Sciatic nerve

The frog's sciatic nerve is a heterogeneous tissue consisting of hundreds of axons with an axon diameter in the range of 15-20 μm [16]. A nerve bundle with diameter 1 mm and length 3 mm is considered with 25 μm thick nerve membrane. Figure 9.9 (a) shows the 3-D models of the nerve with hundreds of axons along the x-direction and Figure 9.9 (b) shows the cross -section view of the nerve bundle surrounded by the conductive tissue. The intracellular space of the axon is embedded either by a membrane or an insulating myelination layer (Figure 9.10). Therefore, using these models, we study the effect of myelination on the induced current distribution. A 3-D impedance network model was created for the nerve bundle and surrounding tissue as shown in Figure 9.8 (c). Figure 9.9(d) shows the random distributions of the axons inside the nerve bundle. The developed numerical model uses the spatial resolution of 0.1 mm, 4 μm, 4 μm in x-, y- and z- direction, respectively. A figure-8 microcoil (outer diameter = 1 mm, inner diameter = 0.8 mm, 4 turns) is used for for the stimulation. Each coil of the figure-8 is driven with a sinusoidal current of 600 A at 2 kHz in the opposite directions to maximize the induced field at the center of the magnetic coil. The coil is placed 1 mm away from the nerve bundle.

Due to low operating frequency f for the operation of the magnetic stimulation, $\sigma \gg 2\pi f \varepsilon$, where σ and ε are the tissue conductivity and permittivity, respectively. Therefore, the branch

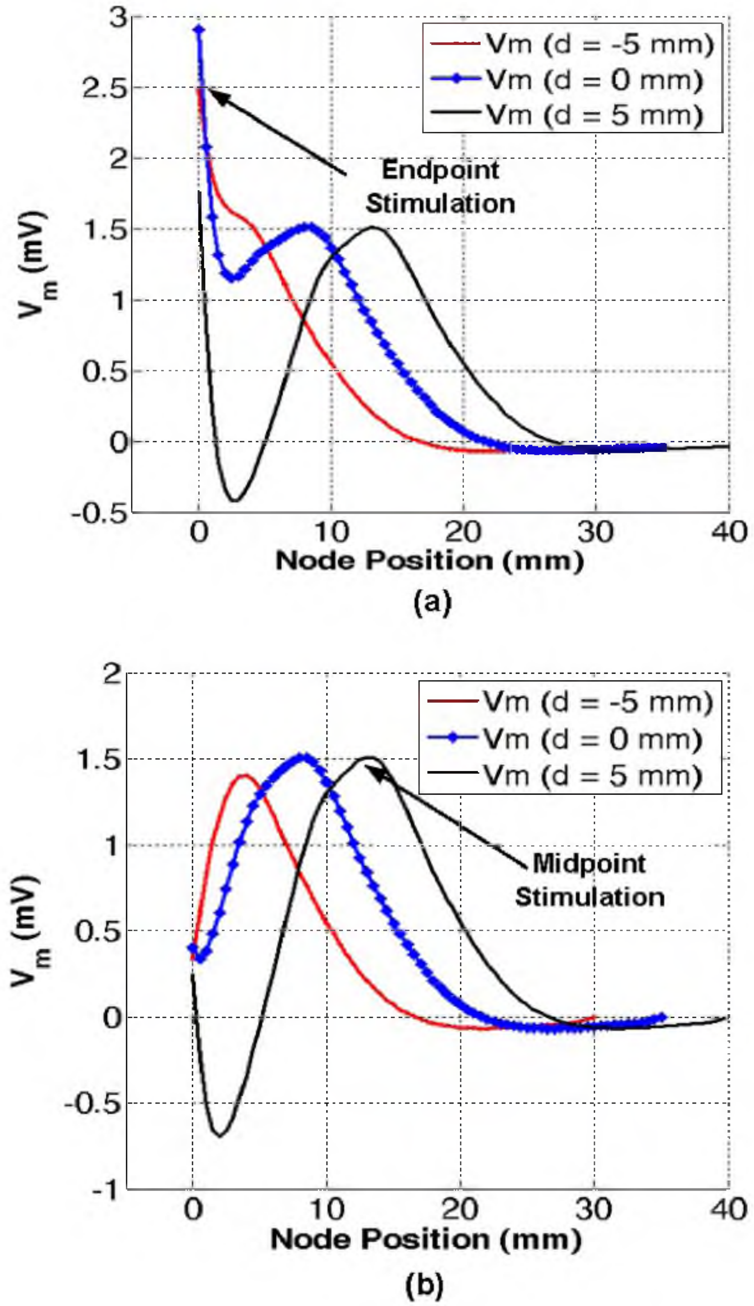

Figure 9.8. Effect of termination impedance on the stimulation site. (a) End-point stimulation for $r_{seal} = r_m$. (b) Midpoint stimulation for $r_{seal} = 0.1{*}r_m$. d is the distance of the nerve end from the figure-8 center.

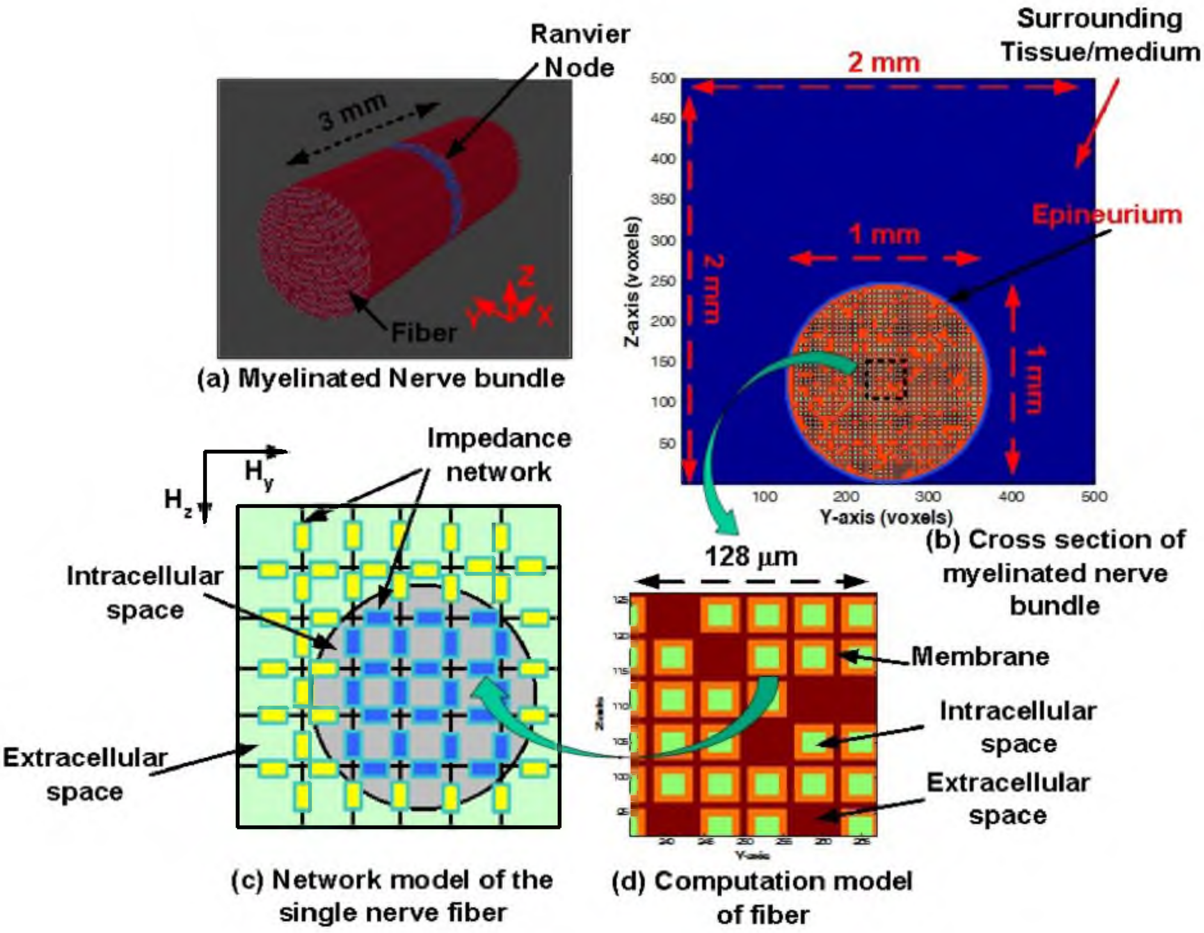

Figure 9.9. Impedance network model: (a) 3-D computational model of nerve bundle (1-mm diameter, 3-mm length). (b) Cross-section view of the numerical model consists of nerve bundle in saline. (c) Impedance model of the single fiber. (d) Computational model of the randomly distributed axons.

impedances of the network model are primarily composed of resistive elements. For the heterogeneous tissue model, the impedances are calculated based on the conductivity parameters presented in Table 9.1.

To study the effect of tissue heterogeneity on the transmembrane potential V_m, two studies were performed. In the following sections, the first simulation model compares the effect of myelination node on the stimulation location. The second model studies the effect of axon density on the peak V_m value to measure the coupling between the axons.

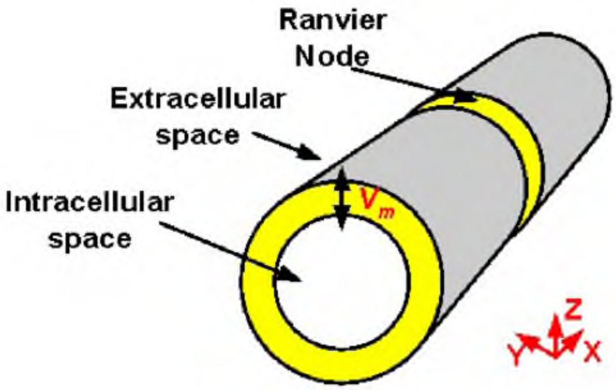

Figure 9.10. 3-D myelinated nerve fiber (axon) along x- direction. Transmembrane potential V_m is defined as the potential difference between intracellular to extracellular space.

Table 9.1. Tissue Property-Frog Sciatic Nerve

Tissue Type	Conductivity $(\sigma_x, \sigma_y, \sigma_z)$ (S/m) [17]
Surrounding tissue	$(0.5, 0.5, 0.5)$
Nerve membrane	$(0.02, 0.02, 0.02)$
Intracellular space	$(0.91, 0.91, 0.91)$
Extracellular space	$(0.33, 0.33, 0.33)$
Myelination (myelinated)	$10^{-9}, 10^{-9}, 10^{-9}$
Ranvier Node (myelinated)	$2.4x10^{-7}, 2.4x10^{-7}, 2.4x10^{-7}$
Axon Membrane (unmyelinated)	$2.4x10^{-7}, 2.4x10^{-7}, 2.4x10^{-7}$

9.6.1 Effect of Myelinated Nodes

Figure 9.10 shows the anatomy of the nerve fiber, consisting of a Ranvier node and high resistive myelination layer over the axon. For the unmyelinated nerve, the intracellular space is embedded inside a conductive membrane for which the conductivity depends on the conductance of the sodium and potassium channels. The nerve bundle is populated with 1000 randomly distributed axons to achieve a filling factor β of 0.77, where $\beta = \frac{\text{Area occupied by the axons}}{\text{Cross-section area of the nerve bundle}}$.

Figure 9.11(a) and (b) show the induced electric field (E_x along nerve) distribution in the cross-section of the unmyelinated and myelinated nerve bundle. The Ranvier node is located at position 1.5 mm and the E_{max} position of the magnetic coil is placed at the location 1.5 mm. Figure 9.11(c) and (d) show the distribution of transmembrane potential along the nerve (x-direction). As expected from the passive nerve model of the unmyelinated axon, the peak V_m coincides with the peak location of $\frac{\partial E_x}{\partial x}$, which is symmetric with respect to the midpoint (x = 1.5 mm). However, for the myelinated axon, the transmembrane current can only pass through the Ranvier node. Therefore, the peak of V_m is achieved at the location of node of Ranvier. Comparison between the peak

V_m for unmyelinated (Figure 9.11(c)) and myelinated (Figure 9.11(d)) axon shows that for the same stimulation current in the magnetic coil, the V_m for the myelinated axon achieve 3 × higher magnitude than the unmyelinated axon. This study indicates that for the same V_m threshold, the myelinated axon requires lower voltage threshold to cause the neural activity.

9.6.2 Effect of Axon Density

Traditionally, V_m is calculated for a single axon placed inside an infinite and homogeneous extracellular space [11]. However, due to the high axon density ($\beta > 0.7$) of the nerve bundle,

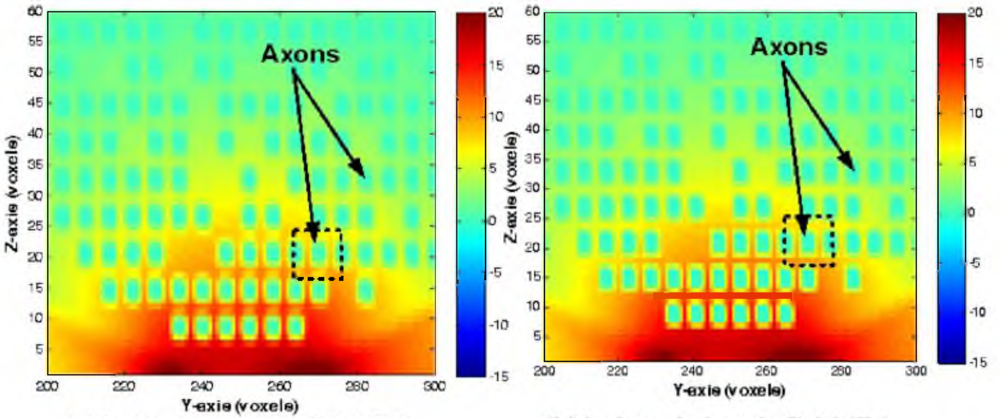

(a) Induced electric field (E_x) distribution in unmyelinated nerve fibers (Fiber count = 1000)

(b) Induced electric field (E_x) distribution in myelinated nerve fibers (Fiber count = 1000)

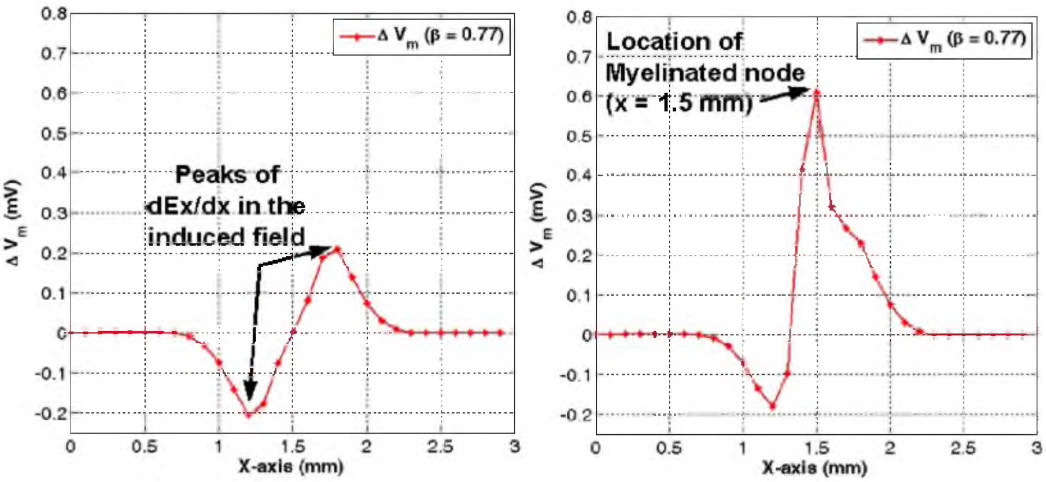

(c) Distribution of membrane potential in unmyelinated nerve fiber

(d) Distribution of membrane potential in myelinated nerve fiber

Figure 9.11. Effect of fiber myelination on the membrane potential. Induced electric field E_x distribution for unmyelinated and myelinated axons. Myelinated fiber shows higher rise in membrane potential at the Ranvier node. All electric field values are in V/m.

extracellular space is limited. This increases the interactions between axons. Therefore, to study the effect of the axon density, two models were created with fill factor β of 0.45 (axon count = 600, Figure 9.12 (a)) and 0.77 (axon count = 1000, Figure 9.12 (b)). The 20-μm diameter myelinated axons are randomly populated inside the nerve bundle. Figures 9.12 (c) and (d) show the distribution of induced electric field in the cross-section of the nerve for β values of 0.45 and 0.77, respectively.

Figure 9.12 (e) shows the distribution of the transmembrane potential V_m along the axon for different axon densities. It compares the peak V_m value at the Ranvier node of the same axon in two conditions and reflects that higher density nerve achieves higher V_m (5% difference). It is seen that due to the high density inside the nerve, the induced current is steered by the heterogeneous boundaries to achieve higher V_m.

9.7 Multiresolution Impedance Method

We used cm-sized coils in our ex-vivo experiment with the frog's sciatic nerve. To compare our simulations with the experiment results, we require an accurate model of the nerve and its surrounding tissue boundaries. For the nerve embedded inside the tissue, the model size needs to be 2-3 times bigger than the coil dimension to ensure the decay of the magnetic field at the model boundaries. Therefore, to resolve μm structures such as axons and nerve boundaries inside a cm-size numerical model, multiresolution discretization is required. Commercial FEM (finite-element method) based field solvers provide an option of multiresolution tetrahedral voxels during the meshing step. However, resolving 1 μm-sized features in a large cm-size (80 cm x-, y-, z-directions) simulation model results in a large simulation model ($\sim$20 million voxels), which limits the convergence of the solution.

Typically, impedance method is developed for fixed resolution simulation models [13]. To extend this approach, a 2-D impedance method is proposed which meshes the simulation model using multiple resolution voxels [15]. The meshing is performed by clustering the same material voxels into a single large voxel, reducing the number in the simulation model. Due to the complexity of the multiresolution meshing, the majority of the computational time is devoted to the network impedance calculation. Moreover, for the dense nerve bundle, the benefits of the proposed multiresolution meshing can not be achieved, which requires multiple voxels of the same tissue to create a a large dimension voxel.

In this section, we propose a multi-step impedance method to achieve a multiresolution impedance method for a 3-D tissue model. To simulate cm-size models, a coarse simulation is performed, which uses high dimension voxels. For each voxel, the induced electric field and branch currents are calculated. To reduce the resolution of the simulation for the region of interest (nerve and surrounding tissue), the induced electric field at the boundaries of the model is extracted from the

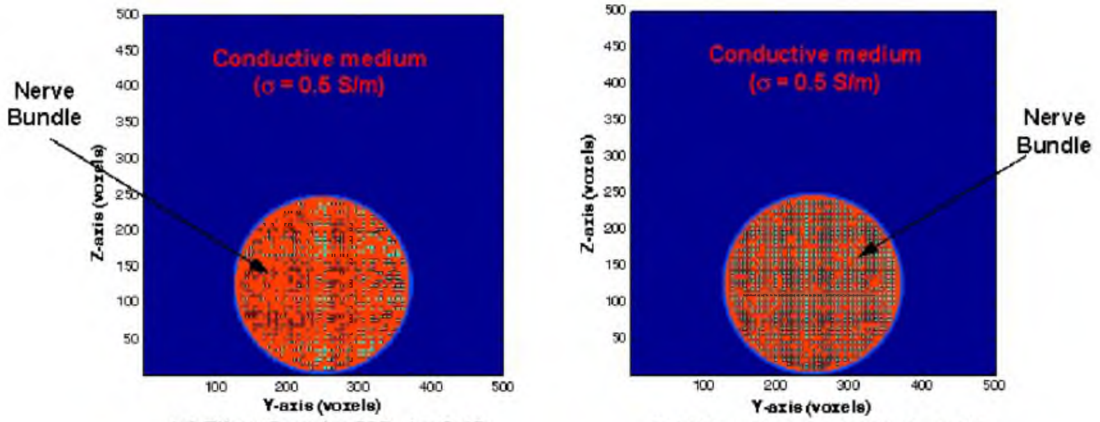

(a) Fiber Count = 600, β= 0.46

(b) Fiber Count = 1000, β= 0.77

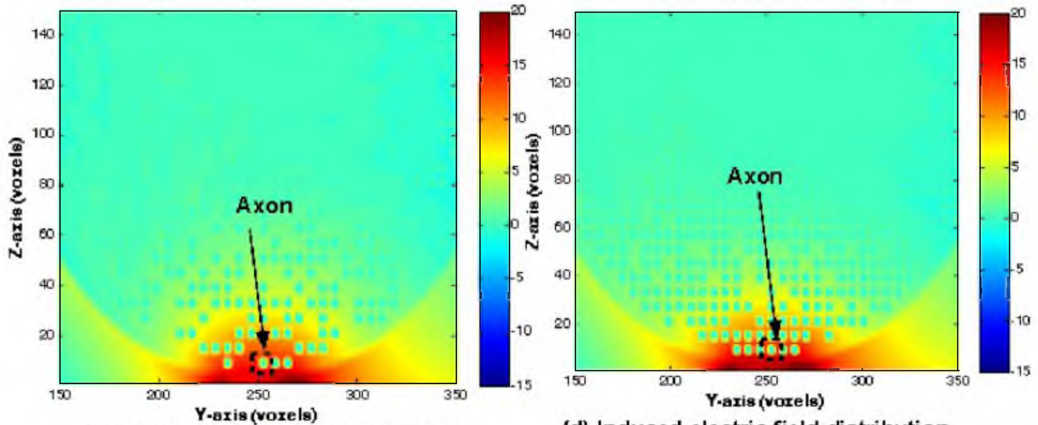

(c) Induced electric field distribution (E_x, Fiber count = 600)

(d) Induced electric field distribution (E_x, Fiber count = 1000)

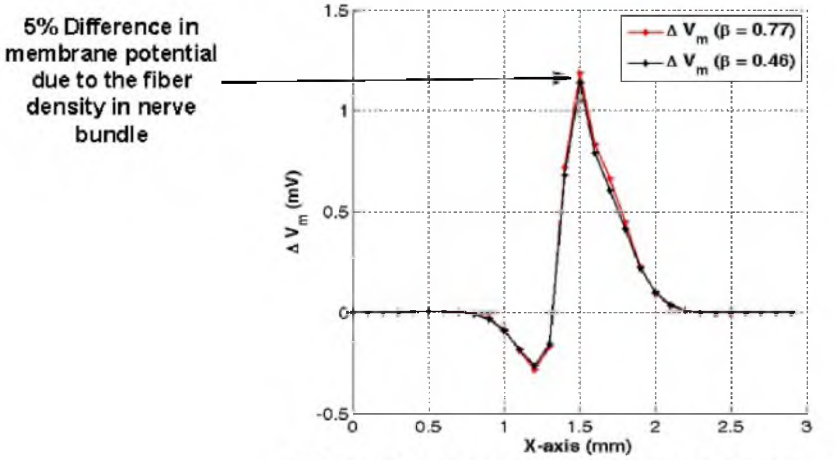

(e) Effect of fiber density on the membrane potential

Figure 9.12. Effect of fiber density on the induced electric field E_x distribution for the myelinated axons. The simulations are performed for two fill factors (a) β = 0.46 (600 axons) and (b) β = 0.77 (1000 axons). Electric field distribution inside nerve bundle for fill factors (c) β = 0.46 (600 axons) and (d) β = 0.77 (1000 axons). For the same axon, the denser nerve (β = 0.77) shows higher transmembrane potential. All electric field values are in V/m. (e) Membrane potential along the axon.

coarse model. The extracted boundary conditions are applied for the finer-resolution model to solve the induced electric field. The same procedure is applied until the target high resolution (e.g., μm) is achieved.

For example, to stimulate the induced electric field for cm-size magnetic coil (33-mm diameter) and to resolve the features down to 1 μm, initially coarse simulation is performed with 1 mm spatial resolution. The model includes the nerve (diameter 1 mm) embedded inside the 10 cm $\times$ 10 cm $\times$ 10 cm conductive media. A multi-step impedance method is performed to achieve a multiresolution simulation model of the nerve. Table 9.2 provides the resolution of the simulation models, number of voxels in each model, convergence criteria, and number of iteration to achieve the solution.

To compare the effectiveness of the proposed multiresolution, simulated branch currents, each high resolution simulation is compared with the imposed low resolution boundary conditions. Figure 9.13 shows the distribution of the branch currents (I_x, I_y and I_z) at the cross-section plane of the nerve for spatial resolution of 40 μm x 40 μm and 20 μm x 20 μm (in nerve cross-section). As seen in the figure, the current values at the boundaries are preserved and the features that cannot be resolved in the low-resolution model can be included in the high-resolution model. For example, for a nerve diameter of 1 mm, the nerve cross-section will occupy only one voxel in the 1-mm resolution model. However, high-resolution model such as 20 μm can include the curvature of the nerve and its membrane. Moreover, to resolve the axon's membrane and intracellular space, a 1 μm resolution model is created for the individual axon.

The simulation accuracy can be improved by increasing the number of steps from the low resolution to high resolution (1 mm $\rightarrow$ 200 μm $\rightarrow$ 40 μm $\rightarrow$ 20 μm $\rightarrow$ 1 μm) and by reducing the convergence error threshold. Therefore, the proposed multiresolution impedance method is an efficient tool to resolve small features (μm and below) in a large simulation model (cm-size) and can provide the trade-off between the computation time and simulation accuracy.

Table 9.2. Simulation Parameters

Resolution (x-, y-, z-)	Voxels (x-, y-, z-)	Convergence Threshold	Iteration
(2 mm, 1 mm, 1 mm)	(52, 102, 102)	4×10^{-4}	10000
(2 mm, 200 μm, 200 μm)	(50, 14, 14)	1×10^{-5}	10000
(2 mm, 40 μm, 40 μm)	(48, 52, 52)	4×10^{-4}	20000
(2 mm, 20 μm, 20 μm)	(46, 100, 100)	1×10^{-4}	23000
(2 mm, 1 μm, 1 μm)	(44, 20, 20)	2.2×10^{-5}	19540

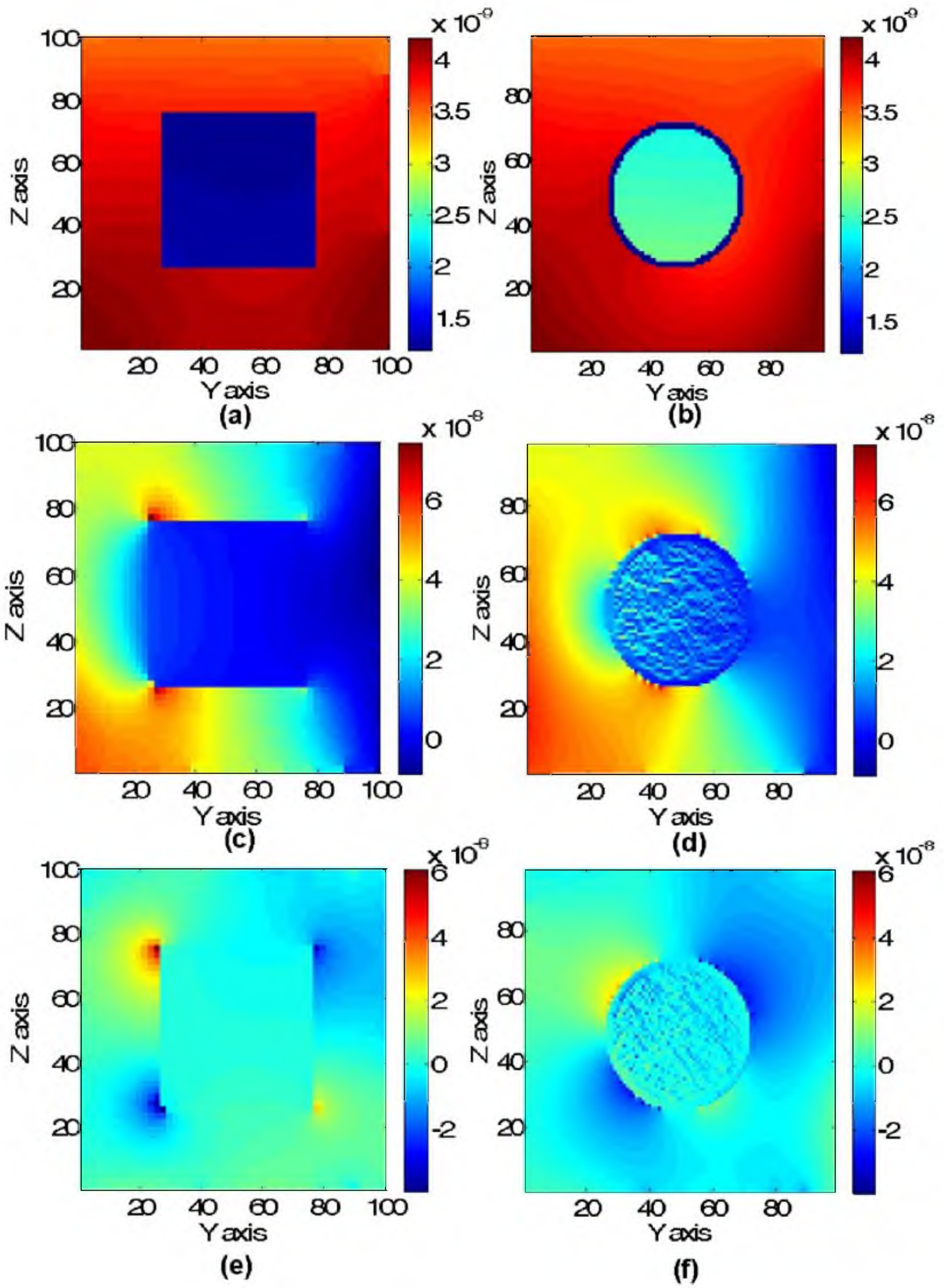

Figure 9.13. Extracted induced currents (a) I_x, (c) I_y and (e) I_z from (2-mm, 40-μm, 40-μm) resolution model that are imposed at the boundaries of the (2-mm, 20-μm, 20-μm) resolution model (Table 9.2). The nerve is represented as the square low-conductive structure. Simulated induced currents (b) I_x, (d) I_y and (f) I_z in the (2-mm, 20-μm, 20-μm) (Table 9.2) resolution model including the exact nerve structure. All currents are in amperes.

9.8 Multiresolution Numerical Model for Frog's Sciatic Nerve

As discussed in Section 9.6, axon density can alter the induced electric field distribution inside the nerve bundle. Therefore, for a cm-size magnetic coil, a multiresolution impedance model was created to study the induced electric field in the nerve bundle and transmembrane current i_m for individual axons. Figure 9.14 (a) shows the cross-section view of the 1-mm diameter nerve bundle in 20 μ x 20 μ resolution (Y-Z plane). In the x-direction, a spatial resolution of 2 mm was used to represent internodal spacing between the Ranvier nodes. The spacing was defined based on the ratio $d/d_0 = 100$, where d is internodal distance and d_0 is the axon diameter [11]. Table 9.3 presents the conductivity of different tissues.

For the simulation, a cm-size figure-8 coil (33-mm outer diameter with 4 turns in each coil) was used and placed 1.5 mm away (z-direction) from the nerve. The coils were excited with a 600 A sinusoidal signal of frequency 2 kHz. The nerve was located along the x-direction and aligned with the E_{max} location of the coil. Figure 9.14(b), (c), and (d) show the distribution of induced electric field in x-, y-, and z- directions, which show the heterogeneous boundaries between extracellular and axons in y- and z- direction affects the field distribution.

To study the effect of axon proximity and finite size extracellular space, a numerical model was created with 600 axons (Figure 9.15 (a)). The model achieves the resolution of 1 μm to resolve axon diameter of 18 μm (Figure 9.15 (b)). To compare the induced electric field for different axons, 4 axons were chosen. Axon-2 and axon-4 are proximal to each other (20-μm separation). Axon-1 and axon-3 are separated in z-direction by 0.5 mm. Figure 9.15 (c) and (d) show the induced intracellular electric field E_x for all four axons along the nerve (x-direction). Figure 9.15 (e) and (f) show the transmembrane current i_m for all four axons along the nerve (x-direction). As seen in Figure 9.15, $i_m \propto -\frac{\partial E_x}{\partial x}$. Therefore, magnetic pulse creates the depolarization (+ve i_m) and hyperpolarization sites (-ve i_m) along the axon. Based on the cable model of the axon, neural activity is initiated at location of peak i_m (depolarization site). Results indicate the induced electric field and transmemebrane current not only depend on the separation of the axon from the coil, but also on the positions of the surrounding axons. Comparing the E_x and i_m of the two proximal axons (axon-2 and axon-4), difference of $\sim 8\%$ is seen which is primarily contributed by the axon distribution inside the nerve.

9.9 Discussion

Numerical modeling and simulation are a key design tool to study the effect of tissue and system heterogeneity on the induced electric field. Compared to commercial field solvers which are limited to moderate complexity of the simulation model, the impedance method is suitable for the analysis of magnetic simulation. It is commonly believed that surrounding tissue does not affect the induced

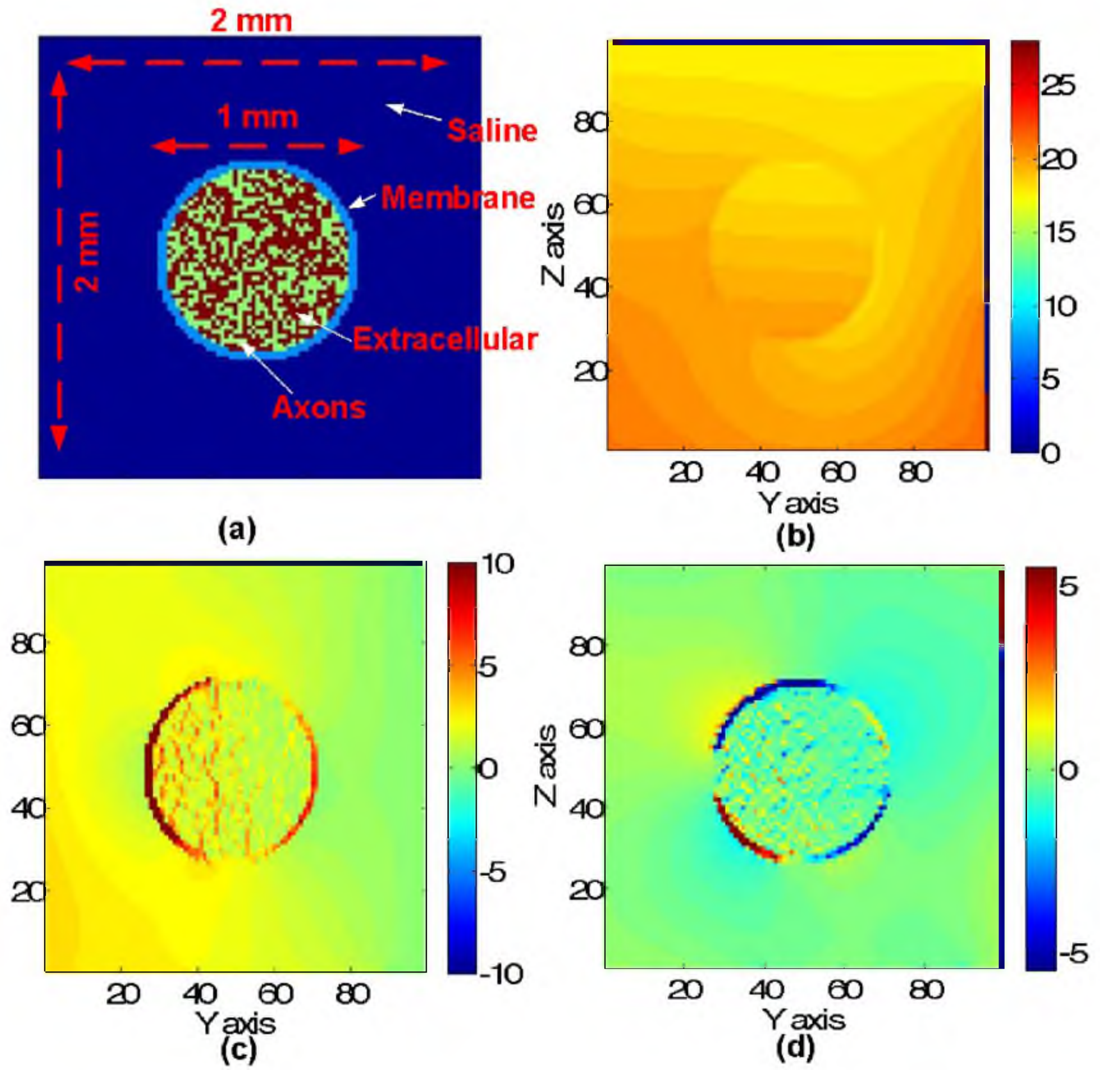

Figure 9.14. Electric field distribution: (a) Cross-section view of the nerve bundle with 600 axons, nerve membrane, extracellular space and surround media. Cross-section view of the induced electric fields (b) E_x, (c) E_y and (d) E_z in x-, y- and z- directions, respectively. All fields are in V/m.

Table 9.3. Tissue Property

Tissue Type	Conductivity $(\sigma_x, \sigma_y, \sigma_z)$ (S/m)
Surrounding tissue	(0.5, 0.5, 0.5)
Nerve membrane	(0.02, 0.02, 0.02)
Intracellular space	(0.91, 0.91, 0.91)
Extracellular space	(0.33, 0.33, 0.33)
Node	$(10^{-3}, 10^{-6}, 10^{-6})$

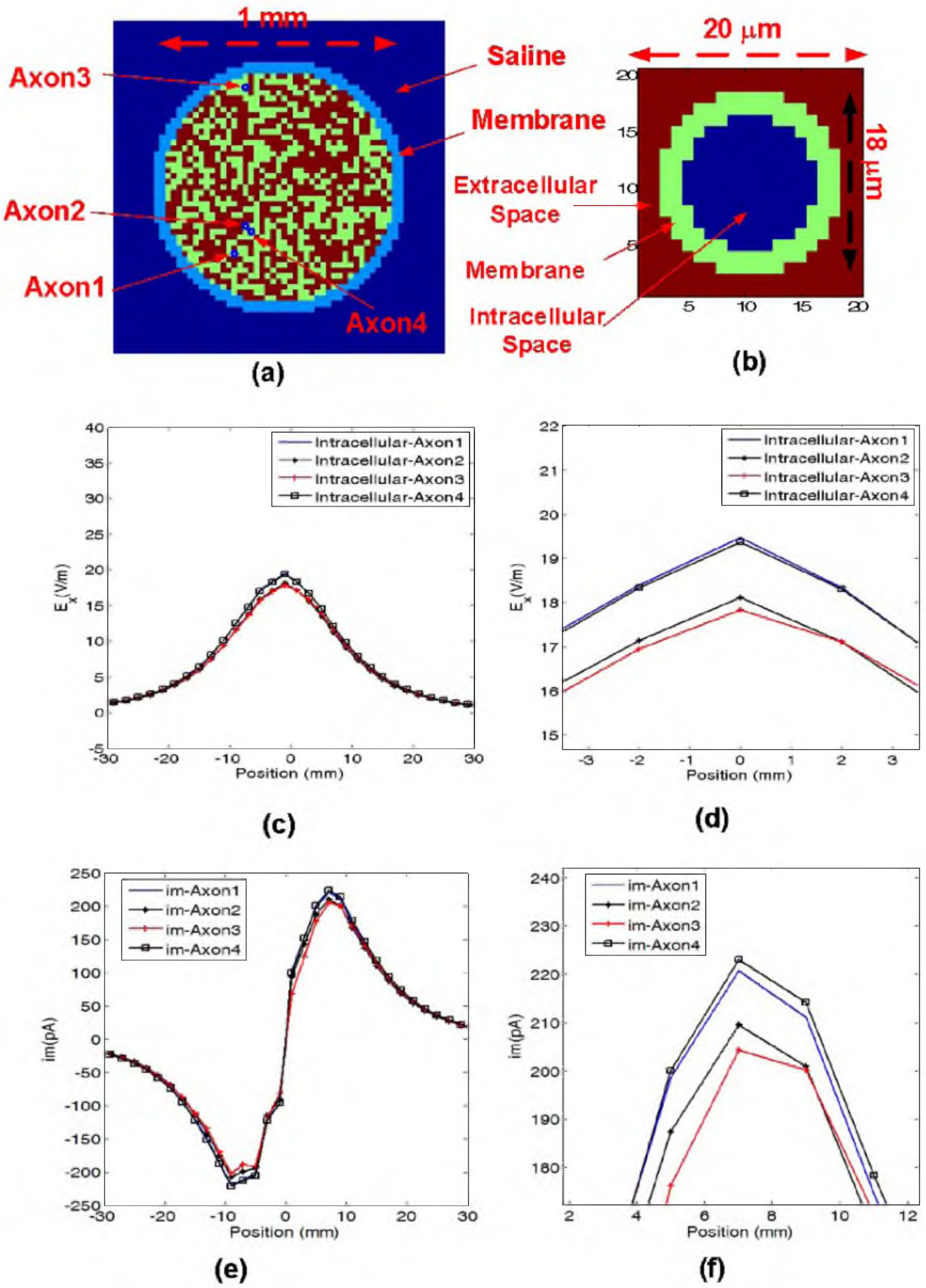

Figure 9.15. Effect of axon position: (a) Cross-section view of the nerve bundle with 600 axons. (b) Cross-section view of the each axon consist of intracellular and extracellular space separated by membrane. (c) Induced electric field E_x along the nerve for four selected axons (1-4). (d) Zoomed E_x plot near the x = 0 mm. (e) Transmembrane current i_m along the nerve for four selected axons (1-4). (f) Zoomed i_m plot near the x = 7 mm.

electric field. However, it is shown using the proposed numerical modeling of the saline embedded nerve that the field distribution and values vary in effect to the saline (conductive tissue) distribution across the nerve. Moreover, using a cable model of the nerve, the stimulation sites are studied as a function of nerve termination impedance. These simulations explain the trends seen in the stimulation threshold variation for Experiment 4 (Chapter 8).

Efficacy of the magnetic stimulation can be characterized by the change in transmembrane potential due to induced electric field. Therefore, simulations are performed with the heterogeneous model of the frog's sciatic nerve to study the coupling effect between densely packed axons inside the nerve bundle. The study is performed for the myelinated axons and it is shown that peak transmembrane potential is achieved at the Ranvier node of the myelinated axon. However, for the unmyelinated axon, the peak transmembrane potential coincides with the peak of $\frac{\partial E_x}{\partial x}$.

To simulate large simulation models (10 cm x 10 cm x 10 cm), the multiresolution impedance method is proposed and developed, which can achieve high resolution (μm), including the axon membrane and intracellular space. It is seen that more than 8% difference in induced field and transmembrane current is achieved for the proximal axons.

9.10 Conclusion

In this work, the impedance method is proven an effective algorithm to simulate the effect of tissue inhomogeneity on the induced electric field in intracellular and extracellular space. Using numerical modeling of the frog's sciatic nerve, it is shown that the fiber density, presence of the myelination layer, and location of the Ranvier node play an important role in determining the change in transmembrane potential due to magnetic stimulation.

For these simulations, single diameter axons are used. However, in the future, more realistic nerve models can be used to study the effect of statistically distributed Ranvier node location on the induced field. The frog's sciatic nerve is a simple structure with no fascicle. Therefore, to design and optimize the magnetic coil for the mammalian animals (human, cat, rat), numerical models need to be created for multifascicular sciatic nerve, which is the key motivation for Chapter 10.

9.11 References

[1] T. Pashut, S. Wolfus, A. Friedman, M. Lavidor, I. Bar-Gad, Y. Yeshurun, and A. Korngreen, "Mechanisms of magnetic stimulation of central nervous system neurons," PLoS Comput. Biol. 7 (2011) e1002022.

[2] T.A. Wagner, M. Zahn, Alan J. Grodzinsky, and A. Pascual-Leone, "Three-dimensional head model Simulation of transcranial magnetic stimulation," IEEE Transactions on Biomedical Engineering, vol. 51, no. 9, pp. 1586-1598, Sept. 2004.

[3] Mai Lu, S. Ueno, T. Thorlin, and M. Persson, “Calculating the activating function in the human brain by transcranial magnetic stimulation,” IEEE Transactions on Magnetics, vol. 44, no. 6, pp. 1438-1441, June 2008.

[4] Jianbin Zheng, Linxia Li, and Xiaolin Huo, “Analysis of electric field in real rat head model during transcranial magnetic stimulation,” in Proc. of IEEE-EMBS, 17-18 Jan. 2006, pp. 1529-1532.

[5] Shuo Yang, Guizhi Xu, Lei Wang, Yaohua Geng, Hongli Yu, and Qingxin Yang, “Circular coil array model for transcranial magnetic stimulation,” IEEE Transactions on Applied Superconductivity, vol. 20, no. 3, pp. 829-833, June 2010.

[6] Mai Lu and S. Ueno, “Calculating the electric field in real human head by transcranial magnetic stimulation with shield plate,” Journal of Applied Physics , vol. 105, no. 7, pp. 07B322-07B322-3, Apr 2009.

[7] V. T. Z. Krasteva, S. P. Papazov, and I. K. Daskalov, “Peripheral nerve magnetic stimulation: Influence of tissue non-homogeneity,” BioMed. Eng. Online, vol. 2, p. 19, 2003.

[8] Seichi Tsuyama, Akira Hyodo, M. Sekino, T. Hayami, S. Ueno, and K. Iramina, “The numeric calculation of eddy current distributions in transcranial magnetic stimulation,” in Proc. of IEEE EMBS, 20-25 Aug. 2008, pp. 4286-4289.

[9] Shuo Yang, Guizhi Xu, Lei Wang, Yong Chen, Huanli Wu, Ying Li, Qingxin Yang, “3D realistic head model simulation based on transcranial magnetic stimulation,” in Proc. of IEEE EMBS, Aug. 30 2006-Sept. 3 2006, pp. 6469-6472, .

[10] Mai Lu, S. Ueno, T. Thorlin, and M. Persson, “Calculating the current density and electric field in human head by multichannel transcranial magnetic stimulation,” IEEE Transactions on Magnetics, vol. 45, no. 3, pp. 1662-1665, March 2009.

[11] P. Basser and B. Roth, “Stimulation of a myelinated nerve axon by electromagnetic induction,” Medical and Biological Engineering and Computing, vol. 29, pp. 261-268, 1991.

[12] K. P. Esselle and M. A. Stuchly, “Neural stimulation with magnetic fields: Analysis of induced electric fields,” IEEE Transactions on Biomedical Engineering, vol. 39, no. 7, pp. 693-700, July 1992.

[13] N. Orcutt and O. P. Gandhi, “A 3-D impedance method to calculate power deposition in biological bodies subjected to time varying magnetic fields,” IEEE Transactions on Biomedical Engineering, vol. 35, no. 8, pp. 577-583, Aug. 1988.

[14] SS Nagarajan, DM Durand, and K. Hsuinghsu, “ Mapping location of excitation during magnetic stimulation effects of coil position,” Ann Biomed Eng 1997, vol. 25, no. 1, pp. 112-125.

[15] M. Eberdt, P.K. Brown, and G. Lazzi, “Two-dimensional SPICE-linked multiresolution impedance method for low-frequency electromagnetic interactions,” IEEE Transactions on Biomedical Engineering, vol. 50, no. 7, pp. 881-889, July 2003.

[16] S Y Chiu, J M Ritchie, R B Rogart, and D Stagg, “A quantitative description of membrane currents in rabbit myelinated nerve,” J Physiol., vol. 292, pp. 149-166, Jul 1979.

[17] Donald R. McNeal, "Analysis of a model for excitation of myelinated nerve," IEEE Transactions on Biomedical Engineering, vol. 23, no. 4, pp. 329-337, July 1976.

[18] C. A. Balanis, Advanced Engineering Electromagnetics. New York: Wiley, 2012.

CHAPTER 10

A μM-RESOLUTION HETEROGENOUS TISSUE MODEL FOR THE MAGNETIC STIMULATION OF MULTIFASCICULAR SCIATIC NERVE

© 2014 IEEE. Reprinted, with permission, from: Anil Kumar RamRakhyani, Zack Kagan, Faisal Khan, David J. Warren, Richard Normann, and Gianluca Lazzi, "A μm-resolution Heterogenous Tissue Model for the Magnetic Stimulation of Multifascicular Sciatic Nerve," accepted for publication in IEEE EMBC, Aug. 2014, Chicago, USA.

10.1 Abstract

Efficacy of magnetic stimulation of the central or peripheral nervous system depends on the spatial and temporal distribution of the induced electric field generated by the magnetic coil. Therefore, accurate estimation of the induced electric field is crucial to the design and optimization of magnetic coils, particularly as the coil dimensions are reduced. In this work, we developed a numerical model of a multifascicular sciatic nerve to study the effect of tissue heterogeneity on the induced electric field. Using a multiresolution electric field solver, we can resolve feature sizes as small as $1\mu m$, allowing inclusion of the nerve membrane and the myelination layer. Preliminary results indicate that fascicle distribution and axons' proximity to each other significantly affect the magnitude and distribution of the induced electric field as compared to traditional homogeneous tissue models for field simulation.

10.2 Introduction

Neural stimulation of the central and peripheral nervous systems is an emerging stimulation technology for sensory and motor neuroprosthetic devices. Compared to electrical stimulation, which requires direct tissue contact, magnetic stimulation is noncontacting, which may result in improved longevity of the stimulating device. Magnetic stimulation, and particularly extracorporeal magnetic stimulation with large coils, has been found effective in clinical practice. Transcranial magnetic stimulation has been proposed as an alternative technique to electroconvulsive therapy for seizure and depression disorders [1]. Magnetic stimulation is also clinically studied for peripheral nerve stimulation [2] and has been commercialized to reduce neuropathic pain [3].

However, for magnetic stimulation to be effective for neuroprosthetic applications, the area stimulated must be much smaller than that possible with large, extracorporeal coils. Recently, we successfully demonstrated the magnetic stimulation of the feline's sciatic nerve via solenoid coils [4], using the ability to generate graded neuronal and muscular action potentials to illustrate its efficacy. Our present research focuses on studying the underlying mechanisms of magnetic stimulation to identify the key coil and stimulator design parameters. There have been multiple studies to investigate the theoretical value of the induced electric field [5], the efficiency of the magnetic stimulation [6], and localization of the excitation [7]. However, these studies have assumed a homogeneous tissue medium to predict the stimulation efficacy [8].

Despite these studies, we recognize that neuronal tissue is heterogeneous. Few studies have been performed to formulate the impact of the surface boundary between differing tissues on the induced electric field distribution. In particular, one study [9] expressed the analytical formulation of the induced field in three dimensions for the semi-infinite boundary between air and the tissue. However, the brain and peripheral nerves are finite-dimensional heterogeneous tissues with curved boundaries [10]. Thus, more accurate prediction of the induced electric field calls for an anatomically driven tissue model. Some studies have used finite element (FEM) based numerical models to study the tissue heterogeneity and anisotropy in peripheral nerves [11]. However, voxels with sizes on the order of $1mm^3$ have been used, which limits the complexity of the model to cm-sized tissue structures. To characterize the effect of heterogeneity inside the peripheral nerve, feature sizes of $1\mu m$ need to be resolved. Therefore, the simulation model should include different conductive mediums such as the axon's membrane, including the impact of myelination and Nodes of Ranvier, the intracellular space, and the extracellular space. To study the effect of the boundary between intracellular and extracellular regions of the axon, a modified cable model for the axon was presented [12]. The modified cable model is limited to simple geometry which has axial symmetry. To study the induced electric field for anatomically correct models [13], the numerical model needs to be created based on the histological data of the nerve.

In this work, we develop a μm-resolution numerical model of a multifascicular sciatic nerve based on a histological cross-section image [13]. The key motive for using this model is to preserve the information of fascicle distribution and to study the effect of the fascicle boundaries on the induced electric fields. We also studied the effect of densely packed, randomly distributed axons on the transmembrane current and induced field (both intracellular and extracellular) for each axon.

10.3 Magnetic Neural Stimulation

Magnetic stimulation uses the induction principle to induce current at the stimulation site (Figure 10.1 (a)). Based on electromagnetic theory, the dependence of the induced electric field $\vec{E}$ on the time varying magnetic field $\vec{B}$ can be represented by Equation 10.1. The induced electric field can be solved in terms of the magnetic vector potential $\vec{A}$ using Equation 10.2.

$$\vec{\nabla} \times \vec{E} = -\frac{\partial \vec{B}}{\partial t} = -\frac{\vec{\nabla} \times \vec{A}}{\partial t} \tag{10.1}$$

$$\vec{E}(r,t) = -\frac{\partial \vec{A}(r,t)}{\partial t} - \vec{\nabla} V(r,t) \tag{10.2}$$

where $\vec{\nabla} V(r,t)$ represents the electric field generated by the surface charge due to the tissue heterogeneity. For homogenous medium, $\vec{\nabla} V(r,t) = 0$ and analytical formulations have been presented to calculate the electric field in the homogeneous media (tissue) due to the magnetic coil [8]. However, in response to the change in tissue conductivity in the direction of induced electric field, significant surface charge can be generated at the heterogeneous interface [9]. Therefore, for the heterogeneous structure such as the multifascicular sciatic nerve, the electric field can be greatly affected by the surface charge density. In the following section, we developed the impedance network based numerical model to include the effect of interfaces between different tissues. To

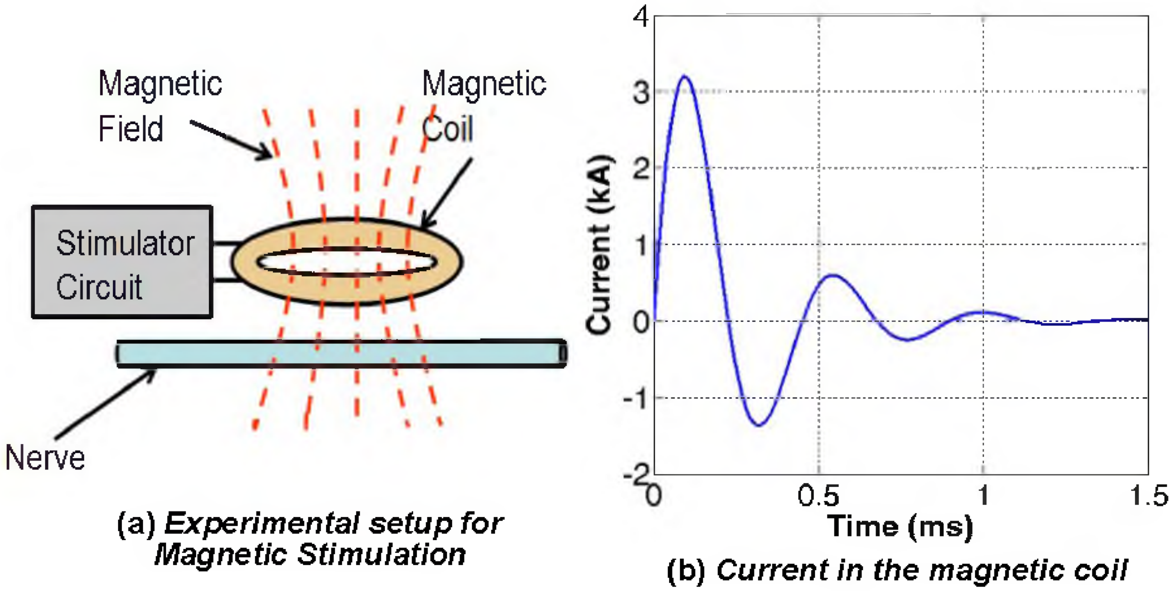

(a) *Experimental setup for Magnetic Stimulation*

(b) *Current in the magnetic coil*

Figure 10.1. Operation of magnetic stimulator: (a) Block diagram of the experimental magnetic stimulator system. (b) Generated time varying current in the magnetic coil for L_{coil} = 10.32μH, C = 450 μF, R = 80 $m\Omega$, and charging voltage = 700 V.

generate the time-varying current in the magnetic coil, a pulse discharge circuit is commonly used [5, 8]. Traditionally, magnetic stimulation requires a high current pulse ($\sim$0.5-4 kA) for very short time (100 μs to 2 ms) [4, 5]. The magnitude and shape of the current pulse can be controlled by the coil inductance L, the discharge capacitor C, and the coil resistance R (Figure 10.1(b)). The temporal distribution of the induced electric field is directly proportional to the time derivative of the current in the coil.

10.4 Impedance Method for Field Simulation

The impedance method is a frequency domain solver of the induced electric field $\vec{E}$ by solving Faraday's induction law (results from Equation 10.1). It discretizes the simulation domain into cuboid voxels (Figure 10.2) [14]. Each voxel is created using a network of lumped impedances and the value of each impedance is derived from the material properties (e.g., conductivity, permittivity), and the voxel's dimensions. For the fixed frequency and coil current, an analytical expression is used to calculate the 3-dimensional magnetic field generated by the magnetic coil. For the voxel index (i,j,k), in response to the applied time-varying magnetic field intensity ($H_x(i,j,k)$, $H_y(i,j,k)$ or $H_z(i,j,k)$) at the voxel's face, loop currents iix(i,j,k), iiy(i,j,k), and iiz(i,j,k) are calculated by the Kirchhoff voltage law. Branch currents (e.g., I_x(i,j,k), I_y(i,j,k), I_z(i,j,k)) are calculated from the loop currents and the electric field for each voxel is calculated from the branch current, dimensions, and conductivities of the each voxel.

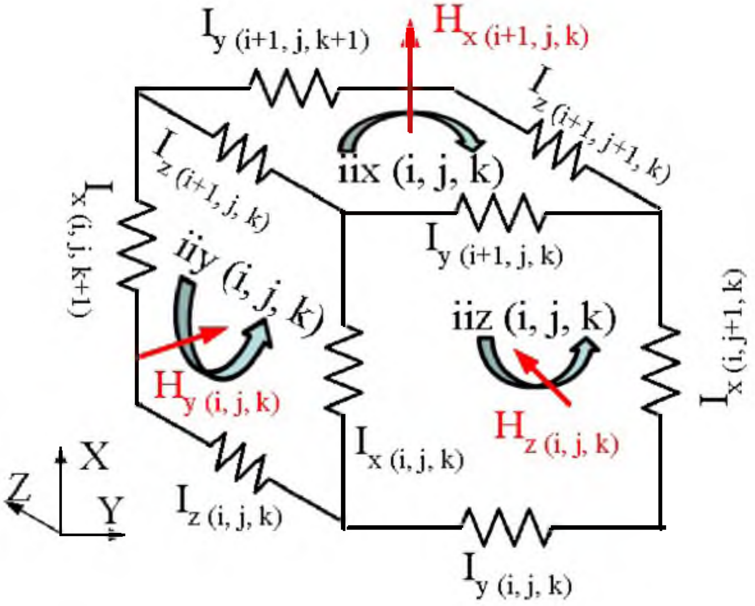

Figure 10.2. 3-dimensional voxel used for the impedance method. Loop current is calculated at each face of the cuboid in response to the time-varying magnetic field.

10.5 Modeling of Multifascicular Sciatic Nerve

The sciatic nerve is a heterogeneous tissue which consists of multiple fascicles [10]. To create a numerical model of the nerve bundle, the fascicle boundaries and their distribution inside the nerve are extracted from the anatomical cross-sectional image of the sciatic nerve [13]. A 3-dimensional model of the nerve bundle is created by extruding the cross sectional image along the nerve and is shown in Figure 10.3 (a). The distributions and boundaries of different fascicles are shown in the cross sectional view (Y-Z plane) of the nerve model (Figure 10.3(b)). The nerve is placed along the x-axis and Table 10.1 shows the conductivities of different tissue types in different directions [10]. Individual fascicles can be populated using randomly distributed axons as shown Figure 10.3(c). Moreover, a impedance network model of each axon cane be created to include the intracellular,

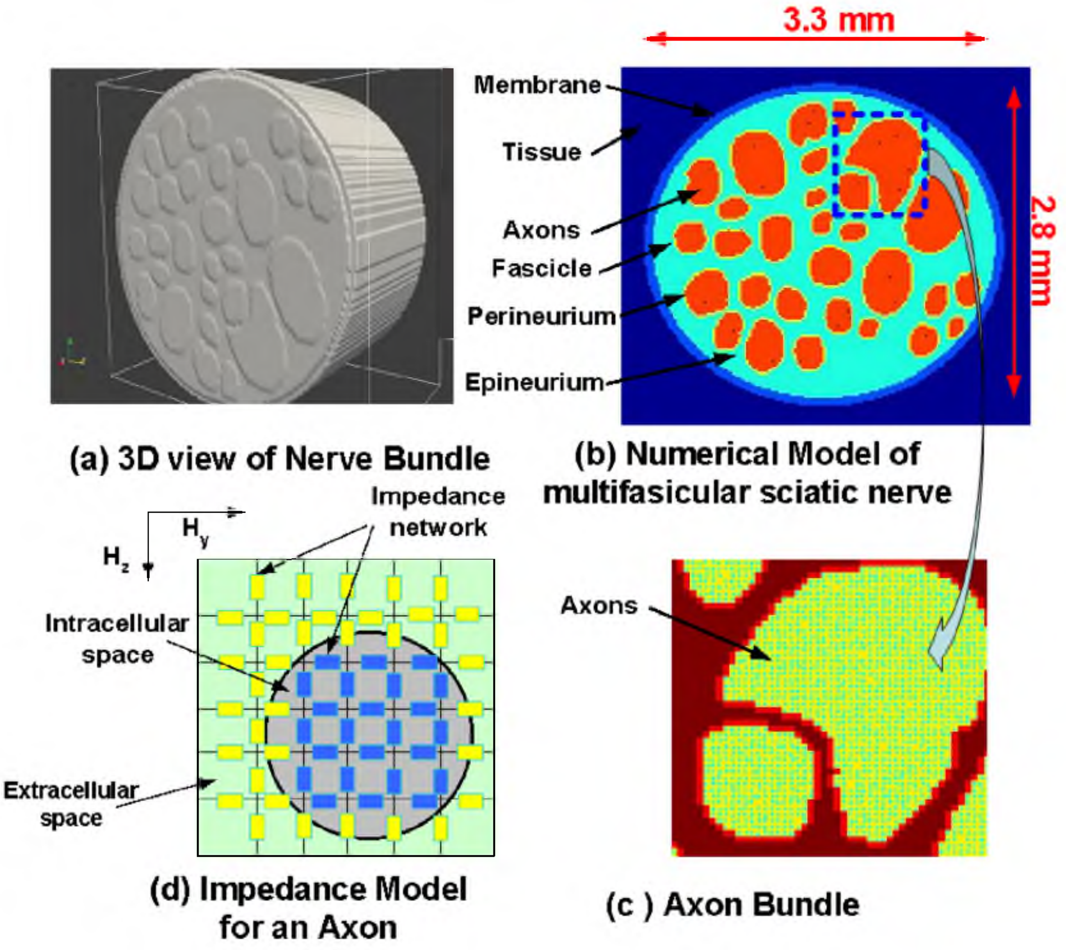

Figure 10.3. Impedance network model: (a) 3-dimensional model of the multifascicular sciatic nerve (b) cross-section view of the nerve consists of different tissue interfaces (c) distribution of the axons inside the fascicle (d) network model of the individual axon consisting intracellular, extracellular space.

Table 10.1. Tissue Property

Tissue Type	Conductivity ($\sigma_x, \sigma_y, \sigma_z$) (S/m) [10]
Surrounding tissue	(0.5, 0.5, 0.5)
Nerve membrane	(0.02, 0.02, 0.02)
Epineurium	(0.1, 0.1, 0.1)
Perineurium	(0.01, 0.01, 0.01)
Intracellular space	(0.91, 0.91, 0.91)
Extracellular space	(0.33, 0.33, 0.33)

extracellular and axonal membrane (myelination layer) regions (Figure 10.3(d)).

10.6 Simulation Model and Induced Electric Field

To correlate our simulation with our in-vivo experimental data [4], a numerical model of the solenoid coil under the same operating conditions was created (Figure 10.4 (a)). A 30-turn, 22-mm outer diameter solenoid coil was placed adjacent to the nerve. The midpoint between the inner and outer diameters of one side of the coil was centered over the nerve. The distance between the coil and the nerve was 1.5 mm (measured at point of smallest separation). The modeled nerve was 80-mm long and had an elliptical cross section of 3.3 mm by 2.8 mm. The nerve was embedded in conductive surrounding tissue (e.g., muscle). To simulate the feature size down to $1\mu m$, a multiresolution impedance method was developed. To include the effect of surrounding tissue for the cm-size magnetic coil, coarse simulation was performed with a resolution of 1 mm over the simulation space of 100 mm (x-dir) x 80 mm (y-dir) x 40 mm (z-dir). To simulate the low resolution region, multistep field simulation was performed that reduces the resolution of each simulation (e.g., 1 mm $\rightarrow$ 200 μm $\rightarrow$ 40 μm $\rightarrow$ 20 μm $\rightarrow$ 1 μm) and reduces the region of interest similarly. Figure 10.3(b) shows the cross-section view of the model at a resolution of 20 μm (in Y-Z directions) that includes the fascicle distribution and their boundaries. Along the nerves long axis (x-dir), a coarse resolution (1 mm) was used based on the average distance between nodes of Ranvier for large myelinated axons.

To evoke neuronal activity, traditional magnetic simulators utilize a pulse current in the magnetic coil. The dominant frequency components of the pulse are in the range of 500 Hz to 20 kHz. The induced electric field is directly proportional to the current and the frequency of the current in the coil. Therefore, the impedance method based field solution, at a single frequency and current, can be used to calculate the induced electric field at all frequency components of the current pulse. For our simulations, we use a sinusoidal current of amplitude 600 A at 2 kHz (fundamental frequency component of the current pulse in Figure 10.1(b)). For the 20 μm resolution heterogeneous model,

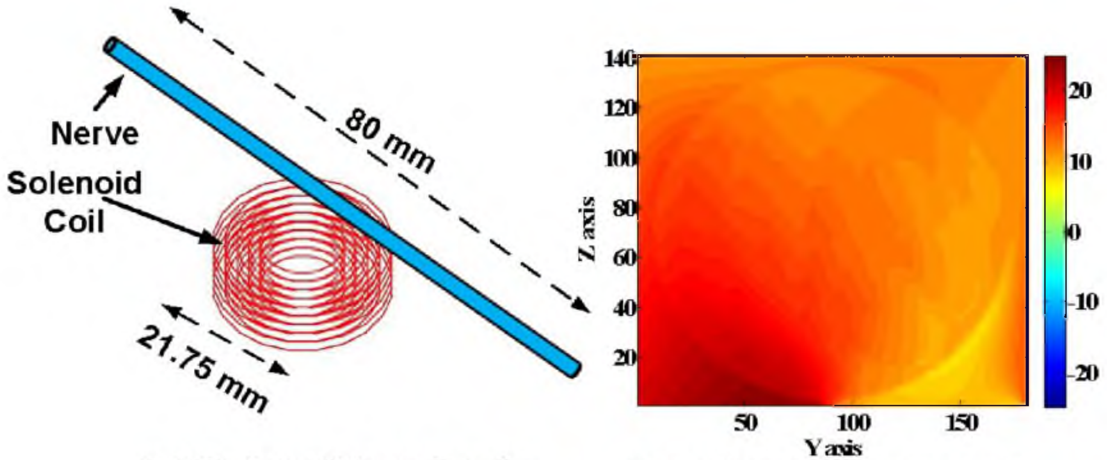

(a) 3D view of Nerve Bundle

(b) E_x Field (Heterogeneous)

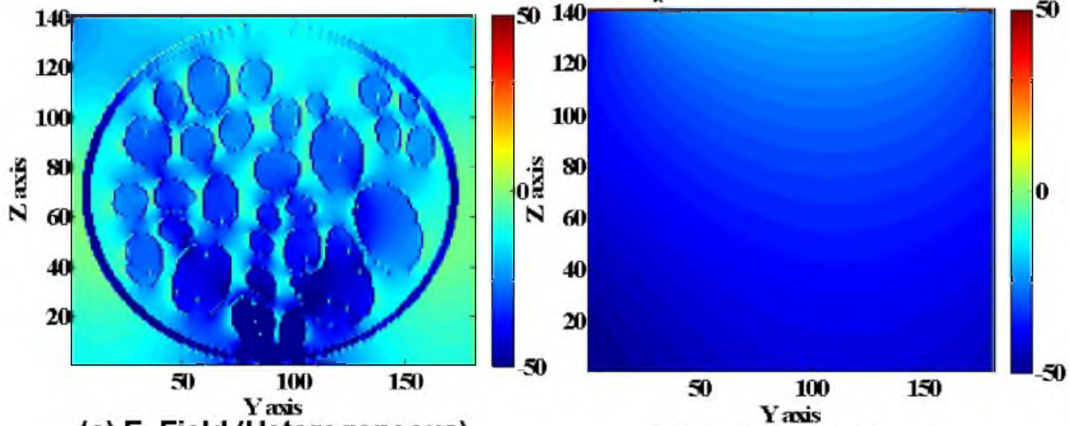

(c) E_y Field (Heterogeneous)

(d) E_y Field (Uniform)

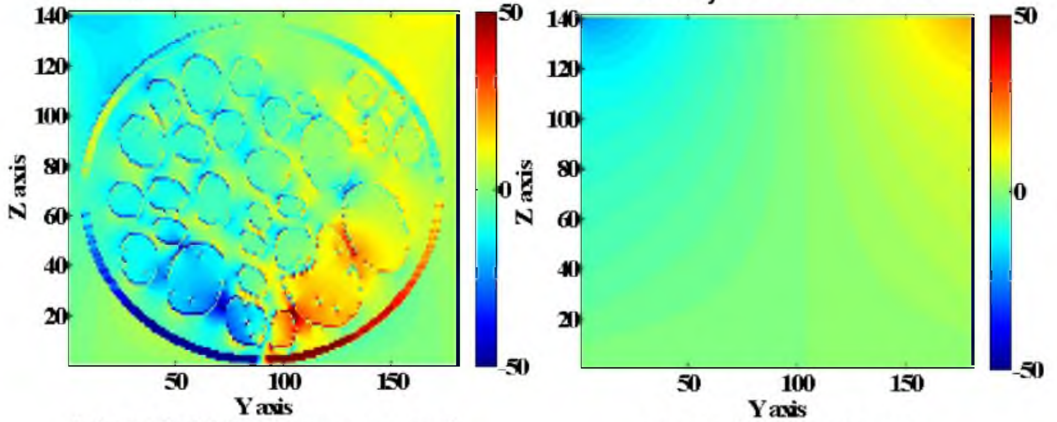

(e) E_z Field (Heterogeneous)

(f) E_z Field (Uniform)

Figure 10.4. Electric field simulation: (a) Orientation and position of the solenoid magnetic coil with respect to nerve bundle. Induced electric field in direction of (b) x- (c) y- and (d) z- directions in effect of fascicle distribution. Induced electric field in (e) y- and (f) z-directions for uniform tissue model. All fields are in V/m. Y-axis and Z-axis are the voxel count in y- and z- direction, respectively (resolution $20\mu m$).

Figure 10.4(b), (c) and (e) show the simulated value of electric field in x-, y-, and z- directions, respectively. As shown in Figure 10.4(b), due to the tissue homogeneity in the x-direction, fascicle boundaries do not affect E_x significantly. To study the impact of heterogeneity, the induced electric field was compared with the field generated in the uniform tissue model under the same operating conditions. As shown for the uniform model, the induced electric field in y- (E_y, Figure 10.4(d)) and z- (E_z, Figure 10.4(f)) directions are homogeneous. However, induced electric fields for the heterogeneous model in y- (E_y, Figure 10.4(c)) and z- (E_z, Figure 10.4(e)) directions demonstrate the field distributions featuring the effect of tissue boundaries.

10.7 The Effect of Axon Proximity

Most axons in the feline's sciatic nerve have a diameter below 20 μm which requires finer resolution voxels ($\sim 1\mu$m) to represent the intracellular and extracellular space for each individual axon. Traditionally, 1-dimensional models are used to model transmembrane current i_m due to the induced electric field [5]. The steady-state passive model of the axon calculates i_m as a function of intracellular resistance and applied electric field distribution along the nerve ($i_m = -\frac{1}{r_i}\frac{\partial E_x}{\partial x}$, where r_i is the intracellular resistance per unit length). However, these analytical expressions were derived with the assumption that the axon was placed in an infinite homogenous extracellular region, and thus there was no interaction between the axon and its surroundings. To study the impact of axon proximity, two test cases are taken. For the first case, a single axon (diameter 16-μm) was placed in a large homogeneous extracellular medium (Figure 10.5 (a)). In the second case, the axon was surrounded by the neighboring axons (Figure 10.5 (b)) to create high fill factor of $\sim$90%.

For both cases, simulation models of 94 mm x 100 μm x 100 μm are created with the spatial resolution of 1 μm in y and z directions and 1 mm in the x direction. For these simulations, the effective nodal impedance of $\sim$40 MΩ is estimated based on the membrane leakage conductance g_L of 35 mS/cm^2. As shown in Figure 10.5 (c), the intracellular electric field (E_x) along the central axon in case 1 has a higher magnitude ($\sim$32%) than central axon in case 2. This was due to the close proximity of the other axons to the central axon for case 2. Figure 10.5 (d) shows the transmembrane current i_m (intracellular to extracellular) along the axon, which reflects the proportionality of the membrane current to the derivative of the induced electric field ($i_m \propto -\frac{\partial E_x}{\partial x}$). In general, fascicles are populated with axons of different radii and can achieve high fill factor $\sim$90% as shown in case 2. This increases the interaction and coupling between different axons. Therefore, electric field simulation for the homogeneous models cannot provide accurate estimation of the induced electric field and requires numerical simulation as shown in this work.

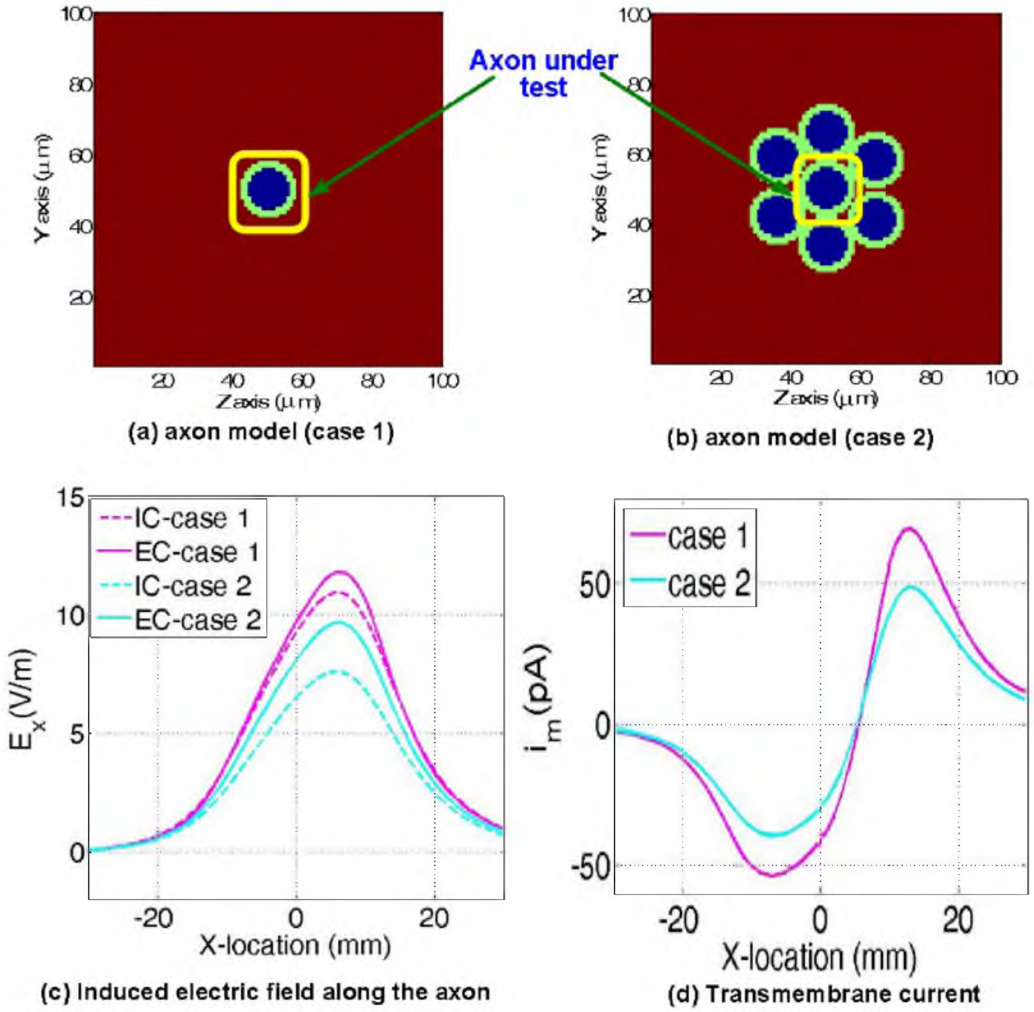

Figure 10.5. Cross section view (Y-Z plane) of the numerical model for (a) a single axon model in case 1, and (b) a multi-axon model in case 2. (c) Intracellular (IC) and extracellular (EC) induced electric field (E_x) for case 1 and case 2. (d) Transmembrane current (i_m) along the axon for the selected axon in case 1 and case 2. Due to the axon proximity, intracellular induced electric field for case 2 has ~32% lower than the electric field for the case 2.

10.8 Conclusion

In this work, we created and simulated a multiresolution numerical model of a multifascicular sciatic nerve to study the effect of fascicle distributions and axon proximity on the magnetically-induced electric field. It was shown that heterogeneity in the different regions (membrane and axons) of the nerve can significantly alter the electric field. For the densely populated (fill factor ~90%) axons inside fascicle, the transmembrane current and induced electric field was ~32% lower than the values for the axon placed in the homogeneous extracellular medium. In the future, we intend to increase the complexity of our numerical model by populating the fascicles with different radii axons based on their statistical distribution [10] to represent an even more realistic sciatic nerve. With this model, we can investigate if mm-size magnetic coils can achieve more selective stimulation and provide a more physiologically normal recruitment order. Further, we believe that through these stimulations we can design and optimize magnetic coils and will subsequently compare the simulated neuronal recruitment results.

10.9 References

[1] M. Sekino and S. Ueno,"Comparison of current distributions in electroconvulsive therapy and transcranial magnetic stimulation," Journal of Applied Physics, vol. 91, no. 10, pp. 8730-8732, May 2002.

[2] K Puvanendran K and R. Pavanni, "Clinical study of magnetic stimulation of peripheral nerves," Ann Acad Med Singapore, 1992 May, vol. 21, no. 3, pp. 349-53.

[3] Magstim,"Peripheral Nerve Stimulation (PNS)", [Online] *Available:"http://www.magstim.com/techniques/peripheral-nerve-stimulation*, February, 2014.

[4] Z. B. Kagan, A. K. RamRakhyani, R. A. Normann, G. Lazzi, F. Khan, and D. J. Warren,"In vivo and in vitro peripheral nerve stimulation via electromagnetic induction," Annual meeting of Biomedical Engineering Society, Sept. 2013.

[5] P. Basser and B. Roth, "Stimulation of a myelinated nerve axon by electromagnetic induction," Medical and Biological Engineering and Computing, vol. 29, pp. 261-268, 1991.

[6] K.-H. Hsu, S. Nagarajan, and D. Durand, "Analysis of efficiency of magnetic stimulation," IEEE Transactions on Biomedical Engineering, vol. 50, no. 11, pp. 1276-1285, 2003.

[7] S. S. Nagarajan, D. M. Durand, and Kai Hsuing-Hsu, "Mapping location of excitation during magnetic stimulation: Effects of coil position," Annals of Biomedical Engineering January/February 1997, Volume 25, Issue 1, pp 112-125.

[8] B. J. Roth, L. G. Cohen, M. Hallett, W. Friauf, and P. J. Basser, "A theoretical calculation of the electric field induced by magnetic stimulation of a peripheral nerve," Muscle Nerve, vol. 13, pp. 734-741, 1990.

[9] D. Durand, A.S. Ferguson, and T. Dalbasti, "Effect of surface boundary on neuronal magnetic stimulation," IEEE Transactions on Biomedical Engineering, vol. 39, no. 1, pp. 58-64, Jan. 1992.

[10] C. R. Butson, "Insights from computational neuroscience: exploring temporal and spatial domains," Ph.D. dissertation, University of Utah, Salt Lake City, UT, USA, 2006.

[11] V. T. Z. Krasteva, S. P. Papazov, and I. K. Daskalov, "Peripheral nerve magnetic stimulation: Influence of tissue non-homogeneity," BioMed. Eng. Online, vol. 2, p. 19, 2003.

[12] S. S. Nagarajan, and D. M. Durand, "A generalized cable equation for magnetic stimulation of axons," IEEE Transactions on Biomedical Engineering, vol. 43, no. 3, pp. 304-312, March 1996.

[13] The McGill Physiology Virtual Lab, "Nerve Anatomy", [Online] *Available:http://www.medicine.mcgill.ca/physio/vlab/cap/nerve-anat.htm*, august, 2008.

[14] N. Orcutt, and O. P. Gandhi, "A 3-D impedance method to calculate power deposition in biological bodies subjected to time varying magnetic fields," IEEE Transactions on Biomedical Engineering, vol. 35, no. 8, pp. 577-583, Aug. 1988.

CHAPTER 11

CONCLUSION

11.1 Summary of Results

In this work, we proposed and demonstrated efficient magnetic coils for biomedical applications. Wireless power transfer (WPT) and data telemetry, which have been proven essential for removing transcutaneous wiring from implantable devices, are considered the key applications to improve the capability of current designs. Our work is primarily motivated by the design challenges in wireless power and telemetry systems for an epiretinal prosthesis implant [1]. Recently, the implant was commercialized to provide partial vision to patients with retinitis pigmentosa (RP) or age-related macular degeneration. The commercialized system, which uses a two-coil-based wireless power transfer system, is limited to a power transfer efficiency of less than 30%. The design used a metallic implant coil and can cause significant electromagnetic energy deposition in the tissue [2]. Moreover, it can interfere with other communication devices [3]. The performance of the WPT system is sensitive to the operating conditions, such as eye rotation, during device operation. To resolve some of the current limitations, we proposed a multi-coil WPT system that can improve the system performance.

In Chapter 2, we introduced a novel multi-coil based telemetry system for power and data transfer over an inductive link, and compared it with an equivalent system employing two coils. The network model and the two-port model for both the two-coil and the multi-coil systems were described, analyzed, and compared to provide insights about their performance in terms of power and data transfer. The analysis for the two-coil and the multi-coil (three-coil and four-coil) systems showed that the multi-coil configuration can be used effectively to improve the PTE and gain-bandwidth product of the system. A multi-coil system provides additional tuning parameters for the designer. It is simpler to adjust a particular configuration for achieving the maximum power transfer in the multi-coil case than in the two-coil system. In addition to the theoretical modeling, two experiments were conducted with two implant coils. For all considered designs, the experimental data show that the multi-coil (three-coil) configurations achieved more than twice the efficiency and higher gain-bandwidth-product compared to the equivalent two-coil system. Further, it is noted that all the simulation results are in close agreement with the experimental results. One significant advantage of the three-coil configuration is that it can be used to upgrade two-coil systems already implanted in patients without any requirement to modify or replace the implanted coil, providing with a nonsurgical, cost-effective higher performance alternative.

Chapter 3, we showed that a multi-coil WPT system can achieve high tolerance for the variation in magnetic coupling between an external and implant coil during WPT system operation. For the presented design example, with the same system dimensions and operating conditions, a three-coil system achieves more than 40% improvement in efficiency and 62.5% improvement in frequency bandwidth as compared to a two-coil WPT system. Due to the high Q-factor of the transmitter coil (Q_t), three-coil systems showed lower variation (average -0.6% per degree rotation) in efficiency with eye model rotation. Similarly, the three-coil design achieved a higher tolerance (average 2.2 khz per degree rotation) for frequency bandwidth as compared to variation of 7.5 khz per degree (averaged) rotation in the two-coil equivalent. However, variation in voltage gain of the two-coil (average -0.0264 per degree) and the three-coil (average -0.0217 per degree) WPT systems are similar. Moreover, a multi-coil based WPT system was shown to improve the efficiency tolerance for the variation in the driver and load resistances. It is demonstrated that due to the high Q-factor transmitter coil in the three-coil system, variation in driver and load resistance causes lesser variation in efficiency. Simulation of the presented two-coil and three-coil systems showed that the three-coil system efficiency has less than half of the variation than the two-coil design.

In Chapter 4, we aimed to reduce the absorbed electromagnetic energy inside tissue. For the proposed design example, which is motivated by the retinal prosthesis design [1], a reduction of 26% in peak 1-gram SAR and a reduction of 15% in peak 10-gram peak were achieved with the improvement of 46% in power transfer efficiency (PTE). The new three-coil design achieves the same voltage gain over frequency as the initial two-coil design without change in driver electronics, implant electronics, or system dimensions. Therefore, it can be seamlessly incorporated into existing two-coil WPT systems. The presented design example used typical dimensions for biomedical WPT systems. However, the design approach is valid for any near field WPT system to reduce the absorbed electromagnetic field in tissue.

In Chapter 5, we proposed a four-coil WPT system to replace the current retinal prosthesis WPT design, which fails to meet the federal regulations for electric field generation [3]. In this work, 37% reduction in the radiated field is achieved using a multi-coil wireless power transfer (WPT) system instead of traditional two-coil WPT design. The four-coil WPT design achieves higher power transfer efficiency and demonstrates the same voltage gain and frequency bandwidth with its two-coil equivalent WPT system over the same operating distance. This ensures the new WPT system can be seamlessly integrated with the existing electronics to reduce the time of design cycle and clinical trials of the new design.

To design a soft implantable coil to reduce mechanical stress on the surrounding tissue, we demonstrated a liquid metal coil based wireless power and data link in Chapter 5. Applications such as the retinal prosthesis often require biocompatible flexible coils for wireless telemetry links that can be deformed during implantation and conformed to the tissue. The coils described here are elastomeric (i.e., stretchable) and encased by a biocompatible polymer. Despite the relatively low conductivity of the liquid metal (relative to gold or copper), we achieved sufficient Q factor (for a given footprint) by varying the cross-sectional geometry of the wire. This liquid metal based coil can be successfully employed in a telemetry system used to deliver power to the implant coil efficiently, with the added benefit of being flexible, stretchable, and conformable. We demonstrated the use of a liquid metal coil in an inductively coupled wireless telemetry link with a power transfer efficiency of 21% and a fractional bandwidth of 5.75%, which is at the higher end of the acceptable efficiency range for a 12 mm separation between coils. Under the same operating conditions and footprint, the proposed flexible coil results in an acceptable degrade in power transfer efficiency (PTE) (reduction by 46%) compared to metal based implant coils, while achieving high flexibility and stretchability for implantation and operation.

Using the multi-coil WPT system, we have achieved an efficient, low tolerance design which causes low electromagnetic energy in the tissue and lower interference with other communication devices. Compared to traditional two-coil based WPT system, the proposed multi-coil WPT system achieves:

1. Higher power transfer efficiency (more than twice at large distances).
2. Higher data bandwidth compare to two-coil based system.
3. Lower power transfer efficiency and frequency bandwidth tolerance to coil misalignment during device operation.
4. Lower power transfer efficiency tolerance with source and load resistance during change in operating conditions.
5. Lower absorbed energy (SAR) in the tissue.
6. Lower radiated electric field from the magnetic coil to comply with the federal regulations for device commercialization.

The second application which requires efficient magnetic coil design is magnetic neural stimulation. Efficacy of the magnetic stimulation depends on the spatial and time distribution of the induced electric field. Therefore, the design of the efficient magnetic coils is essential to achieve a small dimension magnetic stimulator. With the enhancement of numerical methods to model the anatomically correct tissue model, the induced field distribution can be estimated inside the heterogeneous tissue. Threshold values (field distribution and pulse width) of the individual nerve depend on the animal model and nerve condition (in-vivo/ex-vivo). To estimate the threshold value of the nerve, we took a two-way approach in which experiments were performed on the frog‘s sciatic nerve and threshold voltage for magnetic stimulation was measured using different magnetic coils. The experiments provide us with an empirical model of the strength-duration curve of the nerve. In parallel, we developed numerical algorithms for the field simulation in the heterogeneous tissue model.

Chapter 7 is motivated by the need to correctly predict the voltage across terminals of mm size coils with ferrite core. The nonlinear effect of the magnetic core of small coils to be used for implantable magnetic neurostimulation was studied. Five ferrite-loaded coils, of different dimensions, were fabricated and tested. The implemented numerical solver demonstrated the ability to accurately predict the amplitude and waveform of the induced electric fields. For all magnetic coils, measurements show close agreement ($< 10\%$ difference) with the simulated values. The capability of these models to also correctly predict the effects of initial voltages of the capacitors on the induced field intensity and saturation time is instrumental in developing an effective magnetic neuostimulator. In fact, it is confirmed that due to the saturation of the core, the inductance of the coil changes drastically from its nonsaturated value, which causes faster decay in the induced voltage, and ultimately negatively affects the neurostimulator.

In Chapter 8, we discuss the design and optimization of the air-core based magnetic coil. We used fabricated coils for ex-vivo experiments with the frog’s sciatic nerve. Using a 23.5 mm diameter solenoid coil, successful stimulation of the frog’s sciatic nerve was achieved at the 115 V charging voltage. We also discussed the stimulation thresholds for the five magnetic neural stimulation experiments to study different design parameters. It is shown that magnetic stimulation elicits similar neural activity as the electrical stimulation and its efficacy can be characterized by the recruitment curve of the recorded EMG and resultant muscle force. Similar to electrical stimulation, magnetic stimulation thresholds also follow a strength-duration curve. Thus, for the derived S-D curve, the coils can be optimized under the limitation of dimensions, energy requirements, and system constraints. Moreover, it is shown that the stimulation threshold strongly depends on the surrounding conductive media and nerve position with respect to the magnetic coil.

Chapter 9 presents the numerical modeling of the nerve and surrounding media to study the effect of tissue heterogeneity and system boundaries. In this work, an impedance method was shown as an effective algorithm to simulate the effect of tissue inhomogeneity on the induced electric field in intracellular and extracellular space. Using numerical modeling of the frog's sciatic nerve, it was shown that the fiber density, presence of the myelination layer, and location of the ranvier node play an important role in determining the change in transmembrane potential due to magnetic stimulation. For these simulations, single diameter axons are used. However, in the future, a more realistic nerve model can be used to study the effect of statistically distributed ranvier node locations on the induced field. The frog's sciatic nerve is a simple structure with no fascicle. Therefore, to design and optimize the magnetic coil for the mammalian animals (human, cat, rat), numerical models need to be created for multifascicular sciatic nerve, which is the key motivation for Chapter 10.

In Chapter 10, we created and simulated a multi-resolution numerical model of a multifascicular sciatic nerve to study the effect of fascicle distributions and axon proximity on the magnetically-induced electric field. It was shown that heterogeneity in the different regions (membrane and axons) of the nerve can significantly alter the electric field. For the densely populated (fill factor $\sim$90%) axons inside fascicle, the transmembrane current and induced electric field were $\sim$32% lower than the values for the axon placed in the homogeneous extracellular medium.

Using ex-vivo experiments with the frog's sciatic nerve, we have developed a good understanding of stimulation mechanism. Our conclusions based on the different ex-vivo experiments are as follows:

1. Due to the saturation of the core, ferrite-core based magnetic coil demonstrate nonlinear inductance. This causes faster decay in the induced voltage, and ultimately has a negative effect on the neurostimulator. Therefore, we have not seen any stimulation using magnetic-core based solenoid magnetic coils.

2. The magnetic stimulation elicits similar responses (EMG and generated force) to electric stimulation, and the stimulation threshold depends on the position of the nerve end with respect to the E_{max} location (position at which the induced field along the nerve is maximum).

3. High impedance nodes can be created by placing the suture at the nerve end. The nerve termination can alter the stimulation site and threshold.

4. Distribution of the surrounding conductive media with respect to the nerve plays an important role in the generation of the induced electric field (Experiment 1 and 4).

5. Similar to the electrical stimulation, magnetic stimulation can also be characterized based on the strength-duration curve (Experiment 5). The parameters of the S-D curve depend on the coil, the animal model, and the experimental setup (position of the coil).

Similarly, we have demonstrated that the traditional approach of field calculation in a homogeneous model does not reflect the magnetic coil's performance. We have used numerical models of the heterogeneous tissue model to study the effect of tissue boundaries

1. Height of the Ringer solution with respect to nerve diameter, position of the nerve end, and termination impedance plays an important role in the stimulation threshold and site.
2. Fiber density, presence of the myelination layer, and location of the ranvier node play an important role in determining the change in transmembrane potential due to magnetic stimulation.
3. For the mammalian nerve, fascicle boundaries and fiber distribution alter the induced current distribution. They cause a significant difference in the simulated induced electric field compared to the analytical solution for homogeneous tissue model.

11.2 Future Work

In our current implementation of wireless powered systems, we have taken the equivalent model of the driver and implant electronics, and focused primarily on the design of efficient magnetic coils using derived analytical solutions. However, in the future we intend to replace the WPT system of existing commercial medical devices (e.g., retinal prosthesis, cochlear implant, spinal cord neurostimulator) using the proposed multi-coil WPT equivalent. We believe that by taking the step to commercialization, the proposed multi-coil approach can provide an efficient and safe WPT system for implantable medical devices. On the pathway to commercialization, we intend to perform the following tasks:

1. Design an efficient driver circuit (e.g., class E power amplifier) to deliver the energy from the DC battery to the driver coil.
2. Develop a data communication link to utilize high frequency bandwidth supported by the multi-coil link for the data transfer between external and implanted units.
3. Design and optimize a flexible implant coil for the multi-coil WPT system. The design will increase efficiency in WPT systems with flexible coils.

On the other hand, to design a low power mm-size magnetic stimulator for neuronal structures, accurate field estimation needs to be included in the optimization step. Therefore, our current models need to be extended to achieve the following goals:

1. Study the effect of membrane capacitance in the heterogeneous model for its effect on the temporal distribution of the induced field. The dielectric constant of different tissues can be taken from a nerve model [4, 5].
2. Develop of the numerical models of feline's sciatic nerve based on the histological data [6].
3. Utilize of numerical tool such as NEURON to include the nonlinear behavior of the axon, and estimate the stimulation threshold for the magnetic stimulation.
4. Estimate of the strength-duration curve for the heterogeneous sciatic nerve to optimize the magnetic coil for small dimensions and low energy stimulation.

Therefore, in the future, we intend to increase the complexity of our numerical model by populating the fascicles with different radii axons based on their statistical distributions [6] to represent an even more realistic sciatic nerve. With this model, we can investigate if mm-size magnetic coils can achieve more selective stimulation and provide a more physiologically normal recruitment order. Further, we believe that through these stimulations we can design and optimize magnetic coils and will subsequently compare the simulated neuronal recruitment results.

11.3 References

[1] Kuanfu Chen, Zhi Yang, Linh Hoang, J. Weiland, M. Humayun, and Wentai Liu, "An integrated 256-channel epiretinal prosthesis," IEEE Journal of Solid-State Circuits, vol. 45, no. 9, pp. 1946-1956, Sept. 2010.

[2] V. Singh, A. Qusba, A. Roy, R. Castro, K. McClure, R. Dai, R. Greenberg, J. Weiland, M. Humayun, and G. Lazzi, "Specific absorption rate and current densities in the human eye and head induced by the telemetry link of an epiretinal prosthesis," IEEE Transactions on Antennas and Propagation, vol. 57, no. 10, pp. 3110-3118, Oct. 2009.

[3] Federal Communication Commission, "Second sight medical products, inc. request for waiver letter," 2011, http://www.fcc.gov/document/secondsight-medicalproducts-inc-request-waiver-letter.

[4] F. Rattay, M. Aberham, "Modeling axon membranes for functional electrical stimulation," IEEE Transactions on Biomedical Engineering, vol. 40, no. 12, pp. 1201-1209, Dec. 1993.

[5] K. R. Foster, "Dielectric Properties of Tissues," The Biomedical Engineering Handbook: Second Edition. Ed. Joseph D. Bronzino, Boca Raton: CRC Press LLC, 2000.

[6] Michael Benjamin Christensen,"Evaluation of inflammation and morphometric parameters associated with neural device implantation in the sciatic nerve," Ph.D. dissertation, Dept. Electr. Eng., University of Utah, Salt lake city, UT, USA, 2011.

[7] T. Pashut, S. Wolfus, A. Friedman, M. Lavidor, I. Bar-Gad, Y. Yeshurun, A. Korngreen, "Mechanisms of magnetic stimulation of central nervous system neurons," PLoS Comput. Biol. 7 (2011) e1002022.

[8] Duke University, "NEURON for computer simulations of neuron and neural networks," [Online]. Available:http://neuron.duke.edu/, February 11, 2011.

APPENDIX A

OPTIMIZATION OF OPERATING FREQUENCY FOR WIRELESS TELEMETRY SYSTEM

Efficiency of the wireless power transfer increases with the Q-factors of the magnetic coils [1]. Typically, the Q-factor increases with the operating frequency. However, increasing the operating frequency increases the AC resistance of the wire and the proximity effect [1]. Therefore, for given coil dimensions, operating frequency needs to be optimized to maximize the Q-factor of the coil. In the following sections, a circuit model of the inductor (magnetic coil) is presented to optimize the coil's Q-factor as a function of operating frequency.

A.1 Magnetic Coil Model

Magnetic coils can be modeled as an inductor in parallel with a parasitic series resistance and capacitance. For a circular coil, the self inductance with loop radius a and wire radius R (assuming $\frac{R}{a} \ll 1$) can be approximated as in Equation A.1 [1].

$$L(a,R) = \mu_o a \left[ln\left(\frac{8a}{R}\right) - 2 \right] \tag{A.1}$$

Typically, spiral coils are used for the external and implant coils for biomedical implants [1, 3]. For a planar spiral coil with N_a concentric circular loops with different radii $a_i (i = 1, 2, \ldots, N_a)$ and wire radius R, self-inductance can be calculated as:

$$L_a = \sum_{i=1}^{N_a} L(a_i, R) + \sum_{i=1}^{N_a} \sum_{j=1}^{N_a} M(a_i, a_j, \rho = 0, d = 0)(1 - \delta_{ij}) \tag{A.2}$$

where $\delta_{ij} = 1$ for $i = j$ and $\delta_{ij} = 0$ otherwise.

$$M(a,b,\rho,d) = \pi\mu_o\sqrt{ab}\int_0^{\infty} J_1\left(x\sqrt{\frac{a}{b}}\right) J_1\left(x\sqrt{\frac{b}{a}}\right) \times J_0\left(x\frac{\rho}{\sqrt{ab}}\right) exp\left(-x\frac{d}{\sqrt{ab}}\right) dx \tag{A.3}$$

where J_0 and J_1 are the zeroth and first-order Bessel functions .

A.1.1 Parasitic Capacitance

The parasitic capacitance of a spiral coil causes self-resonance and limits the operating frequency of the inductor. For a multilayer solenoid with N_a layers and N_t turns per layer, stray capacitance is approximated by Equation A.4 [1].

$$C_{self} = \frac{1}{N^2}\left[C_b(N_t-1)N_a + C_m\sum_{i=1}^{Nt}(2i-1)^2(N_a-1)\right] \tag{A.4}$$

where N is total turns, C_b is parasitic capacitance between two nearby turns in the same layer and C_m is parasitic capacitance between different layers. For a tightly wound coil, parasitic capacitance between two nearby turns is

$$C_b = \varepsilon_0\varepsilon_r \int_0^{\frac{\pi}{4}} \frac{\pi D_i r_o}{\varsigma + \varepsilon_r r_o(1-cos\theta)}\, d\theta \tag{A.5}$$

$$C_m = \varepsilon_0\varepsilon_r \int_0^{\frac{\pi}{4}} \frac{\pi D_i r_o}{\varsigma + \varepsilon_r r_o(1-cos\theta)+0.5\varepsilon_r h}\, d\theta \tag{A.6}$$

where $D_i, r_0, \varsigma, \varepsilon_r, h$ are the average diameter of the coil, wire radius, thickness, relative permittivity of strand insulation and separation between two layers, respectively.

A.1.2 AC Resistance

To achieve high quality factors, inductors with low effective series resistance (ESR) are required. At high frequencies, skin and proximity effect increases the ESR. To reduce the AC resistance, multi-strand Litz wires are commonly used [1, 4]. The AC resistance of coils made of multi-strand Litz wires including skin and proximity effect can be approximated as [1]:

$$R_{ac} = R_{dc}\left(1+\frac{f^2}{f_h^2}\right) \tag{A.7}$$

where f_h is the frequency at which power dissipation is twice the DC power dissipation and is given by

$$f_h = \frac{2\sqrt{2}}{\pi r_s^2 \mu_0 \sigma \sqrt{N N_s \eta_a \beta}} \tag{A.8}$$

where R_{dc}, r_s, N_s, μ_0, β are the DC resistance of the coil, radius of each single strand, number of strands per bunch, permeability of free space and the area efficiency of the bunch, respectively. η_a is the area efficiency of the coil with width b and thickness t and can be calculated using Figure 1 cited in [1].

DC resistance of the coil with N_a coaxial layers and diameter D_i can be calculated using

$$R_{dc} = \sum_{i=1}^{Na} \rho \frac{N_t \pi D_i}{A} = \sum_{i=1}^{Na} \pi N_t D_i R_{ul} \tag{A.9}$$

where R_{ul} is the DC resistance of the unit-length Litz wire with A, R_s, N_B, N_C, N_s as wire cross-section area, maximum DC resistance of each individual strand, number of bunching operation, number of cabling operation, and number of individual strands, respectively [1, 2].

$$R_{ul} = \frac{\rho R_s (1.015)^{N_B} (1.025)^{N_C}}{A N_s} \tag{A.10}$$

A.1.3 Q-factor of the Magnetic Coil

Considering the effect of the parasitic capacitance and the AC resistance of an inductor, the Q-factor of an unloaded inductor at frequency f can be written as:

$$Q_{unloaded}(f) = \frac{\omega L_{eff}}{ESR} = \frac{2\pi f L_{self}\left(1 - \frac{f^2}{f_{self}^2}\right)}{R_{dc}\left(1 + \frac{f^2}{f_h^2}\right)} \tag{A.11}$$

where f_{self} is the self-resonating frequency of the coil. The effective series resistance (ESR) and effective inductance L_{eff} can be written as:

$$ESR = \frac{R_{ac}}{(1 - \omega^2 L_{self} C_{self})^2} \tag{A.12}$$

$$L_{eff} = \frac{L_{self}}{(1 - \omega^2 L_{self} C_{self})} \tag{A.13}$$

A.2 Q-factor versus Frequency

Under the dimension constraints (e.g., outer diameter) of the magnetic coil, the operating frequency can be optimized to maximize the Q-factor. To reduce the coil AC resistance, multi-strand Litz wire (44/100) is used (Table A.1). Figure A.1 shows the variation in Q-factor for different number of turns in the planar spiral coil. For the coil outer diameter of 4 cm, coil turns are varied from 8 to 20 in steps of 4. The coil's inductance and ESR increases with the increase in coil turns. Therefore, Figure A.1 shows that the peak in the Q-factor is due to the trade-off between the coil inductance and coil's resistance. As seen for a coil diameter of 4 cm, increasing coil turns from 12 to 16 doesn't increase the Qfactor significantly. Moreover, the value is Q-factor is stable ($< 7\%$ variation) within an operating frequency of 2-3 MHz. In our work, we kept the operating frequency at 2-3.2 MHz with 12 coil turns.

Table A.1. Litz Wire Property [2]

Parameter	symbol	Value
Strand gauge	-	AWG 44
Number of Strands	N_s	100
Insulation thickness	ζ	3 μm
Strand radius	r_s	22 μm
Operating Frequency	-	350-850 KHz
Outer Diameter	OD	0.71 mm

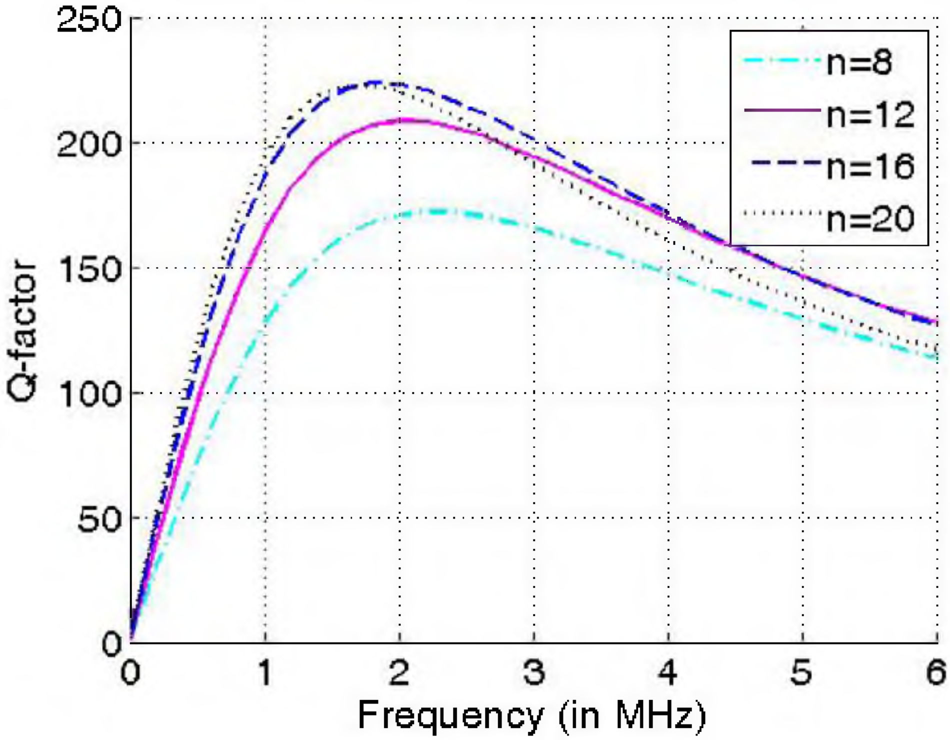

Figure A.1. Variation of Q-factor for different turns (=n) in the magnetic coil. Outer diameter of the coil is fixed to 4 cm. For turns count = 12, the Qfactor is stable (< 7% variation) over the operating range of 2-3 MHz.

A.3 References

[1] A. K. RamRakhyani, S. Mirabbasi, and M. Chiao, "Design and optimization of resonance based efficient wireless power delivery systems for biomedical implants," IEEE Trans. Biomed. Circuits Syst., vol. 5, no. 1, pp. 48-63, Feb. 2011.

[2] N. E. W. Technology, "New england wire technologies - litz wire- technical.pdf, http://www.newenglandwire.com/litz.asp.

[3] G. Wang, W. Liu, M. Sivaprakasam, M. Zhou, J. D. Weiland, and M. S. Humayun, "A dual band wireless power and data telemetry for retinal prosthesis," in Conf. Proc. IEEE EMBS,

Aug. 30-Sept.3 2006, pp. 2838.

[4] A. RamRakhyani and G. Lazzi,"On the design of efficient multi-coil telemetry system for biomedical implants," IEEE Transactions on Biomedical Circuits and Systems, vol. 7, no. 1, pp. 11-23, 2013.

APPENDIX B

EFFECT OF COMPONENT TOLERANCE

Multi-coil based wireless power transfer requires high Q-factor coils to achieve high power transfer efficiency. Therefore, magnetic coils are resonated at the operating frequency of the system using an external capacitor. Typically, the high Q-factor coils suffer from their high sensitivity to the resonating capacitor variation, which shifts the resonating frequency of the high-Q coil from the operating frequency. Therefore, in this section we study the variation in power transfer efficiency for the two-coil and its multi-coil (three-coil) equivalent. The design example is chosen based on the specifications shown in Table B.1. For both designs, the outer dimensions are kept the same for fair comparison.

Figure B.1 shows the variation of power transfer efficiency for the two-coil and three-coil wireless power transfer (WPT) system. As shown, with the change in resonating capacitor of the high-Q coil (transmitter coil in the three-coil system), the PTE drops more drastically than with zero variation. For the moderate Q-factor driver coil of the two-coil WPT system, there is less variation in PTE. However, even with the variation of ± 5 % in the resonating capacitor, the power transfer efficiency for the multi-coil systems is higher than its two-coil equivalent. Therefore, by using the

Table B.1. System Specifications

	Two-Coil		Three-Coil		
Parameters	Driver	Load	Driver	Tx	Load
$D_{out}(cm)$	4.0	1.5	4.0	3.6	1.5
N_{coil}	12	8	2	10	8
$L_{coil}(\mu H)$	5.06	0.687	0.39	3.96	0.687
$R_{coil}(\Omega)$	0.49	0.113	0.16	0.4	0.113
$R_{driver}(\Omega)$	5.1	-	5.1		
$R_{load}(\Omega)$	-	100			100
$Q_{(loaded)}$	16.9	7.24	1.39	187	7.24
Litz wire (AWG)	100/44	100/44	100/44	100/44	100/44
d (mm)	12		12		
f_{res} (MHz)	3		3		
Load Type	Parallel		Parallel		
coupling	k = 0.074		$k_1 = 0.5$, $k_2 = 0.065$, $k_3 = 0.05$		

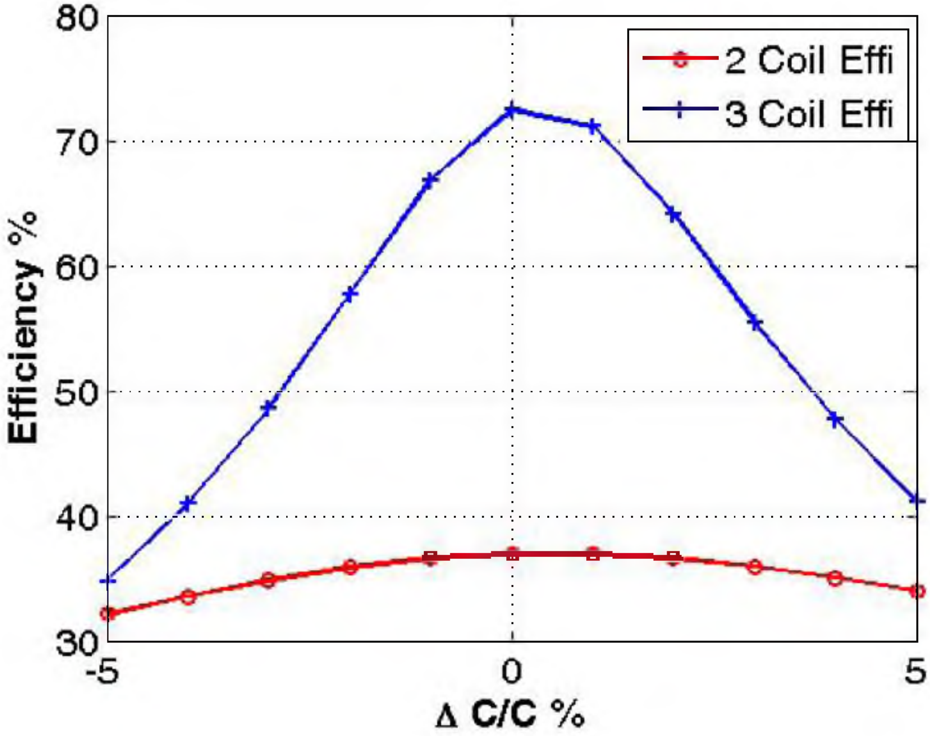

Figure B.1. Variation in power transfer efficiency (PTE) due to the change in resonating capacitor value from its ideal value. Multi-coil WPT system shows higher sensitivity to the capacitance variation due to the use of high Q coil.

low tolerance resonating capacitors (± 1 %), high performance multi-coil systems can be achieved, showing less than a 5% drop in the PTE for the peak capacitance variation.

APPENDIX C

TOROID MAGNETIC COILS FOR MAGNETIC STIMULATION

In Chapter 7, we discussed numerical modeling and coil design with a cylindrical magnetic core. It was shown that due to the solenoid core, which is an open magnetic circuit, the effective permeability of the core is much less (μ_{eff} ~4) than the core permeability (μ_r ~2000). In this section, we discuss the impact of different core structure on the induced electric field. Four structures are studied, including a toroid, a toroid with gap, an U-shape, and an E-shape magnetic core. To compare the effectiveness of different core shape, all coils are stimulated using pulse discharge circuits with an initial capacitor voltage of 5 V. The induced voltage in a test wire is recorded for different locations of the test wire with respect to the coil.

C.1 Toroid based Magnetic Coil

A toroid core is a closed magnetic circuit which confines the magnetic field to inside the core. Figure C.1 (a) shows the structure of the toroid coil with inductance 17.03 mH and resistance 900 $m\Omega$. The coil has an outer diameter of 22 mm, inner diameter of 12 mm, and height of 8 mm. Figure C.1(b) shows the stimulation trigger and induced voltage across the test wire. Due to high inductance, the rate of decay of induced voltage is very low. However, due to the core saturation, the coil's inductance decays significantly and the induced voltage drops with a much higher rate (Figure C.1(b)). The induced field depends on the current flowing in the wire and the magnetization current inside the core. Figure C.1(d) shows that due to the placement of the test wire near the coil wire, the induced voltage in the wire is higher after saturation.

Due to closed structure of the toroid, the toroid coil can't be used for the in-vivo magnetic stimulation of the nerve. Therefore, to study the induced electric field at the circumference of the toroid coil, two new locations are selected as shown in Figure C.2. For case 3, the test wire is placed outside the toroid away from the coil turns. Due to the confinement of the magnetic field inside the core, the induced voltage in the test wire for case 3 and 4 is significantly smaller than case 1 and 2. Below saturation of the core, the induced voltage is negligible. However, after saturation, the

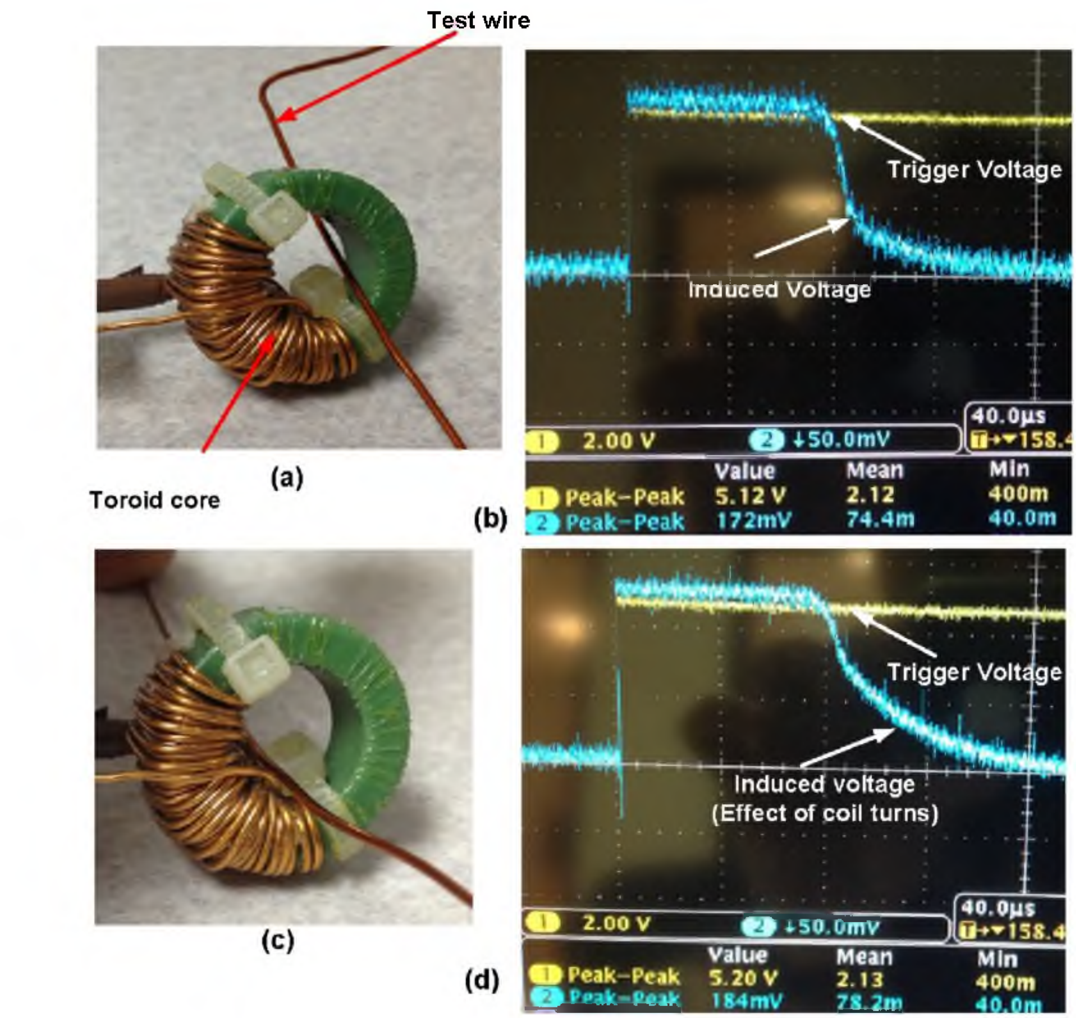

Figure C.1. Toroid coil with test wire (a) near the core (case 1) and (c) near the coil wires (case 2). Trigger and induced voltage in the test wire for (b) case 1 and (d) case 2, respectively. Due to close proximity of the coil wire near the test wire for case 2, the induced voltage after saturation is higher.

current in the coil increases significantly and coil wires can contribute to the induced electric field. For case 4, the induced voltage is higher than in case 3 due to the coil wire's proximity to the test wire.

C.2 Toroid Core with Gap

To design a magnetic coil which can allow placement of the nerve at the location of the peak electric field, a toroid coil with a small gap is created (Figure C.3). The coil has an outer diameter of 23 mm, inner diameter of 13 mm, and height of 6 mm. The gap size is 3.5 mm, which can allow the nerve to pass through it. Due to high μ_r for ferrite cores, the coils have an inductance of 36.8 μH and resistance 26 $m\Omega$. The toroid coil with a gap achieves lower inductance due to the open

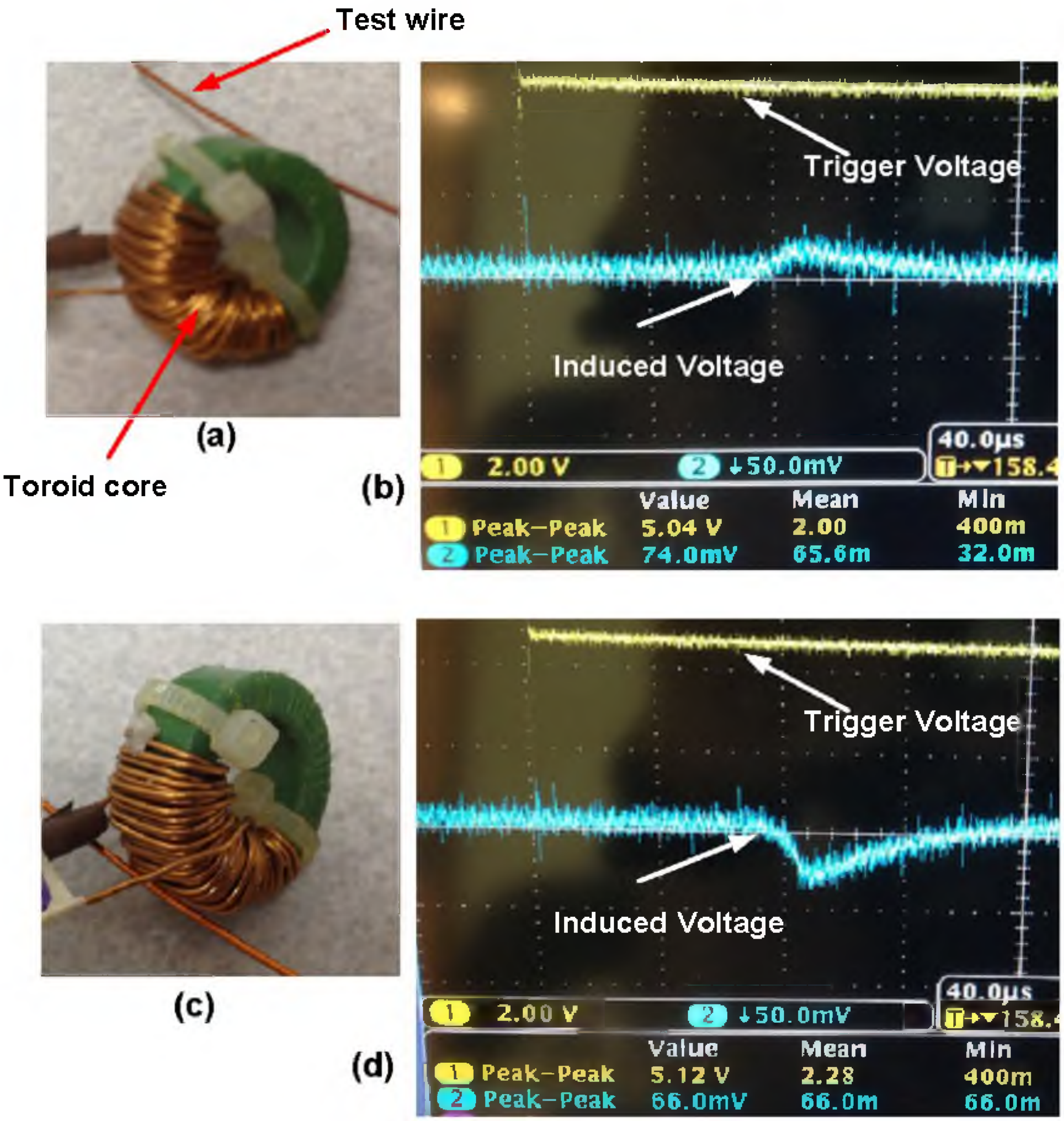

Figure C.2. Toroid coil with test wire (a) near the core (case 3) and (c) near the coil wires (case 4). Trigger and induced voltage in the test wire for (b) case 3 and (d) case 4, respectively. Due to close proximity of the coil wire near the test wire for case 3, the induced voltage after saturation is higher.

magnetic circuit. Therefore, the induced voltage decays faster than the toroid coil in Section C.1.

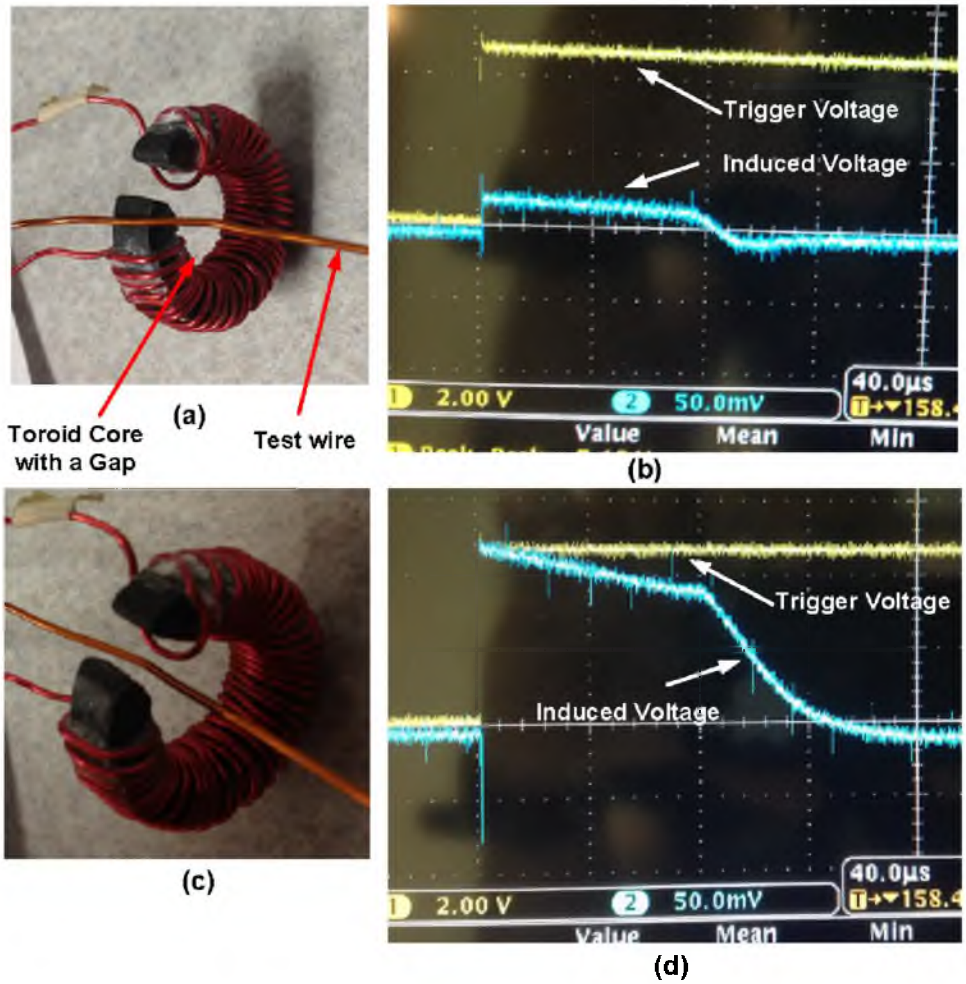

Figure C.3. Toroid coil with gap. The test wire is placed (a) outside the core (case 1) and (c) inside the core (case 2). Trigger and induced voltage in the test wire for (b) case 1 and (d) case 2, respectively. Due to placement of the test wire inside the toroid, the induced voltage for case 2 is higher compared to case 1.

C.3 U-Shape Core

To reduce the dimension of the magnetic coil and achieve high inductance using a close magnetic circuit, an U-shape core structure was chosen. As shown in Figure C.4 (a) and (c), the U-shape core can be extended to a close magnetic circuit using a second U-shape core. Using a closed structure, the inductance of the coil is increased from 1.68 μH to 26 μH. The core is 8 mm in length with a gap size of 3.5 mm. As expected, due to the increased inductance for a closed structure (case 2), the rate of decay in the induced electric field is lower than the open structure (case 1). Due to the increase in the effective μ_{eff} for the closed structure, the generated magnetic field is higher which results in a higher induced electric field.

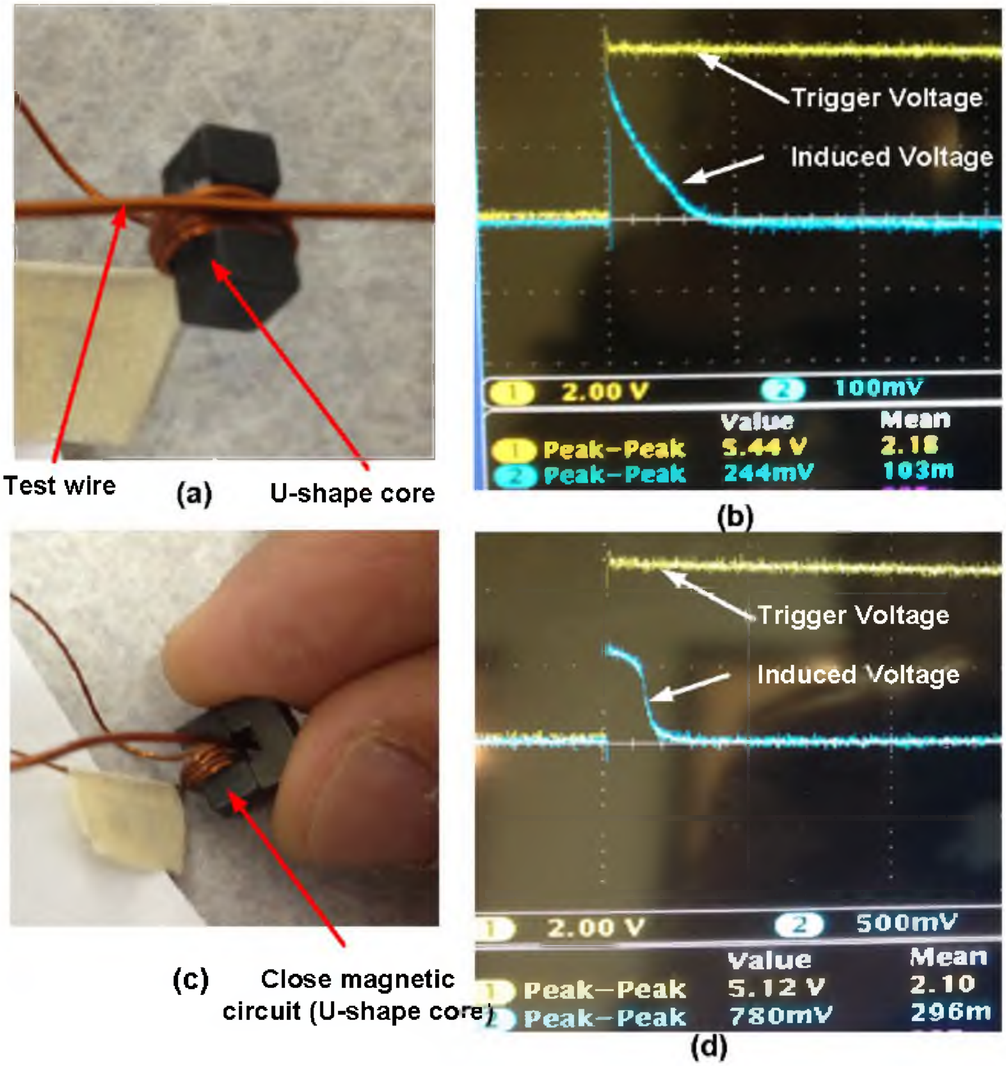

Figure C.4. U-shape core with the test wire. The test wire is placed (a) next to the open core (case 1) and (c) inside the clsoe core (case 2). Trigger and induced voltage in the test wire for (b) case 1 and (d) case 2, respectively. Due to placement of the test wire inside the toroid, the induced voltage for case 2 is higher compared to case 1.

C.4 E-shape Core based Coil

To study the effect of the magnetic field distribution inside the magnetic core, an E-shape core is used. Figure C.5(a) shows the structure of the magnetic coil for which the wire was wrapped over one arm of the E-core. For case 1, the test wire was placed near the coil wire in the first arm. For case 2, the test wire measured the induced voltage with the placement of the wire in the second arm (Figure C.5(c)). Due to the short path taken by the magnetic field, most of the magnetic flux generated by the coil stayed in the first arm of the E-core, which resulted in the higher induced voltage observed in case 1.

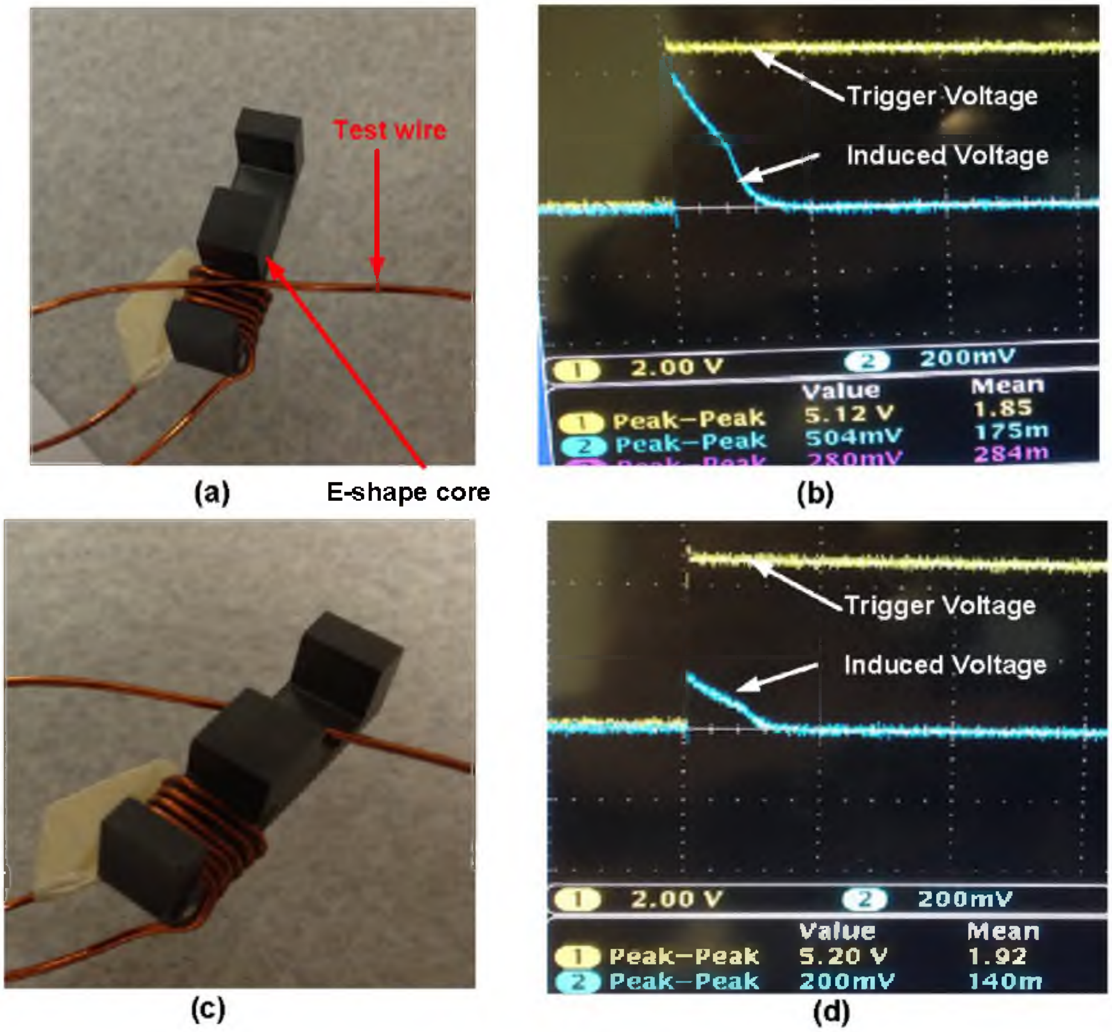

Figure C.5. E-shape core with the test wire. The test wire is placed in (a) the first arm (case 1) and (c) the second arm (case 2) of the E-core. Trigger and induced voltage in the test wire for (b) case 1 and (d) case 2, respectively. Due to placement of the test wire inside the high fluxed arm (case 1), the induced voltage for case 1 is higher compared to case 2.

To study the impact of a closed magnetic circuit on induced voltage, a second E-core was placed over the magnetic coil as shown in Figure C.6(a). Case 3 and 4 study the effect of the test wire position inside a closed magnetic structure (Figure C.6(a) and (c)). The experiments showed that placement of the test wire does not affect the induced voltage, which indicates that nerve can be placed anywhere inside the closed magnetic structure to achieve high induced field. For the closed magnetic circuit, to compare the magnetic field distribution inside the first arm (case 4, Figure C.6(c)) and second arm (case 5, Figure C.6(e)), the test wire was placed in the first and second arm respectively. Similar to case 2, the magnetic flux generated by the coil took the shorter path (least resistance) and caused the higher induced voltage in case 4 compared to case 5.

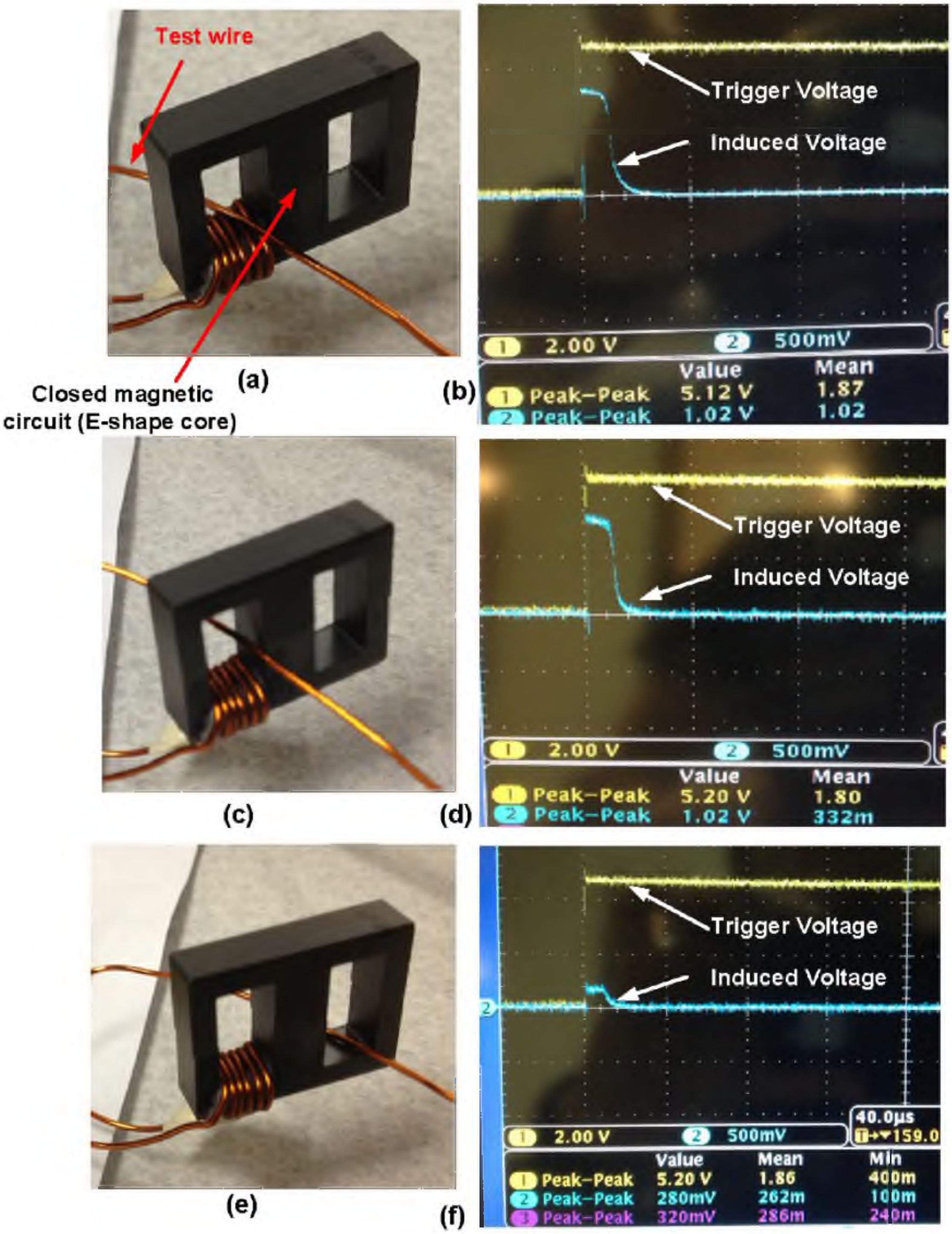

Figure C.6. E-shape core with the test wire. (a) The test wire is placed in the first arm and closed proximity of the coil (case 3). (c) The test wire is placed in arm 1 away from the coil wires (case 4). (e) The test wire is placed in the second arm (case 5) of the E-core. Trigger and induced voltage in the test wire for (b) case 3, (d) case 4, and (f) case 5, respectively. Due to placement of the test wire inside the high fluxed arm (case 4), the induced voltage for case 4 is higher compared to case 5.

C.5 Conclusion

A magnetic core increases the amount of magnetic flux generated by the unit current in the coil wire. The closed core can achieve an effective permeability μ_{eff} close to the core's permeability μ_r. However, the geometry of the closed magnetic circuits (e.g., closed toroid) does not allow the placement of the nerve inside the coil to achieve the highest induced electric field. Using a toroid core with a gap increases the possibility of nerve placement inside the coil at the expense of lowering the effective permeability μ_{eff}. Using a U-shape core, the closed magnetic circuit can be created by sliding the nerve inside the core gap and placing the second U-core to close the magnetic loop. Experiments with the E-shape core demonstrate that it generates magnetic flux that follows the least resistive path (shorter length), which can be useful when designing a magnetic coil that requires controllable flux distribution.